VILNIUS UNIVERSITY
CENTER FOR PHYSICAL SCIENCES AND TECHNOLOGY

Rokas Jasiūnas

Charge Carrier Generation and Extraction in Non-Fullerene Organic Solar Cells

DOCTORAL DISSERTATION

Natural Sciences,
Physics [N 002]

VILNIUS 2023

This doctoral dissertation will be defended in a public meeting of the Dissertation Defence Panel:

Chairman – Prof. Habil. Dr. Leonas Valkūnas (Center for Physical Sciences and Technology; Natural Sciences, Physics – N 002).

Members:
Prof. Dr. Saulius Bagdonas (Vilnius University, Natural Sciences, Physics – N 002)
Prof. Dr. Gagik Gurzadyan (Dalian University of Technology, Natural Sciences, Physics – N 002)
Prof. Dr. Vygintas Jankauskas (Vilnius University; Natural Sciences, Physics – N 002)
Dr. Karolis Kazlauskas (Vilnius University, Natural Sciences, Physics – N 002)

The dissertation shall be defended at a public meeting of the Dissertation Defence Panel at 11:00 am on 5th of January 2023 in Room/meeting room A101 of the Center for Physical Sciences and Technology.
Address: Saulėtekio av. 3, A101, Vilnius, Lithuania
Tel. +370 5 264 8884; e-mail: office@ftmc.lt

The text of this dissertation can be accessed at the libraries of Center for Physical Sciences and Technology and Vilnius University, as well as on the website of Vilnius University:
www.vu.lt/lt/naujienos/ivykiu-kalendorius

VILNIAUS UNIVERSITETAS
FIZINIŲ IR TECHNOLOGIJOS MOKSLŲ CENTRAS

Rokas Jasiūnas

Krūvininkų generacija ir ištraukimas befulereniuose organiniuose saulės elementuose

DAKTARO DISERTACIJA

Gamtos mokslai
Fizika N 002

VILNIUS 2023

Mokslinis vadovas – prof. dr. Vidmantas Gulbinas (Fizinių ir technologijos mokslų centras, gamtos mokslai, fizika – N 002).

Gynimo taryba:
Pirmininkas – prof. habil. dr. Leonas Valkūnas (Fizinių ir technologijos mokslų centras, gamtos mokslai, fizika – N 002).

Nariai:
Prof. dr. Saulius Bagdonas (Vilniaus universitetas, gamtos mokslai, fizika – N 002),
Prof. dr. Gagik Gurzadyan (Daliano technologijos universitetas, Kinija, gamtos mokslai, fizika – N 002),
Prof. dr. Vygintas Jankauskas (Vilniaus universitetas, gamtos mokslai, fizika – N 002),
Dr. Karolis Kazlauskas (Vilniaus universitetas, gamtos mokslai, fizika – N 002).

Disertacija ginama viešame Gynimo tarybos posėdyje 2023 m. sausio mėn. 5 d. 11:00 val. Fizinių ir technologijos mokslų centro A101 auditorijoje.
Adresas: Saulėtekio al. 3, LT-10257, Vilnius, Lietuva.
Tel. +370 5 264 8884; el. paštas: office@ftmc.lt

Disertaciją galima peržiūrėti Vilniaus universiteto ir Fizinių ir technologijos mokslų centro bibliotekose bei VU interneto svetainėje adresu:
https://www.vu.lt/naujienos/ivykiu-kalendorius

Reginos ir Kęstučio

jaunystės svajonių vardan

CONTENTS

INTRODUCTION

Since the Industrial Revolution, global demand for electricity has grown drastically. In the last 25 years, global electricity generation has doubled, exceeding staggering 27000 terawatt-hours in 2019.[1] With the world's population expected to increase by more than 20% to about 10 billion people by 2050, demand for electricity is unlikely to decline. Rather, it is expected to increase by ~30% over the next two decades.[1] Historically, coal and other fossil fuels have always been the primary source of energy and are still predominantly burned to generate electricity - accounting for more than 63% of total electricity production in 2019. However, fossil fuel combustion has several serious drawbacks, namely its finite availability[2] and, more importantly, air pollution, which leads to numerous health problems and climate change.[3] Fossil fuel combustion releases carbon dioxide into the atmosphere, where ~60% of it is permanently trapped.[4] Today, the average atmospheric CO_2 concentration is higher than at any other time in the last 3 million years, the furthest time span that can be tracked.[5] Because carbon absorbs heat that would otherwise be radiated from the Earth's surface to space, high atmospheric CO_2 level is causing global temperatures to increase and, consequently, sea levels to rise due to accelerated glacial melt. [6–9] According to some estimates, up to 20-30% of the world's species are at risk of extinction due to rising temperatures, with coral reefs particularly vulnerable.[10]

To address this unprecedented global challenge, the initiative to achieve net zero CO_2 emission by 2050 is being driven by policymakers worldwide. The initiative focuses on developing strategies to drastically reduce the use of fossil fuels, by far the most significant source of CO_2 emissions. According to its roadmap, two-thirds of the total energy supply in 2050 should come from CO_2-emission-free renewable energy sources, namely wind, bioenergy, geothermal, hydropower, and solar energy.[11] Solar energy in particular is expected to be the largest source of energy, accounting for one-fifth of the total energy supply. This should not be surprising, given the overwhelming abundance of solar radiation, which has been convincingly described by L.R. Brown: "The sunlight striking the earth's surface in just one hour deliver[ing] enough energy to power the world economy for one year."[12]

Basically, solar energy can be divided into three categories: Solar Thermal, Solar Fuels and Photovoltaic (PV). The first uses solar energy in the form of heat to generate steam and drive a turbine, similar to the use of fossil fuels.[13] The second category refers to chemical fuels produced with solar energy through photo- or thermochemical processes.[14] The third category, on the other hand, refers to the direct conversion of solar radiation into electricity. Importantly, global energy consumption is becoming highly electrified due to the increasing use of electric cooling and heating, the popularity of electric vehicles, and the digitization of most aspects of daily life.[15] The direct generation of electricity from solar radiation therefore makes photovoltaics particularly attractive as a future energy source. Today, less than 4% of all electricity is generated from solar power, but the International Energy Agency forecasts a 20-fold increase in PV capacity by 2050.[11] This is an ambitious plan, as it isequivalent to installing the world's current largest solar park roughly every day for the next decade. Nevertheless, the threat of environmental catastrophe from maintaining the status quo of burning fossil fuels for energy and the fact that there is an abundant and reliable source of energy to replace it, is driving the rapid progress of solar energy technology worldwide.

Currently, the most studied and prevalent PV technology is based on crystalline silicon (c-Si), which accounts for 95% of the total installed capacity.[16] The significant drop in the price of manufacturing crystalline silicon solar wafers, combined with the increase in their efficiency over the past decade, has made this technology attractive not only for environmental reasons, but also as a financially competitive form of power generation.[17] Nonetheless, despite its dominance, c-Si solar technology has some major drawbacks that hinder its wider adoption. First, silicon has a very low absorption coefficient, thus a relatively thick (several hundred microns) and opaque absorption layer is required for optimal device efficiency.[18] This significantly increases the final cost of the module and severely limits the application versatility of Si-based solar cells, as modules must be installed either on the ground or on a roof, preferably tilted to achieve higher efficiency, and adjacent modules must be spaced apart and therefore require a lot of space. In densely populated areas, where electricity is most needed, vacant land for solar plants is usually scarce. In addition, the production of crystalline silicon requires very high temperatures. This means that the energy payback time, i.e. the time it takes for the solar cell to produce the same amount of energy that

was required to manufacture it, is quite long – 1.5 – 2 years, depending on the location. [19]

To further increase installed PV capacity on a global scale, technologies must be developed that have mechanically and optically unique properties. For example, if the active layer were semi-transparent, it could be retrofitted into the windows of tall, glazed office buildings and generate electricity precisely where the demand is greatest – in city centers. Flexible solar cells could be built into curved surfaces, such as car roofs. Moreover, solar cells with different coulors would be much easier to integrate into urban architecture and infrastructure, if only for esthetic reasons. Of the many emerging PV technologies, organic solar cells have the particular advantage of being based on flexible, lightweight and semi-transparent materials, which actually makes these niche applications possible.[20,21] Even more, because they can be processed using solutions, they could even be printed and require very little energy to manufacture. There are estimates that the energy payback time for organic solar cells could be as little as a single day. [22]

Although organic photovoltaics (OPV) has been driven by the vision of its myriad applications for more than 30 years, it is still far from being commercialized on a large scale. The main limiting factor is its lower stability and efficiency compared to conventional solar cells. However, the latter has risen sharply in recent years and currently exceeds 18%[23,24], largely due to the introduction of a new generation of acceptor materials, which have greatly boosted academic and industrial interest in the previously slightly stagnant technology.

Despite recent breakthroughs, further technological improvements are strongly needed, but they will be difficult to achieve until the physics behind the operation of OPV devices is fully understood, especially in the case of the new generation of organic solar cells. New materials, i.e. non-fullerene acceptors, have challenged the previous understanding of charge generation. The energy needed for efficient charge generation is far below the previously assumed threshold. However, the minimal energy required for charge separation allows other physical and as yet unstudied phenomena that do not occur in older generation OPV devices. Moreover, the transport of free charge carriers in these novel devices is likely to be different, since the physical properties of, e.g. polymer acceptors are very different from the fullerene-type

acceptors. More so, conventional studies on charge transport under laboratory conditions may not be relevant in real-life, so specific working conditions should be implemented. Thus, a new in-depth analysis of numerous processes involved in energy conversion under specific conditions in devices based on non-fullerene acceptors is required. In this work, we scrutinise the operation of novel OPV devices from an optoelectronic perspective to identify physical processes that are detrimental to energy conversion and how they can be suppressed.

This thesis is organised as follows: In the next section, the aim of this thesis and the tasks for this research work are presented. Then, thesis statements are formulated, followed by a delineation of the novelty and relevance of this work. Then, a detailed introduction to organic photovoltaic technology from material, technical and physical points of view is given in an extensive literature overiew together with an introduction to the experimental methods employed in this work. And finally, the results are summerized in the Discussion and Conclusions section.

1.   The Aim of the Thesis

A recent breakthrough in OPV device technology, triggered by the replacement of an archetypal fullerene acceptor with novel acceptor molecules, has galvanized the development of OPV technology and prompted many scientific groups to set new records in energy conversion efficiency. This is usually achieved by fabricating myriad new materials for an active layer, trying ever new donor-acceptor mixtures, and fine-tuning each step of device fabrication through trial-and-error. While this leads to some success, without a detailed physical understanding of exactly how these new materials work and their limiting factors, it is difficult to significantly accelerate further development of OPV technology. Therefore, this work was carried out with the aim of investigating the main optoelectronic phenomena such as charge carrier generation, extraction, and recombination in various bulk heterojunction organic solar cells based on non-fullerene acceptors, comparing them with well-known fullerene-based devices, and identifying the fundamental-level causes that limit the energy conversion efficiency.

Specific goals of this thesis were:
- To understand the role of spatial traps in charge carrier extraction in bulk heterojunction devices.

- To uncover charge dynamics under close-to-real working conditions in organic solar cells (OSCs).
- To understand the peculiarities of free charge carrier generation in non-fullerene OSC with negligible HOMO level offset.
- To understand charge carrier generation peculiarities in state-of-the-art PM6:Y6 organic solar cells.

2. Tasks of the Research Work

To achieve these goals, specific tasks were set:

- Improve and apply a specific technique for measuring transient photocurrent that allows distinguishing between charge carrier trapping in energetical and spatial traps; evaluate the effects of energetical and spatial charge carrier trapping in fullerene and non-fullerene OPV devices.

- Upgrade and apply specific transient techniques that allow tracking of charge carrier dynamics under close-to-real working conditions; compare charge carrier mobility dynamics in fullerene and non-fullerene acceptor-based OPV devices.

- Trace with high temporal resolution the generation and recombination of free charge carriers; investigate the dependence of generation and recombination on the energy difference between donor and acceptor molecular orbitals; identify limiting factors for energy conversion.

- Investigate charge generation and its temperature dependence in state-of-the-art PM6:Y6 organic solar cell.

3. Statements of the Thesis

1. The spatial trapping effect can impede the extraction of free charge carriers from the as-cast active layer of an all-polymer organic solar cell, enhancing recombination and associated efficiency losses. The effects of spatial trapping can be significantly reduced by annealing, as demonstrated in the case of the TQ1:N2200 all-polymer solar cell.

2. Charge carrier trapping strongly influences carrier mobility in ns-µs timescale in OPV devices with high trap concentration. However, under the actual working conditions of the OPV device, constant illumination leads to the occupation of these trap states, making the mobility less time-dependent and increasing both the extraction and recombination rates. Filling low-energy state occupation does not affect the sharp decrease in mobility on a ps timescale. In highly effective non-fullerene device charge carrier trapping effect is negligible and therefore low energy state occupation has minor effect on carrier extraction.

3. Thermally activated back transfer of electrons from donor to acceptor via the highest occupied molecular orbital levels increases charge carrier recombination and reduces overall device efficiency in non-fullerene OPV devices with an energy offset between donor and acceptor HOMO levels less than ~100meV.

4. Upon excitation of acceptor Y6 in PM6:Y6 organic solar cell, charge carrier generation occurs via two different pathways that are equally efficient at room temperature - via the interfacial CT state and via the intra-moiety xCT state. The conventional pathway via the CT state is almost temperature independent, while charge carrier generation via the xCT state requires thermal support.

4. Novelty and Relevance

Novelty and relevance of this work was several-fold:

- A wide range of transient measurement techniques made it possible to study each step of the OPV device's operating cycle and to link all the different processes into a consistent story, ranging from fs to µs, for the first time for this class of materials.

- In this work, specific upgrades to conventional transient measurement techniques, namely TREFISH, transient photocurrent, and time-delayed collection field, were developed. These upgrades enabled, for the first time, the study of the spatial trapping phenomenon and the

tracking of the charge carrier dynamics under realistic working conditions of a solar cell.

- Detailed analysis of transient absorption measurements has led to the identification of a specific thermally activated recombination channel in non-fullerene OPV devices with small HOMO level offsets between donor and acceptor materials. This finding highlights the importance of carefully matching donor and acceptor energy levels to improve efficiency.

- A detailed investigation of the charge carrier generation mechanism in the PM6:Y6 blend, combining transient absorption and transient photoluminescence at various temperatures, was performed, reaching as low as 15 K for the first time. The wide temperature range has helped to uncover previously undiscovered aspects of charge generation in this state-of-the-art photovoltaic material.

LITERATURE OVERVIEW

1. PHOTOVOLTAIC EFFECT

Photovoltaic energy conversion, as the name implies, occurs through the absorption of light (*photons*) by a semiconducting material that generates electrical energy (*voltage*). In classical inorganic semiconductors, the absorption of photons results in the transfer of electrons from the valance band to the conduction band, creating an electron-hole pair. An analogous electron-hole pair is also created in organic semiconductors by a similar but, as will be discussed in detail in the following sections, slightly different pathway. Photovoltaic devices are designed to convert the energy stored in these electron-hole pairs into electrical energy.

2. CHARACTERIZATION PARAMETERS OF THE SOLAR CELL

Since energy conversion is the sole purpose of a photovoltaic device, the main criterion for evaluating a solar cell is its conversion efficiency. Given that power conversion efficiency (PCE) is highly dependent on the measurement conditions, standardized test conditions have been established in both academia and industry using Air Mass 1.5 Global (AM1.5G) radiation and a cell temperature of 25 C^0. "Air Mass" means that the solar spectrum is corrected for absorption losses in the Earth's atmosphere, while the thickness of 1.5 atmospheres corresponds to the annual average angle of incidence at mid-latitudes. "Global" means that both direct and diffuse sunlight are considered[25]. The AM1.5G spectrum (Fig.1a) has an integrated power of 1000 W/m^2, usually referred to as P_{In}, which is the power entering the solar cell.
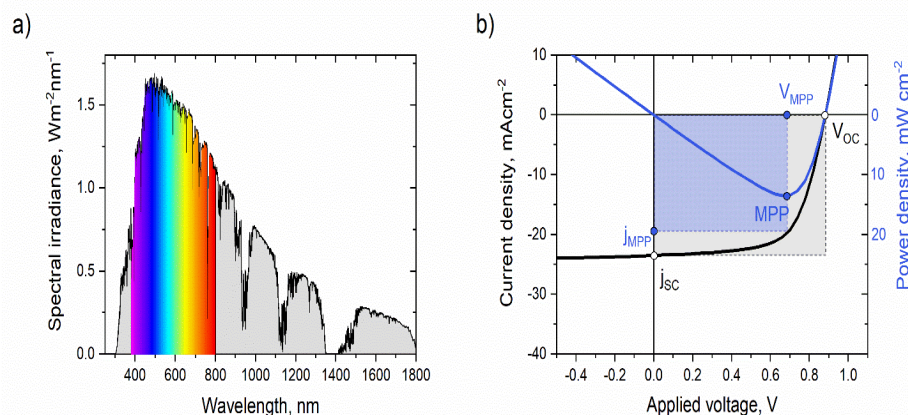
Figure 1. *a) AM1.5G solar spectrum; b) IV characteristic of PM6:Y6 organic solar cell.*

The power coming out of the solar cell is electrical power defined as the product of photocurrent and photovoltage acting on an external load. For constant illumination, such as AM1.5G, the power varies depending on the resistance of the load. Therefore, an optimal load must be determined for the maximum power (P_{max}) of each solar cell. This is usually done by measuring Current-Voltage (IV) characteristic under standard illumination (Fig.1b). The applied voltage sweeps act as a set of different loads and allows the identification of the maximum power point (MPP), i.e. the point at which the PCE is evaluated:

$$PCE = \frac{P_{max}}{P_{In}} = \frac{j_{MPP} V_{MPP}}{P_{In}} \qquad (1)$$

where, j_{MPP} and V_{MPP} refers to current-density and voltage at maximum power point, respectively.

Apart from maximum power point, minimum power points of IV curve are also of great importance for characterization of solar cells. There are two points in the IV curve where the power equals zero. First, where the applied voltage is zero, mimicking the "no load in the external circuit" conditions. The value of the current density in such a case is referred to as the short-circuit current (j_{SC}). Another extreme is when the applied voltage is set to imitate the "infinite load in the external circuit" conditions, in which case no current flows at all. Such voltage value is referred to as open-circuit voltage (V_{OC}).

The product of j_{SC} and V_{OC} gives the theoretical maximum power (P_T) of an idealized solar cell, i.e. one that has a rectangular IV curve. The ratio

$$FF = \frac{P_{MPP}}{P_T} = \frac{j_{MPP} V_{MPP}}{j_{SC} V_{OC}} \qquad (2)$$

is called the fill factor (FF) and is often used to quantify the quality of a solar cell, i.e. how similar the real solar cell is to an idealized cell. FF can be visualized as the ratio between a blue square and a grey square in Figure 1b. The closer the ratio is to unity, the better the solar cell.

In this way, PCE can be described as

$$PCE = \frac{FF j_{SC} V_{OC}}{P_{In}} \qquad (3)$$

Such a PCE definition is very convenient because each of the parameters used here is related to different physical phenomena in the active layer of a solar cell. For instance, j_{SC} depends on the total amount of photogenerated charges that can be extracted from the device and is related to light absorption efficiency, FF mainly refers to the competition between charge carrier recombination and extraction, whereas V_{OC} determines what part of a photon's energy is converted into electrical energy. All the important physical phenomena involved in energy conversion in organic solar cells are discussed in following sections.

3. PHOTOPHYSICAL PROCESSES IN ORGANIC SOLAR CELL

Over the past two decades, our understanding of the physics of organic semiconductors has expanded considerably. Development of novel light-absorbing materials and various breakthroughs in device engineering significantly improved organic solar cell technology in terms of both efficiencies and processing techniques. Multiple physical phenomena take place in OPV devices, the main of which are discussed separately below. However, to fully appreciate the complex operation of this technology, one should first understand why certain organic materials behave like semiconductors.

3.1 Organic Semiconductors

Organic semiconductors are carbon-based materials. The electronic configuration of a carbon in the ground state is $1s^2 2s^2 2p^2$. This means that of the 4 electrons of the outer shell, two are *s*, which are paired, and two are *p*, which are unpaired. The outer shell electrons and their ability to hybridize are critical to the formation of interatomic bonds. There are three possible hybridization configurations: sp, sp^2, and sp^3. In the context of semiconducting materials, sp^2 hybridization (when the s orbital is mixed with two of the *2p* orbitals, producing three sp^2 orbitals) is most important, as it offers intriguing electronic properties within molecules. This is because two of the three orbitals hybridize in the plane of the carbon atoms and form a σ-bond, whereas third orbital is perpendicular to the plane of the carbon atoms and is able to form a π-bond with neighboring carbon atoms. Typical organic semiconductors used in OPVs are such conjugated molecules.

The energy levels of organic semiconductors cannot be described by the classical terms "conduction band" and "valence band" due to discontinuous energy distribution and localized wave functions. Instead, the optical bandgap of an organic semiconductor is defined as the difference between the highest occupied molecular orbital (HOMO) and lowest unoccupied molecular orbital (LUMO) [26,27]. The bandgap of the semiconductor is one of the key parameters as it sets the minimum energy limit for the absorption of photons. Photons with energy below the threshold are either transmitted or reflected, while photons with energy above the bandgap are absorbed.

One of the greatest advantages of organic semiconductors is that both HOMO and LUMO levels can be easily tuned by changing the molecular structure. The same material with a slightly different functional group or conjugation length may have significantly different electrical and optical properties. For example, the HOMO/LUMO energy gap gradually decreases from 6.0 eV in benzene (1 ring) to 2.1 eV in pentacene (5 ring), resulting in a profound change in the absorption spectrum[28].

3.2 Light absorption and exciton formation

Initial step of energy conversion in OPVs is light absorption in a semiconducting active layer. The absorption coefficient of organic semiconductors is generally high ($\sim 10^4$ cm^{-1}), so a photoactive layer only a few hundred nanometers thick is capable of absorbing most of the photons above the bandgap. However, the optimal film thickness is not only determined by the maximum absorption, but also by electron-hole recombination, as will be discussed below. Usually, the highest PCEs are obtained in devices with photoactive layers of 100-150nm thickness.

Although absorption range of organic semiconductors tends to be much smaller compared with inorganic semiconductors, yet state-of-the-art photoactive molecules distinguished by intramolecular electron push-pulling effects, have an absorption range exceeding 300 nm.[29,30] Moreover, the use of two different molecules with complementary absorption blended into single ~130 nm-thick film for the active layer allows the majority (~80%) of photons above the bandgap to be absorbed [31,32].

When the energy of the photons is higher than the bandgap of the absorbing semiconductor, the electron is promoted from the ground state (HOMO level) to one of the excited states. This promotion is followed by an ultrafast ($<10^{-15}$ s) electron relaxation to an excited state with lowest energy, i.e. the LUMO level. The promoted electron leaves a vacancy in the HOMO level, which can be treated as a positively charged particle, commonly referred to as a "hole".

Such an electron-hole pair is bound electrostatically via the Coulomb interaction, with the binding energy determined approximately by the Coulomb potential:

$$V = \frac{q^2}{4\pi\varepsilon_0\varepsilon_r r} \qquad\qquad (4)$$

where q is the elementary charge, r is distance between electron and hole, ε_0 is the vacuum dielectric constant, and ε_r is the relative dielectric constant of the material. The latter is generally high in inorganic semiconductors ($\varepsilon_r \sim 11$-13), which results in a binding energy that is in the range of $1 - 100$ meV.[33] The thermal vibrations of the host material are strong enough to overcome such low binding energies, so the electron-hole pair quickly dissociates into free charge carriers. In organic semiconductors, however, the dielectric constant ε_r is much smaller ($\varepsilon_r \sim 2$-4), leading to significantly higher electron-hole binding energies.[34,35] These tightly bound charge pairs are considered quasiparticles excitons (or Frenkel excitons). In the absence of external influences, these particles relax to the ground state within a timescale of hundreds of ps to a few ns timescale. [26,36–38]

3.3 Exciton Diffusion

Before decaying to the ground state, the excitons diffuse in the organic material, spatially transferring energy. The initial energy transfer occurs as a coherent excitation migration, however, due to the low degree of order of organic materials, this transfer is limited to a few lattice spacings only.[39] Further energy transfer is usually described as localized exciton random-walk or hopping between molecules[40–44] and is based on the Forster's resonant energy transfer (FRET) mechanism via Coulombic dipole-dipole coupling of molecules.[45–47] Typical exciton diffusion lengths in amorphous π-conjugated molecules and polymers fall in 5-15 nm range [48–55], however, there are recent examples of 20-47 nm diffusion lengths in novel photoactive materials used in OPV technology.[56]

In order for the energy stored in the molecular excitation to be converted to electrical energy, the excitons must dissociate into free charge carriers before they recombine, i.e. on a ps timescale. An electric field, traps, or impurities assist in the dissociation of excitons within the host material.[57] However, after dissociation, both holes and electrons must be extracted to the appropriate electrodes. Therefore, effective energy conversion in an OPV device is achieved when the excitons dissociate not in the bulk of the host material, but at the interface of materials with different electron affinities, optimized for

efficient charge separation and their further transport. During the development of OPV technology, several improvements have been made to the solar cell design to improve the dissociation of the excitons.

3.4 Bulk hetero-junction organic solar cells

The first and simplest organic photovoltaic device architecture, called the single-junction solar cell, was copied from inorganic solar cells. In this design, the photoactive layer is located between two electrodes (Fig. 2c). An optically transparent low-resistivity electrode, such as indium tin oxide, is typically used on the front side to allow light to enter and a reflective metal, such as aluminum, is used on the substrate side to reflect unabsorbed light and improve the light output in the active layer. The difference in the work functions of the electrodes creates a built-in electric field in the photoactive layer. However, this field is too weak for efficient dissociation of the excitons, and most of the free charge carriers are generated at the interface between the organic semiconductor and one of the electrodes (see Figure 2a). [58–60] Since a layer thickness of at least 100nm is required for efficient light absorption, the probability of an exciton generated deep within the bulk of a layer reaching an interface is drastically limited by the short diffusion length of the excitons of ~10 nm. Not surprisingly, PCEs of single-layer devices barely exceed 1%. [61]
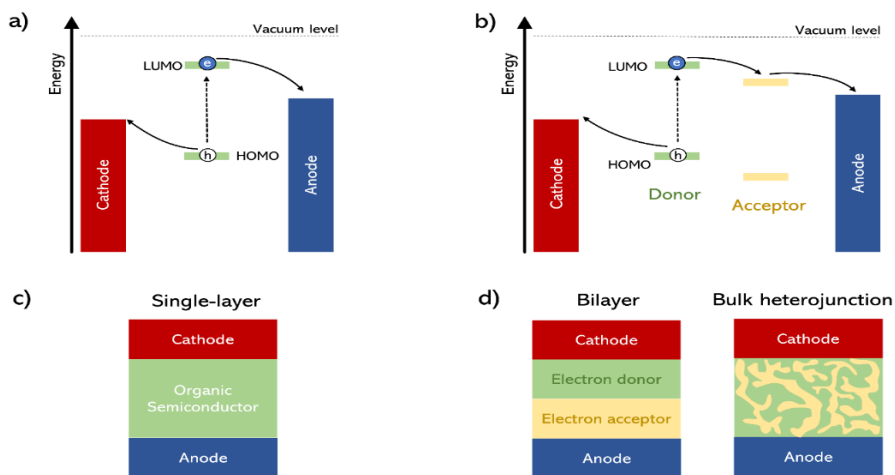

Figure 2. *Schematic diagram of the band structure of a single-layer (a) and a bilayer (b) solar cell. Structure of single layer (c), bilayer and bulk heterojunction (d) solar cell.*

As a means to increase exciton dissociation yield, C.W.Tang introduced two-layer organic solar cell (Figure 2d).[62] In this design, the photoactive layer consists of two types of molecules - one with electron donating properties (donor), the other with electron accepting (acceptor) ones. The difference in electronegativity or ionization potential of the molecules is the driving force for the separation of excitons. Therefore, excitons can dissociate not only at the interface between semiconductor and electrode, but also at the interface between donor and acceptor (Figure 2b). Separated charge carriers would then be transported to the corresponding electrodes, i.e. electrons via the LUMO level of an acceptor and holes via the HOMO level of a donor. Although such a planar heterojunction improves the efficiency of energy conversion (a PCE of ~1% was reported in the work of C. W. Tang), the short exciton diffusion length compared to the thickness of the photoactive layer required for efficient light absorption was still the main factor limiting the PCE.

A real breakthrough came with the novel concept of bulk heterojunction (BHJ), which was proposed almost simultaneously by two groups.[63,64] Today, the absolute majority of OPV devices, including those studied in this thesis, are based on the BHJ concept. In BHJ solar cells, donor and acceptor materials are either co-evaporated or spin-coated, creating an interconnected donor/acceptor network (Figure 2d). In this way, the donor/acceptor interface is spatially distributed throughout the photoactive layer, ensuring that most excitons generated in one of the molecules reach the interface within its diffusion length. This structure enables the highest PCEs in OPV technology (currently above 20% for tandem OSC)[65]. However, the complex hierarchical arrangement of molecules complicates charge extraction. Therefore, the morphology of such a photoactive layer must be carefully optimized by the mixing ratio, the coating rate, the choice of solvent, the thermal annealing, etc.[66–72] Although in the BHJ structure most excitons dissociate at the D/A junction, this alone does not guarantee successful charge generation[73], or extraction of free charge carriers due to other limiting factors, which are discussed in the following.
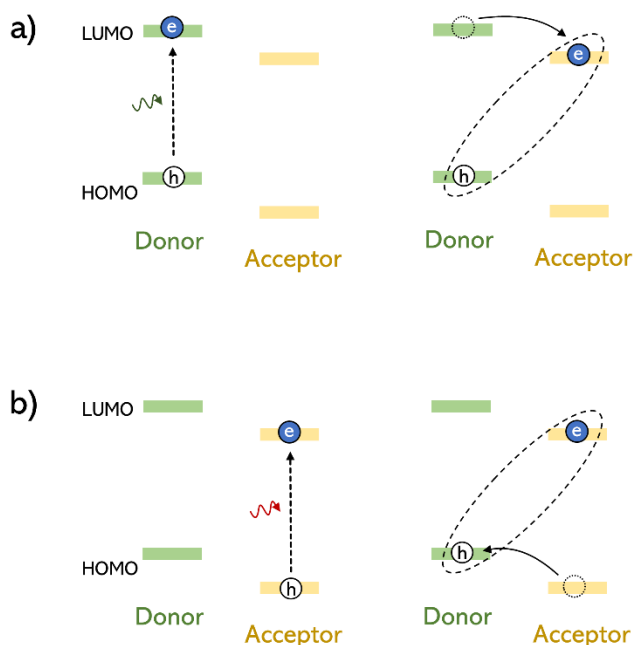
Figure 3. *CT exciton formation scheme.*

When the diffusing exciton encounters the D/A interface, electron transfer occurs due to the favorable arrangement of energy levels between the two molecules. As shown in Figure 3a, when the exciton is generated in the donor material, the electron is transferred between the LUMO levels of the donor and acceptor. When an exciton is first generated in the acceptor material (Figure 3b), electron transfer occurs from the HOMO level of the donor to the HOMO level of the acceptor and is usually depicted as hole transfer from the acceptor to the donor. In modern OPV devices, both charge generation paths are exploited and are referred to as channel I and II, respectively.[74,75] Using ultrafast transient spectroscopy, it was found that electron transfer normally occurs on a time scale of 10-100 fs.[44,73,76–79] However, the charge transfer rate has been shown to correlate with the HOMO/LUMO level differences between donor and acceptor [80,81], and in the case of a negligible difference in the frontier orbital energies, the charge transfer rate can be reduced to a

picosecond time scale.[82,83] Importantly, both channels I and II lead to the same state where the electron and hole are on different materials, but still bounded by Coulomb attraction. Such a state is called a charge transfer (CT) state or CT exciton and is an intermediate state in the charge separation process.[84–86]

The energy of the CT state depends on several factors, such as polarization, aggregation-induced delocalization, molecular orientations, and therefore varies at each junction. This is particularly evident in highly disordered systems, such as bulk hetero-junction OSCs. The set of energetically distributed CT states forms so-called CT manifold, which is characterized by an optical signature and is therefore detectable with spectroscopic instruments.[87–89] Moreover, the CT manifold can be generated by direct excitation even with photons whose energy is lower than the bandgap of an organic semiconductor.[90] However, the absorption of the CT manifold is very weak and its contribution to the generation of free charge carriers is insignificant.

After charge transfer, there are two possible scenarios: either coulombically bound electron-hole pairs recombine or they overcome the binding energy and become free charge carriers. It has been estimated that the distance between charged particles immediately after electron transfer is similar to the distance between molecules, i.e., ~1 nm.[91–93] Given the low dielectric constant of organic semiconductors, the Coulomb attraction between electron-hole pairs at such a small distance is in the range of a few hundred meV, which is much higher than the thermal energy at room temperature. So where does the energy for the generation of free charge carriers come from? In general, the difference between the energy of initial excited state and the energy of the CT state is considered to be the driving force for CT dissociation. It has been shown that a difference of 0.3 eV is required for efficient CT splitting in typical OPV devices based on fullerene acceptors.[80] However, there are numerous other factors stimulating charge dissociation, including entropy [94–96], energetic disorder [97,98], high local mobility in fullerene clusters [99], quadrupole moments of novel acceptors causing energy levels bending at D/A interface [75,100], the delocalization of charges and the high degree of crystallinity of the acceptors [73,101–103], and therefore efficient CT exciton dissociation has been observed in blends even at negligible energy differences [36,104–107]. OPV systems with small energetic offsets, i.e., low driving forces for CT dissociation, tend to have higher V_{oc} values because less energy of the photon is dissipated to enable

dissociation.[105,108] Nonetheless, as will be shown in this work, the absence of an energy barrier, while beneficial for increasing *Voc*, opens up an additional loss channel through the retransfer of an electron.

3.6 Charge Carrier Transport

After free charge carriers are generated at the D/A interface, electrons are transported from the LUMO of one site to the LUMO of another site (correspondingly from HOMO to HOMO for holes) until the charge is dissipated by the corresponding electrodes into an external circuit. In this case, the site could be a conjugated segment of a polymer or a molecule. There are two main factors that favor such transport: the electric field, which induces charge drift, and the gradient of charge carrier density, which favors their diffusion.

Due to their complicated structure, organic semiconductors usually tend to be disordered. For instance, the different chain links of organic polymers, together with conformational defects in the polymer backbone, lead to a variety of site energies (disorder)[109]. Energetic disorder is also caused by crystallinity, aggregation, and molecular orientation, and thus depends on both chemical composition and morphological features. Therefore, despite some crystalline or semi-crystalline domains, charge transport in organic semiconductors is governed by disorder.

To describe the degree of disorder in amorphous organic semiconductors, the Gaussian distribution of density of states (DOS) is usually used:

$$g(E) = \frac{N_0}{\sqrt{2\pi\sigma^2}} \exp\left(-\frac{(E-E_0)^2}{2\sigma^2}\right) \qquad (5)$$

where N_0 is the concertation of the sites, E and E_0 are the energy and the mean energy of the site, respectively, and σ is the standard deviation, also referred to as energetic disorder. In some cases, an exponential tail is included to account for low energy states.[110,111]

High energetic disorder forces rapid charge carrier localization, and although the charge initially migrates through delocalized band states, this migration is extremely short. However, the exact time and distances over which coherence

is lost are still under debate [73,112]. Further, now localized, charge carrier migration is often explained by Bässler model [97], which assumes thermally activated tunnelling between localized states, referred to as hopping, as the means for charge migration. Miller-Abrahams expression describes the hopping rate ν_{if} from an initial state i with energy E_i to a final state f with energy E_f:

$$
\nu_{if} = \begin{cases} \nu_0 \exp(-2\alpha r_{if}) \exp\left(-\dfrac{E_f - E_i}{kT}\right) & if\ \Delta E > 0 \\ \nu_0 \exp(-2\alpha r_{if}) & if\ \Delta E \leq 0 \end{cases} \qquad (6)
$$

Where ν_0 is the attempt-to-hop frequency determined by the phonon frequency in the material, r_{if} is the distance between the sites, k is the Boltzmann constant, T is the temperature, and α describes the decay length of the localized wavefunction. The experimentally obtained values for $1/\alpha$ fall in 0,1-0,2 nm range [113,114], supporting strong localization assumption used in this model.

Bässler, or Gaussian Disorder Model (GDM), has been successfully implemented in charge carrier dynamics analysis for many organic semiconductors [114–116]. Importantly, as "Boltzmann prefactor" is present only for hops upward in energy ($\Delta E > 0$), hops that downward in energy occur at a considerably higher rate. The model therefore predicts a gradual trapping of the photo-generated carriers at lower lying localized sites, i.e. thermalization. While the Miller-Abraham expression suggests, that carrier thermalization occurs through charge carrier hops between localized sites, and therefore does not account for on-site carrier thermalization. However, on-site thermalization takes less than a picosecond [117,118], so it could be considered immediate in the context of the GDM model.
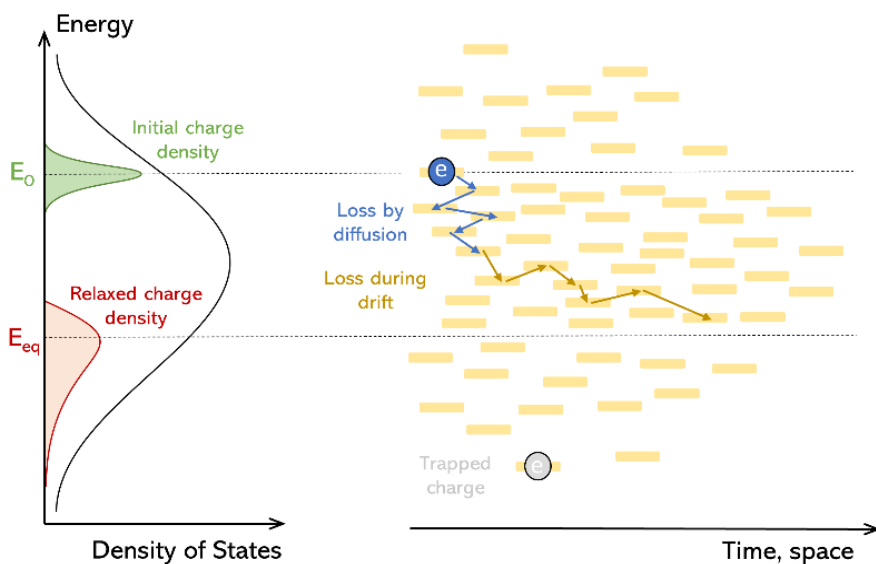
Figure 4. *Schematic representation of photogenerated charge carrier thermalization in organic solar cell.*

As shown in Figure 4, photogenerated charge carrier at certain energy E_0 rapidly thermalize to lower energy sites until reaches quasi-equilibrium E_{eq} transport energy, which depends mainly on temperature and disorder of the system. However, it was shown [119], that charge carriers generated within thin (~100 nm) active layer are extracted without even reaching their full thermalization. Moreover, in the same work, two phases of thermalization were distinguished: first, during 1-100 ns, and the second on the following timescale. During initial stage, rapid energy dissipation occurs due to fast diffusive motion, whereas during the later, when drift component of motion becomes more substantial and extraction towards electrodes could be detected, energy is dissipated at much lower pace. Naturally, part of randomly hopping charge carrier ends up in a site so deep within DOS distribution, that thermal activation energy is insufficient for them to overcome the barrier to next site. They become trapped and eventually recombine, without contributing to a photocurrent.

Both carrier trapping and thermalization leads to a time-dependent carrier mobility, decreasing with time following photoexcitation. There are numerous

works reporting that carrier mobilities decrease by several orders of magnitude from their generation until extraction.[120–125]

3.7 Recombination

In OPV devices, charge carriers are generated in the form of negative-positive charge pairs, i.e., electrons and holes, which tend to recombine under certain conditions. If the generated electron-hole pair is still coulombically bound, they form a geminate pair, and hence their recombination is called geminate recombination. Notably, it comes from the same parent exciton. On the other hand, if free positive and negative charge carriers moving through an organic semiconductor meet and relax into the ground state, such recombination is called non-geminate. Namely, a recombination of carriers originating from different photoexcitations.

Geminate recombination in novel OPV devices is usually insignificant. Most of the photoexcitations quickly converts to free charge carriers, which are then transported to the appropriate electrodes. [104,126,127] However, even if oppositely charged free carriers are transported through different materials, the probability that they will encounter each other is still relatively high given the large number of D/A interfaces in the bulk heterojunction structure. Such recombination can be monitored by measuring the dynamics of the charge carrier density using transient techniques, such as the time-delayed collection field, as will be explained in the experimental section. When the dynamics of the charge carrier density is determined only by recombination, it follows a bimolecular decay pattern:

$$\frac{dn}{dt} = -\gamma n_e(t) n_h(t) \qquad (7)$$

where n is carrier density, n_e and n_h are photogenerated electron and hole densities, and γ is the bimolecular recombination coefficient. Bimolecular recombination is the main parameter determining the optimal thickness of an active layer for an OPV device, since it limits both the short-current density and the open-circuit voltage.

Notably, formalism (7) concerns only bimolecular recombination, however, higher (>2) recombination order, when interaction between more than two charge carriers leads to a recombination, is also possible in organic solar

cells.[128,129] Nonetheless, such recombination, commonly referred to as Auger recombination, requires much higher carrier densities than are normally generated under standard AM 1.5G illumination conditions.

3.8 Non-fullerene acceptors

For many years, the active layer of a typical OPV device consisted of a polymeric donor material and a fullerene-based acceptor.[174] This combination of materials has demonstrated efficiencies of up to 11.7%.[175] Despite relatively high efficiencies and high electron mobility values, fullerene-based acceptors have some serious drawbacks – they are costly, have far from optimal absorption range, difficult to synthesize, and show low stability in air.[176,177]

A possible alternative to expensive fullerene acceptors is polymer-based electron acceptors.[178] Around 2010, numerous publications appeared in which fullerene-based acceptors were replaced by polymer-based acceptors. These so-called all-polymer solar cells initially had lower energy conversion efficiencies than their fullerene-based counterparts, but soon some systems began to rival the efficiencies reported for polymer:fullerene systems. However, the use of polymeric acceptors in organic solar cells also has some drawbacks. For example, the synthesis of semiconducting polymers is lengthy and complicated, which affects the quality of the synthesized polymers, which are known to vary significantly from batch to batch and therefore have limited reproducibility in devices.[179]

These had led to the development of organic acceptor materials based on small molecular structures, which are used as an alternative to both fullerene and polymeric acceptors. They are cheaper to fabricate due to relatively straightforward synthesis, have simple energy level control, and recently it has been reported that these acceptors are significantly less susceptible to degradation in air compared to fullerenes.[180] Small molecule acceptors also have defined molecular structures, which makes them easily reproducible, as well as higher electron mobility compared to their polymer counterparts. In addition, most important of all, small molecule-based acceptor materials have recently significantly outperformed fullerene-based acceptors, currently PCE above 18% in a single-junction OPV device.[23,24]
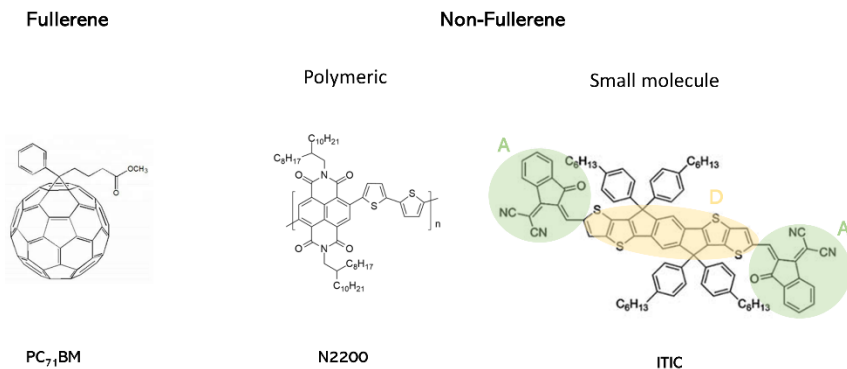
Figure 5. *Typical acceptor molecules used in OPV devices. Green and yellow circles indicate electron accepting and donating parts of the molecule, respectively.*

The most successful small-molecule acceptors to date belong to so-called A-D-A family, which is distinguished by alternately incorporated acceptor and donor building blocks along the main chain of the molecule, as shown in Figure 5.[181] There are several reasons why these molecules are superior to fullerene-based ones. First, the alternating A-D-A framework reduces the band gap of the molecule, resulting in increased absorption of visible photons. This means that, unlike fullerene-based acceptors, small molecule acceptors absorb photons that contribute to the total number of excitons produced. This results in higher Jsc values. Second, the electronic tunability enables favorable alignment of LUMO-HOMO energy levels, which reduces losses and thus improves V_{OC}. Finally, even FF values tend to be higher in devices based on small-molecule acceptors, which is attributed to the balanced charge mobilities between the donor and acceptor materials, reducing recombination caused by accumulation of charge carriers in the donor material with lower mobility.[181]

4. EXPERIMENTAL METHODS

4.1 Transient Absorption Spectroscopy

Each excited state of the molecule is unique and can be distinguished by its absorption and emission spectra. However, because of the relatively short lifetime of an excited state, these states contribute little to the absorption of the molecule in steady state. To specifically study excited states and their dynamics, transient absorption spectroscopy (TAS) is used.
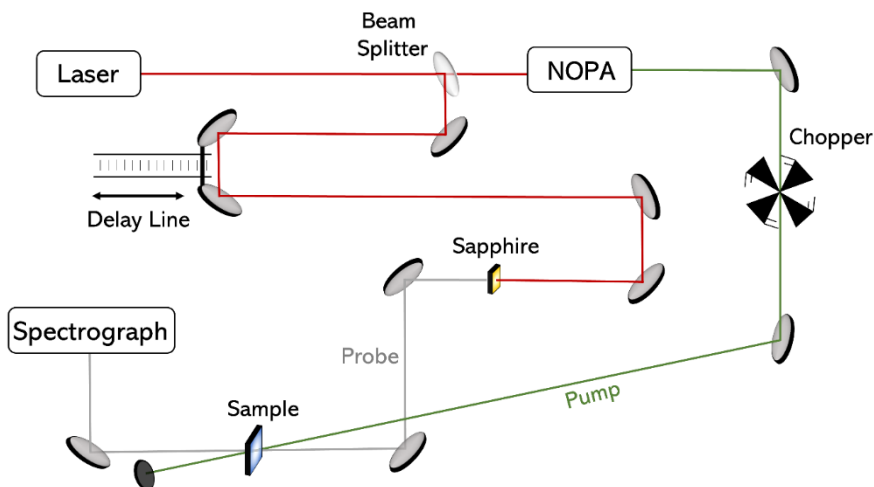
Figure 6. *Schematic illustration of a typical pump-probe measurement setup.*

At TAS, the change in absorbance of the sample is caused by exciting the molecule with a short flash of light, and the evolution of this change is then measured over a specific wavelength range. A typical technique for such a study is the pump-probe, where the light for both excitation (pump) and registration of absorption (probe) comes from a pulsed laser. At time t = 0, a sample is excited with a short laser pulse and after a certain delay Δt, the absorption spectra are recorded with a "probe pulse" with a broad spectrum (e.g. white light supercontinuum). The length of the optical delay line determines the delay time Δt (usually in the ns range) between the pump and probe pulses. A chopper synchronized with the laser pulse is used to block

every other pump pulse. This allows evaluation of the change in absorbance (*ΔA*) at any given delay time according to the Beer-Lambert law:

$$A = -\log\left(\frac{I}{I_0}\right) \tag{8}$$

$$A^* = -\log\left(\frac{I^*}{I_0}\right) \tag{9}$$

$$\Delta A = A^* - A = \log\left(\frac{I}{I^*}\right) \tag{10}$$

where *A* and *A** (*I* and *I**) are absorbance (intensity of the probe pulse) with and without the pump pulse present, respectively. I_0 is the intensity of the probe pulse before entering the sample.
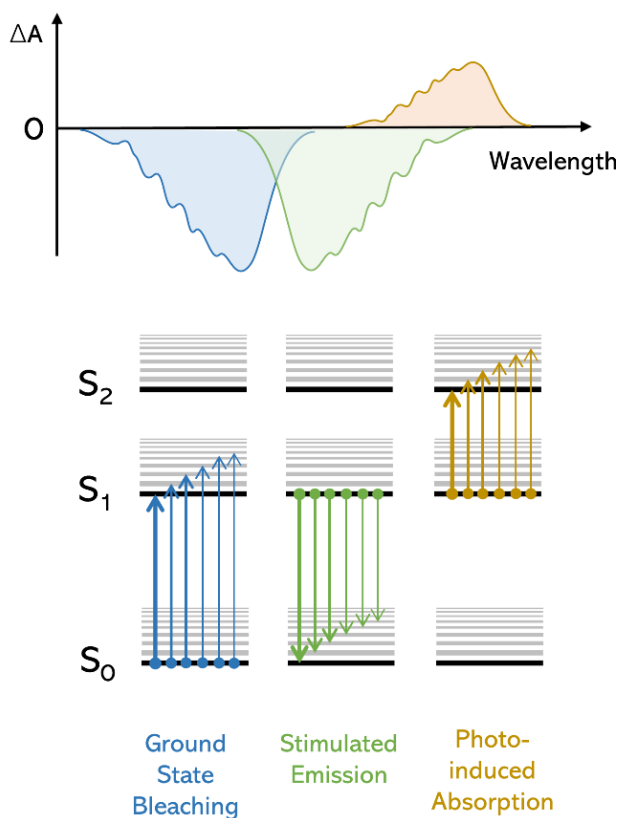

Figure 7. *Schematic illustration of origins for different transient absorption spectrum features.*

Change in molecules absorbance (*ΔA*) occurs due to the disappearance or appearance of electronic states. As can be seen in Figure 7, a typical pump-probe (PP) spectrum consists of negative values, i.e., decreased absorbance, caused by ground state bleaching and stimulated emission, and positive values, i.e. increase in absorbance, due to photo-induced absorption. The detailed analysis of transient absorption spectra usually requires mathematical models of the physical processes involved.

In this work, the measurement setup was based on the amplified femtosecond laser Pharos 10-600- PP (Light Conversion Ltd.), which operates at a fundamental wavelength of 1032 nm, a pulse width of < 250 fs, and a repetition rate of 200 kHZ. The Orpheus PO15F2L noncolinear optical parametric amplifier (NOPA) (Light Conversion Ltd.). The detection equipment consisted of an Andor - Shamrock SR - 500i - B1 - R spectrometer (Andor Technology, 150 lines mm-1 diffraction grating) equipped with an Andor-Newton (Andor Technology) DU970 CCD camera (1600 × 200 pixels).

4.2 Optical Electric Field Probing

Optical electric field probing (OEFP), similar to the pump probe, is a measurement technique used to track the evolution of the absorbance change of the sample. However, unlike the pump probe, the absorption changes in OEFP are not caused by the excitation of the sample, but by the application of a voltage to the sample, which causes what is known as the Stark effect. The Stark effect is the shifting and splitting of spectral lines of molecules due to the presence of an external electric field. As shown in Figure 8 and its caption, there are two parameters that determine the spectral shift in the presence of an electric field, namely the change in dipole moment $\Delta\mu$ and the change in polarizability *Δα*, between the initial and final states.
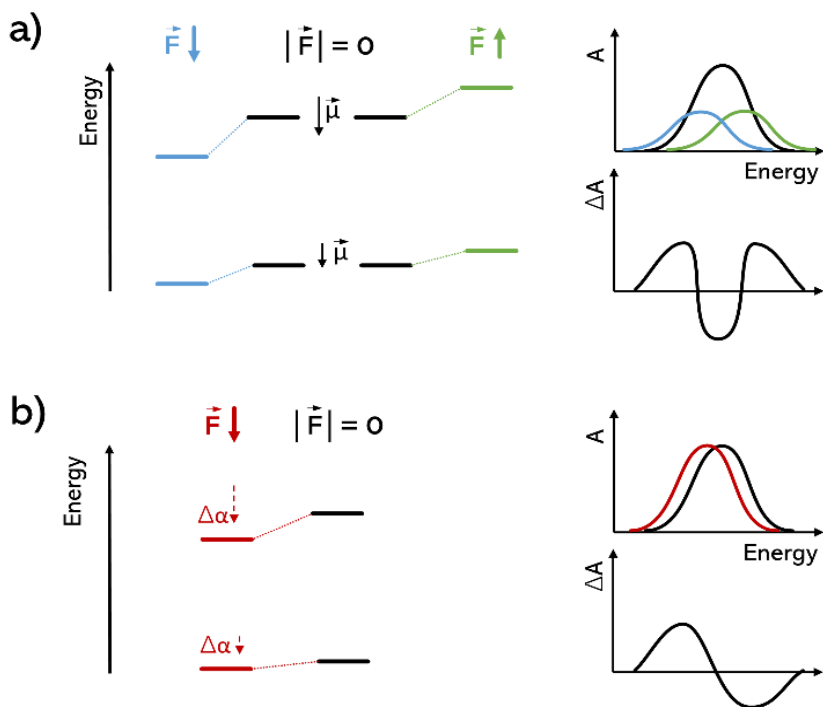
Figure 8. *Schematic representation of the effect of an applied electric field on the absorption spectrum. a) Changes in the absorption of a molecule when the difference in dipole moment μ between the ground and excited states is aligned with or against the electric field. b) Changes in the absorption of a molecule when the transition between the ground and excited states exhibits a difference in polarizability (shown here for Δα > 0).*

OEFP is performed with the same experimental setup as the pump-probe measurements, additionally equipped with a voltage generator synchronized with the laser pulse. Since the depth of the absorption change depends on the strength of the electric field, the OEFP setup allows ultrafast tracking of the electric field evolution within the sample with a much higher temporal resolution than electrical measurements.

In the case of OPV devices, OEFP measurements even allow the study of charge carrier dynamics. For this purpose, a voltage is applied to the sample in the reverse direction so that the charge injection into the sample is negligible. This leads to an extraction of equilibrium carriers from the active medium and the behavior of the device as a simple capacitor with a

homogeneously distributed electric field within the organic layer. Excitation of the film with a short light pulse then generates charge carriers that drift and create opposing dipoles to the electric field within the sample. As a result, the initial strength of the electric field decreases and the change in absorption weakens until the charge carriers are extracted from the film. The dynamics of the charge drift can be reconstructed from the evolution of the observed absorption change.

4.3 Time Resolved Electric Field Induced Second Harmonic Generation

Somewhat similar method to optically probe electric field within the sample is called time resolved electric field induced second harmonic (TREFISH). As the name suggest, it is based on second harmonic generation, specifically within non-centrosymmetric materials. In amorphous organic semiconductors centrosymmetry is broken by electric field, as naturaly isotropic material polarizes according to the electric field direction. As such, the efficiency of second harmonic generation becomes proportional to the square of the electric field. Therfore, by measurring second harmonic generation intensity, electric field within the sample could be monitored.

The time-resolved regime for electric field induced second harmonic measurement is implemented in a pump-probe scheme, analougsly to previously described OEFP. The pump beam creates photo-generated charges and the probe subsequently monitors the decreasing electric field strength.

$$\Delta E(t) = \left[\left(I_{2H}(t)/I_{2H,0}(t)\right)^{1/2} - 1\right] E_0 \qquad (11)$$

Where I_{2H} and $I_{2H,0}$ are the second harmonic intensities with and without pump, respectively. E_0 is the applied electric field strength.
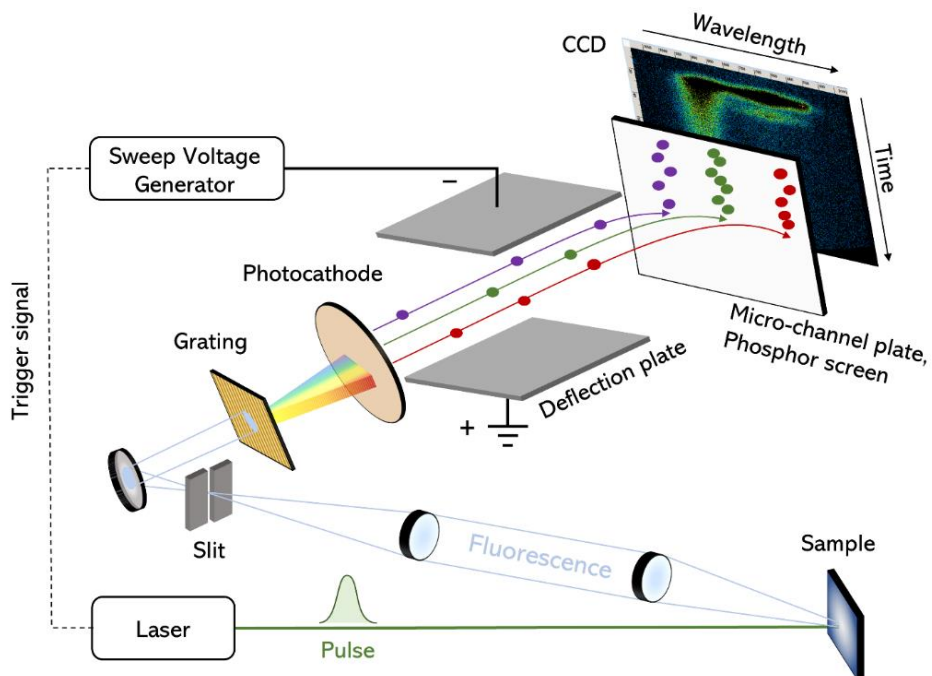
Figure 9. *Schematic representation of transient photoluminescence measurement setup using streak camera.*

Another fundamental feature of the molecule is its emission spectra. In this work, transient photoluminescence measurements were performed to study the excited-state emission spectra and their dynamics. The streak camera was used as an ultrafast detector to detect the fluorescence of the sample. A simplified measurement scheme of the streak camera is shown in Figure 9. The ultrafast laser system is used to excite the sample with a short (< 250 fs) laser pulse. An array of lenses and parabolic mirrors collects the fluorescence from the sample and focuses it through the slit onto the grating. The fluorescence spectrum is then projected onto the photocathode and converted into photoelectrons and accelerated. At the same time, an ultrahigh-speed voltage sweep is applied to deflect the electron flow. This converts the arrival time of the electrons at the microchannel plate (MCP) into a spatial coordinate that is perpendicular to the wavelength. The signal amplified at the MCP is projected onto the phosphor screen and the CCD camera records the final

image. The light intensity of the CCD camera corresponds to the fluorescence intensity, while the distribution of the signal on two spatial coordinates provides information about the time and the wavelength.

In the following work, photoluminescence dynamics were measured using a streak camera system (Hamamatsu C5680) with single sweep units (M5677) coupled to a spectrometer. For sample excitation, a femtosecond Yb:KGW oscillator (Light Conversion Ltd., Vilnius, Lithuania) was used to generate 80-fs pulses at 1030 nm that were frequency-doubled to 515 nm (HIRO harmonics generator, Light Conversion Ltd.). The temporal resolution of the streak images in the range of 0-100 ps was ~3 ps.

4.5 Transient Photocurrent

The conventional technique of transient photocurrent measurement is used to study the carrier dynamics in the ns-µs time domain and obtain several important parameters of the OPV device, such as the carrier extraction rate or mobility. The electrical TPC scheme and time sequence are presented in Figure 10.
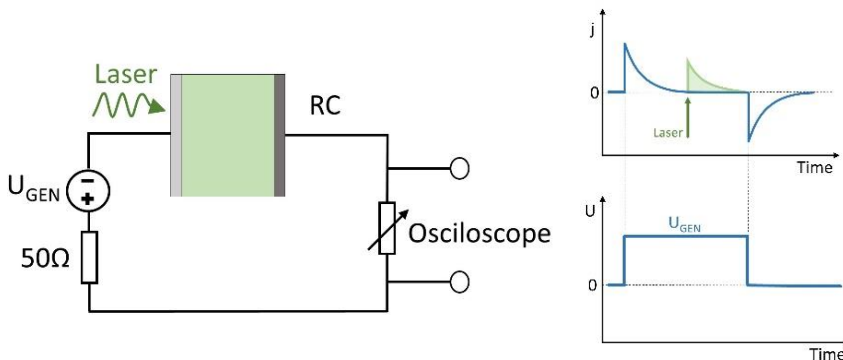
Figure 10. *a) Electrical schematic of transient photocurrent measurement. b) Kinetics of applied voltage (bottom) during measurement and corresponding current without (blue) and with (green) laser excitation.*

In transient photocurrent measurements, samples are excited with short laser pulses when the rectangular voltage signal (U_{GEN}) is applied to the sample. The photogenerated charge carriers are then extracted by the external electric field present in the sample. The dynamics of the photogenerated charge

carriers can be recorded with an oscilloscope due to the change in the resistance of the sample. The temporal resolution of such a measurement is limited by the RC of the circuit (usually ~150 ns), which is determined by the resistance of the oscilloscope, the function generator and the sample capacitance. Notably, analyzing transient photocurrents RC current, obtained when generation voltage is applied without excitation, is subtracted from current obtained after excitation. This enables investigation of photogenerated carriers only.

In this work, samples were excited by radiation from the Topas-C optical parametric amplifier (Light Conversion Ltd.) pumped through the Integra-C femtosecond Ti:sapphire laser from Quantronix Inc. that generates pulses with a duration of ~150 fs and a repetition rate of 430 Hz. A collinear optical parametric amplifier TOPAS -C was used to generate the excitation pulse emitting at different wavelengths. Current transients were recorded using an Agilent Technologies DS05054A oscilloscope (bandwidth 500 MHz), and voltages were set using a Tektronix AFG 3101 function generator.

4.6 Time Delayed Collection Field

Time-delayed collection field (TDCF) technique is a special form of TPC measurement performed with the same instrumentation. It provides additional information on carrier density decay and mobility kinetics. In the simplest implementation of this technique, the sample is excited at zero voltage (U_{GEN}) while the extraction voltage (U_{EXT}) is applied after a variable delay (see Figure 11 for the timing diagram of TDCF measurements). The dependence of the total extracted charge (cumulative current) on the delay time between the optical excitation and the application of the extraction voltage shows the decrease of the charge carrier density at zero bias voltage due to recombination. Analogous carrier density decrease could also be observed in non-zero generation field, however, in such case carrier density decreases due to additional carrier extraction from the active layer. On the other hand, the initial photocurrent is equal to the product of carrier density and carrier mobility; therefore, the TDCF can be used to follow the evolution of the carrier mobility. Furthermore, changing the generation voltage while keeping the time delay short, the field dependence of charge generation can be investigated.
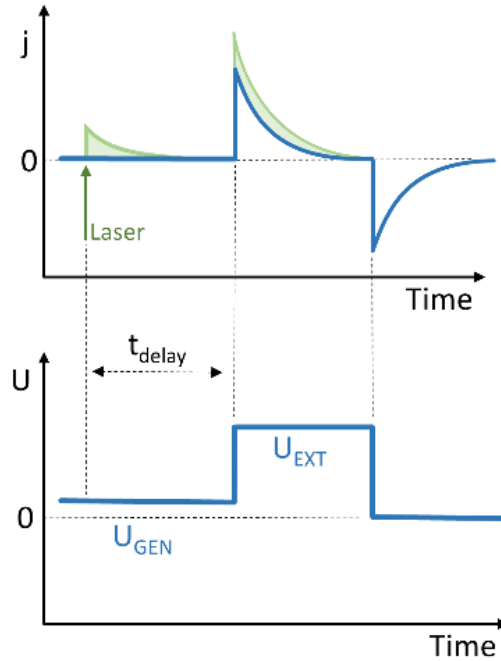
Figure 11. *Kinetics of applied voltage (bottom) during a time-delayed collection field measurement and corresponding current without (blue) and with (green) laser excitation.*

Notably, a novel TDCF adaptation was developed for paper I of this thesis, with opposite U_{GEN} and U_{EXT} signs. In this case, the photogenerated charge carriers initially drift in one direction and are extracted in the opposite direction after a certain time. As shown in Ref.[130,131], such peculiar charge carrier extraction provides valuable information about spatial traps (e.g., dead-ends of polymer sidechains or grain boundaries for perovskite crystals) that hinder charge carrier extraction.

5. MODELLING OF CHARGE CARRIER DYNAMICS

In the paper II of this work and in Ref. [131], an originally developed numerical model was implemented to study the processes of charge carrier extraction and recombination, based on the interpretation of TPC and TDCF data. The mathematical considerations behind the model are as follows:

The photocurrent kinetics, caused by short flash of light, could be described as:

$$j(t) = en(t)\mu(t)F \qquad (12)$$

where e is the elementary charge, $n(t)$ is the time-dependent free charge carrier density, $\mu(t)$ is the time-dependent average charge carrier mobility, and F is the electric-field strength. It follows that the current density decreases due to the deceasing density of free charge carriers within the active layer and their average mobility. The decay of the formal is caused by the carrier extraction of charge carriers and their recombination and can be expressed as:

$$\frac{dn}{dt} = -\gamma(t)n^2 - \frac{j(t)}{de} \qquad (13)$$

where $\gamma(t)$ is the bimolecular recombination rate, n is the carrier density generated by the laser pulse, and d is the sample thickness. In this model, we assumed a 100% photon-to-electron conversion rate and used twice the number of incident photons for n_0 (electron + hole). We have also assumed that the bimolecular recombination rate is proportional to the time-dependent mobility:

$$\gamma(t) = \beta\mu(t) \qquad (14)$$

where β is the proportionality coefficient. β can be evaluated experimentally by TDCF measurements when the effective generation voltage is set to zero. In such case, no carrier extraction takes place and the charge carrier density decays with time only due to recombination, which allows γ to be evaluated. This value was used as the initial value for $\gamma(t)$ when modelling the photocurrent kinetics.
For the time- dependent mobility we used

$$\mu(t) = \mu_0 t^{-\alpha} \tag{15}$$

where α is a free parameter, μ_0 is initial mobility value which is obtained experimentally thru *(12)* using measured initial j value. Such arbitrary time-dependent mobility expression is suitable to describe mobility dynamics within time domain of our experiments. By numerically solving the system of equations (Eqs. *12-15*), we obtain photocurrent kinetics that fit the experimental results, time-dependent mobility kinetics, a time-dependent recombination coefficient, and even evaluate recombined and extracted charge carrier density.

DISCUSSION AND CONCLUSIONS

The development of alternative energy sources to reduce fossil fuel consumption and CO2 emissions is an urgent global need. Solar energy could be used to meet the growing demand for "clean" electricity through the use of photovoltaics. Niche applications for organic photovoltaics, such as cladding glass buildings with transparent solar cells, could improve the typical understanding of solar power plants dominated by c-Si technology and significantly complement cheap electricity generation.

The work presented in this thesis is devoted to the study of processes in new generation organic solar cells based on non-fullerene acceptors. Special attention has been paid to dynamic phenomena such as free charge carrier generation and extraction kinetics, which have been investigated using various transient measurement techniques on a time scale from fs to µs.

*

The first problem addressed in this work was the spatial trapping of charge carriers. It is generally believed that the best way to reduce recombination of free charge carriers during their extraction is to use spatially separated percolating domains of electron-accepting and electron-donating materials for the transport of electrons and holes, respectively. However, in highly phase-separated morphologies, isolated domains and dead ends are likely to form, which would hinder charge carrier extraction.[133] It has been shown that charge carriers in organic semiconductors may indeed be able to move through long-distance tunneling or molecular superexchange over relatively large distances, up to several nm.[134–137] This allows carriers to be transported to sites that are not immediately adjacent. This is especially important when at least one of the constituents is a small molecule, as it allows charge transfer between these molecules when their dispersion in another material is sufficient.[134,136] However, in all-polymer bulk-heterojunction organic solar cells, where both donor and acceptor are conjugated polymers, the required dispersion is much more difficult to realize due to the large number of repeating polymer units and long side chains. Therefore, it is likely that additional transport problems may occur due to the formation of dead ends of the polymer chains. In the study described in paper I, we combined improved transient charge extraction experiments with numerical modeling to investigate charge carrier dynamics

in a prototypical all-polymer OPV device consisting of TQ1 as the donor and N2200 as the acceptor, mixed in a 2:1 ratio by weight, as the active layer.

In short, to invigorate our hypothesis about the importance of spatial traps in our all-polymer OPV devices, we have used a modified TDCF technique. We have used an effective generation voltage (effective means the net sum of built-in and applied voltages) equal to the built-in potential (U_{gen}^{eff} = −0.47 V, no applied bias) and different effective extraction voltages: (a) equal to the generation voltage (degenerate TDCF), (b) increased to −1.47 V, and (c) reversed to 0.33 V. These measurement regimes are schematically shown in the inset of Figure 12a. The main panel of Figure 12a presents the results. Here, we present peak values of the transient photocurrent *j(t)* obtained after switching on the collection field, divided by the electric field strength to get the product of the carrier density *n(t)* and mobility *μ(t)*, according to the relation *j(t) = n(t)μ(t)F*. Because of the sample capacitance, the photocurrent peak appears ≈250 ns after the collection voltage is applied. However, this time is short in comparison with the carrier density decay time, so we may consider the product *n(t)μ(t)* at the photocurrent peak time identical for all three field profiles.

Figure 12. *a) Photocurrent transient versus time at constant field equal to the built-in field (black curve), and peak value of the TDCF photocurrent transient versus collection delay time for different collection field strengths and directions as indicated in the inset (blue and red curves). b) Photocurrent transients at different collection delay times for a reversed collection field (blue curves in panel (a)), the thick blue line highlights one of the current transients. c) Illustration of the characteristic processes in the response to the different field profiles used in (a). e) Chemical structure of donor TQ1 and acceptor N2200. Measurements were taken on the as-cast TQ1:N2200 device.*

If, as suggested above, charge carriers get stuck by drifting into dead ends that act as spatial traps, reversing the field should release them and give rise to a significant increase in the extracted charge. Figure 12b shows the photocurrent transients obtained with the reversed effective voltage at different collection delay times. As the thick blue curve, highlighting one of the current transients, shows, the field flipping increases the magnitude of the photocurrent drastically, even though the extraction field was slightly weaker than the generation field of opposite direction. The increase is particularly strong at long delay times. The blue line in Figure 12a shows the delay time dependence of the peak values of the extracted photocurrent. The extracted photocurrent decays very slowly. Moreover, the photocurrent increases during the initial few µs, that is, precisely the time range for which the decay of the photocurrent at constant field (black curve) was attributed to spatial carrier trapping. These observations confirm the occurrence of spatial trapping of photocreated charges. By comparing the peaks in the black and blue curves in Figure 12a, one can estimate the fraction of charges that get lost through spatial trapping on 0–2 µs timescales to be ≈30%. This number is in excellent agreement with the ≈35% of the charges that were found to be bound in interfacial charge-transfer states and that recombine geminately on basis of a kinetic analysis of transient absorption spectroscopy measurements.[138] Notably, trapping itself is not a loss channel; the actual loss channel is the recombination of charges that do not manage to escape from their countercharge because of spatial trapping. Along the same lines, (spatial) trapping occurring at longer time and length scales will no longer lead to increased geminate recombination but will contribute to losses through bimolecular recombination.

The drawing in Figure 12c illustrates our interpretation of the carrier extraction experiments. A fraction of the carriers drifting in one direction reach a dead end of a particular blend domain (process 1) and discontinue their drift. Occasionally, they can overcome the barrier and continue to drift toward the extracting electrode, causing the weak and slow photocurrent component observed at constant applied voltage. This process (2) is assisted by the electric field. While they are trapped, charges are susceptible to (predominantly geminate) recombination, explaining the poor fill factor of the as-cast devices. When a reversed collection field is applied, charge carriers are detrapped by moving in the opposite direction (process 3).
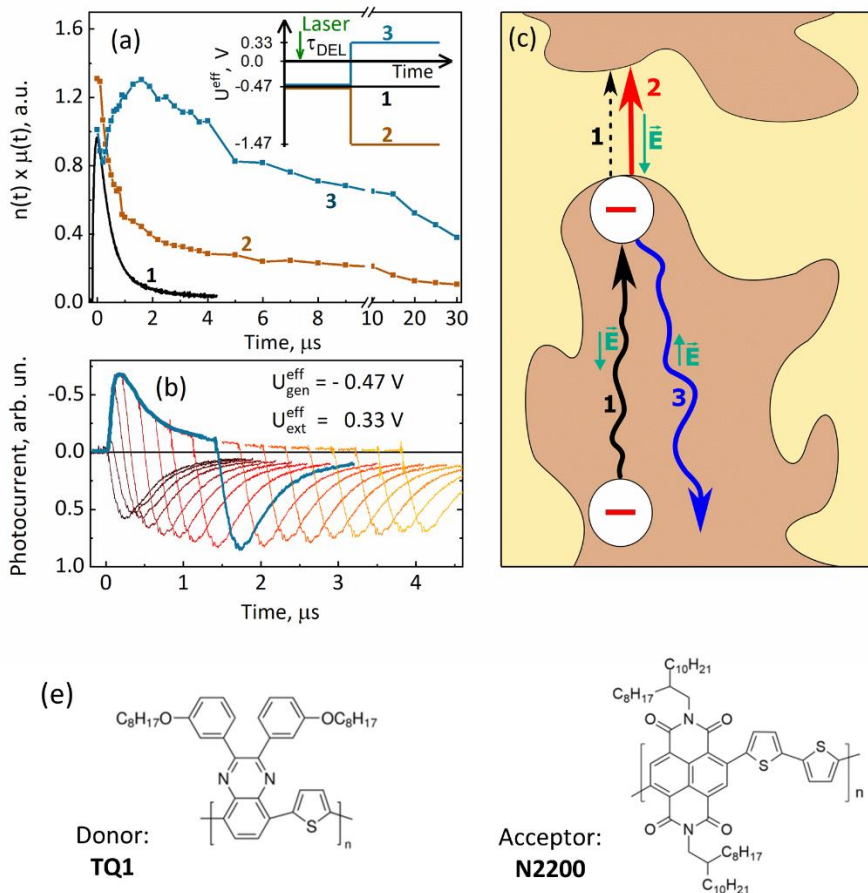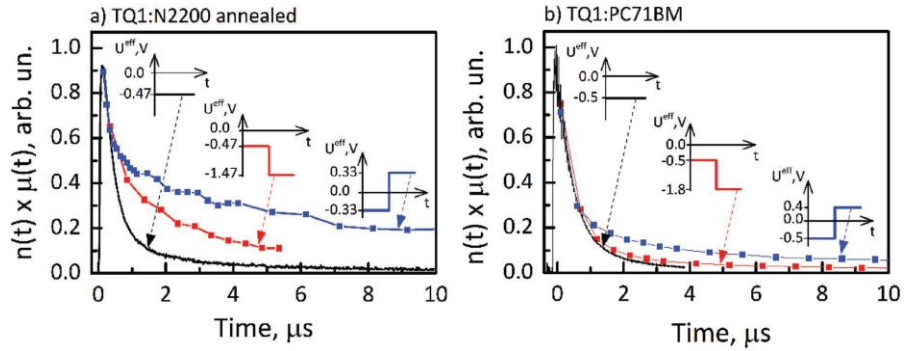
Figure 13. *Photocurrent transient versus time at constant field equal to the built-in field (black curve) and peak values of the TDCF photocurrent transient versus collection delay time for different collection field strengths and directions as indicated in the inset (blue and red curves). Measurements are taken on the a) TQ1:N2200 annealed and b) TQ1:PC$_{71}$BM sample. Figure adopted from paper I.*

According to the suggested interpretation, the spatial trapping effect should be a very sensitive probe of the blend morphology. We have therefore performed the same investigations of annealed samples. Annealing the investigated TQ1:N2200 solar cells roughly doubles their power conversion efficiency to ≈3.15%.[139] Figure 13a shows the TDCF investigation results for different applied field profiles. Most strikingly, the different peak values of the three curves that are found for the as-cast sample (Figure 12) are absent within experimental resolution, indicating that the short-range spatial trapping, and the associated geminate recombination loss, have largely vanished. This provides a transparent explanation of the previously puzzling observation that the geminate recombination loss dropped from ≈35 to ≈7% upon annealing while unaffecting long-range transport.[138] Apparently, annealing removes spatial traps that hamper short-range charge motion required to escape geminate recombination. In view of the nm length scales involved in geminate recombination, these dead ends are most likely associated with individual polymer chain ends. At longer delay times, the (blue) curve corresponding to opposite generation and extraction fields lies above the (red) curve corresponding to generation and extraction fields of equal polarity. Since the plotted data have been corrected for dark currents, the difference cannot be attributed to the difference in forward and reverse injection currents. Instead, they point toward a large fraction of charges surviving in the active layer while

being spatially trapped. This indicates that even after annealing, spatial traps continue to play a role in this all-polymer BHJ. As mentioned above, these trapped charges are predominantly exposed to bimolecular recombination.

Since we associate the spatial trapping with the specific properties of an all-polymer BHJ, we performed a similar investigation as above for a solar cell based on the same donor material TQ1, blended in a bulk heterojunction with $PC_{71}BM$ as acceptor in a mass ratio of 1:2.5. These samples showed only small differences between the transient photocurrent at constant applied field and the carrier concentration decays measured with the TDCF technique (see Figure 13b). Nevertheless, the carrier concentration extracted with the reversed effective voltage was slightly larger than with increased effective voltage, which indicates that spatial trapping taking place in these devices. However, the spatial trapping is significantly less prominent than in both the pristine and annealed TQ1:N2200 blends, in line with the anticipated behavior of polymer:small molecule BHJ discussed above.

In short, we have shown that the as-cast device contains a significant density of spatial traps. These traps most likely originate from individual polymer chain ends, since the spatial trapping effect is much weaker when the acceptor polymer is replaced by a small molecule ($PC_{71}BM$). Notably, the presence of these traps enhances both geminate and bimolecular charge carrier recombination. However, the spatial trapping effect could be significantly reduced by annealing. Finally, this investigation led to the **first statement of the thesis**: The spatial trapping effect can impede the extraction of free charge carriers from the as-cast active layer of an all-polymer organic solar cell, enhancing recombination and associated efficiency losses. The effects of spatial trapping can be significantly reduced by annealing, as demonstrated in the case of the TQ1:N2200 all-polymer solar cell.

**

The second part of the work dealt with the dynamics of the charge carriers under the actual working conditions of a solar cell. The extraction of charge carriers is directly determined by their mobility. Although mobility is often used as a specific characteristic of a material, there are many reports showing that the mobility of charge carriers in organic solar cell blends decreases by several orders of magnitude from their generation to extraction.[122–125,140] This

effect is explained by the thermalization of the charge carriers during transport to lower energy states. On the other hand, there are also reports in which steady-state mobility analysis is successfully used in bulk heterojunction OSCs.[141–144] It has even been argued that the carrier mobility in operating solar cell is actually constant, since low energy states are occupied in continuous illumination, and therefore mobility measurements with short laser pulses are inadequate.[145] Therefore, in work described in paper II, we used numerical modelling and applied several transient methods to cover a wide time window from picoseconds to microseconds and to compare the extraction and recombination of charge carriers generated by weak short laser pulses, either in the absence or presence of additional continuous illumination with a 1-sun intensity light source that mimics real operating conditions for solar cells.

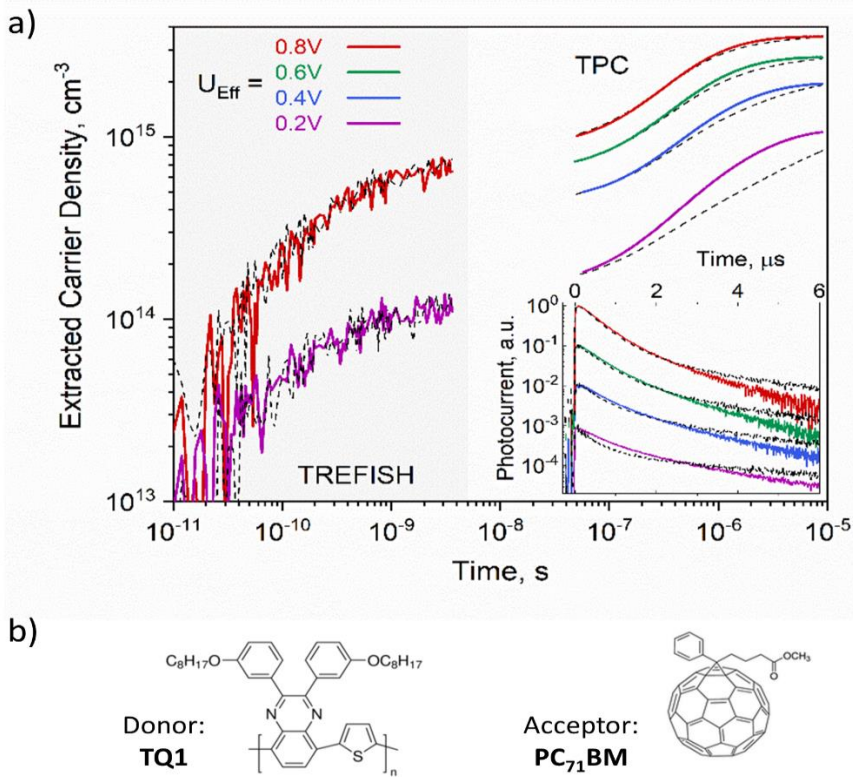**Figure 14.** a) *Extracted laser-carrier dynamics in the TQ1:PC$_{71}$BM device at various effective (*U$_{Eff}$ = U$_{Built-in}$ + U$_{Applied}$*) voltages in the dark (black dashed lines) and under 1 sun illumination (color lines). In the inset, photocurrent transients were normalized and vertically shifted. b) Chemical structure of donor TQ1 and acceptor PC$_{71}$BM.*

Figure 14a shows the charge carrier extraction dynamics in the TQ1:PC$_{71}$BM blend in a wide temporal window evaluated from measurements performed without and under additional 1 sun illumination (further referred as "dark" and 1 sun light conditions, respectively). The measurements "in dark" revealed qualitatively similar carrier extraction dynamics as was reported in ref. [121], which was evaluated as dispersive with a strongly time-dependent mobility. Decay of the carrier mobility by at least one order of magnitude during initial several nanoseconds has been observed in several polymer-PCBM blends[121–123,146], including TQ1:PC$_{71}$BM blend and has been attributed to the energy relaxation within the DOS.

In the case of additional 1 sun illumination, sun carriers were continuously generated, while their concentration was determined by the balance between extraction, recombination, and generation rates. Additional carriers generated by laser pulses (laser carriers) now appear on a background of sun carriers. The sun carriers also create a constant current background, which was subtracted from our data to register the photocurrent created by laser carriers only. Importantly, additional 1 sun illumination alters the conditions under which laser carriers are generated. First, sun carriers fill low-energy states; therefore, laser carriers experience less trapping during their extraction from the active layer. Second, laser carriers recombine with sun carriers. Thus, by using two, "dark" and 1 sun light, measurement conditions, we compare the carrier dynamics when (a) non-geminate recombination is negligible and low-energy states are not occupied (due to low laser-carrier density) and (b) in the presence of sun carriers, which to some extent occupy low-energy states. We shall inquire how 1 sun illumination affects charge extraction on different time scales at different effective electric field strengths.

As the left-hand part of Figure 14a shows, 1 sun illumination does not change the ultrafast carrier extraction and thus the mobility dynamics. This indicates that sun carriers populating low-energy states have no impact on the initial laser-carrier drift. This is expected because laser carriers in this time domain still reside in the high-energy part of DOS and the population of low-energy states by sun carriers plays a non-essential role in their dynamics.

The right-hand side of Figure 14a shows carrier extraction dynamics obtained by integrating TPCs shown in the inset. Notably, as the inset shows, the charge extraction at low effective voltage (the net sum of built-in and applied

voltages, $U_{Eff} = U_{Built-in} + U_{Applied}$) $U_{Eff} = 0.2$ V is faster during initial 1−2 μs in the presence of 1 sun light. This signifies that laser carriers experience weaker decay of mobility because low-energy states are significantly populated under 1 sun light. The 1 sun light influence becomes less pronounced at higher effective voltages. This is reasonable since higher voltages extract charge carriers more rapidly, including those residing in the low-energy states, liberating these states. Consequently, occupation of the low-energy states under 1 sun light decreases with voltage and weakly affects trapping of laser carriers already at $U_{Eff} = 0.4$ V. At longer 2−6 μs times, the photocurrent decays faster under 1 sun light. This decay phase was attributed to the extraction of equilibrated carriers; thus, a faster photocurrent decay indicates faster decay of the carrier density, which we attribute to the Shockley–Read–Hall recombination of laser carriers with trapped sun carriers.

To quantify the influence of 1 sun illumination on bimolecular carrier recombination losses, we performed TPC measurements in complementary TDCF implementation, which enables tracking of laser-carrier density kinetics, as shown in Figure 15a. At zero effective voltage (black dotted curve), photogenerated carriers are not extracted and their density decays due to recombination only. This allows evaluation of the bimolecular recombination rate, which in this case was found being equal to $\gamma = 1.24 \times 10^{-11}$ cm^3 s^{-1}, similar to values reported elsewhere[147,148]. Increasing the effective voltage leads to more rapid carrier density decay due to carrier extraction. The clear difference between carrier density dynamics "in dark" and under 1 sun illumination (dotted and solid curves, respectively) at zero effective voltage supports the idea of pronounced recombination of laser carriers with sun carriers. It is worth noting that the difference in kinetics is much smaller at higher voltages because enhanced extraction causes smaller trapped sun-carrier population.
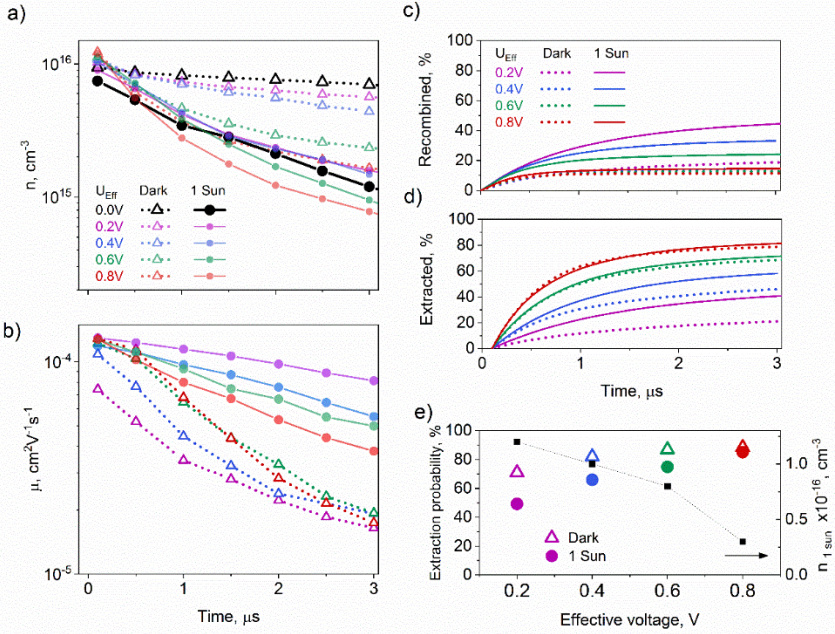
Figure 15. *(a) Charge carrier density kinetics at different effective voltages in the TQ1:PC$_{71}$BM device determined by TDCF measurements. Here and in all plots, solid lines correspond to measurements under 1 sun and dotted lines correspond to measurements "in dark"; (b) carrier mobility dynamics evaluated from TDCF data and TPC data presented in Figure 14; modeled fraction of recombined (c) and extracted (d) charge carriers; and (e) carrier extraction probabilities (color symbols) "in dark" and under 1 sun and sun-carrier density (black symbols) as a function of effective voltage. Figure adopted from paper II.*

Combining *j(t)* obtained from TPC measurements and *n(t)* obtained from TDCF, we can evaluate the mean time-dependent carrier mobility using the relation *j(t) = eFn(t)μ(t)*. The obtained mobility dynamics at different voltages "in dark" and under 1 sun light is shown in Figure 15b. Under 1 sun illumination, the mobility is higher, and its decay is weaker. "In dark," the mobility increases at higher voltages as typically observed in disordered organic semiconductors.[149] A slightly stronger mobility decay at high voltages is caused by faster extraction of non-trapped carriers leaving only low-mobility trapped carriers at longer times. Under 1 sun illumination, the mobility becomes less time-dependent, particularly at low effective electric

field when low-energy states are populated by sun carriers, preventing trapping of laser carriers. However, population of low-energy states by sun carriers decreases with increasing electric field, promoting trapping of laser carriers and causing a stronger decrease of their mobility. Consequently, mobility decreases with electric field, in stark contrast with the typically reported behavior.

To evaluate the role of the low-energy state occupation in the solar cell performance more clearly, we performed numerical modeling of the carrier extraction and recombination processes on the basis of the experimental results. Our numerical model provided us with total bimolecular recombination (between laser−laser and 1 sun−laser carriers combined) and carrier extraction dynamics. The "dark" conditions approximately represent the carrier extraction and recombination kinetics at constant low-intensity illumination of a solar cell. As shown in Figure 15c,d, the carrier recombination dynamics under these conditions is weakly dependent on the effective voltage, while the extraction rate approximately linearly increases with voltage. At 1 sun illumination, the recombination rate strongly increases at low effective voltages because of the high density of carriers trapped in low-energy states (Figure 15c,e). On the other hand, the dependence of the carrier extraction on effective voltage is weaker than "in dark" conditions. Figure 15e shows the summary of the calculation results. It shows that the sun-carrier concentration decreases almost four times when the effective voltage increases from 0.2 V, which is close to the MPP conditions, to 0.8 V, which corresponds to short-circuit. Figure 15e also shows the total probability for the generated carrier to be extracted, rather than to recombine. The carrier extraction probability under 1 sun light is lower than "in dark" because of the increased recombination rate in the presence of sun carriers, but this difference decreases with the effective voltage when the density of the trapped sun carriers decreases.

Analogous analysis was performed on highly efficient non-fullerene solar cell PBDB-T:Y1. However, carrier trapping plays a less significant role in more effective solar cells. Carrier mobility in a PBDB-T:Y1 solar cell is weakly time-dependent on a ns−µs time scale and low-energy state filling by solar illumination plays only a marginal role, even at low, close to MPP effective voltages.

These results lead to **the second statement of the thesis**: Charge carrier trapping strongly influences carrier mobility in ns-µs timescale in OPV devices with high trap concentration. However, under the actual working conditions of the OPV device, constant illumination leads to the occupation of these trap states, making the mobility less time-dependent and increasing both the extraction and recombination rates. Filling low-energy state occupation does not affect the sharp decrease in mobility on a ps timescale. In highly effective non-fullerene device charge carrier trapping effect is negligible and therefore low energy state occupation has minor effect on carrier extraction.

***

The third part of the work dealt with the generation of charge carriers in non-fullerene organic solar cells where the molecular orbital energy difference between donor and acceptor molecules is negligible.

One of the possible strategies to further improve the energy conversion efficiency in OPV devices is to minimize the voltage losses, which are typically ~0.6 V, while they are only 0.3-0.4 V in the most efficient GaAs and the dominant c-Si based devices. [150–152] Although there are examples of organic solar cells with lower voltage losses[153–156], the voltage loss is generally higher than for inorganic solar cells. This is because, unlike inorganic semiconductors in which free charge carriers are generated upon illumination, excitons are formed in OPV devices, requiring additional energy for dissociation. Dissociation is driven by the energy offset between the lowest unoccupied molecular orbitals and the highest occupied molecular orbitals of each component between donor and acceptor materials.[34,157] It is generally accepted that an energy offset of at least 0.3 eV is required for efficient charge separation, as demonstrated in fullerene derivative-based devices. [57,126,158] Contrary to popular belief, however, it has been shown that hole transfer can occur even with negligible HOMO offsets.[159–162] However, the apparent advantage of low voltage losses comes at a price, since a negligible energy offset is not an obstacle to the retransfer of a charge carrier. In papers III and IV, transient absorption and photoluminescence, together with multivariate curve resolution modelling were used to study the effect of charge carrier back-transfer. We investigated its dependence on HOMO offset, as well as its impact on energy conversion efficiency in various non-fullerene based OPV devices.

In paper III, we thoroughly study and disentangle geminate and nongeminate recombination processes in different bulk heterojunction systems. We comparatively investigated OPV systems comprising the well-established poly[(2,6-(4,8-bis(5-(2-ethylhexyl)thiophen-2-yl)-benzo[1,2-b:4,5-b0]dithiophene))-alt-(5,5-(10,30-di-2-thienyl-50,70-bis(2-ethylhexyl)benzo[10,20-c:40,50] dithiophene-4,8-dione))] (PBDB-T) blended with either previously reported[163] electron-deficient-core-based NF acceptor Y1 or archetypal PC$_{71}$BM acceptor. Additionally, BHJ systems based on benchmark NF acceptor (ITIC) with PBDB-T-2Cl and PDCBT-2F donor materials specifically chosen to have small HOMO level offsets were investigated.

In our investigation, we observed rapid, almost uniform, decrease of the total transient absorption spectrum within a few initial ps in all investigated sample. The TA kinetics represents well this decrease in the donor absorption band region, shown in Figure 16a.
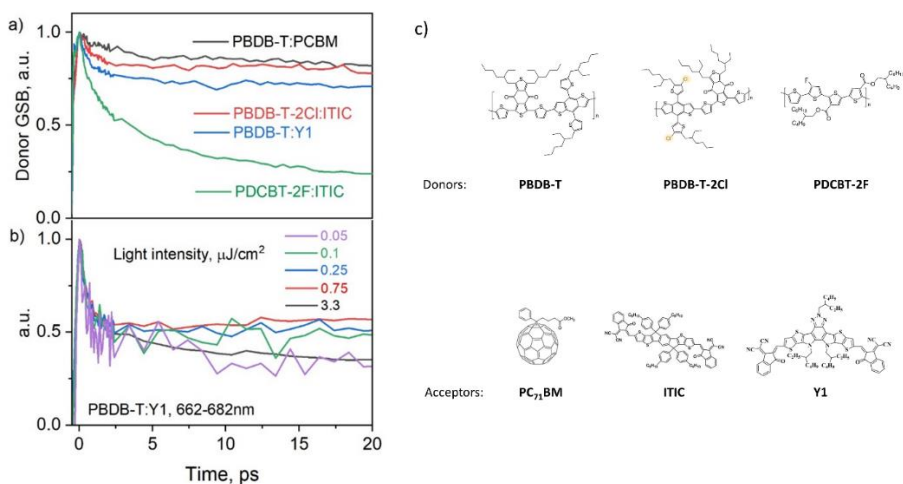

Figure 16. (*a*) *Normalized ground state bleaching decay of a donor in TA spectra of indicated systems; (b) 662−682 nm band decay kinetics in PBDB-T:Y1 blend after different light excitation intensities; 0.1 μJ/cm2 intensity of 515 nm was used in all above presented results. (c) Chemical structures of indicated materials.*

Within 3 ps, the bleaching signal decreases down to 82, 75, and 50% of its peak values in PBDBT- 2Cl:ITIC, PBDB-T:Y1, and PDCBT-2F:ITIC samples, respectively, but the decrease is only marginal in the sample with PCBM. Any other process, then carrier recombination leading to the donor and acceptor ground states, can hardly explain the uniform decrease of the entire TA spectrum. Carriers might recombine geminately or non-geminately. For non-geminate recombination, photogenerated carrier density should be high enough for an electron (or hole) to have a complementary charge in its vicinity to recombine. Such recombination is light fluence-dependent; thus, we have performed TA measurements at different light intensities. As it is shown in Figure 16b, TA signal decay is independent of excitation intensity allowing us to rule out the non-geminate recombination. In a recent study of all-polymer solar cells based on the N2200 NF acceptor, it was found that almost 50% of the charges recombine geminately, which was suggested as being the major factor hindering the device performance compared with polymer/fullerene cells.[164] Similarly, in our study, much stronger geminate recombination is indeed observed in NF samples. Further, we present a simple model explaining the origin of the effective geminate recombination, which lasts for a few ps, in NF OPV devices. Electron transfer from the excited donor LUMO to the acceptor LUMO level takes place on a sub-ps timescale, whereas a hole, created within the donor polymer, can be transferred back to acceptor only by overcoming energetic barrier. If this barrier, regarded as HOMO level offset, is low, some holes may jump to the acceptor domain and regenerate its excited state. Because excited state relaxation of acceptor molecules is very fast ($\tau \sim 2$ ps), such a process leads to very fast geminate carrier recombination. Such a model is strongly supported by the correlation of the geminate recombination efficiency of different blends with their HOMO level offsets. In the case of negligible HOMO offset (~0.02 eV) in PDCBT-2F:ITIC samples, we observe >50% of carriers recombine geminately. This number decreases to ~20% in the case of PBDB-T:Y1 and PBDB-T-2Cl:ITIC devices, where HOMO level offset is ~0.1 eV, and drops to marginal values in the case of PBDBT:PCBM where HOMO offset is the highest (>0.6 eV).

To further investigate possible back-transfer mechanism in NF OSCs, in paper IV, we performed TA measurements in BHJ blends with the benchmark non-fullerene acceptor 3,9-bis(2-methylene-(3-(1,1-dicyanomethylene)-indanone))-5,5,11,11-tetrakis(4-hexylphenyl)-dithieno[2,3-d:2′,3′-d']-s-indaceno[1,2-b:5,6-b']dithiophene, also known as ITIC, and three of its

derivatives with different sidechains – ITM, ITCC and IT4F. In this work we chose the wide band-gap copolymer Poly[(2,6-(4,8-bis(5-(2-ethylhexyl)thiophen-2-yl)-benzo[1,2-b:4,5-b']dithiophene))-alt-(2,2-ethyl-3(or4)-carboxylate-thiophene)] (PTO2) with electron-donating benzodithiophene and electron-withdrawing thiophene carboxylate ester as the main backbone as a donor material, as it matches well with the energy levels of an acceptors.

To assess the rapid initial processes after excitation more precisely, we performed a special global analysis of the transient absorption data, called multivariate curve resolution. Briefly, the analysis assumed that, under excitation of a donor the TA spectra consist of two independently evolving spectral components of D* and CT/CS states. Here we do not distinguish between charge transfer (CT) and charge separated (CS) states, since both states lead to similar transient absorption spectra. We also do not consider other possible processes, such as energy transfer from excited donor to acceptor [100] or formation of triplet states[165]. The two-state model, as discussed below, reproduces the experimental data well, indicating that D* and CT/CS states are dominating. We also demonstrate that the transient absorption dynamics are very different under excitation of donor and acceptor, which should not be the case if excitation of a donor creates excited acceptor state by rapid energy transfer. Whereas formation of the triplet state is expected to occur at longer times than our investigated time domain. Thus, although, we cannot completely rule out these processes, apparently, they do not play essential roles in the investigated blends at our experimental conditions. Unlike conventional global analysis, we did not use the assumption of exponential phenomenon dynamics here but used fixed spectra and modelled their kinetics. The D* spectrum was obtained from the TA spectrum of the neat PTO2 film and was therefore identical for all investigated blends. For the CT/CS state spectral signature, we used the TA signal at times >1.5 ns after excitation, as it is very unlikely that the D* is still present at this time. Despite some oversimplification, this model worked quite well, as fairly good fits were obtained for all investigated samples. The modeling gives time evolutions of D* and CT/CS states concentrations, however, in relative values, presented in Figure 17.
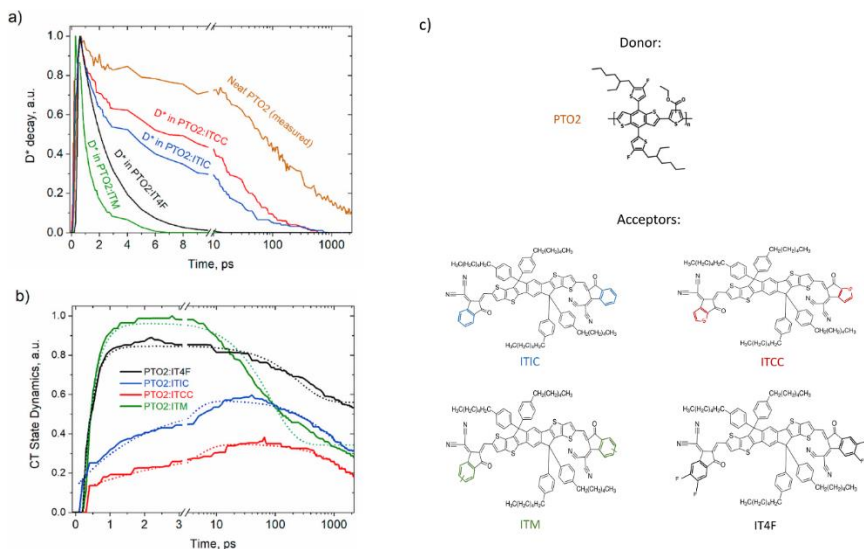
Figure 17. *Multivariate curve resolution modelling results under excitation of donor. Modelled D* (a) and CT/CS (b) state dynamics in indicated blends. Dashed curves in (b) show fitting of the kinetics by biexponential grow-decay function. (c) Chemical structures of indicated materials.*

Even though the absolute values of the CT/CS state generation yield cannot be obtained, the model, nonetheless, enables comparison of CT/CS state yields and their kinetics between different blends. It gives the highest CT/CS formation efficiency in PTO2:ITM blend, while efficiencies are lower by 1.1, 1.7 and 2.6 times for blends with IT4F, ITIC and ITCC respectively. The highest CT/CS concentration for PTO2:IT4F and PTO2:ITM blends is obtained at about 3 ps, while in case of PTO2:ITIC and PTO2:ITCC, the maximal value is reached at about 40 ps and 100 ps, respectively. After reaching the maximum values, the densities of the CT/CS states start to decrease due to recombination, but the decrease rates are significantly different.

To characterize the CT/CS formation and decay rates we have fitted the modelled CT/CS kinetics by simple biexponential function:

$$y = \left[A_1 + (1 - A_1) \times \left(1 - exp\left(-t/\tau_{growth}\right)\right)\right]$$
$$\times \left[A_2 + (1 - A_2) \times exp\left(-t/\tau_{decay}\right)\right],$$

where τ_{growth} and τ_{decay} correspond to formation and decay times of CT/CS states, A_1 shows fraction of CT/CS states formed faster than our time resolution, and A_2 shows a fraction of CT/CS states, which do not experience recombination on a several ns time scale. As seen from Fig. 17b, the fitting is not ideal, since these processes are not expected to be exponential, yet it provides reasonable comparison between the blends. The fitting results are presented in Table 1.

Table 1. *Biexponential fitting parameters for CT/CS dynamics*

Blend	A_1	$\tau_{growth, ps}$	A_2	$\tau_{decay, ps}$	ΔHOMO, meV
PTO2:ITM	0	0.31	0.35	84	50
PTO2:IT4F	0	0.26	0.66	253	130
PTO2:ITIC	0.26	2.09	0.50	819	70
PTO2:ITCC	0.36	3.47	0.18	2500	40

The CT/CS formation rates correlate with the LUMO level offset, again except for the PTO2:ITM blend. A1 values are given only for the blends with the lowest LUMO offsets, because for other two blends, the formation rate was too fast to discriminate it form the apparatus function. While in case of PTO2:ITIC and PTO2:ITCC we clearly observe two formation phases. The ultrafast phase should be attributed to the CT/CS state formation from the non-stabilized D* state.

The fraction A_2 of slowly recombining CT/CS states should be attributed to the CT states, which separate into CS states, thus form free charge carriers, and recombine much slower. Note, that in Figure 17b presented curves are non-normalized to retain approximately accurate CT/CS yield comparison between samples, whereas A_2 coefficient is for curves normalized to 1, thus seeming discrepancy between Table values and y-axis. A_2 fraction increases with the HOMO offsets and together with the formation efficiency of CT/CS states determines charge carrier generation yield. Clear correlation of this fraction with the HOMO offset suggests that efficient dissociation of the CT states depends on the offset value (exception for PTO2:ITM sample is caused by poorer mixing of D/A molecules due to stronger polarity of ITM acceptor, as discussed in depth in paper IV). As discussed above, thermally activated reverse electron transfer from the acceptor to donor's HOMO level may take place in OPV devices with sufficiently low HOMO level offset. We hypothesize that this process causes incomplete charge transfer from donor to

acceptor, as explained in Fig. 18, making CT state dissociation into CS state more difficult. This process should also cause appearance of the excited acceptor state A* during the CT/CS state relaxation. Dynamics of both these states is expected to be similar, therefore, we cannot explicitly distinguish the A* state, however, we cannot exclude that it contributes to the evaluated CT/CS state spectrum.
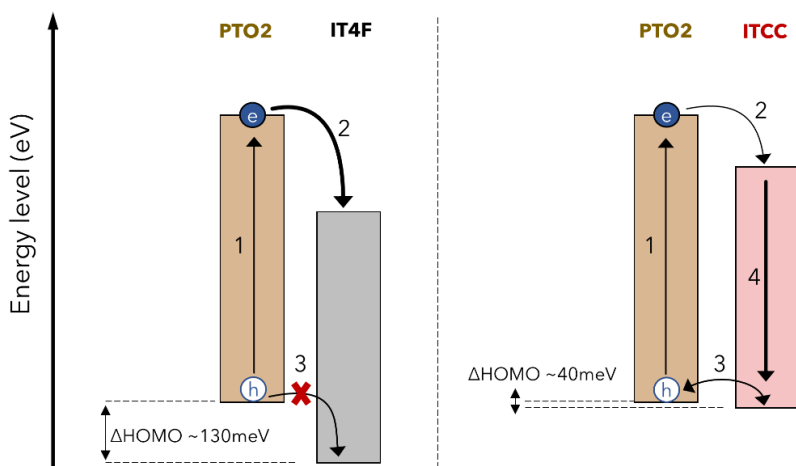
Figure 18. *Schematic comparison of processes in PTO2:IT4F and PTO2:ITCC blends after excitation donor PTO2 (1). Electron transfer to acceptor (2) is very fast in PTO2:IT4F and much slower in PTO2:ITCC. Afterwards, thermally activated hole transfer from HOMO level of a donor to acceptor takes place in PTO2:ITCC sample, due to low HOMO offset (3). It generates excited acceptor state A* which rapidly relaxes to the ground state (4). Such hole transfer is less potent in PTO2:IT4F sample due to a high energetic barrier. Figure adopted from paper IV.*

Investigations performed in paper III and IV led to **the third statement of the thesis**: Thermally activated back transfer of electrons from donor to acceptor via the highest occupied molecular orbital levels increases charge carrier recombination and reduces overall device efficiency in non-fullerene OPV devices with an energy offset between donor and acceptor HOMO levels less than ~100meV.

****

In the final part of the work, paper V, we investigated charge carrier generation mechanisms in state-of-the-art OSC device PM6:Y6 and its temperature dependence. In 2019, Zou et al. reported a novel NFA 2,20-((2Z,20Z)-((12,13-bis(2-ethylhexyl)- 3,9-diundecyl-12,13-dihydro-[1,2,5]thiadiazolo[3,4-e]thieno [2, 00300 :4 0,50]thieno [20,30:4,5]pyrrolo[3,2-g]thieno [20,30:4,5]thieno [3,2-b]indole-2,10-diyl) bis (methanylylidene))bis(5,6-difluoro-3-oxo-2, 3-dihydro-1H-indene-2,1-diylidene)) dimalononitrile (Y6), by employing a ladder-type electron deficient-core-based central fused ring with a benzothiadiazole core.[166] Matched with polymer donor poly[(2,6-(4,8-bis(5-(2-9 ethylhexyl-3-fluoro) thiophen-2-yl)-benzo [1,2-b:4, 5-b0] dithiophene))-alt-(5,5-(10,10 30-di-2-thienyl-50,70-bis(2-ethylhexyl) benzo [10,20-c:40,50-c0]dithiophene-4,8-11 dione))] (PM6), it became one of the best performing material combinations in OPVs, not only in single junction, but also in ternary configuration[167,168] and even in upscaled modules.[169] In recent years, several review articles have been devoted solely to the progress of the PM6:Y6 system.[170,171] Although the technical aspects of optimizing PM6:Y6 devices have been extensively covered, there is a clear lack of a comprehensive understanding of the physical basis of charge generation in these materials, which is critical for further improving device performance and developing even better NFAs. For example, two major works,[75,172] which scrutinize the photo-physics behind the operation of these PM6:Y6 solar cells, reach somewhat different conclusions regarding the role of temperature in electron-hole separation. Wang et al. argue that temperature-assisted charge hopping is involved in charge generation, whereas Perdigón-Toro et al. conclude that the activation energy for dissociation of the CT states is extraordinarily low, at about 6 meV, and therefore photocurrent is efficiently generated down to 100 K. Notably, the studies were limited to 200 and 75 K, lowest temperatures, respectively. Here, we report a detailed investigation of the charge carrier generation mechanism in the PM6:Y6 blend combining transient absorption and transient photoluminescence at various temperatures down to 15 K. The wide temperature range has helped us to uncover previously undiscovered aspects of charge generation in this state-of-the-art photovoltaic material.
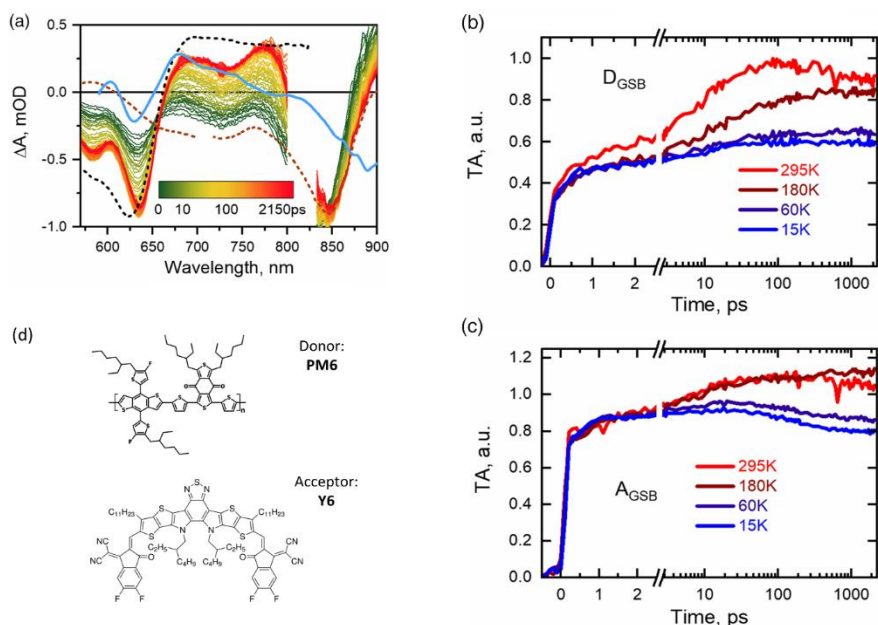
Figure 19. *a) Evolution of the transient absorption spectra of the PM6:Y6 blend after 820 nm laser excitation. The black and brown dashed curves show the normalized TA spectra of donor and acceptor neat films 1 ns after 560 or 820 nm excitation, respectively. The light blue curve shows electroabsorption spectrum; b) Donor ground state bleaching kinetics obtained by integrating the TA spectrum in the donor absorption band region (570–650 nm). c) Acceptor ground state bleaching kinetics, obtained by integrating TA spectrum in the acceptor absorption band region (770–890 nm). d) Chemical structure of donor PM6 and acceptor Y6.*

Let us now examine the path of charge generation by excitation of acceptor Y6. Figure 19 shows the time evolution of the TA spectrum of the PM6:Y6 blend excited at 820 nm at RT. The instantaneous (within experimental resolution) A_{GSB} signal is followed by a two-phase D_{GSB} signal growth (Figure 19 b,c). The fast phase, which is limited by our time resolution, accounts for about 40% of the total DGSB signal at RT. We assign it to conventional direct hole transfer from the excited acceptor (A*) to the donor, which forms identical interface CT states as in the case of excitation of a donor. The remaining ~60% of the D_{GSB} evolves on a timescale of several hundreds of picoseconds. According to Wang et al.,[172] this slow hole transfer channel is mediated via peculiar intramoiety CT state (xCT) of an acceptor, which forms at RT during ~0.2 ps and dissociates into free polarons within ~15 ps. Our data are consistent with this interpretation. Accordingly, we attribute the slow D_{GSB}

growth phase to delayed hole transfer from the xCT state or from free electron-hole pairs formed in the acceptor. An additional contribution to the D_{GSB} growth may come from the formation of CS states. This process is supported by the delayed (~10 ps) appearance of a kink at 570–625 nm (Figure 19a) in the TA signal, which is specifically characteristic of electroabsorption (EA) spectra and absent in the initial D_{GSB} signal. However, the contribution of EA can hardly be greater than in the case of donor excitation, resulting in a D_{GSB} growth by about 20% at RT. Therefore, most of the growth should still be attributed to delayed hole transfer mediated by xCT states. Importantly, D_{GSB} growth slows at low temperatures and is marginal at 15 K, indicating that hole transfer mediated by xCT states requires thermal assistance. The evolution of TA on a timescale of hundreds of picoseconds and a few nanoseconds is very similar to that observed under excitation of the donor: we observe a decay of the entire TA spectrum at RT, which disappears at a temperature reduced to 240 K, but is observed again at even lower temperatures.
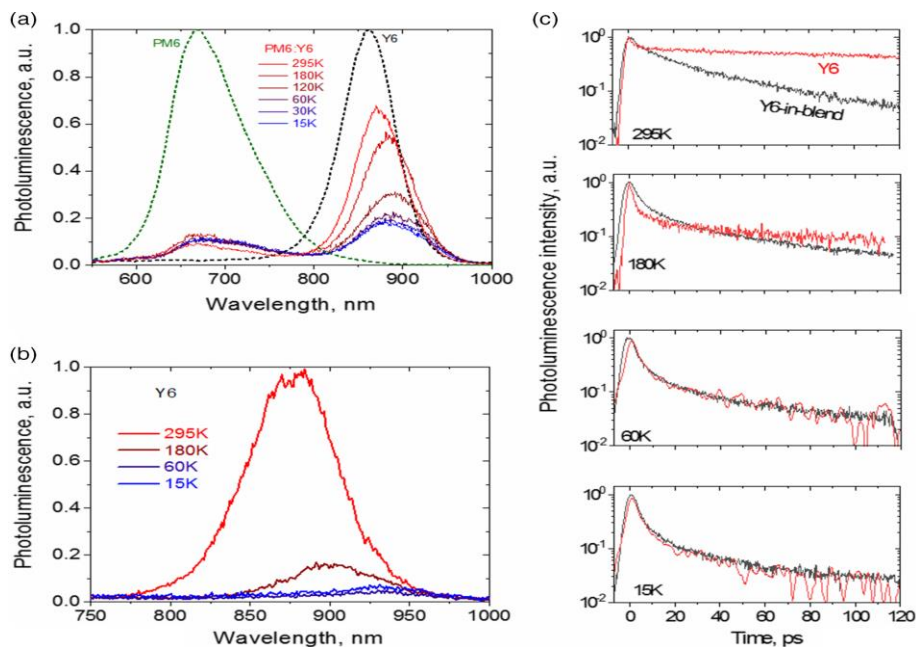

Figure 20. *Temporally integrated (0–120 ps) photoluminescence spectra of a) PM6:Y6 blend and b) Y6 film at various temperatures after excitation with a 515 nm laser pulse. The green and black dashed curves in (a) indicate the photoluminescence spectra of the neat PM6 and Y6 films; c) Y6 and Y6-in-blend photoluminescence kinetics at various temperatures. Figure adopted from paper V.*

To confirm the earlier made conclusions and to further elucidate the mechanisms of charge carrier generation, we have performed transient photoluminescence studies with a temporal resolution of less than 5 ps. We used an excitation wavelength of 515 nm, which predominantly excites the donor, although weak excitation of the acceptor is also present. It was shown in ref.[173] that the CT state manifold in the PM6:Y6 blend emits only very weakly and is even referred to as dark. Therefore, we can state that PL originates only from neutral-excited singlet states of donor and acceptor (D* and A*), so that the intensity of PL unambiguously represents the concentrations of D* and A*.

Figure 20a shows the temporally (0–120 ps) integrated PL spectra of the blend at different temperatures.

Despite the dominant excitation of the donor, the time-integrated PL of the donor is very weak and changes only slightly with temperature, which is in good agreement with the rapid and barrierless formation of interfacial CT states. In contrast, the PL intensity of the acceptor is much stronger and decreases sharply with temperature. Zhu et al. have recently demonstrated that the photoluminescence intensity of pure Y6 film also decreases at lower temperatures.[106] This unconventional behavior was explained by the assumption that strong polarization effects reduce the energy of the charge-separated state (xCT) even below that of the lowest excited singlet state, resulting in effective charge separation within the Y6 material. The fluorescence of Y6 is attributed to thermal repopulation of the A* state—a kind of thermally activated luminescence with an activation energy of ~185 meV, which is easily overcome at RT, but strongly hinders exciton reforming and thus luminescence at lower temperatures. We observe a similar trend in blend, where PL intensity decreases about threefold when the temperature is reduced from RT to 60 K (see Figure 20a) and remains stable at lower temperatures. However, this decrease is much weaker than the ~20-fold PL decrease in the pure Y6 film (Figure 20b). The PL kinetics of Y6 in the neat film and in the PM6:Y6 blend presented in Figure 18c explain the mentioned difference in temperature dependence. At very low temperatures, PL of the neat Y6 film and the PM6:Y6 blend decays identically, indicating that only intramolecular processes in Y6, namely the barrierless formation of nonfluorescent xCT states determines the PL decay. At 180 K and higher temperatures, a slow PL component appears in the neat Y6 film due to thermal repopulation of the A* state and causes a dramatic increase in the steady-state

PL, as shown in Figure 20b. While at high temperatures, the PL decay of the blend becomes much faster than that of the neat Y6 because hole transfer from the xCT state to the donor rapidly decimates the xCT state population and prevents the repopulation of the A* state, thus mitigates the increase of the steady-state PL intensity with temperature making it less impressive than in the pure Y6 film. This agrees well with the TA kinetics of the blend under excitation of the acceptor, which shows that only the ultrafast PM6 bleaching component caused by hole transfer from the "hot" A* state takes place at very low temperatures, while at higher temperatures PM6 bleaching related to the hole transfer continues for hundreds of picoseconds.

These investigations lead to **the fourth statement of the thesis:** Upon excitation of acceptor Y6 in PM6:Y6 organic solar cell, charge carrier generation occurs via two different pathways that are equally efficient at room temperature - via the interfacial CT state and via the intra-moiety xCT state. The conventional pathway via the CT state is almost temperature independent, while charge carrier generation via the xCT state requires thermal support.

ABBREVIATIONS

A*	Excited acceptor
BHJ	Bulk hetero-junction
CS	Charge Separated state
c-Si	Crystalline silicon
CT	Charge Transfer state
D*	Excited donor
D/A	Donor/Acceptor
DOS	Density of States
EA	Electroabsorption
FF	Fill Factor
GDM	Gaussian Disorder Model
GSB	Ground State Bleaching
HOMO	Highest Occupied Molecular Orbit
IT4	3,9-bis(2-methylene-((3-(1,1-dicyanomethylene)-6,7-difluoro)-indanone))-5,5,11,11-tetrakis(4-hexylphenyl)-dithieno[2,3-d:2',3'-d']-s-indaceno[1,2-b:5,6-b']dithiophene acceptor
ITCC	3,9-bis(4-(1,1-dicyanomethylene)-3-methylene-2-oxo-cyclopenta[b]thiophen)-5,5,11,11-tetrakis(4-hexylphenyl)-dithieno[2,3-d':2,3-d']-s-indaceno[1,2-b:5,6-b']-dithiophene acceptor
ITIC	3,9-bis(2-methylene-(3-(1,1-dicyanomethylene)-indanone))-5,5,11,11-tetrakis(4-hexylphenyl)-dithieno[2,3-d:2',3'-d']-s-indaceno[1,2-b:5,6-b']dithiophene acceptor
ITM	3,9-bis(2-methylene-((3-(1,1-dicyanomethylene)-6/7-methyl)-indanone))-5,5,11,11-tetrakis(4-hexylphenyl)-dithieno[2,3-d:2',3'-d']-s-indaceno[1,2-b:5,6-b']dithiophene acceptor
IV	Current Density and voltage characteristics
Jsc	Short-circuit current density
LUMO	Lowest Unoccupied Molecular Orbit
MCP	Multi Channel Plate
MPP	Maximum Power Point

N2200	poly{[N,N′-bis(2-octyldodecyl)-naphthalene-1,4,5,8-bis(dicarboximide)-2,6-diy1]-alt-5,5′-(2,2′-dithiophene)} acceptor
NF	Non-Fullerene
OEFP	Optical Electric Field Probing
OPV	Organic Photovoltaic
OSC	Organic Solar Cell
PBDB-T	Poly[[4,8-bis[5-(2-ethylhexyl)-2-thienyl]benzo[1,2-b:4,5-b′]dithiophene-2,6-diyl]-2,5-thiophenediyl[5,7-bis(2-ethylhexyl)-4,8-dioxo-4H,8H-benzo[1,2-c:4,5-c′]dithiophene-1,3-diyl]] donor
PBDB-T-2Cl	Poly[(2,6-(4,8-bis(5-(2-ethylhexyl-3-chloro)thiophen-2-yl)-benzo[1,2-b:4,5-b']dithiophene))-alt-(5,5-(1',3'-di-2-thienyl-5',7'-bis(2-ethylhexyl)benzo[1',2'-c:4',5'-c']dithiophene-4,8-dione)]
PC$_{71}$BM	6,6]-Phenyl-C71-butyric acid methyl ester acceptor
PCE	Power Conversion Efficiency
PDCBT-2F	3-fluoro-2,2′-bithiophene -4,4′-dicarboxylate donor
PL	Photoluminescence
PM6	Poly[(2,6-(4,8-bis(5-(2-ethylhexyl-3-fluoro)thiophen-2-yl)-benzo[1,2-b:4,5-b']dithiophene))-alt-(5,5-(1',3'-di-2-thienyl-5',7'-bis(2-ethylhexyl)benzo[1',2'-c:4',5'-c']dithiophene-4,8-dione)] donor
PP	Pump-probe
PTO2	Poly[(2,6-(4,8-bis(5-(2-ethylhexyl)thiophen-2-yl)-benzo[1,2-b:4,5-b']dithiophene))-alt-(2,2-ethyl-3(or4)-carboxylate-thiophene)] donor
PV	Photovoltaics
RT	Room temperature
TA	Transient Absorption
TAS	Transient Absorption Spectroscopy
TDCF	Time-Delayed Collection Field
TPC	Transient Photocurrent
tPL	Transient Photoluminescence

TQ1	Poly[[2,3-bis(3-octyloxyphenyl)-5,8-quinoxalinediyl]-2,5-thiophenediyl] donor
TREFISH	Time Resolved Electric Field Induced Second Harmonic Generation
Voc	Open-circuit Voltage
xCT	Intra-moiety Charge Transfer State
Y6	2,2'-((2Z,2'Z)-((12,13-bis(2-ethylhexyl)-3,9-diundecyl-12,13-dihydro-[1,2,5]thiadiazolo[3,4-e]thieno[2'',3'':4',5']thieno[2',3':4,5]pyrrolo[3,2-g]thieno[2',3':4,5]thieno[3,2-b]indole-2,10-diyl)bis(methanylylidene))bis(5,6-difluoro-3-oxo-2,3-dihydro-1H-indene-2,1-diylidene))dimalononitrile acceptor

REFERENCES

(1) IAE. *Key World Energy Statistics 2021*; International Energy Agency: Paris, 2021; p 81.

(2) MacKenzie, J. J. Oil as a Finite Resource. *Nat Resour Res* **1998**, *7* (2), 97–100. https://doi.org/10.1007/BF02767703.

(3) Sommer, A. Burning Fossil Fuels: Impact of Climate Change on Health. *International Journal of Health Services* **2016**, *46* (1), 48–52.

(4) Smith, I. W. The Combustion Rates of Coal Chars: A Review. *Symposium (International) on Combustion* **1982**, *19* (1), 1045–1065. https://doi.org/10.1016/S0082-0784(82)80281-6.

(5) *Climate Milestone: Earth's CO2 Level Nears 400 ppm*. https://www.nationalgeographic.com/pages/article/130510-earth-co2-milestone-400-ppm

(6) Nicholls, R. J.; Cazenave, A. *Sea-Level Rise and Its Impact on Coastal Zones*. Science **2010**, 328 (5985), 1517–1520. https://doi.org/10.1126/science.1185782.

(7) Chen, J. L.; Wilson, C. R.; Tapley, B. D. *Satellite Gravity Measurements Confirm Accelerated Melting of Greenland Ice Sheet*. Science **2006**, 313 (5795), 1958–1960. https://doi.org/10.1126/science.1129007.

(8) Zwally, H. J.; Abdalati, W.; Herring, T.; Larson, K.; Saba, J.; Steffen, K. *Surface Melt-Induced Acceleration of Greenland Ice-Sheet Flow*. Science **2002**, 297 (5579), 218–222. https://doi.org/10.1126/science.1072708.

(9) Idso, S. B. *The Climatological Significance of a Doubling of Earth's Atmospheric Carbon Dioxide Concentration*. Science **1980**, 207 (4438), 1462–1463. https://doi.org/10.1126/science.207.4438.1462.

(10) Hughes, T. P.; Baird, A. H.; Bellwood, D. R.; Card, M.; Connolly, S. R.; Folke, C.; Grosberg, R.; Hoegh-Guldberg, O.; Jackson, J. B. C.; Kleypas, J.; Lough, J. M.; Marshall, P.; Nyström, M.; Palumbi, S. R.; Pandolfi, J. M.; Rosen, B.; Roughgarden, J. *Climate Change, Human Impacts, and the Resilience of Coral Reefs*. Science **2003**, 301 (5635), 929–933. https://doi.org/10.1126/science.1085046.

(11) Bouckaert, S.; Pales, A. F.; McGlade, C.; Remme, U.; Wanner, B.; Varro, L.; D'Ambrosio, D.; Spencer, T. Net Zero by 2050: A Roadmap for the Global Energy Sector. **2021**.

(12) Brown, L. R. (Lester R.; Larsen, J.; Roney, J. M.; Adams, E. E. *The Great Transition : Shifting from Fossil Fuels to Solar and Wind Energy*, First edition.; Shifting from fossil fuels to solar and wind energy; W.W. Norton & Company: New York, 2015.

(13) Charters, W. W. S. *Solar Energy : Theory and Design of Solar Thermal Systems / by William W.S. Charters and Trevor L. Pryor*; Pryor, T. L., Victorian Solar Energy Council, Series Eds.; Australian Syndicators for the Victorian Solar Energy Council: Melbourne, 1982.

(14) Gust, D.; Moore, T. A.; Moore, A. L. Solar Fuels via Artificial Photosynthesis. *Acc. Chem. Res.* **2009**, *42* (12), 1890–1898. https://doi.org/10.1021/ar900209b.

(15) IAE. *World Energy Outlook 2021*; International Energy Agency, 2021; p 386.

(16) Metz, A.; Fischer, M.; Trube, J. International Technology Roadmap for Photovoltaics (ITRPV): Crystalline Silicon Technology-Current Status and Outlook. In *Proceedings of the PV Manufacturing in Europe Conference, Brussels, Belgium*; 2017; pp 18–19.

(17) Timilsina, G. R. Are Renewable Energy Technologies Cost Competitive for Electricity Generation? *Renewable Energy* **2021**, *180*, 658–672. https://doi.org/10.1016/j.renene.2021.08.088.

(18) Rajkanan, K.; Singh, R.; Shewchun, J. Absorption Coefficient of Silicon for Solar Cell Calculations. *Solid-State Electronics* **1979**, *22* (9), 793–795. https://doi.org/10.1016/0038-1101(79)90128-X.

(19) (Mariska) de Wild-Scholten, M. J. Energy Payback Time and Carbon Footprint of Commercial Photovoltaic Systems. *Solar Energy Materials and Solar Cells* **2013**, *119*, 296–305. https://doi.org/10.1016/j.solmat.2013.08.037.

(20) Søndergaard, R.; Hösel, M.; Angmo, D.; Larsen-Olsen, T. T.; Krebs, F. C. Roll-to-Roll Fabrication of Polymer Solar Cells. *Materials Today* **2012**, *15* (1), 36–49. https://doi.org/10.1016/S1369-7021(12)70019-6.

(21) Günes, S.; Neugebauer, H.; Sariciftci, N. S. Conjugated Polymer-Based Organic Solar Cells. *Chem. Rev.* **2007**, *107* (4), 1324–1338. https://doi.org/10.1021/cr050149z.

(22) Espinosa, N.; Hösel, M.; Angmo, D.; Krebs, F. C. Solar Cells with One-Day Energy Payback for the Factories of the Future. *Energy Environ. Sci.* **2012**, *5* (1), 5117–5132. https://doi.org/10.1039/C1EE02728J.

(23) Qin, Y.; Chang, Y.; Zhu, X.; Gu, X.; Guo, L.; Zhang, Y.; Wang, Q.; Zhang, J.; Zhang, X.; Liu, X.; Lu, K.; Zhou, E.; Wei, Z.; Sun, X. 18.4% Efficiency Achieved by the Cathode Interface Engineering in Non-Fullerene Polymer Solar Cells. *Nano Today* **2021**, *41*, 101289. https://doi.org/10.1016/j.nantod.2021.101289.

(24) Liu, Q.; Jiang, Y.; Jin, K.; Qin, J.; Xu, J.; Li, W.; Xiong, J.; Liu, J.; Xiao, Z.; Sun, K.; Yang, S.; Zhang, X.; Ding, L. 18% Efficiency Organic Solar Cells. *Science Bulletin* **2020**, *65* (4), 272–275. https://doi.org/10.1016/j.scib.2020.01.001.

(25) *Reference Air Mass 1.5 Spectra*. https://www.nrel.gov/grid/solar-resource/spectra-am1.5.html.

(26) Köhler, A. & Bässler, H. *Electronic processes in organic semiconductors: An introduct*ion (John Wiley & Sons, 2015)

(27) Tress, W. Organic Solar Cells. In *Organic Solar Cells: Theory, Experiment, and Device Simulation*; Tress, W., Ed.; Springer

International Publishing: Cham, 2014; pp 67–214. https://doi.org/10.1007/978-3-319-10097-5_3.

(28) Leonardi, F. <1986>. Self-Assembled Monolayers (SAMs) in Organic Field-Effect Transistors. Doctoral Thesis, Alma Mater Studiorum - Università di Bologna, 2014. https://doi.org/10.6092/unibo/amsdottorato/6461.

(29) Hou, J.; Inganäs, O.; Friend, R. H.; Gao, F. Organic Solar Cells Based on Non-Fullerene Acceptors. *Nat. Mater.* **2018**, *17* (2), 119–128. https://doi.org/10.1038/nmat5063.

(30) Dai, S.; Zhao, F.; Zhang, Q.; Lau, T.-K.; Li, T.; Liu, K.; Ling, Q.; Wang, C.; Lu, X.; You, W.; Zhan, X. *Fused Nonacyclic Electron Acceptors for Efficient Polymer Solar Cells.* J. Am. Chem. Soc. **2017**, 139 (3), 1336–1343. https://doi.org/10.1021/jacs.6b12755.

(31) Li, C.; Zhou, J.; Song, J.; Xu, J.; Zhang, H.; Zhang, X.; Guo, J.; Zhu, L.; Wei, D.; Han, G.; Min, J.; Zhang, Y.; Xie, Z.; Yi, Y.; Yan, H.; Gao, F.; Liu, F.; Sun, Y. Non-Fullerene Acceptors with Branched Side Chains and Improved Molecular Packing to Exceed 18% Efficiency in Organic Solar Cells. *Nat Energy* **2021**, *6* (6), 605–613. https://doi.org/10.1038/s41560-021-00820-x.

(32) Liu, S.; Yuan, J.; Deng, W.; Luo, M.; Xie, Y.; Liang, Q.; Zou, Y.; He, Z.; Wu, H.; Cao, Y. High-Efficiency Organic Solar Cells with Low Non-Radiative Recombination Loss and Low Energetic Disorder. *Nat. Photonics* **2020**, *14* (5), 300–305. https://doi.org/10.1038/s41566-019-0573-5.

(33) Dvorak, M.; Wei, S.-H.; Wu, Z. Origin of the Variation of Exciton Binding Energy in Semiconductors. *Phys. Rev. Lett.* **2013**, *110* (1), 016402. https://doi.org/10.1103/PhysRevLett.110.016402.

(34) Knupfer, M. Exciton Binding Energies in Organic Semiconductors. *Appl. Phys. A* **2003**, *77* (5), 623–626. https://doi.org/10.1007/s00339-003-2182-9.

(35) Deibel, C.; Mack, D.; Gorenflot, J.; Schöll, A.; Krause, S.; Reinert, F.; Rauh, D.; Dyakonov, V. Energetics of Excited States in the Conjugated Polymer Poly(3-Hexylthiophene). *Phys. Rev. B* **2010**, *81* (8), 085202. https://doi.org/10.1103/PhysRevB.81.085202.

(36) Classen, A.; Chochos, C. L.; Lüer, L.; Gregoriou, V. G.; Wortmann, J.; Osvet, A.; Forberich, K.; McCulloch, I.; Heumüller, T.; Brabec, C. J. The Role of Exciton Lifetime for Charge Generation in Organic Solar Cells at Negligible Energy-Level Offsets. *Nat Energy* **2020**. https://doi.org/10.1038/s41560-020-00684-7.

(37) Lunt, R. R.; Giebink, N. C.; Belak, A. A.; Benziger, J. B.; Forrest, S. R. Exciton Diffusion Lengths of Organic Semiconductor Thin Films Measured by Spectrally Resolved Photoluminescence Quenching. *Journal of Applied Physics* **2009**, *105* (5), 053711. https://doi.org/10.1063/1.3079797.

(38) Shao, Y.; Yang, Y. Efficient Organic Heterojunction Photovoltaic Cells Based on Triplet Materials. *Advanced Materials* **2005**, *17* (23), 2841–2844. https://doi.org/10.1002/adma.200501297.

(39) Spano, F. C.; Clark, J.; Silva, C.; Friend, R. H. Determining Exciton Coherence from the Photoluminescence Spectral Line Shape in Poly(3-Hexylthiophene) Thin Films. *J. Chem. Phys.* **2009**, *130* (7), 074904. https://doi.org/10.1063/1.3076079.

(40) Meskers, S. C. J.; Hübner, J.; Oestreich, M.; Bässler, H. Dispersive Relaxation Dynamics of Photoexcitations in a Polyfluorene Film Involving Energy Transfer: Experiment and Monte Carlo Simulations. *J. Phys. Chem. B* **2001**, *105* (38), 9139–9149. https://doi.org/10.1021/jp0113331.

(41) Kersting, R.; Mollay, B.; Rusch, M.; Wenisch, J.; Leising, G.; Kauffmann, H. F. Femtosecond Site-Selective Probing of Energy Relaxing Excitons in Poly(Phenylenevinylene): Luminescence Dynamics and Lifetime Spectra. *J. Chem. Phys.* **1997**, *106* (7), 2850–2864. https://doi.org/10.1063/1.473094.

(42) Grage, M. M.-L.; Pullerits, T.; Ruseckas, A.; Theander, M.; Inganäs, O.; Sundström, V. Conformational Disorder of a Substituted Polythiophene in Solution Revealed by Excitation Transfer. *Chemical Physics Letters* **2001**, *339* (1), 96–102. https://doi.org/10.1016/S0009-2614(01)00305-0.

(43) Grage, M. M.-L.; Wood, P. W.; Ruseckas, A.; Pullerits, T.; Mitchell, W.; Burn, P. L.; Samuel, I. D. W.; Sundström, V. Conformational Disorder and Energy Migration in MEH-PPV with Partially Broken Conjugation. *J. Chem. Phys.* **2003**, *118* (16), 7644–7650. https://doi.org/10.1063/1.1562190.

(44) Grage, M. M.-L.; Zaushitsyn, Y.; Yartsev, A.; Chachisvilis, M.; Sundström, V.; Pullerits, T. Ultrafast Excitation Transfer and Trapping in a Thin Polymer Film. *Phys. Rev. B* **2003**, *67* (20), 205207. https://doi.org/10.1103/PhysRevB.67.205207.

(45) Westenhoff, S.; Daniel, C.; Friend, R. H.; Silva, C.; Sundström, V.; Yartsev, A. Exciton Migration in a Polythiophene: Probing the Spatial and Energy Domain by Line-Dipole Förster-Type Energy Transfer. *J. Chem. Phys.* **2005**, *122* (9), 094903. https://doi.org/10.1063/1.1855292.

(46) Watkins, P. K.; Walker, A. B.; Verschoor, G. L. B. *Dynamical Monte Carlo Modelling of Organic Solar Cells: The Dependence of Internal Quantum Efficiency on Morphology.* Nano Lett. **2005**, 5 (9), 1814–1818. https://doi.org/10.1021/nl051098o..

(47) Cnops, K.; Rand, B. P.; Cheyns, D.; Verreet, B.; Empl, M. A.; Heremans, P. 8.4% Efficient Fullerene-Free Organic Solar Cells Exploiting Long-Range Exciton Energy Transfer. *Nat Commun* **2014**, *5* (1), 3406. https://doi.org/10.1038/ncomms4406.

(48) Haugeneder, A.; Neges, M.; Kallinger, C.; Spirkl, W.; Lemmer, U.; Feldmann, J.; Scherf, U.; Harth, E.; Gügel, A.; Müllen, K. Exciton Diffusion and Dissociation in Conjugated Polymer/Fullerene Blends and Heterostructures. *Phys. Rev. B* **1999**, *59* (23), 15346–15351. https://doi.org/10.1103/PhysRevB.59.15346.

(49) Markov, D. E.; Amsterdam, E.; Blom, P. W. M.; Sieval, A. B.; Hummelen, J. C. Accurate Measurement of the Exciton Diffusion Length in a Conjugated Polymer Using a Heterostructure with a Side-Chain Cross-Linked Fullerene Layer. *J. Phys. Chem. A* **2005**, *109* (24), 5266–5274. https://doi.org/10.1021/jp0509663.

(50) Scully, S. R.; McGehee, M. D. Effects of Optical Interference and Energy Transfer on Exciton Diffusion Length Measurements in Organic Semiconductors. *Journal of Applied Physics* **2006**, *100* (3), 034907. https://doi.org/10.1063/1.2226687.

(51) Mikhnenko, O. V.; Cordella, F.; Sieval, A. B.; Hummelen, J. C.; Blom, P. W. M.; Loi, M. A. Temperature Dependence of Exciton Diffusion in Conjugated Polymers. *J. Phys. Chem. B* **2008**, *112* (37), 11601–11604. https://doi.org/10.1021/jp8042363.

(52) Mikhnenko, O. V.; Azimi, H.; Scharber, M.; Morana, M.; Blom, P. W. M.; Loi, M. A. Exciton Diffusion Length in Narrow Bandgap Polymers. *Energy Environ. Sci.* **2012**, *5* (5), 6960–6965. https://doi.org/10.1039/C2EE03466B.

(53) Burlakov, V. M.; Kawata, K.; Assender, H. E.; Briggs, G. A. D.; Ruseckas, A.; Samuel, I. D. W. Discrete Hopping Model of Exciton Transport in Disordered Media. *Phys. Rev. B* **2005**, *72* (7), 075206. https://doi.org/10.1103/PhysRevB.72.075206.

(54) Xu, G.; Lu, N.; Wang, W.; Gao, N.; Ji, Z.; Li, L.; Liu, M. Universal Description of Exciton Diffusion Length in Organic Photovoltaic Cell. *Organic Electronics* **2015**, *23*, 53–56. https://doi.org/10.1016/j.orgel.2015.04.006.

(55) Toušek, J.; Toušková, J.; Remeš, Z.; Čermák, J.; Kousal, J.; Kindl, D.; Kuřitka, I. Exciton Diffusion Length and Concentration of Holes in MEH-PPV Polymer Using the Surface Voltage and Surface Photovoltage Methods. *Chemical Physics Letters* **2012**, *552*, 49–52. https://doi.org/10.1016/j.cplett.2012.09.052.

(56) Firdaus, Y.; Le Corre, V. M.; Karuthedath, S.; Liu, W.; Markina, A.; Huang, W.; Chattopadhyay, S.; Nahid, M. M.; Nugraha, M. I.; Lin, Y.; Seitkhan, A.; Basu, A.; Zhang, W.; McCulloch, I.; Ade, H.; Labram, J.; Laquai, F.; Andrienko, D.; Koster, L. J. A.; Anthopoulos, T. D. Long-Range Exciton Diffusion in Molecular Non-Fullerene Acceptors. *Nat Commun* **2020**, *11* (1), 5220. https://doi.org/10.1038/s41467-020-19029-9.

(57) Scharber, M. C.; Mühlbacher, D.; Koppe, M.; Denk, P.; Waldauf, C.; Heeger, A. J.; Brabec, C. J. Design Rules for Donors in Bulk-

Heterojunction Solar Cells—Towards 10 % Energy-Conversion Efficiency. *Advanced Materials* **2006**, *18* (6), 789–794. https://doi.org/10.1002/adma.200501717.

(58) Yao, Y.; Sun, X.; Ding, B.; Li, D.-L.; Hou, X.; Wu, C.-Q. A Combined Theoretical and Experimental Investigation on the Transient Photovoltage in Organic Photovoltaic Cells. *Appl. Phys. Lett.* **2010**, *96* (20), 203306. https://doi.org/10.1063/1.3431289.

(59) Song, Q. L.; Wu, H. R.; Ding, X. M.; Hou, X. Y.; Li, F. Y.; Zhou, Z. G. Exciton Dissociation at the Indium Tin Oxide-N,N′-Bis(Naphthalen-1-Yl)-N,N′-Bis(Phenyl) Benzidine Interface: A Transient Photovoltage Study. *Appl. Phys. Lett.* **2006**, *88* (23), 232101. https://doi.org/10.1063/1.2209203.

(60) Li, D.-L.; Si, W.; Yang, W.-C.; Yao, Y.; Hou, X.-Y.; Wu, C.-Q. Spike in Transient Photocurrent of Organic Solar Cell: Exciton Dissociation at Interface. *Physics Letters A* **2012**, *376* (4), 227–230. https://doi.org/10.1016/j.physleta.2011.11.055.

(61) Chamberlain, G. A. Organic Solar Cells: A Review. *Solar Cells* **1983**, *8* (1), 47–83. https://doi.org/10.1016/0379-6787(83)90039-X.

(62) Tang, C. W. Two-layer Organic Photovoltaic Cell. *Appl. Phys. Lett.* **1986**, *48* (2), 183–185. https://doi.org/10.1063/1.96937.

(63) Yu, G.; Gao, J.; Hummelen, J. C.; Wudl, F.; Heeger, A. J. Polymer Photovoltaic Cells: Enhanced Efficiencies via a Network of Internal Donor-Acceptor Heterojunctions. *Science* **1995**, *270* (5243), 1789–1791. https://doi.org/10.1126/science.270.5243.1789.

(64) Halls, J. J. M.; Walsh, C. A.; Greenham, N. C.; Marseglia, E. A.; Friend, R. H.; Moratti, S. C.; Holmes, A. B. Efficient Photodiodes from Interpenetrating Polymer Networks. *Nature* **1995**, *376* (6540), 498–500. https://doi.org/10.1038/376498a0.

(65) Zheng, Z.; Wang, J.; Bi, P.; Ren, J.; Wang, Y.; Yang, Y.; Liu, X.; Zhang, S.; Hou, J. Tandem Organic Solar Cell with 20.2% Efficiency. *Joule* **2022**, *6* (1), 171–184. https://doi.org/10.1016/j.joule.2021.12.017.

(66) Kadem, B. Y.; Hassan, A. K.; Cranton, W. *The Effects of Organic Solvents and Their Co-Solvents on the Optical, Structural, Morphological of P3HT:PCBM Organic Solar Cells*. AIP Conference Proceedings **2016**, 1758 (1), 020006. https://doi.org/10.1063/1.4959382.

(67) Zhao, J.; Li, Y.; Yang, G.; Jiang, K.; Lin, H.; Ade, H.; Ma, W.; Yan, H. Efficient Organic Solar Cells Processed from Hydrocarbon Solvents. *Nature Energy* **2016**, *1* (2), 15027. https://doi.org/10.1038/nenergy.2015.27.

(68) Kim, Y.; Choulis, S. A.; Nelson, J.; Bradley, D. D. C.; Cook, S.; Durrant, J. R. *Device Annealing Effect in Organic Solar Cells with Blends of Regioregular Poly(3-Hexylthiophene) and Soluble Fullerene*. Appl. Phys. Lett. **2005**, 86 (6), 063502. https://doi.org/10.1063/1.1861123..

(69) Shin, P.-K.; Kumar, P.; Kumar, A.; Kannappan, S.; Ochiai, S. *Effects of Organic Solvents for Composite Active Layer of PCDTBT/PC71BM on Characteristics of Organic Solar Cell Devices*. International Journal of Photoenergy 2014, **2014**, 786468. https://doi.org/10.1155/2014/786468.

(70) Qin, Y.; Xu, Y.; Peng, Z.; Hou, J.; Ade, H. Low Temperature Aggregation Transitions in N3 and Y6 Acceptors Enable Double-Annealing Method That Yields Hierarchical Morphology and Superior Efficiency in Nonfullerene Organic Solar Cells. *Advanced Functional Materials* **2020**, *30* (46), 2005011. https://doi.org/10.1002/adfm.202005011.

(71) Uğur, Ş.; Pekcan, Ö. Effects of Annealing on Morphology of Polymer/Polymer (PS/PMMA) Blend; a Fluorescence Study. *Journal of Applied Polymer Science* **2006**, *100* (3), 2104–2110. https://doi.org/10.1002/app.23458.

(72) Kietzke, T.; Shin, R. Y. C.; Egbe, D. A. M.; Chen, Z.-K.; Sellinger, A. *Effect of Annealing on the Characteristics of Organic Solar Cells: Polymer Blends with a 2-Vinyl-4,5-Dicyanoimidazole Derivative.* Macromolecules **2007**, 40 (13), 4424–4428. https://doi.org/10.1021/ma0706273

(73) Gélinas, S.; Rao, A.; Kumar, A.; Smith, S. L.; Chin, A. W.; Clark, J. Ultrafast Long-Range Charge Separation in Organic Semiconductor Photovoltaic Diodes. **2014**, *343*, 6.

(74) Stoltzfus, D. M.; Donaghey, J. E.; Armin, A.; Shaw, P. E.; Burn, P. L.; Meredith, P. Charge Generation Pathways in Organic Solar Cells: Assessing the Contribution from the Electron Acceptor. *Chemical Reviews* **2016**, *116* (21), 12920–12955. https://doi.org/10.1021/acs.chemrev.6b00126.

(75) Perdigón-Toro, L.; Zhang, H.; Markina, A.; Yuan, J.; Hosseini, S. M.; Wolff, C. M.; Zuo, G.; Stolterfoht, M.; Zou, Y.; Gao, F.; Andrienko, D.; Shoaee, S.; Neher, D. Barrierless Free Charge Generation in the High-Performance PM6:Y6 Bulk Heterojunction Non-Fullerene Solar Cell. *Adv. Mater.* **2020**, *32* (9), 1906763. https://doi.org/10.1002/adma.201906763.

(76) Chen, S.; Myeon Lee, S.; Xu, J.; Lee, J.; Cheol Lee, K.; Hou, T.; Yang, Y.; Jeong, M.; Lee, B.; Cho, Y.; Jung, S.; Oh, J.; Zhang, Z.-G.; Zhang, C.; Xiao, M.; Li, Y.; Yang, C. Ultrafast Channel II Process Induced by a 3-D Texture with Enhanced Acceptor Order Ranges for High-Performance Non-Fullerene Polymer Solar Cells. *Energy & Environmental Science* **2018**, *11* (9), 2569–2580. https://doi.org/10.1039/C8EE01546E.

(77) Müller, J. G.; Lupton, J. M.; Feldmann, J.; Lemmer, U.; Scharber, M. C.; Sariciftci, N. S.; Brabec, C. J.; Scherf, U. Ultrafast Dynamics of Charge Carrier Photogeneration and Geminate Recombination in

Conjugated Polymer:Fullerene Solar Cells. *Phys. Rev. B* **2005**, *72* (19), 195208. https://doi.org/10.1103/PhysRevB.72.195208.

(78) Tamura, H.; Burghardt, I. Ultrafast Charge Separation in Organic Photovoltaics Enhanced by Charge Delocalization and Vibronically Hot Exciton Dissociation. *J. Am. Chem. Soc.* **2013**, *135* (44), 16364–16367. https://doi.org/10.1021/ja4093874.

(79) Tamai, Y.; Fan, Y.; Kim, V. O.; Ziabrev, K.; Rao, A.; Barlow, S.; Marder, S. R.; Friend, R. H.; Menke, S. M. Ultrafast Long-Range Charge Separation in Nonfullerene Organic Solar Cells. *ACS Nano* **2017**, *11* (12), 12473–12481. https://doi.org/10.1021/acsnano.7b06575.

(80) Ward, A. J.; Ruseckas, A.; Kareem, M. M.; Ebenhoch, B.; Serrano, L. A.; Al-Eid, M.; Fitzpatrick, B.; Rotello, V. M.; Cooke, G.; Samuel, I. D. W. The Impact of Driving Force on Electron Transfer Rates in Photovoltaic Donor–Acceptor Blends. *Advanced Materials* **2015**, *27* (15), 2496–2500. https://doi.org/10.1002/adma.201405623.

(81) Jakowetz, A. C.; Böhm, M. L.; Zhang, J.; Sadhanala, A.; Huettner, S.; Bakulin, A. A.; Rao, A.; Friend, R. H. What Controls the Rate of Ultrafast Charge Transfer and Charge Separation Efficiency in Organic Photovoltaic Blends. *J Am Chem Soc* **2016**, *138* (36), 11672–11679. https://doi.org/10.1021/jacs.6b05131.

(82) Eastham, N. D.; Logsdon, J. L.; Manley, E. F.; Aldrich, T. J.; Leonardi, M. J.; Wang, G.; Powers-Riggs, N. E.; Young, R. M.; Chen, L. X.; Wasielewski, M. R.; Melkonyan, F. S.; Chang, R. P. H.; Marks, T. J. Hole-Transfer Dependence on Blend Morphology and Energy Level Alignment in Polymer: ITIC Photovoltaic Materials. *Advanced Materials* **2018**, *30* (3), 1704263. https://doi.org/10.1002/adma.201704263.

(83) Li, S.; Zhan, L.; Sun, C.; Zhu, H.; Zhou, G.; Yang, W.; Shi, M.; Li, C.-Z.; Hou, J.; Li, Y.; Chen, H. Highly Efficient Fullerene-Free Organic Solar Cells Operate at Near Zero Highest Occupied Molecular Orbital Offsets. *J. Am. Chem. Soc.* **2019**, *141* (7), 3073–3082. https://doi.org/10.1021/jacs.8b12126.

(84) Brédas, J.-L.; Norton, J. E.; Cornil, J.; Coropceanu, V. Molecular Understanding of Organic Solar Cells: The Challenges. *Acc. Chem. Res.* **2009**, *42* (11), 1691–1699. https://doi.org/10.1021/ar900099h.

(85) Coropceanu, V.; Chen, X.-K.; Wang, T.; Zheng, Z.; Brédas, J.-L. Charge-Transfer Electronic States in Organic Solar Cells. *Nat Rev Mater* **2019**, *4* (11), 689–707. https://doi.org/10.1038/s41578-019-0137-9.

(86) Deibel, C.; Strobel, T.; Dyakonov, V. Role of the Charge Transfer State in Organic Donor–Acceptor Solar Cells. *Advanced Materials* **2010**, *22* (37), 4097–4111. https://doi.org/10.1002/adma.201000376.

(87) Tvingstedt, K.; Vandewal, K.; Gadisa, A.; Zhang, F.; Manca, J.; Inganäs, O. Electroluminescence from Charge Transfer States in Polymer Solar

Cells. *Journal of the American Chemical Society* **2009**, *131* (33), 11819–11824. https://doi.org/10.1021/ja903100p.

(88) Tvingstedt, K.; Vandewal, K.; Zhang, F.; Inganäs, O. On the Dissociation Efficiency of Charge Transfer Excitons and Frenkel Excitons in Organic Solar Cells: A Luminescence Quenching Study. *The Journal of Physical Chemistry C* **2010**, *114* (49), 21824–21832. https://doi.org/10.1021/jp107587h.

(89) Vandewal, K.; Tvingstedt, K.; Inganäs, O. Polarization Anisotropy of Charge Transfer Absorption and Emission of Aligned Polymer:Fullerene Blend Films. *Phys. Rev. B* **2012**, *86* (3), 035212. https://doi.org/10.1103/PhysRevB.86.035212.

(90) Vandewal, K.; Albrecht, S.; Hoke, E. T.; Graham, K. R.; Widmer, J.; Douglas, J. D.; Schubert, M.; Mateker, W. R.; Bloking, J. T.; Burkhard, G. F.; Sellinger, A.; Fréchet, J. M. J.; Amassian, A.; Riede, M. K.; McGehee, M. D.; Neher, D.; Salleo, A. Efficient Charge Generation by Relaxed Charge-Transfer States at Organic Interfaces. *Nature Mater* **2014**, *13* (1), 63–68. https://doi.org/10.1038/nmat3807.

(91) Peumans, P.; Forrest, S. R. Separation of Geminate Charge-Pairs at Donor–Acceptor Interfaces in Disordered Solids. *Chemical Physics Letters* **2004**, *398* (1), 27–31. https://doi.org/10.1016/j.cplett.2004.09.030.

(92) Offermans, T.; Meskers, S. C. J.; Janssen, R. A. J. Monte-Carlo Simulations of Geminate Electron–Hole Pair Dissociation in a Molecular Heterojunction: A Two-Step Dissociation Mechanism. *Chemical Physics* **2005**, *308* (1), 125–133. https://doi.org/10.1016/j.chemphys.2004.08.015.

(93) *Excited State and Charge Photogeneration Dynamics in Conjugated Polymers | The Journal of Physical Chemistry B*. https://pubs.acs.org/doi/10.1021/jp068864f (accessed 2022-05-17).

(94) Clarke, T. M.; Durrant, J. R. Charge Photogeneration in Organic Solar Cells. *Chem. Rev.* **2010**, *110* (11), 6736–6767. https://doi.org/10.1021/cr900271s.

(95) Monahan, N. R.; Williams, K. W.; Kumar, B.; Nuckolls, C.; Zhu, X.-Y. Direct Observation of Entropy-Driven Electron-Hole Pair Separation at an Organic Semiconductor Interface. *Phys. Rev. Lett.* **2015**, *114* (24), 247003. https://doi.org/10.1103/PhysRevLett.114.247003.

(96) Gao, F.; Tress, W.; Wang, J.; Inganäs, O. Temperature Dependence of Charge Carrier Generation in Organic Photovoltaics. *Phys. Rev. Lett.* **2015**, *114* (12), 128701. https://doi.org/10.1103/PhysRevLett.114.128701.

(97) Bässler, H. Charge Transport in Disordered Organic Photoconductors a Monte Carlo Simulation Study. *Phys. Status Solidi (b)* **1993**, *175* (1), 15–56. https://doi.org/10.1002/pssb.2221750102.

(98) Arkhipov, V. I.; Emelianova, E. V.; Adriaenssens, G. J. Effective Transport Energy versus the Energy of Most Probable Jumps in Disordered Hopping Systems. *Phys. Rev. B* **2001**, *64* (12), 125125. https://doi.org/10.1103/PhysRevB.64.125125.

(99) Veldman, D.; İpek, Ö.; Meskers, S. C. J.; Sweelssen, J.; Koetse, M. M.; Veenstra, S. C.; Kroon, J. M.; van Bavel, S. S.; Loos, J.; Janssen, R. A. J. Compositional and Electric Field Dependence of the Dissociation of Charge Transfer Excitons in Alternating Polyfluorene Copolymer/Fullerene Blends. *J. Am. Chem. Soc.* **2008**, *130* (24), 7721–7735. https://doi.org/10.1021/ja8012598.

(100) Karuthedath, S.; Gorenflot, J.; Firdaus, Y.; Chaturvedi, N.; De Castro, C. S. P.; Harrison, G. T.; Khan, J. I.; Markina, A.; Balawi, A. H.; Peña, T. A. D.; Liu, W.; Liang, R.-Z.; Sharma, A.; Paleti, S. H. K.; Zhang, W.; Lin, Y.; Alarousu, E.; Lopatin, S.; Anjum, D. H.; Beaujuge, P. M.; De Wolf, S.; McCulloch, I.; Anthopoulos, T. D.; Baran, D.; Andrienko, D.; Laquai, F. Intrinsic Efficiency Limits in Low-Bandgap Non-Fullerene Acceptor Organic Solar Cells. *Nat. Mater.* **2021**, *20* (3), 378–384. https://doi.org/10.1038/s41563-020-00835-x.

(101) Bässler, H.; Köhler, A. "Hot or Cold": How Do Charge Transfer States at the Donor–Acceptor Interface of an Organic Solar Cell Dissociate? *Phys. Chem. Chem. Phys.* **2015**, *17* (43), 28451–28462. https://doi.org/10.1039/C5CP04110D.

(102) Savoie, B. M.; Jackson, N. E.; Chen, L. X.; Marks, T. J.; Ratner, M. A. Mesoscopic Features of Charge Generation in Organic Semiconductors. *Acc. Chem. Res.* **2014**, *47* (11), 3385–3394. https://doi.org/10.1021/ar5000852.

(103) Huix-Rotllant, M.; Tamura, H.; Burghardt, I. Concurrent Effects of Delocalization and Internal Conversion Tune Charge Separation at Regioregular Polythiophene–Fullerene Heterojunctions. *J. Phys. Chem. Lett.* **2015**, *6* (9), 1702–1708. https://doi.org/10.1021/acs.jpclett.5b00336.

(104) Liu, J.; Chen, S.; Qian, D.; Gautam, B.; Yang, G.; Zhao, J.; Bergqvist, J.; Zhang, F.; Ma, W.; Ade, H.; Inganäs, O.; Gundogdu, K.; Gao, F.; Yan, H. Fast Charge Separation in a Non-Fullerene Organic Solar Cell with a Small Driving Force. *Nat Energy* **2016**, *1* (7), 16089. https://doi.org/10.1038/nenergy.2016.89.

(105) Chen, S.; Wang, Y.; Zhang, L.; Zhao, J.; Chen, Y.; Zhu, D.; Yao, H.; Zhang, G.; Ma, W.; Friend, R. H.; Chow, P. C. Y.; Gao, F.; Yan, H. Efficient Nonfullerene Organic Solar Cells with Small Driving Forces for Both Hole and Electron Transfer. *Advanced Materials* **2018**, *30* (45), 1804215. https://doi.org/10.1002/adma.201804215.

(106) Zhu, L.; Zhang, J.; Guo, Y.; Yang, C.; Yi, Y.; Wei, Z. Small Exciton Binding Energies Enabling Direct Charge Photogeneration Towards

Low-Driving-Force Organic Solar Cells. *Angew. Chem. Int. Ed.* **2021**, *60* (28), 15348–15353. https://doi.org/10.1002/anie.202105156.

(107) Nakano, K.; Chen, Y.; Xiao, B.; Han, W.; Huang, J.; Yoshida, H.; Zhou, E.; Tajima, K. Anatomy of the Energetic Driving Force for Charge Generation in Organic Solar Cells. *Nat Commun* **2019**, *10* (1), 2520. https://doi.org/10.1038/s41467-019-10434-3.

(108) Qian, D.; Zheng, Z.; Yao, H.; Tress, W.; Hopper, T. R.; Chen, S.; Li, S.; Liu, J.; Chen, S.; Zhang, J.; Liu, X.-K.; Gao, B.; Ouyang, L.; Jin, Y.; Pozina, G.; Buyanova, I. A.; Chen, W. M.; Inganäs, O.; Coropceanu, V.; Bredas, J.-L.; Yan, H.; Hou, J.; Zhang, F.; Bakulin, A. A.; Gao, F. Design Rules for Minimizing Voltage Losses in High-Efficiency Organic Solar Cells. *Nature Mater* **2018**, *17* (8), 703–709. https://doi.org/10.1038/s41563-018-0128-z.

(109) Felekidis, N. *Effects of Energetic Disorder on the Optoelectronic Properties of Organic Solar Cells*; Linköping Studies in Science and Technology. Dissertations; Linköping University Electronic Press: Linköping, 2018; Vol. 1943. https://doi.org/10.3384/diss.diva-150998.

(110) Koster, L. J. A.; Smits, E. C. P.; Mihailetchi, V. D.; Blom, P. W. M. Device Model for the Operation of Polymer/Fullerene Bulk Heterojunction Solar Cells. *Phys. Rev. B* **2005**, *72* (8), 085205. https://doi.org/10.1103/PhysRevB.72.085205.

(111) Garcia-Belmonte, G.; Boix, P. P.; Bisquert, J.; Sessolo, M.; Bolink, H. J. Simultaneous Determination of Carrier Lifetime and Electron Density-of-States in P3HT:PCBM Organic Solar Cells under Illumination by Impedance Spectroscopy. *Solar Energy Materials and Solar Cells* **2010**, *94* (2), 366–375. https://doi.org/10.1016/j.solmat.2009.10.015.

(112) Heeger, A. J. 25th Anniversary Article: Bulk Heterojunction Solar Cells: Understanding the Mechanism of Operation. *Advanced Materials* **2014**, *26* (1), 10–28. https://doi.org/10.1002/adma.201304373.

(113) Gill, W. D. *Drift Mobilities in Amorphous Charge-transfer Complexes of Trinitrofluorenone and Poly-n-vinylcarbazole.* Journal of Applied Physics **1972**, 43 (12), 5033–5040. https://doi.org/10.1063/1.1661065.

(114) Tanase, C.; Meijer, E. J.; Blom, P. W. M.; de Leeuw, D. M. Unification of the Hole Transport in Polymeric Field-Effect Transistors and Light-Emitting Diodes. *Phys. Rev. Lett.* **2003**, *91* (21), 216601. https://doi.org/10.1103/PhysRevLett.91.216601.

(115) Coehoorn, R.; Pasveer, W. F.; Bobbert, P. A.; Michels, M. A. J. Charge-Carrier Concentration Dependence of the Hopping Mobility in Organic Materials with Gaussian Disorder. *Physical Review B* **2005**, *72* (15). https://doi.org/10.1103/PhysRevB.72.155206.

(116) Pasveer, W. F.; Cottaar, J.; Tanase, C.; Coehoorn, R.; Bobbert, P. A.; Blom, P. W. M.; de Leeuw, D. M.; Michels, M. A. J. Unified Description of Charge-Carrier Mobilities in Disordered Semiconducting

Polymers. *Phys. Rev. Lett.* **2005**, *94* (20), 206601. https://doi.org/10.1103/PhysRevLett.94.206601.

(117) Němec, H.; Nienhuys, H.-K.; Perzon, E.; Zhang, F.; Inganäs, O.; Kužel, P.; Sundström, V. Ultrafast Conductivity in a Low-Band-Gap Polyphenylene and Fullerene Blend Studied by Terahertz Spectroscopy. *Phys. Rev. B* **2009**, *79* (24), 245326. https://doi.org/10.1103/PhysRevB.79.245326.

(118) Lane, P. A.; Cunningham, P. D.; Melinger, J. S.; Esenturk, O.; Heilweil, E. J. Hot Photocarrier Dynamics in Organic Solar Cells. *Nature Communications* **2015**, *6* (1), 7558. https://doi.org/10.1038/ncomms8558.

(119) Melianas, A.; Etzold, F.; Savenije, T. J.; Laquai, F.; Inganäs, O.; Kemerink, M. Photo-Generated Carriers Lose Energy during Extraction from Polymer-Fullerene Solar Cells. *Nat Commun* **2015**, *6*. https://doi.org/10.1038/ncomms9778.

(120) Devižis, A.; Serbenta, A.; Meerholz, K.; Hertel, D.; Gulbinas, V. Ultrafast Dynamics of Carrier Mobility in a Conjugated Polymer Probed at Molecular and Microscopic Length Scales. *Phys. Rev. Lett.* **2009**, *103* (2), 027404. https://doi.org/10.1103/PhysRevLett.103.027404.

(121) Melianas, A.; Pranculis, V.; Devižis, A.; Gulbinas, V.; Inganäs, O.; Kemerink, M. Dispersion-Dominated Photocurrent in Polymer:Fullerene Solar Cells. *Advanced Functional Materials* **2014**, *24* (28), 4507–4514. https://doi.org/10.1002/adfm.201400404.

(122) Abramavičius, V.; Amarasinghe Vithanage, D.; Devižis, A.; Infahsaeng, Y.; Bruno, A.; Foster, S.; Keivanidis, P. E.; Abramavičius, D.; Nelson, J.; Yartsev, A.; Sundström, V.; Gulbinas, V. Carrier Motion in As-Spun and Annealed P3HT:PCBM Blends Revealed by Ultrafast Optical Electric Field Probing and Monte Carlo Simulations. *Phys. Chem. Chem. Phys.* **2014**, *16* (6), 2686. https://doi.org/10.1039/c3cp54605e.

(123) Augulis, R.; Devižis, A.; Peckus, D.; Gulbinas, V.; Hertel, D.; Meerholz, K. High Electron Mobility and Its Role in Charge Carrier Generation in Merocyanine/Fullerene Blends. *J. Phys. Chem. C* **2015**, *119* (11), 5761–5770. https://doi.org/10.1021/jp5054698.

(124) Cunningham, P. D.; Hayden, L. M. Carrier Dynamics Resulting from Above and Below Gap Excitation of P3HT and P3HT/PCBM Investigated by Optical-Pump Terahertz-Probe Spectroscopy. *J. Phys. Chem. C* **2008**, *112* (21), 7928–7935. https://doi.org/10.1021/jp711827g.

(125) Ponseca, C. S.; Yartsev, A.; Wang, E.; Andersson, M. R.; Vithanage, D.; Sundström, V. Ultrafast Terahertz Photoconductivity of Bulk Heterojunction Materials Reveals High Carrier Mobility up to Nanosecond Time Scale. *J. Am. Chem. Soc.* **2012**, *134* (29), 11836–11839. https://doi.org/10.1021/ja301757y.

(126) Vandewal, K.; Ma, Z.; Bergqvist, J.; Tang, Z.; Wang, E.; Henriksson, P.; Tvingstedt, K.; Andersson, M. R.; Zhang, F.; Inganäs, O. Quantification of Quantum Efficiency and Energy Losses in Low Bandgap Polymer:Fullerene Solar Cells with High Open-Circuit Voltage. *Advanced Functional Materials* **2012**, *22* (16), 3480–3490. https://doi.org/10.1002/adfm.201200608.

(127) Park, S. H.; Roy, A.; Beaupré, S.; Cho, S.; Coates, N.; Moon, J. S.; Moses, D.; Leclerc, M.; Lee, K.; Heeger, A. J. Bulk Heterojunction Solar Cells with Internal Quantum Efficiency Approaching 100%. *Nature Photonics* **2009**, *3* (5), 297–302. https://doi.org/10.1038/nphoton.2009.69.

(128) Gorenflot, J.; Paulke, A.; Piersimoni, F.; Wolf, J.; Kan, Z.; Cruciani, F.; Labban, A. E.; Neher, D.; Beaujuge, P. M.; Laquai, F. From Recombination Dynamics to Device Performance: Quantifying the Efficiency of Exciton Dissociation, Charge Separation, and Extraction in Bulk Heterojunction Solar Cells with Fluorine-Substituted Polymer Donors. *Advanced Energy Materials* **2018**, *8* (4), 1701678. https://doi.org/10.1002/aenm.201701678.

(129) Shuttle, C. G.; O'Regan, B.; Ballantyne, A. M.; Nelson, J.; Bradley, D. D. C.; de Mello, J.; Durrant, J. R. Experimental Determination of the Rate Law for Charge Carrier Decay in a Polythiophene: Fullerene Solar Cell. *Appl. Phys. Lett.* **2008**, *92* (9), 093311. https://doi.org/10.1063/1.2891871.

(130) Jasiūnas, R.; Melianas, A.; Xia, Y.; Felekidis, N.; Gulbinas, V.; Kemerink, M. Dead Ends Limit Charge Carrier Extraction from All-Polymer Bulk Heterojunction Solar Cells. *Advanced Electronic Materials* **2018**, *4* (8), 1800144. https://doi.org/10.1002/aelm.201800144.

(131) Jasiūnas, R.; Gegevičius, R.; Franckevičius, M.; Jašinskas, V.; Gulbinas, V. Energy Barriers Restrict Charge Carrier Motion in MAPI Perovskite Films. *Adv. Optical Mater.* **2020**, *8* (16), 2000036. https://doi.org/10.1002/adom.202000036.

(132) Jasiūnas, R.; Jašinskas, V.; Zhang, H.; Upreti, T.; Gao, F.; Kemerink, M.; Gulbinas, V. Carrier Mobility Dynamics under Actual Working Conditions of Organic Solar Cells. *J. Phys. Chem. C* **2021**, *125* (27), 14567–14575. https://doi.org/10.1021/acs.jpcc.1c04245.

(133) Koster, L. J. A. Charge Carrier Mobility in Disordered Organic Blends for Photovoltaics. *Physical Review B* **2010**, *81* (20). https://doi.org/10.1103/PhysRevB.81.205318.

(134) Symalla, F.; Friederich, P.; Massé, A.; Meded, V.; Coehoorn, R.; Bobbert, P.; Wenzel, W. Charge Transport by Superexchange in Molecular Host-Guest Systems. *Physical Review Letters* **2016**, *117* (27). https://doi.org/10.1103/PhysRevLett.117.276803.

(135) Massé, A.; Friederich, P.; Symalla, F.; Liu, F.; Meded, V.; Coehoorn, R.; Wenzel, W.; Bobbert, P. A. Effects of Energy Correlations and Superexchange on Charge Transport and Exciton Formation in Amorphous Molecular Semiconductors: An *Ab Initio* Study. *Physical Review B* **2017**, *95* (11). https://doi.org/10.1103/PhysRevB.95.115204.

(136) Melianas, A.; Pranculis, V.; Spoltore, D.; Benduhn, J.; Inganäs, O.; Gulbinas, V.; Vandewal, K.; Kemerink, M. Charge Transport in Pure and Mixed Phases in Organic Solar Cells. *Advanced Energy Materials* **2017**, *7* (20), 1700888. https://doi.org/10.1002/aenm.201700888.

(137) Abdalla, H.; Zuo, G.; Kemerink, M. Range and Energetics of Charge Hopping in Organic Semiconductors. *Physical Review B* **2017**, *96* (24). https://doi.org/10.1103/PhysRevB.96.241202.

(138) Karuthedath, S.; Melianas, A.; Kan, Z.; Pranculis, V.; Wohlfahrt, M.; Khan, J. I.; Gorenflot, J.; Xia, Y.; Inganäs, O.; Gulbinas, V.; Kemerink, M.; Laquai, F. Thermal Annealing Reduces Geminate Recombination in TQ1:N2200 All-Polymer Solar Cells. *Journal of Materials Chemistry A* **2018**. https://doi.org/10.1039/C8TA01692E.

(139) Xia, Y.; Musumeci, C.; Bergqvist, J.; Ma, W.; Gao, F.; Tang, Z.; Bai, S.; Jin, Y.; Zhu, C.; Kroon, R.; Wang, C.; Andersson, M. R.; Hou, L.; Inganäs, O.; Wang, E. Inverted All-Polymer Solar Cells Based on a Quinoxaline–Thiophene/Naphthalene-Diimide Polymer Blend Improved by Annealing. *Journal of Materials Chemistry A* **2016**, *4* (10), 3835–3843. https://doi.org/10.1039/C6TA00531D.

(140) Ai, X.; Beard, M. C.; Knutsen, K. P.; Shaheen, S. E.; Rumbles, G.; Ellingson, R. J. Photoinduced Charge Carrier Generation in a Poly(3-Hexylthiophene) and Methanofullerene Bulk Heterojunction Investigated by Time-Resolved Terahertz Spectroscopy. 10.

(141) Mihailetchi, V. D.; Xie, H. X.; de Boer, B.; Koster, L. J. A.; Blom, P. W. M. Charge Transport and Photocurrent Generation in Poly(3-Hexylthiophene): Methanofullerene Bulk-Heterojunction Solar Cells. *Adv. Funct. Mater.* **2006**, *16* (5), 699–708. https://doi.org/10.1002/adfm.200500420.

(142) Bartelt, J. A.; Lam, D.; Burke, T. M.; Sweetnam, S. M.; McGehee, M. D. Charge-Carrier Mobility Requirements for Bulk Heterojunction Solar Cells with High Fill Factor and External Quantum Efficiency >90%. *Adv. Energy Mater.* **2015**, *5* (15), 1500577. https://doi.org/10.1002/aenm.201500577.

(143) Bartesaghi, D.; Pérez, I. del C.; Kniepert, J.; Roland, S.; Turbiez, M.; Neher, D.; Koster, L. J. A. Competition between Recombination and Extraction of Free Charges Determines the Fill Factor of Organic Solar Cells. *Nat Commun* **2015**, *6* (1), 7083. https://doi.org/10.1038/ncomms8083.

(144) Proctor, C. M.; Love, J. A.; Nguyen, T.-Q. Mobility Guidelines for High Fill Factor Solution-Processed Small Molecule Solar Cells. *Adv. Mater.* **2014**, *26* (34), 5957–5961. https://doi.org/10.1002/adma.201401725.

(145) Le Corre, V. M.; Chatri, A. R.; Doumon, N. Y.; Koster, L. J. A. Charge Carrier Extraction in Organic Solar Cells Governed by Steady-State Mobilities. *Adv. Energy Mater.* **2017**, *7* (22), 1701138. https://doi.org/10.1002/aenm.201701138.

(146) Jasiūnas, R.; Zhang, H.; Yuan, J.; Zhou, X.; Qian, D.; Zou, Y.; Devižis, A.; Šulskus, J.; Gao, F.; Gulbinas, V. From Generation to Extraction: A Time-Resolved Investigation of Photophysical Processes in Non-Fullerene Organic Solar Cells. *J. Phys. Chem. C* **2020**, *124* (39), 21283–21292. https://doi.org/10.1021/acs.jpcc.0c05263.

(147) Karuthedath, S.; Gorenflot, J.; Melianas, A.; Kan, Z.; Kemerink, M.; Laquai, F. Buildup of Triplet-State Population in Operating TQ1:PC$_{71}$BM Devices Does Not Limit Their Performance. *J. Phys. Chem. Lett.* **2020**, *11* (8), 2838–2845. https://doi.org/10.1021/acs.jpclett.0c00756.

(148) Andersson, L. M.; Melianas, A.; Infahasaeng, Y.; Tang, Z.; Yartsev, A.; Inganäs, O.; Sundström, V. Unified Study of Recombination in Polymer:Fullerene Solar Cells Using Transient Absorption and Charge-Extraction Measurements. *J. Phys. Chem. Lett.* **2013**, *4* (12), 2069–2072. https://doi.org/10.1021/jz4009745.

(149) Upreti, T.; Wang, Y.; Zhang, H.; Scheunemann, D.; Gao, F.; Kemerink, M. Experimentally Validated Hopping-Transport Model for Energetically Disordered Organic Semiconductors. *Phys. Rev. Applied* **2019**, *12* (6), 064039. https://doi.org/10.1103/PhysRevApplied.12.064039.

(150) Yao, J.; Kirchartz, T.; Vezie, M. S.; Faist, M. A.; Gong, W.; He, Z.; Wu, H.; Troughton, J.; Watson, T.; Bryant, D.; Nelson, J. Quantifying Losses in Open-Circuit Voltage in Solution-Processable Solar Cells. *Phys. Rev. Applied* **2015**, *4* (1), 014020. https://doi.org/10.1103/PhysRevApplied.4.014020.

(151) Vandewal, K.; Tvingstedt, K.; Gadisa, A.; Inganäs, O.; Manca, J. V. On the Origin of the Open-Circuit Voltage of Polymer–Fullerene Solar Cells. *Nature Mater* **2009**, *8* (11), 904–909. https://doi.org/10.1038/nmat2548.

(152) Polman Albert; Knight Mark; Garnett Erik C.; Ehrler Bruno; Sinke Wim C. Photovoltaic Materials: Present Efficiencies and Future Challenges. *Science* **2016**, *352* (6283), aad4424. https://doi.org/10.1126/science.aad4424.

(153) Baran, D.; Kirchartz, T.; Wheeler, S.; Dimitrov, S.; Abdelsamie, M.; Gorman, J.; Ashraf, R. S.; Holliday, S.; Wadsworth, A.; Gasparini, N.; Kaienburg, P.; Yan, H.; Amassian, A.; Brabec, C. J.; Durrant, J. R.; McCulloch, I. Reduced Voltage Losses Yield 10% Efficient Fullerene Free Organic Solar Cells with >1 V Open Circuit Voltages. *Energy*

Environ. *Sci.* **2016**, *9* (12), 3783–3793. https://doi.org/10.1039/C6EE02598F.

(154) Yang, D.; Wang, Y.; Sano, T.; Gao, F.; Sasabe, H.; Kido, J. A Minimal Non-Radiative Recombination Loss for Efficient Non-Fullerene All-Small-Molecule Organic Solar Cells with a Low Energy Loss of 0.54 EV and High Open-Circuit Voltage of 1.15 V. *Journal of Materials Chemistry A* **2018**, *6* (28), 13918–13924. https://doi.org/10.1039/C8TA04665D.

(155) Mishra, A.; Keshtov, M. L.; Looser, A.; Singhal, R.; Stolte, M.; Würthner, F.; Bäuerle, P.; Sharma, G. D. Unprecedented Low Energy Losses in Organic Solar Cells with High External Quantum Efficiencies by Employing Non-Fullerene Electron Acceptors. *J. Mater. Chem. A* **2017**, *5* (28), 14887–14897. https://doi.org/10.1039/C7TA04703G.

(156) Zhang, H.; Li, S.; Xu, B.; Yao, H.; Yang, B.; Hou, J. Fullerene-Free Polymer Solar Cell Based on a Polythiophene Derivative with an Unprecedented Energy Loss of Less than 0.5 EV. *J. Mater. Chem. A* **2016**, *4* (46), 18043–18049. https://doi.org/10.1039/C6TA07672F.

(157) Zhu, L.; Yi, Y.; Wei, Z. Exciton Binding Energies of Nonfullerene Small Molecule Acceptors: Implication for Exciton Dissociation Driving Forces in Organic Solar Cells. *The Journal of Physical Chemistry C* **2018**, *122* (39), 22309–22316. https://doi.org/10.1021/acs.jpcc.8b07197.

(158) Li, W.; Hendriks, K. H.; Furlan, A.; Wienk, M. M.; Janssen, R. A. J. High Quantum Efficiencies in Polymer Solar Cells at Energy Losses below 0.6 EV. *J. Am. Chem. Soc.* **2015**, *137* (6), 2231–2234. https://doi.org/10.1021/ja5131897.

(159) Chen, S.; Liu, Y.; Zhang, L.; Chow, P. C. Y.; Wang, Z.; Zhang, G.; Ma, W.; Yan, H. A Wide-Bandgap Donor Polymer for Highly Efficient Non-Fullerene Organic Solar Cells with a Small Voltage Loss. *J. Am. Chem. Soc.* **2017**, *139* (18), 6298–6301. https://doi.org/10.1021/jacs.7b01606.

(160) Bin, H.; Yang, Y.; Peng, Z.; Ye, L.; Yao, J.; Zhong, L.; Sun, C.; Gao, L.; Huang, H.; Li, X.; Qiu, B.; Xue, L.; Zhang, Z.-G.; Ade, H.; Li, Y. Effect of Alkylsilyl Side-Chain Structure on Photovoltaic Properties of Conjugated Polymer Donors. *Advanced Energy Materials* **2018**, *8* (8), 1702324. https://doi.org/10.1002/aenm.201702324.

(161) Li, C.; Yue, Q.; Wu, H.; Li, B.; Fan, H.; Zhu, X. Small Bandgap Non-Fullerene Acceptor Enables Efficient PTB7-Th Solar Cell with near 0 EV HOMO Offset. *Journal of Energy Chemistry* **2021**, *52*, 60–66. https://doi.org/10.1016/j.jechem.2020.03.058.

(162) Chen, S.; Yao, H.; Li, Z.; Awartani, O. M.; Liu, Y.; Wang, Z.; Yang, G.; Zhang, J.; Ade, H.; Yan, H. Surprising Effects upon Inserting Benzene Units into a Quaterthiophene-Based D-A Polymer–Improving Non-Fullerene Organic Solar Cells via Donor Polymer Design. *Advanced*

Energy Materials **2017**, *7* (12), 1602304. https://doi.org/10.1002/aenm.201602304.

(163) Yuan, J.; Huang, T.; Cheng, P.; Zou, Y.; Zhang, H.; Yang, J. L.; Chang, S.-Y.; Zhang, Z.; Huang, W.; Wang, R.; Meng, D.; Gao, F.; Yang, Y. Enabling Low Voltage Losses and High Photocurrent in Fullerene-Free Organic Photovoltaics. *Nat Commun* **2019**, *10* (1), 570. https://doi.org/10.1038/s41467-019-08386-9.

(164) Yuan, J.; Guo, W.; Xia, Y.; Ford, M. J.; Jin, F.; Liu, D.; Zhao, H.; Inganäs, O.; Bazan, G. C.; Ma, W. Comparing the Device Physics, Dynamics and Morphology of Polymer Solar Cells Employing Conventional PCBM and Non-Fullerene Polymer Acceptor N2200. *Nano Energy* **2017**, *35*, 251–262. https://doi.org/10.1016/j.nanoen.2017.03.050.

(165) Gillett, A. J.; Privitera, A.; Dilmurat, R.; Karki, A.; Qian, D.; Pershin, A.; Londi, G.; Myers, W. K.; Lee, J.; Yuan, J.; Ko, S.-J.; Riede, M. K.; Gao, F.; Bazan, G. C.; Rao, A.; Nguyen, T.-Q.; Beljonne, D.; Friend, R. H. The Role of Charge Recombination to Triplet Excitons in Organic Solar Cells. *Nature* **2021**, *597* (7878), 666–671. https://doi.org/10.1038/s41586-021-03840-5.

(166) Yuan, J.; Zhang, Y.; Zhou, L.; Zhang, G.; Yip, H.-L.; Lau, T.-K.; Lu, X.; Zhu, C.; Peng, H.; Johnson, P. A.; Leclerc, M.; Cao, Y.; Ulanski, J.; Li, Y.; Zou, Y. Single-Junction Organic Solar Cell with over 15% Efficiency Using Fused-Ring Acceptor with Electron-Deficient Core. *Joule* **2019**, *3* (4), 1140–1151. https://doi.org/10.1016/j.joule.2019.01.004.

(167) Yan, T.; Song, W.; Huang, J.; Peng, R.; Huang, L.; Ge, Z. 16.67% Rigid and 14.06% Flexible Organic Solar Cells Enabled by Ternary Heterojunction Strategy. *Adv. Mater.* **2019**, *31* (39), 1902210. https://doi.org/10.1002/adma.201902210.

(168) Yu, K.; Song, W.; Li, Y.; Chen, Z.; Ge, J.; Yang, D.; Zhang, J.; Xie, L.; Liu, C.; Ge, Z. Achieving 18.14% Efficiency of Ternary Organic Solar Cells with Alloyed Nonfullerene Acceptor. *Small Structures* **2021**, *2* (11), 2100099. https://doi.org/10.1002/sstr.202100099.

(169) Distler, A.; Brabec, C. J.; Egelhaaf, H. Organic Photovoltaic Modules with New World Record Efficiencies. *Prog Photovolt Res Appl* **2021**, *29* (1), 24–31. https://doi.org/10.1002/pip.3336.

(170) Guo, Q.; Guo, Q.; Geng, Y.; Tang, A.; Zhang, M.; Du, M.; Sun, X.; Zhou, E. Recent Advances in PM6:Y6-Based Organic Solar Cells. *Mater. Chem. Front.* **2021**, *5* (8), 3257–3280. https://doi.org/10.1039/D1QM00060H.

(171) Wen, Z.-C.; Yin, H.; Hao, X.-T. Recent Progress of PM6:Y6-Based High Efficiency Organic Solar Cells. *Surfaces and Interfaces* **2021**, *23*, 100921. https://doi.org/10.1016/j.surfin.2020.100921.

(172) Wang, R.; Zhang, C.; Li, Q.; Zhang, Z.; Wang, X.; Xiao, M. Charge Separation from an Intra-Moiety Intermediate State in the High-Performance PM6:Y6 Organic Photovoltaic Blend. *J. Am. Chem. Soc.* **2020**, *142* (29), 12751–12759. https://doi.org/10.1021/jacs.0c04890.

(173) Perdigón-Toro, L.; Phuong, L. Q.; Zeiske, S.; Vandewal, K.; Armin, A.; Shoaee, S.; Neher, D. Excitons Dominate the Emission from PM6:Y6 Solar Cells, but This Does Not Help the Open-Circuit Voltage of the Device. *ACS Energy Lett.* **2021**, *6* (2), 557–564. https://doi.org/10.1021/acsenergylett.0c02572.

(174) Thompson, B. C.; Fréchet, J. M. J. Polymer–Fullerene Composite Solar Cells. Angewandte Chemie International Edition 2008, 47 (1), 58–77. https://doi.org/10.1002/anie.200702506.

(175) Zhao, J.; Li, Y.; Yang, G.; Jiang, K.; Lin, H.; Ade, H.; Ma, W.; Yan, H. Efficient Organic Solar Cells Processed from Hydrocarbon Solvents. Nature Energy 2016, 1 (2), 15027. https://doi.org/10.1038/nenergy.2015.27.

(176) McAfee, S. M.; Topple, J. M.; Hill, I. G.; Welch, G. C. Key Components to the Recent Performance Increases of Solution Processed Non-Fullerene Small Molecule Acceptors. J. Mater. Chem. A 2015, 3 (32), 16393–16408. https://doi.org/10.1039/C5TA04310G.

(177) Jørgensen, M.; Norrman, K.; Krebs, F. C. Stability/Degradation of Polymer Solar Cells. Solar Energy Materials and Solar Cells 2008, 92 (7), 686–714. https://doi.org/10.1016/j.solmat.2008.01.005.

(178) Facchetti, A. Polymer Donor–Polymer Acceptor (All-Polymer) Solar Cells. Materials Today 2013, 16 (4), 123–132. https://doi.org/10.1016/j.mattod.2013.04.005.

(179) Lee, H. K. H.; Li, Z.; Constantinou, I.; So, F.; Tsang, S. W.; So, S. K. Batch-to-Batch Variation of Polymeric Photovoltaic Materials: Its Origin and Impacts on Charge Carrier Transport and Device Performances. Advanced Energy Materials 2014, 4 (16), 1400768. https://doi.org/10.1002/aenm.201400768.

(180) Wang, C.; Ni, S.; Braun, S.; Fahlman, M.; Liu, X. Effects of Water Vapor and Oxygen on Non-Fullerene Small Molecule Acceptors. J. Mater. Chem. C 2019, 7 (4), 879–886. https://doi.org/10.1039/C8TC05475D.

(181) Zhang, G.; Zhao, J.; Chow, P. C. Y.; Jiang, K.; Zhang, J.; Zhu, Z.; Zhang, J.; Huang, F.; Yan, H. Nonfullerene Acceptor Molecules for Bulk Heterojunction Organic Solar Cells. Chem. Rev. 2018, 118 (7), 3447–3507. https://doi.org/10.1021/acs.chemrev.7b00535.

SANTRAUKA

Įvadas

Nuo pat industrinės revoliucijos pradžios elektros paklausa visame pasaulyje nuolatos augo. Per paskutiniuosius 25 metus pagaminamas elektros kiekis padvigubėjo ir 2019 metais viršyjo 27000 teravatvalandes.[1] Prognozuojama, kad 2050-aisiais žmonių skaičius turėtų pasiekti 10 milijardų, t.y. 20% daugiau nei šiandien, o su tuo turėtų augti ir elektros paklausa. Šiandien, pagrindinis elektros gamybos išteklis yra anglis ir kitas iškastinis kuras. 2019-aisiais net ~63% elektros pasauliniu mastu buvo sugeneruota naudojant iškastinį kurą. Tačiau šis resursas turi kelis rimtus trūkumus: iškastinio kuro kiekis baigtinis[2], o jų deginimas didina oro užterštumą, ko pasekoje žalojama žmonių sveikata ir stimuliuojama klimato kaita.[3] Iškastinio kuro deginimo metu į atmosferą išsiskiriamas anglies dvideginis, kur ~60% jo lieka įstrigęs.[4] Šiandien vidutinė atmosferoje esančio CO_2 koncentracija yra didžiausia per pastaruosius 3 milijonų metų, seniausiai kiek įmanoma išmatuoti.[5] Atmosferoje esančiai angliai sugeriant šilumą sklindančią nuo žemės paviršiaus, kyla tiek vidutinė žemės temperatūra, tiek dėl sparčiai tirpstančių ledynų ir jūros lygis.[6–9] Skaičiuojama, kad kylanti temperatūra kelia grėsmę net 20-30% gyvybės rūšių išnykimui, pradedant nuo ypatingai jautrių koralinių rifų.[10]

Šiam beprecedentiniam iššūkiui spręsti, pradėta „nulinės CO_2 emisijos iki 2050" iniciatyva. Ja mėginama surasti būdus kaip drastiškai sumažinti iškastinio kuro, didžiausio CO_2 dujų šaltinio, naudojimą. Remiantis ja, du trečdaliai visos sunaudojamos energijos 2050-aisiais metais turėtų būti išgauta iš atsinaujinančių, netaršių šaltinių – vėjo, bioenergijos, geoterminės, hidro ir saulės.[11] Įdomu, kad būtent saulės energetikai numatyta didžiausia dalis, ji turėsianti sugeneruoti penktadalį visos energijos paklausos. Milžinišką saulės radiacijos energijos potencialą puikiai iliustruoja žinoma L.R. Brown'o citata „saulės šviesos energijos, kuri pasiekia žemės paviršių per vieną valandą, pakaktų pasaulio ekonomikai visiem metams". [12]

Saulės energetika skirstoma į tris dalis: terminę, cheminę ir fotovoltainę. Pirmoje, elektra gaunama iš saulės spinduliuotės gaminamų garų, kurie suka turbiną, analogiškai iškastinio kuro deginimui.[13] Antroje, cheminė energija gaunama naudojant saulės šviesą per įvairius foto ir termocheminius

procesus.[14] Tuo tarpu trečioju atveju saulės šviesa verčiama tiesiogiai į elektrą. Pastebėtina, kad dėl augančų šaldymo ir šildymo sistemų poreikio, elektromobilių populiarumo bei daugelio kasdienių paslaugų skaitmenizavimo, pasaulyje vis daugiau energijos išnaudojama elektros pavidalu.[15] Todėl, tiesioginė elektros generacija iš saulės šviesos tampa itin patraukliu energijos šaltiniu ateičiai. Šiandien mažiau nei 4% elektros pagaminama naudojant saulės elementus, tačiau Tarptautinė Energijos Agentūra prognozuoja, kad iki 2050 metų šios apimtys užaugs dvidešimt kartų.[11] Tokio ambicingo plano įgyvendinimas būtų tapatus šiai dienai didžiausios pasaulyje saulės jėgainės įdiegimui kiekvieną dieną, ateinantį dešimtmetį! Nepaisant to, aplinkosauginės katastrofos pavojus, kylantis išlaikant *status que,* t.y. deginant iškastinį kurą energijai, skatina spartų saulės energetikos vystymą visame pasaulyje.

Šiandien dominuojanti saulės elementų technologija gaminama kristalinio silicio (c-Si) pagrindu. Ja išgaunama apie 95% saulės elementais generuojamos galios.[16] Per pastarąjį dešimtmetį ženkliai atpigus puslaidininkinio silicio gamybai ir išaugus Si elementų efektyvumui, ši technologija tapo ne tik patraukli dėl aplinkosauginių priežasčių, bet ir finansiškai konkurencinga elektros gamybos sritimi.[17] Nepaisant to, c-Si technologija turi kelis svarbius trūkumus. Visų pirma, silicio sugerties koeficientas yra mažas, ko pasekoje didžiausiam efektyvumui išgauti Si sluoksnis saulės elemente turi būti sąlyginai storas (kelių šimtų mikronų) ir tamsus.[18] Šitai nulemia ne tik aukštą galutinę saulės modulio kainą, bet ir stipriai apriboja įvairias c-Si pritaikomumo galimybes. Moduliai montuojami arba ant žemės, arba ant stogų, padengiant kuo didesnį plotą. Tačiau stipriai apgyvendintose vietovėse, kur elektros poreikis yra didžiausias, tuščių žemės plotų saulės jėgainei nėra lengva rasti. Negana to, kristalinio silicio gamybai reikalinga labai aukšta temperatūra. Tai reiškia, kad energetinis atsiperkamumas, tai yra laikas, per kurį saulės elementas pagamina tiek energijos, kiek buvo sunaudota jo gamybai, yra ilgas – 1.5-2 metai, priklausomai nuo lokacijos.[19]

Siekiant globaliu mastu didinti saulės elementais išgaunamą elektros kiekį, reikalingos naujos technologijos, pasižyminčios unikaliomis mechaninėmis ir optinėmis savybėmis. Pavyzdžiui, saulės elementui esant pusiau skaidriu, jį būtų galima montuoti ant dangoraižių stiklų. Tokiu būdu elektra būtų generuojama ten, kur jos poreikis didžiausias – didmiesčių centre. Lankstūs

saulės elementų moduliai galėtų būti įmontuojami and lenktų paviršių, tokių kaip automobilio stogas. Taipogi, skirtingų atspalvių saulės elementų modulių inkorporavimas miesto infrastruktūroje taptų daug priimtinesnis dėl estetinių priežasčių. Įdomu, kad iš daugybės besivystančių fotovoltainių technologijų, būtent organiniai saulės elementai galėtų būti pritaikomi tokiose nišinėse sferose dėl jų išskirtinių lengvumo, lankstumo ir skaidrumo savybių.[20,21] Negana to, organinių puslaidininkių gamybos energetiniai kaštai itin maži. Skaičiavimai rodo, kad organinių saulės elementų energetinis atsiperkamumas gali būti pasiekiamas vos per vieną dieną.[22]

Nors organinė fotovoltaika jau vystoma daugiau nei tris dešimtmečius, tačiau ši technologija dar nėra plačiai paplitusi. Pagrindiniai ribojantys faktoriai yra sąlyginai prastas organinių puslaidininkių stabilumas ir žemesnis energijos konversijos efektyvumas, lyginant su jau veikiančiais saulės elementais. Kitąvertus, per pastaruosius kelis metus organinių saulės elementų efektyvumas drastiškai išaugo ir šiai dienai viršyja 18%. [23,24] Šis šuolis buvo nulemtas naujos kartos akceptorinių molekulių atsiradimu, kuris sugrąžino didžiulį mokslo ir industrijos atstovų susidomėjimą šia, pastarąjį dešimtmetį kiek stagnavusia, technologija.

Nepaisant šio proveržio, organinių saulės elementų techonlogijai reikalingas tolimesnis plėtojimas, kurį smarkiai apriboja šių elementų veikimo pilno fizikinio supratimo nebuvimas, ypač prietaisų su naujos kartos akceporinėmis molekulėmis. Šios naujos medžiagos, befulereniai akceptoriai, paneigė prieš tai nusistovėjusį suvokimą apie krūvininkų generacijai būtinas sąlygas, todėl išsami visų fizikinių procesų, vysktančių organiniame saulės elemente, analizė yra būtina. Šiame darbe išsamiai tyrinėjami naujos kartos organinių saulės elementuose vykstantys fizikiniai reiškiniai, idant būtų atskleisti energijos konversijos efektyvumą ribojančios priežastys, bei suprasti jų pašalinimo mechanizmai.

Disertacijos tikslai

Organinės fotovoltaikos prietaisų efektyvumo proveržis, sąlygotas archetipinio fulereninio tipo akceptorinės molekulės pakeitimu naujos kartos akceptoriais, sukėlė didelį ažiotažą mokslinėje bendruomenėje, ko pasekoje mokslininkų grupės viena po kitos puolė skelbti naujus efektyvumo rekordus. Įprastai, šie rekordai pasiekiami gaminant daugybę naujų medžiagų, tinkamų aktyviam prietaiso sluoksniui, bandant vis naujus donoras:akceptorius mišinius ir kruopščiai sustyguojant kiekvieną gamybos etapą atsitiktinio bandymo būdu. Nors ši strategija iš dalies pasiteisina, tačiau be išsamaus suvokimo kaip šios naujos medžiagos veikia ir kokie faktoriai riboja jų našumą, sunku tikėtis spartaus technologinio progreso. Būtent todėl šis darbas buvo atliktas siekiant detaliai išnagrinėti pagrindinius optoelektroninius procesus, tokius kaip krūvininkų generacija, ištraukimas ir rekombinacija, įvariuose befulereniuose tūrinės heterosandūros organiniuose saulės elementuose. Taipogi, juos palyginti su įprastais fulereniniais saulės elementais ir identifikuoti pagrindinius energijos konversiją ribojančius faktorius.

Ypatingas dėmesys buvo skirtas dinaminių procesų, krūvininkų generacijos ir ištraukmo, analizei. Vyksmų kinetikoms nustatyti buvo pasitelkta kelios laikinių matavimų bei skaitmeninio modeliavimo technikos. Pagrindiniai keliami tikslai buvo:

- Suprasti erdvinių gaudyklių įtaką krūvininkų ištraukimui tūrinės heterosandūros elementuose.
- Įvertinti krūvininkų ištraukimo dinamiką artimose darbinėms saulės elementų veikimo sąlygose.
- Suprasti laisvų krūvininkų generacijos ypatybes befulereniuose saulės elementuose, pasižyminčiuose minimaliu molekulinių orbitalių energijų skirtumu tarp donoro ir akceptoriaus.
- Suprasti laisvų krūvininkų generacijos ypatumus PM6:Y6 organiniuose saulės elementuose.

Disertacijos uždaviniai

Šiems tikslams pasiekti buvo suformuluoti atitinkami uždaviniai:

- Išvystyti ir pritaikyti specialią nenuostaviosios fotosrovės matavimo techniką, leidžiančią identifikuoti krūvininkų pagavimą žemos energijos ar erdvinėse gaudyklėse; įvertinti krūvininkų pagavimo erdvinėse ir žemos energijos gaudyklėse įtaką krūvininkų ištraukimui fulereniniuose ir befulereniuose organiniuose saulės elementuose.

- Patobulinti ir panaudoti specialias laikines matavimo technikas, kurios leistų išmatuoti krūvininkų judėjimą artimose tikroms saulės elementų veikimo sąlygomis; palyginti krūvininkų judrio dinamikas fulereniniuose ir befulereniniuose organiniuose saulės elementuose.

- Išmatuoti su aukšta laikine rezoliucija laisvų krūvininkų generacijos ir jų rekombinacijos priklausomybę nuo molekulinių orbitalių energijų skirtumo tarp donoro ir akceptoriaus molekulių; jų priklausomybę nuo temperatūros; identifikuoti energijos efektyvumą ribojančius faktorius.

Ginamieji teiginiai

1. Laisvų fotogeneruotų krūvininkų pagavimas erdvinėse gaudyklėse gali riboti jų judėjimą tik-išlietame, polimeras:polimeras tipo organiniame saulės elemente, ko pasekoje išauga rekombinaciniai ir efektyvumo nuostoliai. Erdvinių gaudyklių įtaką galima ženkliai sumažinti bandinį pakaitinus, kaip pademonstruota TQ1:N2200 polimeras:polimeras tipo saulės elemente.

2. Organiuose saulės elementuose su aukšta gaudyklių koncentracija laisvų krūvininkų pagavimas gaudyklėsė nulemia stiprų krūvininkų judrio mažėjimą ns-μs laiko skalėje. Esant relioms saulės elementų veikimo sąlygoms, nuolatinio apšvietimo generuoti fotokrūvininkai užpildo gaudykles, ko pasekoje judris laikui einant kinta mažiau, išauga tiek krūvininkų rekombinacijos, tiek ištraukimo spartos. Žemų energijų būsenų užpildymas nedaro įtakos stipriai mažėjančiam judriui pikosekundinėje laiko skalėje. Efektyviuose befulereniuose saulės elementuose krūvininkų pagavimas gaudyklėse nėra ženklus, ko pasekoje žemų energijų būsenų užpildymas nedaro pastebimos įtakos krūvininkų ištraukimui.

3. Termiškai aktyvuota atbulinė elektrono pernaša iš donoro į akceptoriaus aukščiausią užpildytą molekulinę orbitalę nulemia didesnę krūvininkų

rekombinaciją ir sumažina befulerenių organinių saulės elementų efektyvumą, kurių molekulinių orbitalių energijų tarpas mažesnis nei 100meV.

4. PM6:Y6 organiniame saulės elemente, žadinant akceptorių Y6 lasivi krūvininkai generuojami dviem, kambario temperatūroje vienodo efektyvumo, būdais – per krūvio pernašos ir vidinės krūvio pernašos būsenas. Įprastas krūvio pernašos mechanizmas beveik nepriklauso nuo temperatūros, tuo tarpu krūvininkų generacijos efektyvumas per vidinę krūvio pernašos būseną smarkai sumažėja krentant temperatūrai.

Naujumas ir aktualumas

Šio darbo naujumas ir aktualumas parodomas šiais teiginiais:

- Įvairūs laikinių matavimų techikos leido nuodugniai ištirti kiekvieną organinių saulės elementų veikimo etapą ir juos visus apjungti į vieną nuoseklų paveikslą, apimanti vyksmus itin plačioje fs-μs laiko skalėje, pirmą sykį šiai bandinių klasei.

- Šiame darbe buvo išvystyti specialūs įprastų laikinių matavimo technikų, tokių kaip TREFISH, nestacionarioji fotosrovė ir laike užvėlinto ištraukimo lauko, patobulinimai. Šie patobulinimai leido pirmą sykį ištirti krūvininkų pagavimą erdvinėse gaudyklėse bei užfiksuoti krūvininkų dinamiką artimose tikroms organinių saulės elementų veikimo sąlygomis.

- Išsami nestacionariosios sugerties matavimų analizė leido identifikuoti specifinį termiškai aktyvuotą rekombinacijos kanalą befulereniuose organiniuose saulės elementuose su mažu molekulinių orbitalių energijų skirtumu tarp donoro ir akceptoriaus molekulių. Šis atradimas demonstruoja būtinybę kruopščiai sureguliuoti molekulių energijų lygmenis siekiant toliau pagerinti enrgijos konversijos našumą.

- Išsamus krūvininkų generacijos mechanizmo tyrimas PM6:Y6 bandiniuose bei jų temperatūrinė priklausomybė buvo pirmą sykį išmatuota itin žemose temperatūrose (iki 15K). Platus temperatūrų diapazonas padėjo atskleisti prieš tai nematytus laisvų krūvininkų generacijos aspektus šiuose bandiniuose.

Metodika

Šiame darbe be įprastų saulės elementų charakterizavimo metodų, tokių voltamperinės priklausomybės nustatymas ar bandinių nuostaviosios sugerties matavimas, buvo išskirtinai daug naudojami dinaminiai matavimai su laikine skyra, apimantys itin platų laikinį diapazoną. Procesai vykstantys femto – pikosekundžių laiko skalėje buvo nagrinėjami nestacionariosios sugerties, TREFISH ir nestacionariosios fotoliuminiscencijos matavimų technikomis. Procesai ns-µs laiko skalėje, buvo tyrinėjami nestacionariosios fotosrovės ir laike užvėlinto ištraukimo lauko matavimo technikomis. Šiame darbe buvo pristatyti ir pastarųjų matavimų specifiniai patobulinimai, pritaikyti specialiai šiam darbui. Taipogi, duomenų analizei buvo naudojamas ir skaitmeninis modeliavimas.

Diskusija ir išvados

Naujų energijos šaltinių vystimas yra neatideliotinas pasaulinis prioritetas siekiant sumažinti iškastinio kuro naudojimą ir su tuo susijusią CO_2 emisiją. Saulės energija galėtų būti plačiai išnaudojama atliepiant sparčiai augančiam švarios elektros poreikiui. Nišiniai organinių saulės elementų pritaikymai, tokie kaip dalinai skaidrių saulės elementų įdiegimas ant dangoraižio stiklų, galėtų praplėsti nusistovėjusį c-Si suformuotą supratimą apie saulės jėgaines, kaip plotui ir energijos gamybai reiklią technologiją, bei ženkliai prisidėti prie pigios elektros generacijos.

Ši disertacija skirta tyrinėti optoelektroninius procesus naujos kartos organinių saulės elementų befulerenių akceptorių pagrindu. Ypatingas dėmesys buvo skirtas dinaminiams vyksmams, tokiems kaip laisvų krūvininkų generacijos bei jų ištraukimo kinetikoms. Jos buvo išmatuotos pasitelkiant kelias skirtingas matavimo technikas, drauge apimančias ypatingai platų laikinį diapazoną – nuo fs iki µs.

*

Pirmoji problema nagrinėta šiame darbe susijusi su laisvų krūvininkų pagavimu erdvinėse gaudyklėse. Plačiai priimta manyti, kad geriausias būdas sumažinti laisvų krūvininkų rekombinaciją ištraukimo metu yra elektrono ir skylės transportui naudoti erdviškai atskirtus elektronus priemančius ir atiduodančius domenus. Tačiau stipriai išskirta morfologija pasižymi aukšta izoliuotų domenų ir aklaviečių gausa, ko pasekoje prastėja laisvų krūvininkų ištraukimas.[133] Žinoma, kad organiniuose puslaidininkiuose krūvininkai gali šokuoti sąlyginai tolimus atstumus, iki kelių nm, tuneliuodami. [134–137] Tai

leidžia krūvininkams patekti į toliau nei artimiausią esančią būseną. Šitai ypač aktualu kai nors viena iš aktyvaus sluoksnio mišinio komponenčių yra maža molekulė, nes esant jų pakankamai dispersijai kitoje medžiagoje, krūvininkai gal per ją keliauti.[134,136] Tačiau tūrinės heterosandūros organiniame saulės elemente, kur abi aktyvaus sluoksnio medžiagos yra polimerai tokią dispersiją pasiekti yra daug sunkiau dėl labai ilgų polimero grandinių. Ko pasekoje, susiformavusios aklavietės gali riboti krūvininkų judėjimą. Šiame darbe, siekiant ištirti laisvų krūvininkų judėjimą prototipiniame polimeras:polimeras tipo saulės elemente, pagamintame donoro TQ1 ir akceptoriaus N2200 pagrindu, buvo panaudotos patobulintos įprastos krūvininkų ištraukimo matavimo metodikos kartu su skaitmeniniu modeliavimu. Darbe buvo parodyta, kad tik išlieti saulės elementai pasižymi aukšta erdvinių gaudyklių koncentracija. Šių gaudyklių prigimtis sietina su aklavietėmis pavienėse polimero grandinėse, nes pakeitus akceptorinį polimerą mažos molekulės akceptoriumi erdvinių krūvininkų kiekis ženkliai sumažėja. Pažymėtina, kad didelė erdvinių gaudyklių koncentracija didina tiek geminalinę, tiek bimolekulinę rekombinaciją. Taip pat svarbu, kad erdvinių gaudyklių koncentracija ženkliai sumažėja bandinį pakaitinus. Šie tyrimai privedė prie **pirmojo disertacijos teiginio:** Laisvų fotogeneruotų krūvininkų pagavimas erdvinėse gaudyklėse gali riboti jų judėjimą tik-išlietame, polimeras:polimeras tipo organiniame saulės elemente, ko pasekoje išauga rekombinaciniai ir efektyvumo nuostoliai. Erdvinių gaudyklių įtaką galima ženkliai sumažinti bandinį pakaitinus, kaip pademonstruota TQ1:N2200 polimeras:polimeras tipo saulės elemente.

**

Antroje disertacijos dalyje buvo nagrinėjama laisvų krūvininkų dinamika kvazirealiomis darbinėmis organinių saulės elementų veikimo sąlygomis. Laisvų krūvininkų ištraukimas tiesiogiai priklauso nuo jų judrio. Nors judris dažnai naudojamas kaip medžiagą charekterizuojantis dydis, tačiau yra nemažai darbų demonstruojančių, kad organiniuose saulės elementuose krūvininkų judris sumažėja keliomis eilėmis nuo jų generacijos iki ištraukimo.[122–125,140] Tai paaiškinama krūvininkų termalizacijos į žemesnes energetines būsenas reiškiniu. Kitąvertus, yra darbų, kuriuose sėkminga analizė atilkta naudojant nekintantį judrį.[141–144]
Buvo teigiama, kad veikiant saulės elementui krūvininkų judris yra pastovus, nes nuolatinės šviesos generuoti krūvininkai užima žemos energijos būsenas. To pasekoje, judrio matavimai naudojant trumpus lazerio impulsus nėra

korektiški.[145] Šiame darbe buvo panaudotos kelios matavimo technikos, drauge apimančios platų laikinį diapazoną nuo femto iki mikro sekundžių. Taip pat palyginti trumpu lazerio impulsu fotogeneruotų krūvininkų ištraukimas bei rekombinacija, su ir be papildomu nuolatiniu vienos saulės intensyvumo apšvietimu, imituojančiu realias veikimo sąlygas. Šio tyrimo rezultatai atsispindi **antrajame disertacijos teiginyje:** Organiuose saulės elementuose su aukšta gaudyklių koncentracija laisvų krūvininkų pagavimas gaudyklėsė nulemia stiprų krūvininkų judrio mažėjimą ns-μs laiko skalėje. Esant relioms saulės elementų veikimo sąlygoms, nuolatinio apšvietimo generuoti fotokrūvininkai užpildo gaudykles, ko pasekoje judris laikui einant kinta mažiau, išauga tiek krūvininkų rekombinacijos, tiek ištraukimo spartos. Žemų energijų būsenų užpildymas nedaro įtakos stipriai mažėjančiam judriui pikosekundinėje laiko skalėje. Efektyviuose befulereniuose saulės elementuose krūvininkų pagavimas gaudyklėse nėra ženklus, ko pasekoje žemų energijų būsenų užpildymas nedaro pastebimos įtakos krūvininkų ištraukimui.

***

Trečioje šios disertacijos dalyje buvo nagrinėjama laisvų krūvininkų generacija befulereniuose organiniuose saulės elementuose su mažu molekulinių orbitalių energijų skirtumu tarp donoro ir akceptoriaus molekulių. Viena iš galimų strategijų, kaip pagerinti energijos konversijos efektyvumą organiniuose saulės elementuose, yra mažinti įtampos nuostolius. Šie nuostoliai įprastai siekia ~0.6V, kai tuo tarpu efektyviausiuose GaAs, ar labiausiai paplitusiuose c-Si saulės elementuose šie nuostoliai tesiekia 0.3-0.4V. [150–152] Nors yra organinių saulės elemetų pavyzdžių su mažais įtampos nuostoliais[153–156], bet bendrai šie nuostoliai yra didesni nei neorganiniuose saulės elementuose dėl to, kad priešingai nei neorganiniuose puslaidininkiuose, kur šviesa tiesiogiai generuoja laisvuosius krūvininkus, organiniuose puslaidininkiuose generuojami eksitonai, kurių disocijacijai reikalinga papildoma energija. Šiais disocijacijai aktyvuoti reikalingas energijų tarpas tarp molekulinių orbitalių energijų tarp donoro ir akceptoriaus molekulių.[34,157] Yprastai laikoma, kad efektyviam krūvininkų atskyrimui reikia mažiausiai 0.3V, kaip demonstruota fulereniniuose saulės elementuose. [57,126,158] Tačiau, priešingai nei įprastai manoma, naujos kartos befulereniuose saulės elementuose krūvininkų atskyrimas įvyksta, kuomet energijų tarpas nykstamai mažas. [159–162] Nepaisant to, maži įtampos nuostoliai dėl tokios krūvininkų atskyrimo savybės turi ir savo kainą, nes mažas energijų tarpas

nesudaro barjero krūvininko perkelimui atgal. III-oje ir IV-oje publikacijose buvo išsamiai tyrinėta ši krūvininko atbulinė pernaša, naudojant nestacionariosios sugerties, nestacionariosios fotoliuminscencijos ir skaitmeninį modeliavimą. Tyrinėta šios pernašos priklausomybė nuo molekulinių orbitalių energijų skirtumo. Taipogi, šios pernašos įtaką befulerenių organinių saulės elementų energijos konversijos efektyvimui. Šių tyrimų išvadomis grindžiamas **trečiasis disertacijos teiginys:** Termiškai aktyvuota atbulinė elektrono pernaša iš donoro į akceptoriaus aukščiausią užpildytą molekulinę orbitalę nulemia didesnę krūvininkų rekombinaciją ir sumažina befulerenių organinių saulės elementų efektyvumą, kurių molekulinių orbitalių energijų tarpas mažesnis nei 100meV.

****

Paskutinėje šio darbo dalyje, aprašytoje V-oje publikacijoje, buvo tyrinėta laisvų krūvininkų generacijos mechanizmai vienoje moderniausių organinių saulės elementų PM6:Y6 ir jų temperatūrinės priklausomybės. 2019-aisiais buvo pristatytas naujas befulerenis akceptorius Y6. [166] Jo mišinys su polimeru PM6 tapo viena efektyviausių organinių saulės elementų medžiagų. [167,168] Per pastaruosius metus net keli apžvalgos tipo straipsniai buvo išskirtinai skirti PM6:Y6 sistemų progresui apžvelgti.[170,171] Nepaisant to, kad techniniai PM6:Y6 prietaiso optimizavimo aspektai yra gan išsamiai išnagrinėti, vistik platus fizikinio supratimo apie laisvų krūvininkų generaciją šios medžiagose nėra. Pavyzdžiui, du didžiuliai darbai [75,172], nuodugniai nagrinėjantys fotofizikinius reiškinius ir ypač temperatūrinę laisvų krūvininkų generacijos priklausomybę šiose medžiagose, priėjo kiek skirtingas išvadas. Pirmajame darbe teigiama, kad krūvininkų šokavimas, skatinamas temperatūros, yra būtinas laisvų krūvininkų generacijai, tuo tarpu antrajame darbe teigiama, kad krūvio pernašos būsenų disociacijos aktyvacijos energija yra išskirtinai žema, apie 6 meV, todėl krūvininkai efektyviai generuojami žemose temperatūrose, net iki 100 K. Pastebėtina, kad šie tyrimai buvo atitinkamai atliekami iki 200 K ir 75 K žemiausių temperatūrų. Šiame darbe, pasitelkiant nestacionariosios sugerties ir fotoliuminiscencijos matavimai, detaliai išnagrinėjome laisvų krūvininkų generacijos mechanizmus PM6:Y6 saulės elementuose itin plačiame temperatūriniame diapazone, pasiekiant net 15 K temperatūrą.

Šių tyrimų rezultatai atsispindi **ketvirtajame disertacijos teiginyje**: PM6:Y6 organiniame saulės elemente, žadinant akceptorių Y6 lasivi krūvininkai generuojami dviem, kambario temperatūroje vienodo efektyvumo, būdais –

per krūvio pernašos ir vidinės krūvio pernašos būsenas. Įprastas krūvio pernašos mechanizmas beveik nepriklauso nuo temperatūros, tuo tarpu krūvininkų generacijos efektyvumas per vidinę krūvio pernašos būseną smarkai sumažėja krentant temperatūrai.

Publikacijos darbo tema

I. **Jasiūnas, R.**; Melianas, A.; Xia, Y.; Felekidis, N.; Gulbinas, V.; Kemerink, M. Dead Ends Limit Charge Carrier Extraction from All-Polymer Bulk Heterojunction Solar Cells. Advanced Electronic Materials 2018, 4 (8), 1800144.

II. **Jasiūnas, R.**; Jašinskas, V.; Zhang, H.; Upreti, T.; Gao, F.; Kemerink, M.; Gulbinas, V. Carrier Mobility Dynamics under Actual Working Conditions of Organic Solar Cells. J. Phys. Chem. C 2021, 125 (27), 14567–14575.

III. **Jasiūnas, R.**; Zhang, H.; Yuan, J.; Zhou, X.; Qian, D.; Zou, Y.; Devižis, A.; Šulskus, J.; Gao, F.; Gulbinas, V. From Generation to Extraction: A Time-Resolved Investigation of Photophysical Processes in Non-Fullerene Organic Solar Cells. J. Phys. Chem. C 2020, 124 (39), 21283–21292.

IV. **Jasiūnas, R.**; Zhang, H.; Gelžinis, A.; Chmeliov, J.; Franckevičius, M.; Gao, F.; Gulbinas, V. Interplay between Charge Separation and Hole Back Transfer Determines the Efficiency of Non-Fullerene Organic Solar Cells with Low Energy Level Offset. Organic Electronics 2022, 108, 106601.

V. **Jasiūnas, R.**; Zhang, H.; Devižis, A.; Franckevičius, M.; Gao, F.; Gulbinas, V. Thermally Activated Reverse Electron Transfer Limits Carrier Generation Efficiency in PM6:Y6 Non-Fullerene Organic Solar Cells. Solar RRL 2022, 6 (6), 2100963.

Autoriaus indėlis

Šio teksto autorius yra pirmasis visų penkių straipsnių autorius, tad buvo atsakingas už didžiąją dalį teksto parašyto straipsniuose. Autorius taip pat atliko didžiąją dalį eksperimentų, surinko ir išanalizavo duomenis.

I-ame darbe TPC ir TDCF matavimus, jų analizę, bei skaitmeninį judrio modeliavimą atliko autorius. Y.Xia ir N. Felekidis gamino bandinius. A. Melianas, M. Kemerink ir V. Gulbinas kuravo visą darbą, koregavo tekstą.

II-ame darbe TPC, TDCF matavimus, jų analizę bei skaitmeninį modeliavimą atliko autorius. V. Jašinskas atliko TREFISH matavimus. H. Zhang, T.Upreti gamino bandinius. F. Gao, M. Kemereink ir V. Gulbinas kuravo visą darbą, koregavo tekstą.

III-ame darbe TPC, TDCF matavimus, jų analizę atliko autorius. H. Zhang, J.Yuan, X. Zhou, D. Qian, Y. Zou gamino bandinius, sintetino Y1 akceptorių. A. Devižis atliko TA ir EA matavimus. J. Šulskus atliko teorinius skaičiavimus. F. Gao ir V. Gulbinas kuravo visą darbą, koregavo tekstą.

IV-ame darbe TA matavimus ir jų analizę atliko autorius, taipogi kartu su H. Zhang gamino bandinius. A. Gelžinis ir J. Chmeliov atliko teorinį modeliavimą. M. Franckevičius atlikos tPL matavimus. F. Gao ir V. Gulbinas kuravo visą darbą, koregavo tekstą.

V-ame darbe autorius kartu su H.Zhang gamino bandinius, atliko TA eksperimentų analizę. A. Devižis atiko TA matavimus. M. Franckevičius atliko tPL matavimus. F. Gao ir V. Gulbinas kuravo visą darbą, koregavo tekstą.

Autoriaus straipsniai neįtraukti į disertaciją

VI.   Xia, R.; Fei, Z.; Drigo, N.; Bobbink, F. D.; Huang, Z.; **Jasiūnas, R.**; Franckevičius, M.; Gulbinas, V.; Mensi, M.; Fang, X.; Roldán-Carmona, C.; Nazeeruddin, M. K.; Dyson, P. J. Retarding Thermal Degradation in Hybrid Perovskites by Ionic Liquid Additives. Adv. Funct. Mater. 2019, 1902021.

VII.   **Jasiūnas, R.**; Gegevičius, R.; Franckevičius, M.; Jašinskas, V.; Gulbinas, V. Energy Barriers Restrict Charge Carrier Motion in MAPI Perovskite Films. Adv. Optical Mater. 2020, 8 (16), 2000036.

VIII.   **Jasiūnas, R.**; Gegevičius, R.; Franckevičius, M.; Phung, N.; Abate, A.; Gulbinas, V. Suppression of Electron Trapping in MAPbI3 Perovskite by Sr2+ Doping. Phys. Status Solidi RRL 2020, 5.

Darbo rezultatai buvo pristatyti šiose konferencijose

1. FizTech konferencija, 2018, Vilnius, Lietuva. Stendinis pranešimas. <u>Laimėtas apdovanojimas už geriausią stendinį panešimą.</u>
2. Hybrid and Organic Photovoltaics (HOPV), 2019, Roma, Italija. Stendinis pranešimas.
3. LMA Jaunųjų Mokslininkų Konferencija, 2019, Vilnius, Lietuva. Žodinis pranešimas.
4. XXIV Galyna Puchkovska International School-Seminar Spectroscopy of Molecules and Crystals, 2019, Odesa, Ukraina. Stendinis pranešimas.
5. Open Readings, 2019, Vilnius, Lietuva. Žodinis pranešimas.
6. Optical Probes, 2019, Vilnius, Lietuva. Stendinis pranešimas.
7. Advanced Materials and Technology, 2019, Palanga, Lietuva. Stendinis pranešimas. <u>Laimėtas apdovanojimas už geriausią stendinį panešimą.</u>
8. Advanced Properties and Processes in Optoelectronic Materials and Systems - APROPOS 17, 2020, Vilnius, Lietuva. Stendinis pranešimas.
9. FizTech conference, 2020, Vilnius, Lithuania. Žodinis pranešimas.
10. Advanced Materials and Technology, 2020, Palanga, Lithuania. Stendinis pranešimas.
11. Open Readings, 2020, Vilnius, Lietuva. Žodinis pranešimas.
12. nanoGe Fall Meeting, 2021, Online. E-poster tipo pranešimas.
13. Advanced Materials and Technology, 2021, Palanga, Lietuva. Stendinis pranešimas.
14. FizTech konferencija, 2021, Vilnius, Lietuva. Žodinis pranešimas. <u>Laimėtas apdovanojimas už geriausią žodinį panešimą.</u>
15. Open Readings, 2021, Vilnius, Lietuva. Žodinis pranešimas.
16. 2nd Global Webinar on Materials Science and Engineering" (GWMSE-2021), 2021, online. Žodinis pranešimas.
17. EDS 2022: Hanseatic Workshop on Exciton Dynamics and Spectroscopy, 2022, Vilnius, Lietuva. Žodinis pranešimas.

Apie autorių

Rokas Jasiūnas gimė 1988 metais Vilniuje. 2007 metais baigė Vilniaus Gabijos gimnaziją. 2016 metais baigė Fizikos bakalauro studijų programą Vilniaus universitete. 2018 metais baigė Optoelektronikos magistrantūros studijų programą Magnum cum Laude diplomu, Vilniaus universitete. 2018 metais buvo priimtas į doktorantūros studijas Fizinių ir technologijos mokslų centre. 2020 metais atliko stažuotę Linšiopingo universitete, Švedijoje.

LIST OF PUBLICATIONS, AUTHOR'S CONTRIBUTION AND COPIES OF PUBLICATIONS

This thesis is based upon results that have been published in scientific papers:

VI. **Jasiūnas, R.**; Melianas, A.; Xia, Y.; Felekidis, N.; Gulbinas, V.; Kemerink, M. Dead Ends Limit Charge Carrier Extraction from All-Polymer Bulk Heterojunction Solar Cells. Advanced Electronic Materials 2018, 4 (8), 1800144.

VII. **Jasiūnas, R.**; Jašinskas, V.; Zhang, H.; Upreti, T.; Gao, F.; Kemerink, M.; Gulbinas, V. Carrier Mobility Dynamics under Actual Working Conditions of Organic Solar Cells. J. Phys. Chem. C 2021, 125 (27), 14567–14575.

VIII. **Jasiūnas, R.**; Zhang, H.; Yuan, J.; Zhou, X.; Qian, D.; Zou, Y.; Devižis, A.; Šulskus, J.; Gao, F.; Gulbinas, V. From Generation to Extraction: A Time-Resolved Investigation of Photophysical Processes in Non-Fullerene Organic Solar Cells. J. Phys. Chem. C 2020, 124 (39), 21283–21292.

IX. **Jasiūnas, R.**; Zhang, H.; Gelžinis, A.; Chmeliov, J.; Franckevičius, M.; Gao, F.; Gulbinas, V. Interplay between Charge Separation and Hole Back Transfer Determines the Efficiency of Non-Fullerene Organic Solar Cells with Low Energy Level Offset. Organic Electronics 2022, 108, 106601.

X. **Jasiūnas, R.**; Zhang, H.; Devižis, A.; Franckevičius, M.; Gao, F.; Gulbinas, V. Thermally Activated Reverse Electron Transfer Limits Carrier Generation Efficiency in PM6:Y6 Non-Fullerene Organic Solar Cells. Solar RRL 2022, 6 (6), 2100963.

Author's contribution:

The author of this thesis is the first author of all five manuscripts presented here and as such wrote most of the text. Author also performed absolute majority of the measurements, collected and analyzed data, numerically modeled mobility dynamics.

In paper I, author perfomed TPC and TDCF measurements, analyzed data

and numerically modeled the results. Y.Xia and N. Felekidis fabricated samples. A. Melianas, M. Kemerink ir V. Gulbinas supervised the work, edited the text.

In paper II, author performed TPC and TDCF measurements, analyzed data and numerically modeled the results. V. Jašinskas performed TREFISH measurements. H. Zhang and T.Upreti fabricated samples. F. Gao, M. Kemereink ir V. Gulbinas supervied the work, edited text.

In paper III, author performed TPC and TDCF measurements, analyzed data. H. Zhang, J.Yuan, X. Zhou, D. Qian, Y. Zou fabricated samples, including synthesos of Y1 acceptor. A. Devižis performed TA and EA measurements. J. Šulskus performed theoretical calculations. F. Gao and V. Gulbinas supervised the work, edited text.

In paper IV, author performed TA measurements, analyzed data. Also, together with H. Zhang fabricated samples. A. Gelžinis and J. Chmeliov performed theoretical calculations. M. Franckevičius performed tPL measurements. F. Gao and V. Gulbinas supervised the work, edited text.

In paper V, author analyzed TA data, together with H.Zhang fabricated samples. A. Devižis performed TA measurements. M. Franckevičius performed tPL measurements. F. Gao and V. Gulbinas supervised the work, edited text.

Scientific publications that were not included into the thesis:

XI.   Xia, R.; Fei, Z.; Drigo, N.; Bobbink, F. D.; Huang, Z.; **Jasiūnas, R.**; Franckevičius, M.; Gulbinas, V.; Mensi, M.; Fang, X.; Roldán-Carmona, C.; Nazeeruddin, M. K.; Dyson, P. J. Retarding Thermal Degradation in Hybrid Perovskites by Ionic Liquid Additives. Adv. Funct. Mater. 2019, 1902021.

XII. **Jasiūnas, R.**; Gegevičius, R.; Franckevičius, M.; Jašinskas, V.; Gulbinas, V. Energy Barriers Restrict Charge Carrier Motion in MAPI Perovskite Films. Adv. Optical Mater. 2020, 8 (16), 2000036.

XIII. **Jasiūnas, R.**; Gegevičius, R.; Franckevičius, M.; Phung, N.; Abate, A.; Gulbinas, V. Suppression of Electron Trapping in MAPbI3 Perovskite by Sr2+ Doping. Phys. Status Solidi RRL 2020, 5.

The results of the thesis were presented at the following conferences:

1. FizTech conference, 2018, Vilnius, Lithuania. Poster presentation. Rewarded as best poster presentation.
2. Hybrid and Organic Photovoltaics (HOPV), 2019, Rome, Italy. Poster presentation.
3. LMA Jaunųjų Mokslininkų Konferencija, 2019, Vilnius, Lithuania. Oral presentation.
4. XXIV Galyna Puchkovska International School-Seminar Spectroscopy of Molecules and Crystals, 2019, Odesa, Ukraine. Poster presentation.
5. Open Readings, 2019, Vilnius, Lithuania. Oral presentation.
6. Optical Probes, 2019, Vilnius, Lithuania. Poster presentation.
7. Advanced Materials and Technology, 2019, Palanga, Lithuania. Poster presentation. Rewarded as best poster presentation.
8. Advanced Properties and Processes in Optoelectronic Materials and Systems - APROPOS 17, 2020, Vilnius, Lithuania. Poster presentation.
9. FizTech conference, 2020, Vilnius, Lithuania. Oral presentation.
10. Advanced Materials and Technology, 2020, Palanga, Lithuania. Poster presentation.
11. Open Readings, 2020, Vilnius, Lithuania. Oral presentation.
12. nanoGe Fall Meeting, 2021, Online. E-poster presentation.
13. Advanced Materials and Technology, 2021, Palanga, Lithuania. Poster presentation.
14. FizTech conference, 2021, Vilnius, Lithuania. Oral presentation. Rewarded as best oral presentation.
15. Open Readings, 2021, Vilnius, Lithuania. Oral presentation.
16. 2nd Global Webinar on Materials Science and Engineering" (GWMSE-2021), 2021, online. Oral presentation.
17. EDS 2022: Hanseatic Workshop on Exciton Dynamics and Spectroscopy, 2022, Vilnius, Lithuania. Oral presentation.

About the author

Rokas Jasiūnas was born in 1988 in Vilnius. In 2007 he graduated Vilniaus Gabijos gymnasium. In 2016 he received bachelor degree in Physics at Vilnius University. In 2018 he received master's degree in Optoelectronics with Magnum cum Laude at Vilnius University. In 2018 he started his PhD studies at Center for Physical Sciences and Technology.

FULL PAPER

Spatial Traps

**ADVANCED
ELECTRONIC
MATERIALS**
www.advelectronicmat.de

Check for updates

Dead Ends Limit Charge Carrier Extraction from All-Polymer Bulk Heterojunction Solar Cells

Rokas Jasiūnas,* Armantas Melianas, Yuxin Xia, Nikolaos Felekidis, Vidmantas Gulbinas, and Martijn Kemerink

Extraction of photocreated charge carriers from a prototypical all-polymer organic solar cell is investigated by combining transient photocurrent and time-delayed collection field experiments with numerical simulations. It is found that extraction is significantly hampered by charges getting trapped in spatial traps that are tentatively attributed to dead ends in the intermixed polymer network—in photovoltaic devices based on the same donor polymer and a fullerene acceptor this effect is much weaker. The slow-down in charge extraction leads to enhanced recombination and associated performance losses. These effects are observed in addition to the dispersive behavior that is characteristic of charge motion in energetically disordered media. Upon annealing the effects of spatial traps diminish, rationalizing the doubling in device power conversion efficiency after annealing.

1. Introduction

Extraction of photogenerated charge carriers from organic bulk-heterojunction (BHJ) solar cells is one of the most important processes determining device performance. Slow carrier extraction causes their accumulation in the active layer and, as a consequence, an increased bimolecular recombination, which reduces the short-circuit current and particularly the fill factor.[1] It is commonly assumed that the optimal morphology for efficient BHJ solar cells is one where photogenerated electrons and holes avoid recombination by moving via spatially separated percolating domains consisting (predominantly) of electron

accepting material in one phase and electron donating material in the other.[2] However, such strongly phase-separated morphologies are prone to cause extraction problems due to the formation of dead ends and/or isolated domains.[3]

Fortunately, in state-of-the-art polymer:fullerene and polymer:small molecule organic photovoltaic (OPV) devices performance is not limited by recombination losses during extraction (but mostly by voltage losses) as witnessed by large fill factors and relatively high internal quantum efficiency (IQE) values.[4] As a consequence, extraction of photocreated charge carriers can often be well described using models that consider the BHJ as an effective medium with the energy levels of the medium reflecting the highest occupied molecular orbital (HOMO) of the donor and the lowest unoccupied molecular orbital (LUMO) of the acceptor.[5,6] In such models, morphological effects are only implicitly accounted for by the values of the (effective) transport and disorder parameters. One may wonder why this evident simplification works so well. It has recently become clear that one important reason might be that charge carriers in organic semiconductors may actually be able to move over relatively large distances, up to several nm, by long-range tunneling or molecular superexchange.[7–10] This enables transport to non-nearest neighbor sites, and thereby greatly relaxes the need to have connected phases of pure material for efficient charge transport.

OPV devices using non-fullerene acceptors are currently receiving increased attention and start to outperform fullerene-based devices.[11–13] While having evident benefits over fullerenes in terms of improved absorption and larger energy level tunability, charge transport and extraction in non-fullerene BHJ is still less understood. In particular all-polymer BHJ, in which both donor and acceptor materials are polymers, are in many respects in their infancy. While the entanglement of polymer chains in such BHJ is expected to lead to a much needed increased morphological stability at elevated temperatures inherent to solar cell operation,[14] the same entanglement can also lead to extraction problems. Such problems are less pronounced in BHJ where at least one of the constituents is a small molecule and dispersion of a minor fraction of the small molecule in the other compound is sufficient to enable reasonably efficient charge transport between these molecules.[7,9] However, the required "molecular" dispersion, in which sites of

R. Jasiūnas, Prof. V. Gulbinas
Center for Physical Sciences and Technology
Saulėtekio av. 3, LT-10257, Vilnius, Lithuania
E-mail: rokas.jasiunas@ftmc.lt
Dr. A. Melianas,[+] Y. Xia
Biomolecular and Organic Electronics
Department of Physics, Chemistry and Biology (IFM)
Linköping University
58183 Linköping, Sweden
N. Felekidis, Prof. M. Kemerink
Complex Materials and Devices
Department of Physics, Chemistry and Biology (IFM)
Linköping University
58183 Linköping, Sweden

The ORCID identification number(s) for the author(s) of this article can be found under https://doi.org/10.1002/aelm.201800144.

[+]Present address: Department of Materials Science and Engineering, Stanford University, Stanford, CA 94305, USA

104

**ADVANCED
SCIENCE NEWS**
www.advancedsciencenews.com

**ADVANCED
ELECTRONIC
MATERIALS**
www.advelectronicmat.de

a given material are located within a few nm one from another is much harder to realize with polymer chains containing a significant number of repeat units and long side chains, rendering a large fraction of the volume insulating. In all-polymer OPV, one may therefore anticipate additional transport problems associated with isolated polymer clusters or polymer chains forming dead ends.

An analogous situation has been observed for 1,1-bis[(di-4-tolylamino)phenyl]cyclohexane (TAPC) in a polycarbonate matrix, where the carrier mobility has been found to decrease with increasing electric field strength.[15] This was attributed to dead ends where carriers need to hop against the direction of the field to escape the spatial trap and continue drift.[16]

Here, we combine transient charge extraction experiments with numerical modeling to demonstrate that in a prototypical all-polymer OPV device, consisting of TQ1 as the donor and N2200 as the acceptor, spatial traps indeed lead to charge extraction problems and, concomitantly, to increased recombination. Upon annealing the effect of these spatial traps largely vanishes. We have previously shown that annealing roughly doubles the device's power conversion efficiency while, surprisingly, the ps–μs charge extraction kinetics were unaffected.[17] We tentatively associate spatial traps with chain ends that hamper the initial, short-range separation of the photocreated electron–hole pair, leading to strongly enhanced geminate recombination. In a broader perspective, these results highlight a morphological problem which may occur in all bulk-heterojunction OPVs, and show that relatively simple processing steps, such as thermal annealing, can possibly at least partly resolve the issue.

2. Results

Figure 1 shows the time-delayed collection field (TDCF) investigation results obtained for the as-spun TQ1:N2200 sample with a constant extraction (collection) delay of 300 ns but at different generation voltages U_{gen}. Note that all voltages specified here and below are effective values that account for the applied voltage and the built-in potential $U^{eff} = U_{appl} + V_{BI}$ ($V_{BI} = -0.47$ V). The effective extraction voltage was kept constant at $U_{ext} = -1.47$ V, where the minus sign corresponds to reverse bias. The delay time of 300 ns used for the measurements presented in Figure 1 was chosen to make sure that the specified collection field was indeed fully applied at this time. Similar measurements were also performed at close to zero effective generation voltage ($U_{appl} + V_{BI}$) = 0 V by changing the collection voltage, yielding consistent results (kinetics not shown). Even though some charges may be lost by early-time recombination, the time resolution of the measurements was sufficient to obtain the dependences of the total extracted charge on generation and extraction voltages. The inset in Figure 1 summarizes the results. The strong dependence of the collected charge on the extraction voltage is consistent with the modest fill factor of the as-cast devices.[18] The dependence on the generation voltage suggests that the carrier generation efficiency is dependent on the electric field, which would indicate a charge generation problem due to geminate recombination. In fact, in a previous work we used a detailed analysis of the recombination kinetics on the ps–μs timescale to

identify field-dependent geminate recombination as the major loss channel in the as-cast devices compared to the annealed ones.[17]

Figure 2a shows the dependence of the TDCF photocurrent kinetics on the collection delay time measured at close to zero effective generation voltage. The measurement process is schematically shown in the inset. These measurements correspond to conditions when the built-in voltage was compensated by the applied voltage. Perfect compensation of the internal electric field to reach flatband is hardly possible due to band bending; nevertheless, the net field under these conditions is weak and is for simplicity defined as zero.

As expected, the intensity of the photocurrent burst in Figure 2a decreases with delay time, which may be related to three processes. First, a decay of the charge carrier density due to recombination and, possibly, some diffusion to the electrodes; second, a decrease of the carrier mobility due to charges relaxing in the tail of the density of states (DOS)—this process could also be referred to as energetic trapping; third, a decay in the fraction of mobile charges due to charges "getting stuck" in spatial traps.

Decrease in carrier mobility can be ruled out from the fact that the shape of the photocurrent burst does not change with the collection delay time, as shown in the inset of Figure 2b, indicating that carrier mobility does not change within the used collection delay time (otherwise the burst would broaden by slower carrier extraction). This is expected since charge carrier relaxation in the DOS and the associated mobility decay usually terminate on a sub-microsecond timescale.[6,19,20] Consequently, the integrated areas of the current bursts that are plotted in the gradient colored curve with symbols in Figure 2b correspond to the carrier densities that can be extracted from the device after the delay time, reflecting the charges that have not recombined or moved to electrodes, and did not get stuck in spatial traps.
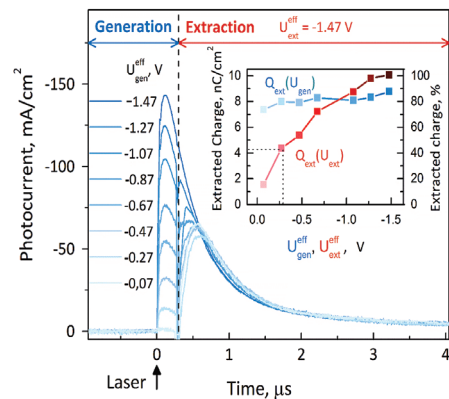

Figure 1. TDCF photocurrent kinetics for the as-cast sample at different effective generation voltages measured with a constant effective extraction voltage $U_{ext}^{eff} = -1.47$ V at a delay time of 300 ns. The inset shows the total charge extracted versus generation voltage at $U_{ext}^{eff} = -1.47$ V (blue line + symbols) and versus extraction voltage at zero effective generation voltage, that is, $U_{appl} = -U_{BI} = 0.47$ V (red line + symbols). The black dashed line is a guide to the eye.

**ADVANCED
SCIENCE NEWS**
www.advancedsciencenews.com

**ADVANCED
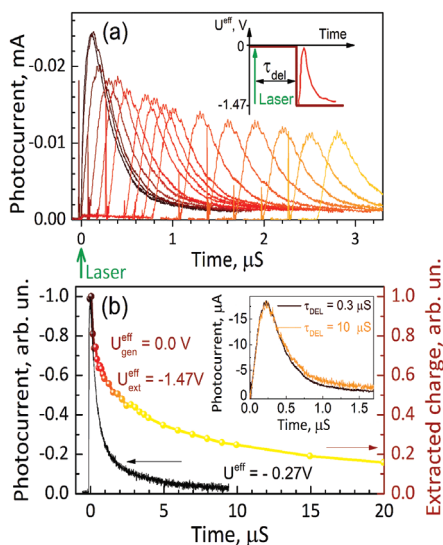ELECTRONIC
MATERIALS**
www.advelectronicmat.de

Figure 2. a) Transient photocurrent measured under −1.47 V effective collection voltage turned on at different delay times following optical excitation ($U_{gen}^{eff} = 0$). b) Normalized conventional photocurrent transient at a constant effective voltage $U^{eff} = −0.27$ V (black line) and the dependence of the total collected charge on the collection delay time corresponding to panel (a), that is for $U_{gen}^{eff} = 0$ and $U_{ext}^{eff} = −1.47$ V (red-yellow line with symbols). Measurements are taken on the as-cast device. The inset shows the normalized photocurrent transients at collection field switching delays of 0.3 and 10 µs.

The black line in Figure 2b shows the conventional transient photocurrent response obtained at the same excitation intensity for a low, constant effective voltage of −0.27 V, when, according to the inset in Figure 1 (follow the dashed horizontal and vertical lines), no more than 40% of the photogenerated charge carriers were extracted (assuming all carriers are extracted at $U_{ext}^{eff} = −1.47$ V). Thus, carrier extraction can only explain a minor fraction of the photocurrent drop at low constant voltage. This is confirmed by the fact that the conventional photocurrent decay (black curve in Figure 2b) reaches zero at ≈10 µs, whereas the TDCF measurements (red-yellow curve) show that there is still a significant amount of charge left in the sample after 10 µs. Since the TDCF data were taken under flatband conditions, they represent an upper limit to charge carrier recombination, that is, recombination in the conventional photocurrent experiment will be weaker, leaving more charges that could potentially be extracted. For these reasons, the photocurrent decay at constant voltage is only in part determined by recombination and extraction. Apparently, at small electric fields, a significant fraction of charge carriers gets trapped on a timescale of several microseconds.

On the other hand, the slow decay of the total extracted charge in the TDCF experiments indicates that the carrier trapping plays a relatively minor role in carrier extraction by delayed collection field (red-yellow symbols in panel (b)). Note

that, in contrast to the conventional photocurrent experiment in Figure 2b, the generation field in the TDCF experiments is close to zero. The straightforward explanation could be that the about five times stronger collection field facilitates the release of trapped carriers. An alternative explanation would be that carriers get less trapped at the flatband conditions during the waiting time in TDFC experiment, when their motion is caused only by undirected diffusion, but do get trapped at finite electric fields, when they experience directed motion by drift and reach dead ends in the phase-separated morphology, that is, get stuck in spatial traps. This scenario bears strong resemblance to the findings on the small molecule:insulator blends discussed in the Introduction.[15,16] We also note that charge motion under weak electric fields is of utmost relevance for device performance since the maximum power point of a solar cell is typically close to flatband.

To invigorate our hypothesis about the importance of spatial traps in our all-polymer OPV devices, we have used a modified TDCF technique. We have used an effective generation voltage equal to the built-in potential ($U_{gen}^{eff} = −0.47$ V, no applied bias) and different effective extraction voltages: (a) equal to the generation voltage (degenerate TDCF), (b) increased to −1.47 V, and (c) reversed to 0.33 V. These measurement regimes are schematically shown in the inset of **Figure 3**a. The main panel of Figure 3a presents the results. In contrast to Figure 2, we here present peak values of the transient photocurrent $j(t)$ obtained after switching on the collection field, divided by the electric field strength to get the product of the carrier density $n(t)$ and mobility $\mu(t)$ from $j(t) = n(t)\mu(t)F$. Because of the sample capacitance, the photocurrent peak appears ≈250 ns after application of the collection voltage. However, this time is short in comparison with the carrier density decay time, so we may consider the $n(t)\mu(t)$ product at the photocurrent peak time identical for all three field profiles.

The differences between $n(t)\mu(t)$ values obtained for the different field profiles represent only differences in the fraction of mobile carriers: first, the total carrier densities were identical because of the equal pump intensities and equal generation fields and, second, relaxation phenomena are unimportant at the µs timescales probed here (cf. Figure 2b inset). The black line shows $n(t)\mu(t)$ under constant applied voltage, and the red line shows the same for an increased extraction field. In absence of spatial trapping, one would not expect any additional extraction upon increasing the (negative) extraction voltage after the constant voltage curve has dropped to zero. Instead, the increased field leads to the additional extraction of a significant number of photocreated charges, as witnessed by the red curve lying above the black one. The slow decay of this component is similar to the collection kinetics measured at zero generation field, cf. Figure 2b. The presence of this additional, field-activated component is consistent with the above made conclusions, indicating the presence of spatially trapped charges that can survive tens of microseconds and that can be extracted by stronger electric fields.

If, as suggested above, charge carriers get stuck by drifting into dead ends that act as spatial traps, reversing the field should release them and give rise to a significant increase in the extracted charge. Figure 3b shows the photocurrent transients obtained with the reversed effective voltage at different
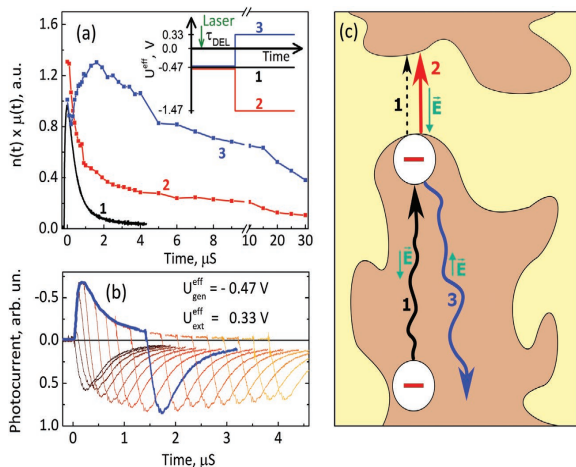
**ADVANCED
SCIENCE NEWS**
www.advancedsciencenews.com

**ADVANCED
ELECTRONIC
MATERIALS**
www.advelectronicmat.de

Figure 3. a) Photocurrent transient versus time at constant field equal to the built-in field (black curve) and peak value of the TDCF photocurrent transient versus collection delay time for different collection field strengths and directions as indicated in the inset (blue and red curves). b) Photocurrent transients at different collection delay times for a reversed collection field (blue curves in panel (a)), the thick blue line highlights one of the current transients. c) Illustration of the characteristic processes in the response to the different field profiles used in (a). Measurements are taken on the as-cast device.

overcome the barrier and continue to drift toward the extracting electrode, causing the weak and slow photocurrent component observed at constant applied voltage. This process (2) is assisted by the electric field. While they are trapped, charges are susceptible to (predominantly geminate) recombination, explaining the poor fill factor of the as-cast devices. When a reversed collection field is applied, charge carriers are detrapped by moving in the opposite direction (process 3).

The ns–μs timescale of the experiments in Figure 3 may appear long compared to the ps–ns timescales that are commonly associated with geminate recombination. However, conventional geminate recombination is associated with charges not escaping from the exciton or CT state, that is, with electron–hole pairs that have substantial wavefunction overlap. In the present case, we are monitoring charges that did escape the exciton/CT state in first instance but get stuck afterward. When these charge pairs eventually reform a (CT) exciton and recombine, the kinetics are still first order, but occur on extended time scales associated with the reforming process. We note that the ns–μs timescales in Figure 3 are consistent with the (geminate) recombination timescales observed in ref. [17].

According to the suggested interpretation, the spatial trapping effect should be a very sensitive probe of the blend morphology. We have therefore performed the same investigations of annealed samples. Annealing the investigated TQ1/N2200 solar cells roughly doubles their power conversion efficiency to ≈3.15%.[18] **Figure 4**a shows the TDCF investigation results for different applied field profiles. Most strikingly, the different peak values of the three curves that are found for the as-cast sample (Figure 3) are absent within experimental resolution, indicating that the short-range spatial trapping, and the associated geminate recombination loss, have largely vanished. This provides a transparent explanation of the previously puzzling observation that the geminate recombination loss dropped from ≈35 to ≈7% upon annealing while unaffecting long-range transport.[17] Apparently, annealing removes spatial traps that hamper short-range charge motion required to escape geminate recombination. In view of the nm length scales involved in geminate recombination, these dead ends are most likely associated with individual polymer chain ends.

At longer delay times, the (blue) curve corresponding to opposite generation and extraction fields lies above the (red) curve corresponding to generation and extraction fields of equal polarity. Since the plotted data have been corrected for dark currents, the difference cannot be attributed to the difference in forward and reverse injection currents. Instead, they point toward a large fraction of charges surviving in the active layer while being spatially trapped. This indicates that even after annealing, spatial traps continue to play a role in this all-polymer BHJ. As mentioned above, these trapped charges are predominantly exposed to bimolecular recombination.
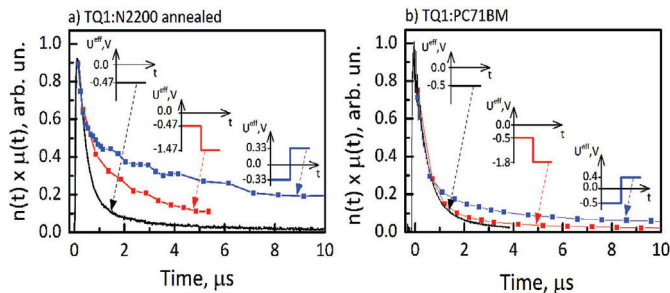
collection delay times. As the thick blue curve, highlighting one of the current transients, shows, the field flipping increases the magnitude of the photocurrent drastically, even though the extraction field was slightly weaker than the generation field of opposite direction. The increase is particularly strong at long delay times. The blue line in Figure 3a shows the delay time dependence of the peak values of the extracted photocurrent. The extracted photocurrent decays very slowly. Moreover, the photocurrent increases during the initial few μs, that is, precisely the time range for which the decay of the photocurrent at constant field (black curve) was attributed to spatial carrier trapping. These observations confirm the occurrence of spatial trapping of photocreated charges.

By comparing the peaks in the black and blue curves in Figure 3a, one can estimate the fraction of charges that get lost through spatial trapping on 0–2 μs timescales to be ≈30%. This number is in excellent agreement with the ≈35% of the charges that were found to be bound in interfacial charge-transfer states and that recombine geminately on basis of a kinetic analysis of transient absorption spectroscopy measurements.[17] We should point out that trapping itself is not a loss channel; the actual loss channel is the recombination of charges that do not manage to escape from their countercharge because of spatial trapping. Along the same lines, (spatial) trapping occurring at longer time and length scales will no longer lead to increased geminate recombination but will contribute to losses through bimolecular recombination.

The drawing in Figure 3c illustrates our interpretation of the carrier extraction experiments. A fraction of the carriers drifting in one direction reach a dead end of a particular blend domain (process 1) and discontinue their drift. Occasionally, they can

107

**ADVANCED
SCIENCE NEWS**
www.advancedsciencenews.com

**ADVANCED
ELECTRONIC
MATERIALS**
www.advelectronicmat.de

Figure 4. Photocurrent transient versus time at constant field equal to the built-in field (black curve) and peak values of the TDCF photocurrent transient versus collection delay time for different collection field strengths and directions as indicated in the inset (blue and red curves). Measurements are taken on the a) TQ1:N2200 annealed and b) TQ1:PC71BM devices.

Although the associated rate constant in as-cast and annealed BHJ is roughly the same (essentially because the mobility is the same), the loss to bimolecular recombination will be largest in the as-cast films because of a starker spatial trapping, and presumably due to larger trap densities. Combined with the geminate loss discussed above, this explains the roughly factor of two difference in power conversion efficiency between the two devices.

Potential minima that can occur due to band bending near contacts at near-flatband conditions could in principle also act as "spatial traps," although it would be hard to rationalize why they would predominantly give rise to geminate recombination. Nevertheless, we confirmed that such potential wells are not at work in our experiments by comparing photocurrent transients at opposite (net) fields of equal magnitude. The photocurrent transients were identical and are presented in the Supporting Information. Since processes leading to band bending in the vicinity of contacts like Schottky barrier formation,[21] thermal diffusion of charges from the contacts,[22] or minority carrier accumulation[23] are asymmetric, the complete equivalence of the obtained current transients rules out such scenarios.

In principle, an effective medium with only diagonal disorder can also give rise to dead ends. Diagonal disorder here refers to energetic disorder in the site energies; spatial traps would be considered a manifestation of off-diagonal disorder, that is, a variation in the tunneling barrier between neighboring sites. In the case of diagonal (on-site) disorder, dead ends are sites that are connected to the percolating cluster but only from one side. Such "energetic dead ends" might give rise to the same behavior as observed in our experiments—a charge can, for example, move into (a series of) sites by "easy" hops along the direction of the applied field but then run into a "difficult" hop and get stuck. To rule out this scenario, we ran explicit kinetic Monte Carlo simulations of the TDCF experiment (see the Supporting Information). The results clearly did not match the experimental observations indicating that the diagonal disorder alone cannot explain the presence of effective spatial traps.

Since we associate the spatial trapping with the specific properties of an all-polymer BHJ, we performed a similar investigation as above for a solar cell based on the same donor material TQ1, blended in a bulk heterojunction with $PC_{71}BM$ as acceptor

in a mass ratio of 1:2.5. These samples showed only small differences between the transient photocurrent at constant applied field and the carrier concentration decays measured with the TDCF technique (see Figure 4b). Nevertheless, the carrier concentration extracted with the reversed effective voltage was slightly larger than with increased effective voltage, which indicates that spatial trapping taking place in these devices. However, the spatial trapping is significantly less prominent than in both the pristine and annealed TQ1/N2200 blends, in line with the anticipated behavior of polymer:small molecule BHJ discussed in the Introduction. Also, in view of the stoichiometry of our samples the limited spatial trapping is not particularly surprising. However, in previous work[24] we found a strong decrease of the electron drift rate upon decreasing the PCBM stoichiometric ratio in blends below ≈50% by weight, which might point toward spatial trapping in dead ends of fullerene-rich domains under these conditions.

3. Conclusion

We have investigated charge carrier motion in an archetypical all-polymer organic solar cell by a combination of carrier extraction experiments and numerical modeling. We find that in the as-cast active layer, the bulk heterojunction morphology contains a significant concentration of spatial traps that we tentatively associate with individual polymer chain ends. The presence of these spatial traps manifests in a suppressed yield of free charge generation due to one of the charges in the splitting CT pair "getting stuck" close to its countercharge, leading to enhanced geminate recombination. Likewise, spatial trapping of otherwise free charges occurs and leads to enhanced bimolecular recombination. The effects of the off-diagonal disorder, that is, the spatial traps, occur in addition to those of the diagonal (on-site) disorder that we previously identified as the cause for highly dispersive, nonequilibrium charge motion. While these findings highlight a morphological problem that seems most likely to arise in all-polymer BHJ (in BHJ based on the same polymer donor with a small molecule (PCBM) acceptor spatial trapping is much weaker) they also show that the number of spatial traps can, at least in the present case, be drastically reduced by thermal annealing.

4. Experimental Section

All-polymer solar cells of inverted geometry were prepared from poly[2,3-bis-(3-octyloxyphenyl)quinoxaline-5,8-diyl-*alt*-thiophene-2,5-diyl] (TQ1), which served as an electron donor, and poly{[*N*,*N*′-bis(2-octyldodecyl)naphthalene-1,4,5,8-bis(dicarboximide)-2,6-diyl]-*alt*-5,5′-(2,2′-bithiophene)} (known as P(NDI2OD-T2), PNDI-2T, or N2200) acting as electron acceptor.[25,26] BHJ active layers of TQ1:N2200 (2:1 ratio by weight) were spin-coated from a 9 g L^{-1} (total) chloroform solution on ZnO/ITO/glass substrates, yielding an active layer thickness of 85 nm. A MoO$_3$/Al top electrode was thermally evaporated through a shadow mask. Annealed samples were prepared by heating the substrate with the active layer for 10 min at 120 °C before top electrode deposition. Samples were fabricated inside an N$_2$-filled glove box and encapsulated with epoxy glue. Detailed information on OPV device preparation can be found elsewhere.[18] The annealed solar cells had a PCE of ≈3%, while PCE of as-spun samples was roughly twice lower.

Bulk heterojunction polymer-fullerene inverted solar cells were fabricated on precleaned glass substrates. Ti(2 nm)/Al(80 nm)/Ti(2.5 nm) contact (cathode) was first thermally evaporated on glass under high vacuum conditions. The samples were exposed to ambient for 1 min to form TiOx. PFPA-1 in toluene with a concentration of 2 mg mL^{-1} was spin-coated on top of the TiOx surface at 1000 rpm for 60 s (in the glove box), followed by rinsing with *o*-dichlorobenzene (oDCB) to create a monolayer of PFPA-1.[27] [6,6]-Phenyl C$_{71}$ butyric acid methyl ester (PC$_{71}$BM) was selected as an electron acceptor while TQ1 as an electron donor. The TQ1:PC$_{71}$BM active layer (1:2.5 weight ratio, 20 g L^{-1} in oDCB) was spin-coated on the PFPA-1 monolayer at 500 rpm for 60 s and dried at 3000 rpm for 30 s. PEDOT:PSS PH1000 mixed with 5% dimethyl sulfoxide (DMSO) and 0.5% surfactant (Zonyl FS 300) was spin-coated on the active layer in ambient at 1000 rpm for 60 s. The samples were annealed at 60 °C for 1 min before encapsulation in the glove box. The thickness of the active layer was around 80 nm as measured by a Dektak surface profilometer.

Transient photocurrent investigations were performed with an Agilent Technologies DS05054A oscilloscope and a Tektronix AFG 3101 function generator. Samples were illuminated by sub-nanosecond 532 nm laser pulses with a 5 Hz repetition rate. Transient photocurrent was measured using the 50 Ω input resistor of the oscilloscope. The time resolution of the current measurements was about 100–200 ns, mainly determined by the oscilloscope input resistance and the sample capacitance of ≈1.5 nF. In integral-mode measurements, the 1 MΩ oscilloscope input resistor was used instead, while the sample and the oscilloscope capacitances served as the integrating capacitor. The time resolution of integral-mode measurements is about 100 ns, limited by the capacitance and inductivity of the electrical circuit.

TDCF[28] investigations were performed with the same experimental setup as used in transient photocurrent measurements. An adjustable voltage was applied to the sample during the optical excitation (generation voltage). Following a variable time delay, the collection voltage was switched on. The voltage generator was triggered by the optical excitation pulse. To compensate the triggering delay of the voltage generator for the experiments in Figures 2–4, the excitation pulse passed a 100 m long optical fiber, acting as an ≈300 ns delay line, before reaching the sample. This allowed reducing the shortest effective delay time to ≈10 ns. The shown charge extraction kinetics corresponds to the difference between the current transients with and without optical excitation.

Supporting Information

Supporting Information is available from the Wiley Online Library or from the author.

Acknowledgements

Conflict of Interest

The authors declare no conflict of interest.

Keywords

[1] R. Mauer, I. A. Howard, F. Laquai, *J. Phys. Chem. Lett.* **2010**, *1*, 3500.
[2] C. Deibel, V. Dyakonov, *Rep. Prog. Phys.* **2010**, *73*, 096401.
[3] L. J. A. Koster, *Phys. Rev. B* **2010**, *81*, 205318.
[4] S. H. Park, A. Roy, S. Beaupré, S. Cho, N. Coates, J. S. Moon, D. Moses, M. Leclerc, K. Lee, A. J. Heeger, *Nat. Photonics* **2009**, *3*, 297.
[5] L. J. A. Koster, E. C. P. Smits, V. D. Mihailetchi, P. W. M. Blom, *Phys. Rev. B* **2005**, *72*, 085205.
[6] A. Melianas, F. Etzold, T. J. Savenije, F. Laquai, O. Inganäs, M. Kemerink, *Nat. Commun.* **2015**, *6*, 8778.
[7] F. Symalla, P. Friederich, A. Massé, V. Meded, R. Coehoorn, P. Bobbert, W. Wenzel, *Phys. Rev. Lett.* **2016**, *117*, 276803.
[8] A. Massé, P. Friederich, F. Symalla, F. Liu, V. Meded, R. Coehoorn, W. Wenzel, P. A. Bobbert, *Phys. Rev. B* **2017**, *95*, 115204.
[9] A. Melianas, V. Pranculis, D. Spoltore, J. Benduhn, O. Inganäs, V. Gulbinas, K. Vandewal, M. Kemerink, *Adv. Energy Mater.* **2017**, *7*, 1700888.
[10] H. Abdalla, G. Zuo, M. Kemerink, *Phys. Rev. B* **2017**, *96*, 241202(R).
[11] W. Zhao, S. Li, H. Yao, S. Zhang, Y. Zhang, B. Yang, J. Hou, *J. Am. Chem. Soc.* **2017**, *139*, 7148.
[12] Y. Li, J.-D. Lin, X. Che, Y. Qu, F. Liu, L.-S. Liao, S. R. Forrest, *J. Am. Chem. Soc.* **2017**, *139*, 17114.
[13] Y. Lin, F. Zhao, Y. Wu, K. Chen, Y. Xia, G. Li, S. K. K. Prasad, J. Zhu, L. Huo, H. Bin, Z.-G. Zhang, X. Guo, M. Zhang, Y. Sun, F. Gao, Z. Wei, W. Ma, C. Wang, J. Hodgkiss, Z. Bo, O. Inganäs, Y. Li, X. Zhan, *Adv. Mater.* **2017**, *29*, 1604155.
[14] T. Kim, J. Choi, H. J. Kim, W. Lee, B. J. Kim, *Macromolecules* **2017**, *50*, 6861.
[15] P. M. Borsenberger, L. Pautmeier, H. Bässler, *J. Chem. Phys.* **1991**, *94*, 5447.
[16] D. Hertel, H. Bässler, *ChemPhysChem* **2008**, *9*, 666.
[17] S. Karuthedath, A. Melianas, Z. Kan, V. Pranculis, M. Wohlfahrt, J. I. Khan, J. Gorenflot, Y. Xia, O. Inganäs, V. Gulbinas, M. Kemerink, F. Laquai, *J. Mater. Chem. A* **2018**, *6*, 7428.
[18] Y. Xia, C. Musumeci, J. Bergqvist, W. Ma, F. Gao, Z. Tang, S. Bai, Y. Jin, C. Zhu, R. Kroon, C. Wang, M. R. Andersson, L. Hou, O. Inganäs, E. Wang, *J. Mater. Chem. A* **2016**, *4*, 3835.
[19] A. Devižis, A. Serbenta, K. Meerholz, D. Hertel, V. Gulbinas, *Phys. Rev. Lett.* **2009**, *103*, 027404.
[20] A. Melianas, V. Pranculis, Y. Xia, N. Felekidis, O. Inganäs, V. Gulbinas, M. Kemerink, *Adv. Energy Mater.* **2017**, *7*, 1602143.
[21] I. Lange, J. C. Blakesley, J. Frisch, A. Vollmer, N. Koch, D. Neher, *Phys. Rev. Lett.* **2011**, *106*.
[22] M. Kemerink, J. M. Kramer, H. H. P. Gommans, R. A. J. Janssen, *Appl. Phys. Lett.* **2006**, *88*, 192108.
[23] G. Garcia-Belmonte, A. Munar, E. M. Barea, J. Bisquert, I. Ugarte, R. Pacios, *Org. Electron.* **2008**, *9*, 847.
[24] V. Pranculis, Y. Infahsaeng, Z. Tang, A. Devižis, D. A. Vithanage, C. S. Ponseca, O. Inganäs, A. P. Yartsev, V. Gulbinas, V. Sundström, *J. Am. Chem. Soc.* **2014**, *136*, 11331.

[25] E. Wang, J. Bergqvist, K. Vandewal, Z. Ma, L. Hou, A. Lundin, S. Himmelberger, A. Salleo, C. Müller, O. Inganäs, F. Zhang, M. R. Andersson, *Adv. Energy Mater.* **2013**, *3*, 806.

[26] D. Mori, H. Benten, I. Okada, H. Ohkita, S. Ito, *Adv. Energy Mater.* **2014**, *4*, 1301006.

[27] Z. Tang, L. M. Andersson, Z. George, K. Vandewal, K. Tvingstedt, P. Heriksson, R. Kroon, M. R. Andersson, O. Inganäs, *Adv. Mater.* **2012**, *24*, 554.

[28] J. Kniepert, M. Schubert, J. C. Blakesley, D. Neher, *J. Phys. Chem. Lett.* **2011**, *2*, 700.

Carrier Mobility Dynamics under Actual Working Conditions of Organic Solar Cells

Rokas Jasiūnas,* Vidmantas Jašinskas, Huotian Zhang, Tanvi Upreti, Feng Gao, Martijn Kemerink, and Vidmantas Gulbinas

ACCESS | Metrics & More | Article Recommendations | Supporting Information

ABSTRACT: Although organic photovoltaics has made significant progress since its appearance decades ago, the underlying physics of charge transport in working cells is still under debate. Carrier mobility, determining the carrier extraction and recombination, is one of the most important but complex and still poorly understood parameters. Low-energy charge carrier states acting as traps play a particularly important role in carrier transport. Occupation of these states under real operation conditions of solar cells induces additional complexity. In this study, we use several transient methods and numerical modeling to address carrier transport under actual working conditions of bulk heterojunction organic solar cells based on fullerene and nonfullerene acceptors. We show that occupation of low-energy states strongly depends on the blend materials and the effective electric field. We define conditions when such occupation increases carrier mobility, making it less time-dependent on the microsecond time scale, and when its influence is only marginal. We also show that the initial mobility, determined by carrier relaxation within the high-energy part of the distributed density of states, strongly decreases with time independently of the low-energy state population.
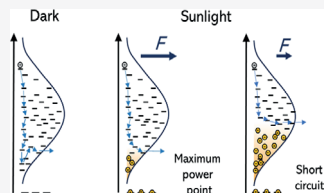
INTRODUCTION

Organic photovoltaics (OPV) has been steadily developing for more than 30 years as a promising solar-to-electrical power conversion technology.[1] Although organic solar cells have been thoroughly investigated and currently reached market-appropriate efficiencies,[2,3] the underlying physics is still not fully understood.

Charge carriers photogenerated in an active layer of an OPV device are either extracted, contributing to current, or recombine, which is the loss channel. These processes depend on extraction and recombination rates. The first is subject to carrier mobility, which in the general case changes with time and depends on the internal electric field. The recombination rate coefficient and carrier density determine recombination losses. Moreover, all these processes are strongly affected by the carrier trapping, which reduces carrier mobility and might enhance the fraction of recombined carriers. Therefore, high trap concentrations lead to reduced open-circuit voltage (V_{oc}), fill factor (FF), and short-circuit current (J_{sc}).[4−6] In this context, we should distinguish between the broad density of states (DOS) distribution of localized states within the band gap that is characteristic for disordered materials that are typically used in the OPV-active layers, which are also referred to as tail states,[7,8] and possible additional distributions of trap states that may be formed deep below these tail states due to impurities, defects, etc.[9] However, experimental differentiation of the tail and trap states is complicated; therefore, here we address the combined effect of all low-energy states. We will analyze their influence on carrier transport, which depends on their depth, density, energetics, and even spatial distribution.[9−11]

Carrier extraction is directly determined by their mobility. Moreover, the recombination rate is also determined by mobility through the Einstein relation between mobility and diffusivity. Carrier mobility in organic materials is usually not constant. It depends on temperature and electric field strength and decreases with time.[12−15] Carrier mobilities in blends of organic solar cells were also reported to decrease by several orders of magnitude from their generation until extraction.[16−23] On the other hand, there are also reports claiming that steady-state mobility analysis can be successfully applied to OPV devices.[24−27] Recently, Koster's group argued that carrier mobility in operating solar cells is indeed constant and that transient methods, where the sample is excited by a short laser pulse, are inadequate for the mobility dynamics investigation in operating solar cells because of low-energy state occupation under steady-state illumination.[28] This study was disputed,[29] but so far there is no clear experimental data to reveal the role of low-energy state population in carrier
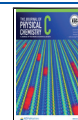
extraction and recombination. Even more, it remains unclear how and if steady-state illumination leads to a low-energy state population, hindering mobility decay.

The aim of this study is to shed light on the above discussed processes by comparing extraction and recombination of charge carriers generated by weak short laser pulses in either the absence or presence of additional continuous illumination using a 1 sun light source, imitating real solar cell operation conditions. We have investigated the population of low-energy states by solar irradiation in bulk heterojunction organic solar cells with fullerene and nonfullerene acceptors and its influence on charge carrier transport. We demonstrate that low-energy state population in low-efficiency solar cells becomes significant at voltages similar to those of working conditions, causing faster carrier extraction and increased recombination. In contrast, in efficient nonfullerene solar cells, carrier trapping plays no significant role. Nevertheless, the initial carrier mobility remains strongly time-dependent regardless of solar illumination even in cells with the strongest carrier trapping.

■ METHODS

We investigated three types of solar cells: the archetypical TQ1:PC$_{71}$BM device, which has been exhaustively studied in recent years as a standard model of the polymer-fullerene solar cell,[30−32] PCE10:PC$_{71}$BM devices with different donor and acceptor stoichiometric ratios, and the efficient nonfullerene device PBDB-T:Y1 based on the record-breaking Y-series acceptor.[33] Chemical structures of the used materials and photoelectrical properties of the investigated solar cells are presented in Figure S1 of the Supporting Information. The device fabrication procedures are also described in the Supporting Information.

To investigate the whole charge carrier extraction dynamics, starting from their generation on a subpicosecond time scale up to their extraction during microseconds, we applied three time-resolved techniques: transient photocurrent (TPC) and time-delayed collection field (TDCF) techniques were used to address carrier motion on a nanosecond−microsecond time scale and time-resolved electric field-induced second harmonic (TREFISH) generation technique was used for ultrafast carrier motion investigation.[16,18] To address the influence of low-energy state occupation under real operation conditions, all the measurements were performed with and without an additional steady-state 1.5 AM intensity illumination, which in the following text will be called as 1 sun light.

Transient Photocurrent. During conventional TPC measurements, samples were excited with short laser pulses at a specific effective voltage U_{Eff}. Here, the effective voltage is regarded as a sum of the applied external voltage and the built-in voltage, that is, $U_{Eff} = U_{App} + U_{Built-in}$. Majority of measurements were performed at voltages below V_{oc} when current flows in the backward direction; therefore, for convenience in the following text, we consider current values to be positive (voltage, respectively) when flowing in the backward direction. The electric scheme and time sequences of TPC are presented in the Supporting Information.

Samples were excited by radiation of the optical parametric amplifier TOPAS-C (Light Conversion Ltd.) pumped by a femtosecond Ti:sapphire laser Integra-C from Quantronix Inc. generating ∼150 fs duration pulses at a 430 Hz repetition rate. The collinear optical parametric amplifier TOPAS-C was used to generate the excitation pulse at 515 nm. Current transients were recorded using the Agilent Technologies DS05054A

oscilloscope (bandwidth 500 MHz), and voltages were set using a Tektronix AFG 3101 function generator. Time resolution of the measurement was limited by the RC of the circuit equal to about 150 ns determined by the resistance of the oscilloscope and generator and the sample capacitance.

TDCF. TDCF is a specific TPC measurement implementation where the sample is excited at zero, or a low effective voltage, called generation voltage U_{GEN} and after some particular delay time, a strong extraction voltage U_{EXT} is applied to collect all carriers and evaluate their density. Here, we assume that an effective extraction voltage of 1.8 V can extract all charge carriers present in the sample at its application time. The schematic representation of TDCF measurement is shown in Figure S3. If the generation voltage is set to compensate for the internal build-in electric field, then the photocurrent equals zero and the carrier density during the delay time before extraction decreases only because of recombination. Therefore, TDCF is one of the routine methods for investigating the carrier recombination dynamics.[17,32,37,38] TDCF measurements were performed using the same experimental setup as for the TPC measurements.

Time-Resolved Electric Field-Induced Second Harmonic. We used this ultrafast optical pump−probe technique to evaluate the carrier mobility kinetics on a ps−ns time scale. It is explained in detail elsewhere.[16,34] In short, drifting charge carriers produced by a femtosecond laser pulse screen the electric field, which is probed by recording the intensity of the electric field-induced second harmonic (EFISH) signal created by the probe pulse applied after a variable delay. The EFISH signal depends on the electric field strength quadratically. Considering the active layer as an insulator sandwiched between two electrodes as a capacitor, the electric field change can then be straightforwardly transformed into the amount of extracted charges using a simple capacitor relation: $\Delta Q = C\Delta U$. Assuming that for carriers to be extracted on average, they have to travel half the thickness of an active layer, which allows evaluating the average carrier drift and consequently the time-dependent carrier mobility. The TREFISH investigations were performed using the same femtosecond laser as the TPC measurements.

Model Description. Numerical modeling of carrier extraction and recombination processes was also applied for TPC and TDCF data interpretation. TPC created by a short laser pulse may be formally expressed as:

$$j(t) = e\, n(t)\mu(t)F \tag{1}$$

where e is the elementary charge, F is the electric field strength, $n(t)$ is the carrier density, and $\mu(t)$ is the average carrier mobility. Therefore, photocurrent decay is determined using two time-dependent parameters: $n(t)$ and $\mu(t)$. The carrier density decays with time because of the carrier recombination and their extraction from the active layer to electrodes. Generally, the charge carrier mobility is also time-dependent because charge carriers gradually populate low-energy states within the distributed DOS and become less mobile, get trapped, and in some cases are stopped by barriers.[10]

The density of charge carriers generated by the laser pulse n_{laser} (in the following text, we call them as laser carriers) decreases due to their recombination and extraction and may be formally expressed as:

$$\frac{dn_{laser}}{dt} = -\gamma(t)\, n_{laser}{}^2 + \gamma(t)n_{laser}n_{Sun} - \frac{j(t)}{de} \tag{2}$$

where $\gamma(t)$ is the bimolecular recombination rate, d is the sample thickness, and n_{sun} is the density of charge carriers generated by constant 1 sun light (in the following text, we call them as sun carriers). A fraction of sun carriers is trapped; thus, the second term also accounts for the Shockley−Read−Hall (SRH) recombination of laser carriers with the trapped sun carriers. In the case of measurements in the absence of additional continuous illumination, the second term is absent and we ignore the SRH recombination because of weak population of low-energy states by the used low-intensity and low-repetition rate laser pulses. Here, we assumed that the bimolecular recombination rate is time-dependent and proportional to time-dependent mobility:

$$\gamma(t) = \beta\mu(t) \tag{4}$$

where β is the coefficient of proportionality, which was obtained setting the initial $\gamma(t)$ value to time-independent γ obtained from TDCF measurements in the case of zero effective generation voltage.

The time-dependent mobility was obtained by combining TPC and TDCF measurements. For this, we used an assumption that all the extracted charges constituted the photocurrent value at the time of extraction voltage application, therefore neglecting charge carrier losses during noninstantaneous (~few ns) extraction voltage application. Knowing $j(t)$ values from the TPC measurement and $n(t)$ from TDCF, we were able to evaluate mobility values using eq 1.

RESULTS AND DISCUSSION

We started the analysis of the experimental data with the well-established TQ1:PC$_{71}$BM blend. Although the investigated device showed a decent power conversion efficiency (PCE) of 5.3%, its FF was only 0.39, which could be due to increased carrier trapping compared to the more conventional TQ1:PC$_{71}$BM devices. However, for the present purpose, these samples are excellently suited to demonstrate the role of strong carrier trapping in carrier mobility and recombination dynamics.

The analysis and interpretation of the experimental results become simpler by using low-intensity laser excitation where we can neglect bimolecular recombination taking place between laser carriers. Importantly, in this limit, the laser carriers experience identical experimental conditions as sun carriers and thus correctly represent the dynamics of individual charge carriers under real solar cell operation conditions. We determined this limit from the excitation intensity dependence of photocurrent kinetics.

Figure 1 shows the photocurrent transients at various excitation intensities measured at an effective internal voltage of 0.2 V, which is close to the maximal power point (MPP) of the solar cell. Several nonlinear processes are expected to take place and be responsible for the changes of the photocurrent transients at increased excitation intensity: exciton annihilation, bimolecular carrier recombination, and occupation of low-energy states. At the two lowest intensity values, the current kinetics has a very similar shape indicating that nonlinear processes still play only a marginal role. Therefore, the photocurrent shape during the first microsecond is mainly determined by the carrier relaxation to low-energy states within DOS, which reduces their mobility,[18] while at longer times, the current decays due to extraction of equilibrated charge carriers. By increasing the excitation intensity, we do not observe significant changes in the current decay kinetics during the first
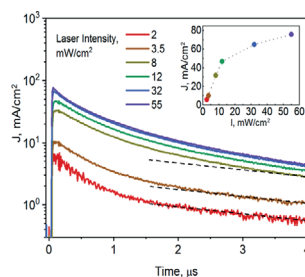

Figure 1. Photocurrent kinetics dependence on 515 nm laser excitation intensity for the TQ1:PC$_{71}$BM sample. Parallel dotted lines are guide to the eye, indicating different decay rates. The inset shows peak values of the photocurrent.

microsecond, which could take place in the case of significant occupation of low-energy states changing the carrier mobility decay. However, the photocurrent peak starts to saturate at high intensities (see the inset in Figure 1), most likely due to the exciton annihilation. The photocurrent decay during 1−5 ms also becomes faster after exceeding 3.5 mW/cm^2, indicating the increased role of bimolecular carrier recombination. Consequently, these measurements show that all discussed nonlinear processes are insignificant at excitation intensities below 3.5 mW/cm^2. Similar results were also obtained for other investigated solar cells, thus a laser intensity of 2.5 mW/cm^2 was used to avoid nonlinearities in all belowdiscussed investigations.

Figure 2 shows the charge carrier extraction dynamics in the TQ1:PC$_{71}$BM blend in a wide temporal window evaluated
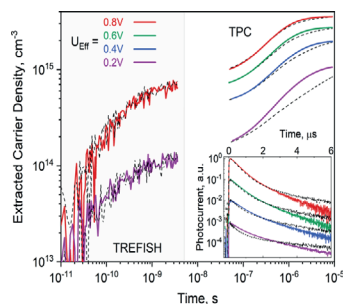

Figure 2. Extracted laser-carrier dynamics in the TQ1:PC$_{71}$BM device at various effective voltages in the dark (black dashed lines) and under 1 sun illumination (color lines). Here and in all following measurements, 515 nm laser excitation at a 432 Hz repetition rate and ~2.5 mW/cm^2 average power were used. In the inset, photocurrent transients were normalized and vertically shifted.

from measurements performed without and under additional 1 sun illumination (further referred as "dark" and 1 sun light conditions, respectively). The measurements "in dark" revealed qualitatively similar carrier extraction dynamics as was reported in ref 18, which was evaluated as dispersive with a strongly time-dependent mobility. Decay of the carrier mobility by at least one order of magnitude during initial several nanoseconds has been observed in several polymer-PCBM blends[17−20]
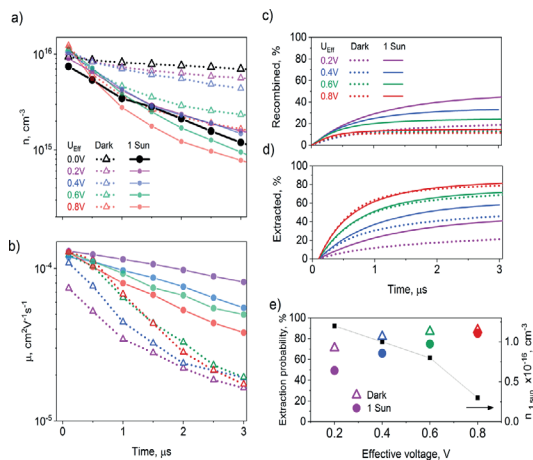
Figure 3. (a) Charge carrier density kinetics at different effective voltages in the TQ1:PC$_{71}$BM device determined by TDCF measurements. Here and in all plots, solid lines correspond to measurements under 1 sun and dotted lines correspond to measurements "in dark"; (b) carrier mobility dynamics evaluated from TDCF data and TPC data presented in Figure 2; modeled fraction of recombined (c) and extracted (d) charge carriers; and (e) carrier extraction probabilities (color symbols) "in dark" and under 1 sun and sun-carrier density (black symbols) as a function of effective voltage.

including TQ1:PC$_{71}$BM blend[18] and has been attributed to the energy relaxation within the DOS. For the given sample, carrier extraction at time below 10^{-8} s is slightly suppressed, which we attribute to the charge carrier trapping that we aim to study.

In the case of additional 1 sun illumination, sun carriers were continuously generated, while their concentration was determined by the balance between extraction, recombination, and generation rates. Additional carriers generated by laser pulses (laser carriers) now appear on a background of sun carriers. The sun carriers also create a constant current background, which was subtracted from our data to register the photocurrent created by laser carriers only. Importantly, additional 1 sun illumination alters the conditions under which laser carriers are generated. First, sun carriers fill low-energy states; therefore, laser carriers experience less trapping during their extraction from the active layer. Second, laser carriers recombine with sun carriers. Thus, by using two, "dark" and 1 sun light, measurement conditions, we compare the carrier dynamics when (a) nongeminate recombination is negligible and low-energy states are not occupied (due to low laser-carrier density, as discussed above) and (b) in the presence of sun carriers, which to some extent occupy low-energy states. We shall inquire how 1 sun illumination affects charge extraction on different time scales at different effective electric field strengths.

As the left-hand part of Figure 2 shows, 1 sun illumination does not change the ultrafast carrier extraction and thus the mobility dynamics. This indicates that sun carriers populating low-energy states have no impact on the initial laser-carrier drift. This is expected because laser carriers in this time domain still reside in the high-energy part of DOS and the population of low-energy states by sun carriers plays a nonessential role in their dynamics. This allows us to conclude that individual charge carriers generated by sun light under real solar cell operation conditions also experience identical fast mobility

decay on a ps–ns time scale as reported in previous studies.[18,34]

The right-hand side of Figure 2 shows carrier extraction dynamics obtained by integrating TPCs shown in the inset. Notably, as the inset shows, the charge extraction at low U_{Eff} = 0.2 V is faster during initial 1–2 μs in the presence of 1 sun light. This signifies that laser carriers experience weaker decay of mobility because low-energy states are significantly populated under 1 sun light. The 1 sun light influence becomes less pronounced at higher effective voltages. This is reasonable since higher voltages extract charge carriers more rapidly, including those residing in the low-energy states, liberating these states. Consequently, occupation of the low-energy states under 1 sun light decreases with voltage and weakly affects trapping of laser carriers already at U_{Eff} = 0.4 V. At longer 2–6 μs times, the photocurrent decays faster under 1 sun light. This decay phase was attributed to the extraction of equilibrated carriers; thus, a faster photocurrent decay indicates faster decay of the carrier density, which we attribute to the SRH recombination of laser carriers with trapped sun carriers (second term in eq 2).

To quantify the influence of 1 sun illumination on bimolecular carrier recombination losses, we performed TPC measurements in complementary TDCF implementation. As explained in the Methods section, TPC measurements enable tracking of laser-carrier density kinetics, which is shown in Figure 3a. At zero effective voltage (black dotted curve), photogenerated carriers are not extracted and their density decays due to recombination only. This allows evaluation of the bimolecular recombination rate, which in this case was found being equal to $\gamma = 1.24 \times 10^{-11}$ cm^3 s^{-1}, similar to values reported elsewhere.[30,31] Increasing the effective voltage leads to more rapid carrier density decay due to carrier extraction. The clear difference between carrier density dynamics "in dark" and under 1 sun illumination (dotted and solid curves, respectively) at zero effective voltage supports the idea of

pronounced recombination of laser carriers with sun carriers. It is worth noting that the difference in kinetics is much smaller at higher voltages because enhanced extraction causes smaller trapped sun-carrier population.

Combining $j(t)$ obtained from TPC measurements and $n(t)$ obtained from TDCF, we can evaluate the mean time-dependent carrier mobility using the relation $j(t) = eFn(t)\mu(t)$. The obtained mobility dynamics at different voltages "in dark" and under 1 sun light is shown in Figure 3b. Under 1 sun illumination, the mobility is higher and its decay is weaker. "In dark," the mobility increases at higher voltages as typically observed in disordered organic semiconductors.[35] A slightly stronger mobility decay at high voltages is caused by faster extraction of nontrapped carriers leaving only low-mobility trapped carriers at longer times. Under 1 sun illumination, the mobility becomes less time-dependent, particularly at low effective electric field when low-energy states are populated by sun carriers (as shown in Scheme 1) preventing trapping of

Scheme 1. Schematic Representation of Charge Carrier Relaxation within DOS "in Dark" (Blue Arrows) and under Solar Illumination (Red Arrows) at Low and High Effective Electric Field Values
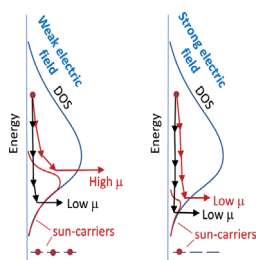
laser carriers. However, population of low-energy states by sun carriers decreases with increasing electric field, promoting

trapping of laser carriers and causing a stronger decrease of their mobility. Consequently, mobility decreases with electric field, in stark contrast with the typically reported behavior.

It should also be noted that the population of low-energy states and its influence is expected to be less distinct at lower illumination intensities. Therefore, a significant impact of trapped sun carriers on the carrier extraction dynamics is expected only at full 1.5 AM solar illumination.

To evaluate the role of the low-energy state occupation in the solar cell performance more clearly, we performed numerical modeling of the carrier extraction and recombination processes on the basis of the experimental results. A detailed description of our model is presented in the Methods section, whereas fitted curves are shown in the Supporting Information. Our numerical model provided us with total bimolecular recombination (between laser−laser and 1 sun−laser carriers combined) and carrier extraction dynamics. The "dark" conditions approximately represent the carrier extraction and recombination kinetics at constant low-intensity illumination of a solar cell. As shown in Figure 3c,d, the carrier recombination dynamics under these conditions is weakly dependent on the effective voltage, while the extraction rate approximately linearly increases with voltage. At 1 sun illumination, the recombination rate strongly increases at low effective voltages because of the high density of carriers trapped in low-energy states (Figure 3c,e). On the other hand, the dependence of the carrier extraction on effective voltage is weaker than "in dark" conditions. Figure 3e shows the summary of the calculation results. It shows that the sun-carrier concentration decreases almost four times when the effective voltage increases from 0.2 V, which is close to the MPP conditions, to 0.8 V, which corresponds to short-circuit. Figure 3e also shows the total probability for the generated carrier to be extracted, rather than to recombine. The carrier extraction probability under 1 sun light is lower than "in dark" because of the increased recombination rate in the presence of sun carriers, but this difference decreases with the effective voltage when the density of the trapped sun carriers decreases.
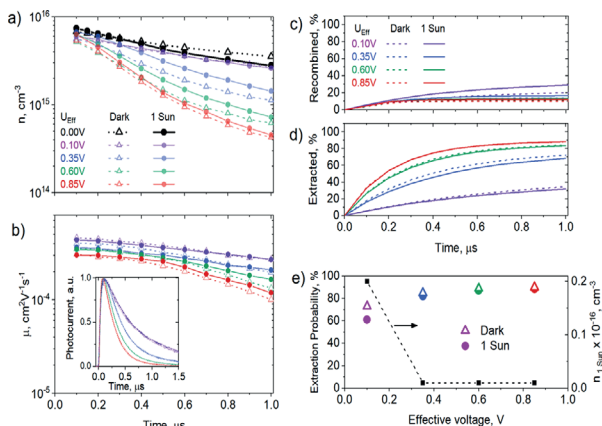
Figure 4. Carrier density (a) and mobility (b) kinetics in the PBDB-T:Y1 device obtained from TPC and TDCF measurements combined. The inset in (b) shows the normalized photocurrent kinetics. Modeled recombination (c) and extraction (d) dynamics. (e) Carrier extraction probabilities (color symbols) "in dark" and under 1 sun illumination and sun-carrier density (black symbols) as a function of effective voltage.

It should be noted that at 1 sun illumination conditions, the extraction probabilities for laser carriers and sun carriers are approximately equal because recombination between two laser carriers is insignificant at low laser-carrier concentrations.

An analogous analysis of the carrier dynamics on a microsecond time scale was performed on an effective (PCE = 13.2%) nonfullerene acceptor (NFA) device PBDB-T:Y1 (Figure 4a–e). Photocurrent decay in the NFA sample was faster than in the present TQ1:PC$_{71}$BM blend. For instance, at 0.8 V voltage and 1 μs after excitation, only 3% of the initial photocurrent value was present in the PBDB-T:Y1 device (Figure 4b inset), compared to 30% in the TQ1:PC$_{71}$BM sample with increased carrier trapping. This signifies that either carrier recombination or extraction, or both, is much faster in the PBDB-T:Y1 device. Second, there was no rapid photocurrent decay "in dark" at low voltages that was clearly expressed in TQ1:PC$_{71}$BM and that we attributed to carrier trapping. It shows that carrier trapping in PBDB-T:Y1 is not a dominant factor determining photocurrent decay on a submicrosecond time scale. Third, differences between photocurrent kinetics "in dark" and under 1 sun light are insignificant at all applied voltages. It shows that the sun-carrier concentration is minute at any voltage, again suggesting the relative scarcity of low-energy states or their shallow depth in this device.

Furthermore, TDCF measurements show that carrier density and mobility kinetics are only weakly affected by 1 sun illumination (Figure 4b,c) and depend only on the effective voltage. This shows that low-energy state occupation by sun carriers does not affect the drift of laser carriers. Also, in these devices, the carrier mobility decreases with effective voltage but to a lesser extent than in the TQ1:PC$_{71}$BM blend. This further illustrates the fact that carrier mobility is not a perfect parameter to characterize carrier motion in organic solar cells. In these experiments, the effective carrier mobility decreases with voltage because highly mobile charge carriers are extracted from the sample, leaving low-mobility carriers relaxed to deep tail states within the DOS. The fraction of extracted highly mobile carriers increases with time and effective voltage. At high effective voltages, highly mobile carriers are extracted faster than the time resolution of our TDCF measurements; thus, already at 100 ns, our technique probes a reduced carrier mobility. The data obtained at low U_{Eff} are less affected by this effect and represent the behavior of the dominating fraction of carriers more correctly. Nevertheless, even at low effective voltages of 0.1 and 0.35 V, that is, close to MPP of the solar cell, the carrier mobility still decreases by about 30–50% in the sub-μs time scale both "in dark" and at 1 sun illumination. This minor but significant decrease is consistent with the concept of a nearly constant mobility for this time range. Note, however, that significant (dispersive) extraction can take place at shorter time scales as further discussed below.[28,29]

Computational modeling shows that at close to MPP voltages, the sun-carrier concentration in the PBDB-T:Y1 device is indeed lower by one order of magnitude than in the here investigated TQ1:PC$_{71}$BM device. Even though TDCF measurements at U_{Eff} = 0 V gives a bimolecular recombination rate of $\gamma = 2.2 \times 10^{-10}$ cm^3 s^{-1} for the PBDB-T:Y1 sample, which is significantly higher than that of the TQ1:PC$_{71}$BM device, the lower carrier concentration still leads to a weak enhancement of nongeminate recombination in the presence of sun carriers (Figure 4d). Even at the lowest effective voltage

of 0.1 V, when carrier extraction is relatively slow, nongeminate recombination losses increase no more than 10% in the presence of 1 sun illumination. Moreover, a few times higher mobility values compared to the TQ1:PC$_{71}$BM device leads to much faster and more effective carrier extraction, as shown in Figure 4e.

Ultrafast TREFISH investigations were not possible for this device because of the significantly lower second harmonic generation efficiency in the nonfullerene blend. However, previous investigations performed using an alternative ultrafast time-resolved electroabsorption technique revealed mobility decrease "in dark" by more than an order of magnitude during the initial couple of nanoseconds.[17] Taking into account that mobility on this ultrafast time scale was independent of the 1 sun illumination even in the TQ1:PC$_{71}$BM blend, where the influence of illumination on the microsecond mobility was much stronger, we do not expect any significant illumination influence on the ultrafast mobility in the PBDB-T:Y1 blend as well. Consequently, these data allow us to conclude that the carrier mobility in the PBDB-T:Y1 solar cell under real operation conditions is strongly time-dependent on the ps−ns time scale.

Investigations of the TQ1:PC$_{71}$BM and PBDB-T:Y1 blends have shown that precise measurements of TPC kinetics at a low laser intensity performed "in dark" and under 1 sun illumination are sufficient to estimate the role of a low-energy state population in the carrier extraction.

To determine the role of blend morphology in the formation and properties of low-energy states, we also performed TPC measurements on three different devices using the efficient donor polymer PCE10 and the PC$_{71}$BM acceptor mixed at different D/A weight ratios of 1:0.5, 1:1.5, and 1:3 (further referred to as samples 0.5, 1.5, and 3.0, respectively). As shown in the table presented in Figure S1, the optimal concentration was 1:1.5, which resulted in a PCE of 6.5% and the highest values of other photovoltaic parameters.

The carrier motion dynamics in fullerene-based solar cells was found to be strongly dependent on the stoichiometric ratio of donor and acceptor materials.[36] The slow carrier extraction component at $t > 1$ μs clearly decreases at higher PC$_{71}$BM concentrations and therefore can be attributed to the electron extraction via PC$_{71}$BM domains, which may lose percolation pathways at low PC$_{71}$BM concentrations, causing the formation of dead ends in the electron transfer pathways.[7] The current TPC investigation results (Figure 5a–c) agree with this conception. At a low PC$_{71}$BM concentration (sample 0.5), the TPC kinetics is qualitatively similar to that obtained for the TQ1:PC$_{71}$BM sample, indicating the increased density of low-energy states, which are occupied under 1 sun illumination. However, TPC kinetics in samples 1.5 and 3.0 shows almost no influence of the 1 sun illumination, similar to the PBDB-T:Y1 blend, suggesting that carrier trapping and occupation of low-energy states by 1 sun illumination are marginal. Considering that chemical structures and fabrication procedures of all PCE10:PC$_{71}$BM samples were identical, the more expressed influence of low-energy states on the sample with a low PC$_{71}$BM concentration suggests that especially dead ends in the electron pathways create additional traps, causing a significant decrease in the electron extraction rate. Note that we cannot exclude that the low-energy states in the investigated TQ1:PCBM blend are also to some degree geometrical in nature although geometrical trapping is
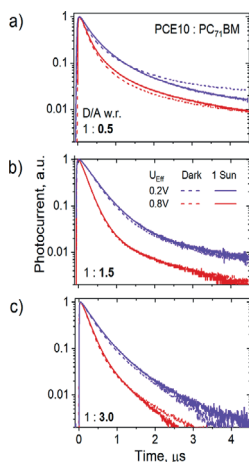
Figure 5. TPC kinetics at 0.2 (red curves) and 0.8 V (purple curves) effective voltages "in dark" (dotted lines) and under 1 sun light (solid lines) conditions for PCE10:PC$_{71}$BM samples (a) 0.5, (b) 1.5, and (c) 3.0.

normally weak in this system due to the presence of a significant fraction of fullerene in the donor-rich phase.[10,39]

CONCLUSIONS

In conclusion, we have addressed the role of population of low-energy states in carrier dynamics in organic solar cells operating under quasi-real conditions. We applied several transient methods to cover a wide temporal window from picoseconds to microseconds and analyzed the influence of solar illumination on carrier mobility, extraction, and recombination. Carrier trapping strongly influences the carrier mobility on a ns−µs time scale in TQ1:PC$_{71}$BM devices possessing deep low-energy states, but steady-state solar illumination causes occupation of these states, making the carrier mobility less time-dependent. At low electric fields, close to the MPP conditions, the low-energy state filling increases both recombination and extraction rates and reduces the extraction efficiency. However, the low-energy state population becomes less significant and weakly affects carrier dynamics when the internal electric field is sufficiently strong, which happens close to short-circuit conditions. On the other hand, low-energy state filling does not affect the strongly decreasing mobility on a ps-time scale.

Carrier trapping plays a less significant role in more effective solar cells. Carrier mobility in a nonfullerene PBDB-T:Y1 solar cell is weakly time-dependent on a ns−µs time scale and low-energy state filling by solar illumination plays only a marginal role, even at low, close to MPP effective voltages. Carrier trapping in PCE10:PC$_{71}$BM solar cells with different donor/acceptor stoichiometric ratios was found to be more significant at low PCBM concentrations, when poor PCBM domain percolation caused the formation of geometrical electron traps.

The investigation results also show that carrier mobility is strongly time-dependent on a ps−ns time scale during carrier relaxation within high-energy states of DOS in all investigated organic solar cells, independently of the occupation of low-

energy states by solar illumination, while at longer times, the occupation of low-energy states significantly changes the charge carrier mobility and recombination rate in cells with increased carrier trapping, but its influence was found to be only marginal in efficient solar cells.

ASSOCIATED CONTENT

ⓢ Supporting Information

The Supporting Information is available free of charge at https://pubs.acs.org/doi/10.1021/acs.jpcc.1c04245.

Materials, device fabrication, photovoltaic characteristics, measurements schemes, and model fits (PDF)

AUTHOR INFORMATION

Corresponding Author

    Rokas Jasiūnas − *Center for Physical Sciences and Technology, Vilnius 10257, Lithuania;* ⓞ orcid.org/0000-0002-0259-408X; Email: rokas.jasiunas@ftmc.lt

Authors

    Vidmantas Jašinskas − *Center for Physical Sciences and Technology, Vilnius 10257, Lithuania;* ⓞ orcid.org/0000-0001-5982-8214

    Huotian Zhang − *Department of Physics Chemistry and Biology (IFM), Linköping University, Linköping SE-58183, Sweden*

    Tanvi Upreti − *Department of Physics Chemistry and Biology (IFM), Linköping University, Linköping SE-58183, Sweden; Centre for Advanced Materials, Ruprecht-Karls-Universität Heidelberg, D-69120 Heidelberg, Germany*

    Feng Gao − *Department of Physics Chemistry and Biology (IFM), Linköping University, Linköping SE-58183, Sweden;* ⓞ orcid.org/0000-0002-2582-1740

    Martijn Kemerink − *Department of Physics Chemistry and Biology (IFM), Linköping University, Linköping SE-58183, Sweden; Centre for Advanced Materials, Ruprecht-Karls-Universität Heidelberg, D-69120 Heidelberg, Germany;* ⓞ orcid.org/0000-0002-7104-7127

    Vidmantas Gulbinas − *Center for Physical Sciences and Technology, Vilnius 10257, Lithuania*

Complete contact information is available at:
https://pubs.acs.org/10.1021/acs.jpcc.1c04245

Notes

The authors declare no competing financial interest.

ACKNOWLEDGMENTS

REFERENCES

(1) Inganäs, O. Organic Photovoltaics over Three Decades. *Adv. Mater.* **2018**, *30*, No. 1800388.

(2) Zhu, L.; Zhang, M.; Zhou, G.; Hao, T.; Xu, J.; Wang, J.; Qiu, C.; Prine, N.; Ali, J.; Feng, W.; et al. Efficient Organic Solar Cell with 16.88% Efficiency Enabled by Refined Acceptor Crystallization and Morphology with Improved Charge Transfer and Transport Properties. *Adv. Energy Mater.* **2020**, *10*, No. 1904234.

(3) Cui, Y.; Yao, H.; Zhang, J.; Zhang, T.; Wang, Y.; Hong, L.; Xian, K.; Xu, B.; Zhang, S.; Peng, J.; et al. Over 16% Efficiency Organic

Photovoltaic Cells Enabled by a Chlorinated Acceptor with Increased Open-Circuit Voltages. *Nat. Commun.* **2019**, *10*, 2515.

(4) Mandoc, M. M.; Kooistra, F. B.; Hummelen, J. C.; de Boer, B.; Blom, P. W. M. Effect of Traps on the Performance of Bulk Heterojunction Organic Solar Cells. *Appl. Phys. Lett.* **2007**, *91*, 263505.

(5) Venkateshvaran, D.; Nikolka, M.; Sadhanala, A.; Lemaur, V.; Zelazny, M.; Kepa, M.; Hurhangee, M.; Kronemeijer, A. J.; Pecunia, V.; Nasrallah, I; et al. Approaching Disorder-Free Transport in High-Mobility Conjugated Polymers. *Nature* **2014**, *515*, 384–388.

(6) Wu, J.; Lee, J.; Chin, Y.-C.; Yao, H.; Cha, H.; Luke, J.; Hou, J.; Kim, J.-S.; Durrant, J. R. Exceptionally Low Charge Trapping Enables Highly Efficient Organic Bulk Heterojunction Solar Cells. *Energy Environ. Sci.* **2020**, *13*, 2422–2430.

(7) Melianas, A.; Etzold, F.; Savenije, T. J.; Laquai, F.; Inganäs, O.; Kemerink, M. Photo-Generated Carriers Lose Energy during Extraction from Polymer-Fullerene Solar Cells. *Nat. Commun.* **2015**, *6*, 8778.

(8) Wu, J.; Luke, J.; Lee, H. K. H.; Shakya Tuladhar, P.; Cha, H.; Jang, S.-Y.; Tsoi, W. C.; Heeney, M.; Kang, H.; Lee, K.; et al. Tail State Limited Photocurrent Collection of Thick Photoactive Layers in Organic Solar Cells. *Nat. Commun.* **2019**, *10*, 5159.

(9) Fischer, J.; Ray, D.; Kleemann, H.; Pahner, P.; Schwarze, M.; Koerner, C.; Vandewal, K.; Leo, K. Density of States Determination in Organic Donor-Acceptor Blend Layers Enabled by Molecular Doping. *J. Appl. Phys.* **2015**, *117*, 245501.

(10) Jasiūnas, R.; Melianas, A.; Xia, Y.; Felekidis, N.; Gulbinas, V.; Kemerink, M. Dead Ends Limit Charge Carrier Extraction from All-Polymer Bulk Heterojunction Solar Cells. *Adv. Electron. Mater.* **2018**, *4*, No. 1800144.

(11) Cha, H.; Wu, J.; Wadsworth, A.; Nagitta, J.; Limbu, S.; Pont, S.; Li, Z.; Searle, J.; Wyatt, M. F.; Baran, D.; et al. An Efficient, "Burn in" Free Organic Solar Cell Employing a Nonfullerene Electron Acceptor. *Adv. Mater.* **2017**, *29*, No. 1701156.

(12) Moses, D.; Sinclair, M.; Heeger, A. J. Carrier Photogeneration and Mobility in Polydiacetylene: Fast Transient Photoconductivity. *Phys. Rev. Lett.* **1987**, *58*, 2710–2713.

(13) Bässler, H. Charge Transport in Disordered Organic Photoconductors a Monte Carlo Simulation Study. *Phys. Status Solidi B* **1993**, *175*, 15–56.

(14) Devižis, A.; Meerholz, K.; Hertel, D.; Gulbinas, V. Hierarchical Charge Carrier Motion in Conjugated Polymers. *Chem. Phys. Lett.* **2010**, *5*.

(15) Devizis, A.; Meerholz, K.; Hertel, D.; Gulbinas, V. Ultrafast Charge Carrier Mobility Dynamics in Poly(Spirobifluorene-co-Benzothiadiazole): Influence of Temperature on Initial Transport. *Phys. Rev. B* **2010**, *82*, No. 155204.

(16) Devižis, A.; Serbenta, A.; Meerholz, K.; Hertel, D.; Gulbinas, V. Ultrafast Dynamics of Carrier Mobility in a Conjugated Polymer Probed at Molecular and Microscopic Length Scales. *Phys. Rev. Lett.* **2009**, *103*, No. 027404.

(17) Jasiunas, R; Zhang, H.; Yuan, J.; Zhou, X.; Qian, D.; Zou, Y.; Devižis, A.; Sulskus, J.; Gao, F.; Gulbinas, V. From Generation to Extraction: A Time-Resolved Investigation of Photophysical Processes in Non-Fullerene Organic Solar Cells. *J. Phys. Chem. C* **2020**, *124*, 21283–21292.

(18) Melianas, A; Pranculis, V.; Devižis, A.; Gulbinas, V.; Inganäs, O.; Kemerink, M. Dispersion-Dominated Photocurrent in Polymer:-Fullerene Solar Cells. *Adv. Funct. Mater.* **2014**, *24*, 4507–4514.

(19) Abramavičius, V.; Amarasinghe Vithanage, D.; Devižis, A.; Infahsaeng, Y.; Bruno, A.; Foster, S.; Keivanidis, P. E.; Abramavičius, D.; Nelson, J.; Yartsev, A.; et al. Carrier Motion in As-Spun and Annealed P3HT:PCBM Blends Revealed by Ultrafast Optical Electric Field Probing and Monte Carlo Simulations. *Phys. Chem. Chem. Phys.* **2014**, *16*, 2686.

(20) Augulis, R.; Devižis, A.; Peckus, D.; Gulbinas, V.; Hertel, D.; Meerholz, K. High Electron Mobility and Its Role in Charge Carrier Generation in Merocyanine/Fullerene Blends. *J. Phys. Chem. C* **2015**, *119*, 5761–5770.

(21) Cunningham, P. D.; Hayden, L. M. Carrier Dynamics Resulting from Above and Below Gap Excitation of P3HT and P3HT/PCBM Investigated by Optical-Pump Terahertz-Probe Spectroscopy. *J. Phys. Chem. C* **2008**, *112*, 7928–7935.

(22) Ai, X.; Beard, M. C.; Knutsen, K. P.; Shaheen, S. E.; Rumbles, G.; Ellingson, R. J. Photoinduced Charge Carrier Generation in a Poly(3-Hexylthiophene) and Methanofullerene Bulk Heterojunction Investigated by Time-Resolved Terahertz Spectroscopy. *J. Phys. Chem. B* **2006**, *110*, 25462–25471.

(23) Ponseca, C. S.; Yartsev, A.; Wang, E.; Andersson, M. R.; Vithanage, D.; Sundström, V. Ultrafast Terahertz Photoconductivity of Bulk Heterojunction Materials Reveals High Carrier Mobility up to Nanosecond Time Scale. *J. Am. Chem. Soc.* **2012**, *134*, 11836–11839.

(24) Mihailetchi, V. D.; Xie, H. X.; de Boer, B.; Koster, L. J. A.; Blom, P. W. M. Charge Transport and Photocurrent Generation in Poly(3-Hexylthiophene): Methanofullerene Bulk-Heterojunction Solar Cells. *Adv. Funct. Mater.* **2006**, *16*, 699–708.

(25) Bartelt, J. A.; Lam, D.; Burke, T. M.; Sweetnam, S. M.; McGehee, M. D. Charge-Carrier Mobility Requirements for Bulk Heterojunction Solar Cells with High Fill Factor and External Quantum Efficiency >90%. *Adv. Energy Mater.* **2015**, *5*, No. 1500577.

(26) Bartesaghi, D.; del Carmen Pérez, I; Kniepert, J.; Roland, S.; Turbiez, M.; Neher, D.; Koster, L. J. A. Competition between Recombination and Extraction of Free Charges Determines the Fill Factor of Organic Solar Cells. *Nat. Commun.* **2015**, *6*, 7083.

(27) Proctor, C. M.; Love, J. A.; Nguyen, T.-Q. Mobility Guidelines for High Fill Factor Solution-Processed Small Molecule Solar Cells. *Adv. Mater.* **2014**, *26*, 5957–5961.

(28) Le Corre, V. M.; Chatri, A. R.; Doumon, N. Y.; Koster, L. J. A. Charge Carrier Extraction in Organic Solar Cells Governed by Steady-State Mobilities. *Adv. Energy Mater.* **2017**, *7*, No. 1701134.

(29) Felekidis, N.; Melianas, A.; Aguirre, L. E.; Kemerink, M. Comment on "Charge Carrier Extraction in Organic Solar Cells Governed by Steady-State Mobilities.". *Adv. Energy Mater.* **2018**, *8*, No. 1800419.

(30) Karuthedath, S.; Gorenflot, J.; Melianas, A.; Kan, Z.; Kemerink, M.; Laquai, F. Buildup of Triplet-State Population in Operating TQ1:PC$_{71}$BM Devices Does Not Limit Their Performance. *J. Phys. Chem. Lett.* **2020**, *11*, 2838–2845.

(31) Andersson, L. M.; Melianas, A.; Infahasaeng, Y.; Tang, Z.; Yartsev, A.; Inganäs, O.; Sundström, V. Unified Study of Recombination in Polymer:Fullerene Solar Cells Using Transient Absorption and Charge-Extraction Measurements. *J. Phys. Chem. Lett.* **2013**, *4*, 2069–2072.

(32) Roland, S.; Kniepert, J.; Love, J. A.; Negi, V.; Liu, F.; Bobbert, P.; Melianas, A.; Kemerink, M.; Hofacker, A.; Neher, D. Equilibrated Charge Carrier Populations Govern Steady-State Nongeminate Recombination in Disordered Organic Solar Cells. *J. Phys. Chem. Lett.* **2019**, *10*, 1374–1381.

(33) Li, S.; Li C.-Z.; Shi, M.; Chen, H. New Phase for Organic Solar Cell Research: Emergence of Y-Series Electron Acceptors and Their Perspectives. *ACS Energy Lett.* **2020**, *5*, 1554–1567.

(34) Gulbinas, V. Charge Carrier Mobility Dynamics in Organic Semiconductors and Solar Cells. *Lith. J. Phys.* **2020**, *60*, 1.

(35) Upreti, T.; Wang, Y.; Zhang, H.; Scheunemann, D.; Gao, F.; Kemerink, M. Experimentally Validated Hopping-Transport Model for Energetically Disordered Organic Semiconductors. *Phys. Rev. Appl.* **2019**, *12*, No. 064039.

(36) Pranculis, V.; Infahsaeng, Y.; Tang, Z.; Devižis, A.; Vithanage, D. A.; Ponseca, C. S.; Inganäs, O.; Yartsev, A. P.; Gulbinas, V.; Sundström, V. Charge Carrier Generation and Transport in Different Stoichiometry APFO3:PC61BM Solar Cells. *J. Am. Chem. Soc.* **2014**, *136*, 11331–11338.

(37) Perdigón-Toro, L.; Zhang, H.; Markina, A.; Yuan, J.; Hosseini, S. M.; Wolff, C. M.; Zuo, G.; Stolterfoht, M.; Zou, Y.; Gao, F.; Andrienko, D.; et al. Barrierless Free Charge Generation in the High-Performance PM6:Y6 Bulk Heterojunction Non-Fullerene Solar Cell. *Adv. Mater.* **2020**, *32*, No. 1906763.

118

(38) Kurpiers, J.; Neher, D. Dispersive Non-Geminate Recombination in an Amorphous Polymer:Fullerene Blend. *Sci. Rep.* **2016**, *6*, 26832.

(39) Wilken, S.; Upreti, T.; Melianas, A.; Dahlström, S.; Persson, G.; Olsson, E.; Österbacka, R.; Kemerink, M. Experimentally Calibrated Kinetic Monte Carlo Model Reproduces Organic Solar Cell Current−Voltage Curve. *Sol. RRL* **2020**, *4*, No. 2000029.

119

Article

From Generation to Extraction: A Time-Resolved Investigation of Photophysical Processes in Non-fullerene Organic Solar Cells

Rokas Jasiūnas, Huotian Zhang, Jun Yuan, Xuehong Zhou, Deping Qian, Yingping Zou, Andrius Devižis, Juozas Šulskus, Feng Gao, and Vidmantas Gulbinas*

Read Online

ACCESS | 📊 Metrics & More | 📖 Article Recommendations | 🆂🅸 Supporting Information

ABSTRACT: Non-fullerene organic solar cells (NFOSCs) demonstrate record efficiencies exceeding 16%. In comparison with cells with the fullerene-based acceptor, the NFOSCs benefit from a longer wavelength absorption, which leads to a small highest occupied molecular orbital (HOMO) level offset. Here, we use several advanced transient investigation techniques, covering timescale from sub-ps to μs, to address all sequence of processes starting from photoexcitation of donors or acceptors to carrier extraction in several NFOSCs and cells with phenyl-C71-butyric acid methyl ester (PCBM). Though small offsets result in higher open-circuit voltage, we show that at the same time, it limits cell performance because of inefficient hole transfer from excited acceptors to donors and enhanced geminate recombination. We demonstrate that 100 meV HOMO level offset and proper acceptor molecule structures are sufficient for efficient hole transfer (>70%) and for reduction of the geminate recombination losses down to about 20%. Subsequent extraction of unbound charge carriers in all NFOSCs is slightly faster than in cells with PCBM, while non-geminate carrier recombination causing additional losses is slightly slower in the best performing NFOSCs than in cells with PCBM.
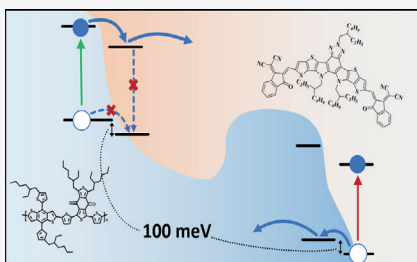
1. INTRODUCTION

Organic photovoltaics (OPVs) have been persistently developing for over three decades as one of the alternative solar energy-harvesting technologies.[1] Advantages of being lightweight, flexible, transparent, and low-cost stimulated the research in materials design, morphology optimization, device engineering, and mechanism study to increase solar-to-electrical power conversion efficiency (PCE).[2−4] Even though it has risen remarkably since their appearance, and now record values exceed 16%[5] for single-junction OPV devices, yet it is still insufficient to compete with state-of-the-art silicon or perovskite photovoltaic technology. During the last few years, a rapid PCE increase was achieved by employing small low-band gap molecules as an alternative to well-established fullerene type acceptors. There are few advantages of non-fullerene (NF) molecules over fullerene-based acceptors, including complimentary absorption with respect to the solar spectrum, which results in higher short-circuit current (J_{SC}) and tunability of energy levels that allow gaining open-circuit voltage (V_{OC}). The superior photovoltaic performance of NF OSCs is believed to originate not only from the prominent electronic and optical characteristics of NF molecules but also from the favorable morphology and superior charge dynamics in blends, the latter of which is, however, still obscure and requires better in-depth understanding.[6]

One of the drawbacks of fullerene-based OSCs is the inevitable energy loss originating from high exciton binding energy of a donor—typically within 0.25−0.7 eV.[7,8] It requires a large energy offset of the lowest unoccupied molecular orbital (LUMO) levels between the donor (D) and acceptor (A) molecules to be overcome. On the other hand, owing to low-energy photon absorption of an acceptor, there are two possible charge transfer channels in NF-based systems: the so-called channel I, when an electron is transferred from excited D to A, and channel II, when a hole is transferred from A to D via highest occupied molecular orbital (HOMO) energy levels. Interestingly, multiple reports show that NF-based systems with an energy offset less than the exciton binding energy (∼0.3 eV) can still function well, producing high PCEs exceeding 10%.[9−12] Therefore, the charge transfer dynamics, especially the mechanism of channel II, is currently being re-evaluated by the OPV community. However, despite the wide range of reported polymer donors and NF acceptors, a
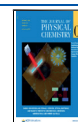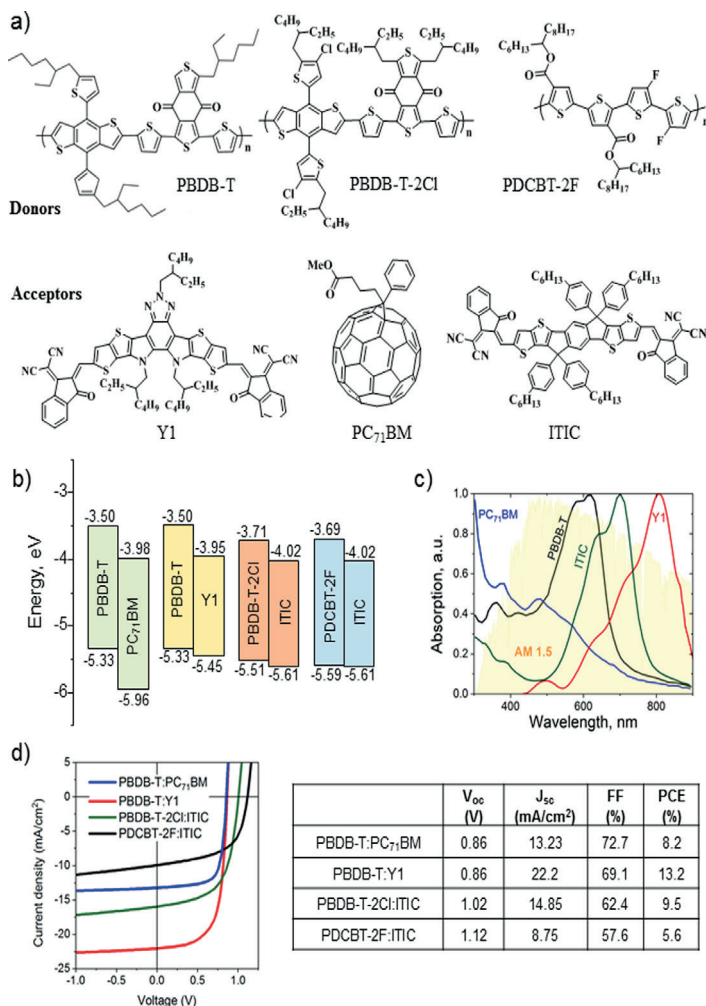
Figure 1. Chemical structure (a) and energy levels (b) of used materials. (c) Absorption of acceptors and AM1.5 solar irradiation spectra. (d) Current−voltage characteristics and photovoltaic parameters table.

comprehensive study of the interplay between polymer donors and NF acceptors is still lacking.

In this study, we employ several time-resolved electro-optical measurement techniques covering exceptionally wide time ranges (from sub-ps up to μs) to investigate the whole life cycle of photogenerated charge carriers, from their generation to extraction. We thoroughly study carrier mobility kinetics and disentangle geminate and nongeminate recombination processes in different bulk heterojunction (BHJ) systems. We comparatively investigated OPV systems comprising the well-established poly[(2,6-(4,8-bis(5-(2-ethylhexyl)thiophen-2-yl)-benzo[1,2-b:4,5-b0]dithiophene))-alt-(5,5-(10,30-di-2-thienyl-50,70-bis(2-ethylhexyl)benzo[10,20-c:40,50-c0]dithiophene-

4,8-dione))] (PBDB-T) blended with either previously reported[13] electron-deficient-core-based (DAD) NF acceptor Y1 or archetypal PC71BM acceptor. Additionally, BHJ systems based on benchmark NF acceptor (ITIC) with PBDB-T-2Cl and PDCBT-2F donor materials specifically chosen to have small HOMO level offsets were investigated.

2. RESULTS AND DISCUSSION

2.1. Materials and Solar Cell Performance. The main criterion by which materials were chosen for this work was a small difference in HOMO energy levels. Second, we have tried to include different donors and acceptors, which are typical, accessible, and with obvious performance difference.

ITIC and Y1 were chosen because they are among the most representative NF acceptor materials. ITIC is a groundbreaking material in OPVs, marking the era of the NF acceptor material. It has an electron-rich central unit with non-conjugated side groups and electron-deficient end-capping units, which shows intramolecular electron push-pulling effects. Y1 belongs to the currently most popular Y series NF acceptors, which have a similar ADA′DA structure, exhibiting higher performance than ITIC. PBDB-T and its derivatives are widely used as polymer donors to pair with high-performance NF acceptors. Here, PBDB-T and PBDB-T-2Cl were chosen to make the HOMO offsets of PBDB-T:Y1 and PBDB-T-2Cl:ITIC close. PDCBT-2F was selected as a reference donor polymer because of its structure difference and accessibility. Fullerene derivatives were believed to be a critical component for the efficient operation of organic solar cells. Unique to fullerene derivatives is their ball-like fully conjugated structure, which provides strong electron-accepting and isotropic electron-transport capabilities and facilitates electron delocalization at the D:A interfaces. Moreover, fullerene devices have been widely studied and can be used as reference easily. Thus, it is valuable to have phenyl-C71-butyric acid methyl ester (PCBM) as a comparison.

OPV cells were fabricated with an inverted device structure of ITO/ZnO/active layer/MoO$_3$/Ag. Figure 1 shows the current density versus voltage ($J-V$) characteristics under the illumination of AM 1.5. The table in Figure 1d summarizes the photovoltaic parameters of these OPV devices based on the different active material blend. Absorption peak (Figure 1c) of Y1 at about 800 nm, compared to PCBM or even ITIC acceptor, enabled additional lower energy photon-to-electron conversion and resulted in the highest PCE of 13.2% empowered by a high short-circuit current of 22.2 mA/cm^2. Nevertheless, PBDB-T:PCBM blend showed a decent PCE value of 8.2%, distinguished by the highest fill factor (FF) among all investigated samples. Devices based on ITIC acceptors expressed lower PCE values of 9.5% in the case of PBDB-T-2Cl donor and only 5.6% with the PDCBT-2F donor. However, these devices showed larger VOC, later of which exceeding 1.1 V, due to a large donor HOMO−acceptor LUMO energy gap of ∼1.5 eV (Figure 1b), which is few hundreds of meV larger than in other investigated systems.

Before addressing dynamic processes in solar cells, we examined excited state dynamics in neat films of the donor (PBDB-T) and acceptor (Y1) materials of the best performing solar cell. After excitation of the PBDB-T film (λ_{ex} = 515 nm), bleaching of the main absorption band and a wide induced absorption band at longer wavelengths are observed (Figure 2a), whereas the excited Y1 film (λ_{ex} = 730 nm) is distinguished by a strong ground state bleaching (GSB) in the long-wavelength range together with a notable induced absorption band at about 530 nm, as shown in Figure 2b. It is noteworthy that bleaching rapidly decays in both films with ∼50 and ∼75% of the excited molecules recovering to the ground state in less than 10 ps in PBDB-T and Y1 films accordingly (Figure 2b inset). Such rapid relaxation of a donor PBDB-T has been also reported in previous publications.[14,15]

2.2. Formation of the Interfacial CT State.
In BHJ structures, where donor and acceptor materials are mixed, light absorption causes the formation of a Frenkel exciton within one of the materials. Then stochastically diffusing, the exciton can reach a D−A interface, where electron (or hole) transfer from excited to nonexcited molecules of another material takes
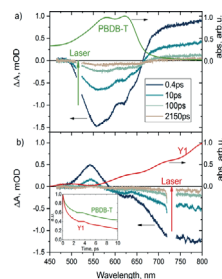

Figure 2. TA spectra at indicated delay time and steady-state absorption spectra of (a) PBDB-T and (b) Y1 neat films. Inset shows normalized TA signal decay kinetics of Y1 (535−540 nm) and PBDB-T (555−560 nm).

place. Interfacial charge-transfer (CT) exciton is formed, where despite being on separate material domains, electron and hole remain 0.5−1 nm apart bound by Coulomb binding energy. An equivalent CT state is obtained after either electron transfer from the donor to the acceptor (Channel I) or hole transfer from the acceptor to the donor (Channel II). A unique absorption spectrum distinguishes each state; thus, the CT state formation kinetics could be traced by employing transient absorption (TA) measurements. After CT state formation, the donor loses an electron and becomes ionized. Such a state in the following will be denoted as D$^+$. Analogously, after receiving additional electron, the acceptor becomes negatively charged (A$^-$). We performed TA measurements in 2 ns time window investigating the visible absorption range of all four BHJ systems. Excitation wavelengths were chosen to specifically excite either the donor or acceptor.

Now let us discuss the TA dynamics for the PBDB-T:Y1 blend under excitation at 515 and 730 nm. When the PBDB-T donor molecule is excited in the blend by 515 nm pulse, we immediately observe a very different TA spectrum from the TA spectrum of PBDB-T. Moreover, the shape of the TA spectrum does not change in time. The strongest negative band at about 630 nm is absent in both PBDB-T and Y1 TA spectra; therefore, apparently, it should be attributed to the new, CT state formed in the blend. We cannot identify any excited PBDB-T contribution to the TA spectrum, neither immediately after excitation nor anytime afterward, as it is shown in Figure 3a. This could be explained by the ultrafast electron transfer from the donor to the acceptor, which converts the S1 state of PBDB-T to the CT state faster than our time resolution of ∼200 fs. Such ultrafast transfer has been widely observed in other NF-based OPV cells[10,16−19] as well as for the PBDB-T donor with Y5, kindred polymer to Y1, and BTTPC acceptors.[20] In this case, negative TA bands at 580 and 630 nm could be attributed to the ground state absorption bleaching of the donor (PBDB-T) because of the formation of the ionized donor (D$^+$), which has no or only weak absorption in this spectral region.

On the other hand, ionized acceptor A$^-$ should be formed simultaneously with D$^+$, yet there is no bleaching whatsoever in the longer wavelength range where bleaching of A is expected. To clarify this unexpected property, we have performed quantum chemistry calculations of electronic transitions causing absorption of different Y1 electronic states. Calculation details and description of the results are presented in
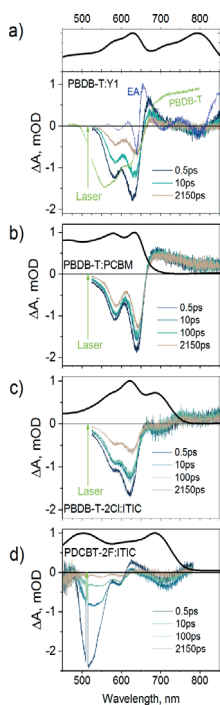
122

Figure 3. Steady-state (thick black curves) and TA spectra at indicated delay time, after excitation with 515 nm, for (a) PBDB-T:Y1; (b) PBDB-T:PCBM; (c) PBDB-T-2Cl:ITIC; and (d) PDCBT-2F:ITIC blend films. The blue curve in (a) represents the EA spectrum in PBDB-T:Y1 device, whereas the light-green curve shows TA of the neat PBDB-T film at 0.5 ps delay time.

Supporting Information. Briefly, the calculations showed that A^- should have a similar lowest energy absorption band as A, only with about twice reduced oscillator strength. Thus, apparently, a very weak TA signal of the blend in the A absorption region is caused by the compensation of the partial bleaching of A ground-state absorption by the induced absorption of created D^+ and A^- ions. Similar weak bleaching of the acceptor absorption was also observed in blends with another investigated acceptor ITIC (Figure 3c).

Another peculiar TA feature is a notable narrow induced absorption band at about 670 nm, which would be difficult to expect by combining only D^*, D^+, and A^- spectral signatures. It inevitably implies the existence of at least one more yet unidentified constituent of the TA spectrum. A similar induced absorption band has been observed in other D−A blends[21−23] and explained as follows. The created CT state has a strong dipole moment forming an electric field in its vicinity. Created electrical field shifts energy levels of neighboring molecules by the so-called Stark effect, causing a change in electronic transition energies and an associated electroabsorption (EA) signature. Indeed, under the application of −2 V steady-state voltage to the device, similar changes of the absorption spectrum are observed, that is EA spectrum (blue line, Figure 3a). The EA spectrum in the 630−700 nm region has strikingly

similar features as the TA spectrum, only shifted to the short wavelength side by about 10 nm. Despite this difference, we attribute the induced absorption band in the TA spectrum at 670 nm to EA. Some long-wavelength shift of the TA band in comparison with the EA spectrum is apparently caused by the contribution of the donor absorption bleaching. The additional difference may appear because the applied external field influences all donor polymer chains within the bulk, while the CT state, created at the D−A interface, influences those donor polymers selectively stronger, which are close to the interface. Because we observe the EA component already immediately after the sample excitation, it further supports the idea of sub-ps CT exciton formation.

Very fast CT state formation under excitation of the donor, much faster than the relaxation of the donor exciton, suggests that CT state formation strongly dominates. We also do not observe any modifications of the TA spectrum on a ps time scale, which could be attributed to the decay of the donor excited state. These observations lead to the conclusion that exciton losses are small; thus, the Frenkel-to-CT conversion rate is close to 100%. Similar TA dynamics revealing no signatures of donor excitons were also observed for PBDB-T:PCBM and PBDB-T-2Cl:ITIC blends, indicating efficient CT formation. However, in the case of PDCBT-2F:ITIC, the situation is different. The initial spectrum and those observed at 100 ps and longer times are significantly different. The initial spectrum resembles an inverted absorption spectrum of PDCBT-2F (see Figure S1 in Supporting Information); thus, it should be mainly attributed to the excitation of the donor (D^*). The dominating 520 nm band decays during hundreds of ps, and a weak spectrum with bleaching bands at about 550, 600 and 725 nm appears. A similar long-time spectrum was also obtained under excitation of the acceptor (see below). This spectrum should be assigned to the CT state, which is a common state, created at both excitation wavelengths. We attempted to decompose the TA spectra at different delays to D^* and CT components (see Figure S7 in Supporting Information). The decomposition shows that the CT component is much weaker than D^* both in the initial TA spectrum and at 2150 ps indicating that the majority of donor excitations decays to the ground state and only minor fraction is converted to CT states.

Under the excitation of the PBDB-T:Y1 blend at 730 nm when Y1 is excited, we also immediately observe bleaching of the donor absorption band. It shows that similar ultrafast CT state formation takes place, in this case by the hole transfer. However, the 530 nm-induced absorption band in the initial TA spectrum together with the weak GSB signal in the long-wavelength region also clearly signifies the A^* state. However, the GSB of the Y1 absorption band is very weak, which shows that majority of Y1 excitations are converted to the CT state already during the excitation pulse action. A^* state features disappear during several ps, and we also observe some growth of the donor bleaching signal (light blue curve, Figure 4a inset) attributed to the formation of D^+. By comparing A^* absorption decay kinetics at 530 nm in blend versus neat film (dark blue and red curves, Figure 4a inset), we see that decay is about twice faster in the blend indicating that about half of A^* remaining at 0.5 ps also form CT states. Consequently, CT state formation takes place in two steps.

We can roughly estimate the CT state formation efficiency by comparing the bleaching of donor and acceptor absorption bands. For this task, we assume that an excited state of Y1
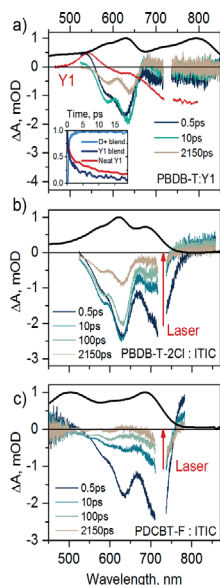
Figure 4. Steady-state (thick black curves) and TA spectra at indicated delay time after 730 nm excitation of (a) PBDB-T:Y1; (b) PBDB-T-2Cl:ITIC; and (c) PDCBT-F:ITIC blend films. Red curve in (a) shows TA spectrum of the neat Y1 film at 0.5 ps delay time. Inset in (a) shows kinetics of the ionized donor signal (573−593 nm band) in blend (light blue curve); relaxation of Y1 excited state (525−545 nm band) in blend (dark blue curve), and in neat film (red curve).

causes only bleaching of its absorption band, while the CT state, as discussed above, causes only bleaching of the donor PBDB-T absorption. We also account that extinction coefficients of Y1 and repeat units of PBDB-T are approximately equal (evaluated form their concentrations in the blend and related absorption bands intensities). Under these assumptions, the ratio of the donor and acceptor absorption bleaching intensities shows the ratio of concentrations of the CT states and Y1 excited states. Consequently, roughly 6 times stronger bleaching of PBDB-T in comparison with bleaching of Y1 in the 0.5 ps TA spectrum suggests that CT state concentration at this time is about 6 times larger than the concentration of Y1 excitations, which means that about 6/7 of Y1 excitations are already converted to CT states. Accounting additional conversion on a ps time scale, we obtain that the total conversion efficiency is of about 90% or even more. This high efficiency is in agreement with the reported about 70% EQE values for PBDB-T:Y1 solar cells obtained both in donor and acceptor absorption regions.[13]

In the case of PBDB-T-2Cl:ITIC (Figure 4b), the acceptor and donor bleaching bands in the initial spectrum are approximately proportional to their intensities in the steady-state absorption spectrum. Accounting that the extinction coefficient of ITIC is about 2 times larger, we estimate that about 66% of acceptor excitations form CT states during 0.5 ps. In this case, we do not observe the growth of the donor bleaching band when the acceptor bleaching band decays. Apparently, CT state formation from the stabilized acceptor

excited state is inefficient and the majority of excitations decay to the ground state. Thus, this rough estimation suggests that the efficiency of the CT state formation by photons absorbed by the ITIC acceptor is of about 60−70%.

In the case of PDCBT-F:ITIC (Figure 4c), the initial TA spectrum closely resembles the spectrum of ITIC, which shows that majority of excitations do not form CT states. Only at 100 ps when the excited state of ITIC almost decays, a weak band at about 600 nm reveals, which, as was discussed, should be considered as a signature of the CT state. Using the above-described estimation procedure, from the intensity of this band, we obtain that the CT state formation efficiency under excitation of the acceptor hardly exceeds 20−30%.

Taking into account small energy differences between donor and acceptor HOMO levels, this inefficient CT state formation by the hole transfer from the excited acceptor is not surprising. The hole transfer apparently takes place only from the unstabilized exciton state, and its efficiency correlates with the HOMO level offset. However, we do not see any indications of the CT state formation at longer times. Exciton stabilization (formation of excitonic polaron) apparently reduces its energy and blocks or at least strongly impedes the hole transfer.

2.3. Geminate Recombination. Once formed, the CT exciton can either overcome its binding energy and separate into free charge carriers or undergo relaxation and recombine geminately to the ground state resulting in an energy loss. Such recombination is usually observed from sub-ps to hundreds of ps time scale,[24,25] before electron−hole pair separates beyond the geminate recombination range (Langevin radius), which is about 15 nm.

In our investigation, we observe rapid, almost uniform, decrease of the total TA spectrum within a few initial ps in all investigated samples (see Figure 3) (slightly faster decay of the EA component will be discussed below). The TA kinetics represents well this decrease in the donor absorption band region, shown in Figure 5a. Within 3 ps, the bleaching signal decreases down to 82, 75, and 50% of its peak values in PBDB-T-2Cl:ITIC, PBDB-T:Y1, and PDCBT-2F:ITIC samples respectively, but the decrease is only marginal in the sample with PCBM. Any other process, then carrier recombination leading to the donor and acceptor ground states, can hardly explain the uniform decrease of the entire TA spectrum.

Carriers might recombine geminately or non-geminately. For non-geminate recombination, photogenerated carrier density should be high enough for an electron (or hole) to have a complementary charge in its vicinity to recombine. Such recombination is light fluence-dependent; thus, we have performed TA measurements at different light intensities (Figure S5). As it is shown in Figure 5c, TA signal decay is independent of excitation intensity allowing us to rule out the non-geminate recombination. In a recent study of all-polymer solar cells based on the N2200 NF acceptor, it was found that almost 50% of the charges recombine geminately, which was suggested as being the major factor hindering the device performance compared with polymer/fullerene cells.[26] Similarly, in our study, much stronger geminate recombination is indeed observed in NF samples.

In Figure 6, we present a simple model explaining the origin of the effective geminate recombination, which lasts for a few ps, in NF OPV devices. As was discussed, electron transfer from the excited donor LUMO to the acceptor LUMO level (process 2) takes place on a sub-ps timescale, whereas a hole,
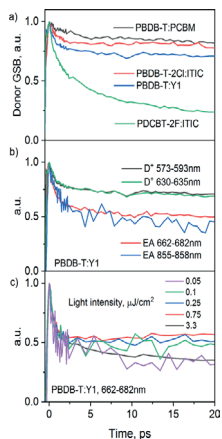
Figure 5. (a) Normalized GSB decay of a donor in TA spectra of indicated systems; (b) donor ionization induced GSB and EA signal decay kinetics in TA spectra in PBDB-T:Y1 blend film; (c) 662−682 nm band decay kinetics in PBDB-T:Y1 blend after different light excitation intensities; 0.1 $\mu J/cm^2$ intensity of 515 nm was used in all above presented results.
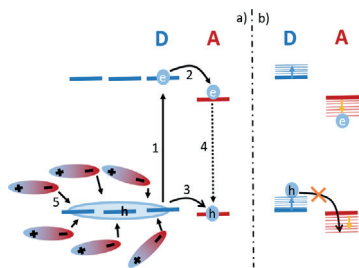

Figure 6. Schematic representation. (1)—donor excitation; (2)—CT formation; (3)—hole transfer from the donor to the acceptor; (4)—geminate recombination in the acceptor domain; (5)—environment polarization in the vicinity of the delocalized hole.

created within the donor polymer, can be transferred back to acceptor only by overcoming energetic barrier (hole energy increases when it is transferred down). If this barrier, regarded as HOMO level offset, is low, some holes may jump to the acceptor domain and regenerate its excited state. Because excited state relaxation of acceptor molecules is very fast ($\tau \sim 2$ ps), such a process leads to very fast geminate carrier recombination (process 4). Such a model is strongly supported by the correlation of the geminate recombination efficiency of different blends with their HOMO level offsets. In the case of negligible HOMO offset ($\sim$0.02 eV) in PDCBT-2F:ITIC samples, we observe >50% of carriers recombine geminately. This number decreases to $\sim$20% in the case of PBDB-T:Y1 and PBDB-T-2Cl:ITIC devices, where HOMO level offset is $\sim$0.1 eV, and drops to marginal values in the case of PBDB-T:PCBM where HOMO offset is the highest (>0.6 eV). However, such a model does not explain why the geminate recombination stops after a few ps. The straightforward

explanation could be based on the splitting of CT states into separated charges. However, as will be discussed below, this process is significantly slower. Another reason could be the stabilization of the CT state. Both donor and acceptor materials contain electrically charged donor and acceptor functional groups; therefore, strong polaron formation effects are expected (process 5). We suggest that CT state stabilization (formation of CT polaron) taking place during the several initial ps reduces electron and hole energies, as shown in Figure 6b, and blocks the hole transfer to an acceptor. This explanation is additionally supported by the stronger decay of the EA spectral component during the geminate recombination process (see Figure 5b). It suggests that the hole created in PBDB-T polymer is initially delocalized over few monomeric units. Such a delocalized state has large effective e-h separation distance, thus strong dipole moment, which causes a strong Stark shift of the donor absorption band. Formation of the CT polaron not only reduces the CT state energy but also screens electric field, in the vicinity of a delocalized hole or/and electron by the polarization of the surrounding media, and reduces the EA spectral component. This process is much weaker in the case of PBDB-T:PCBM blend (see Figure 7b); however, the large HOMO level offset in this case prevents fast geminate recombination.
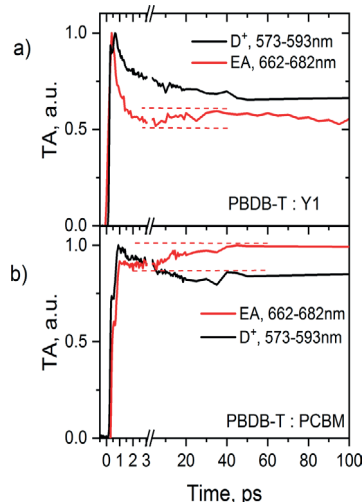

Figure 7. GSB of a donor (black curves) and EA (red curves) kinetics in (a) PBDB-T:Y1 and (b) PBDB-T:PCBM blend films after 515 nm excitation. Dotted red lines are guide-for-an-eyes.

2.4. Dissociation of the Interfacial CT Exciton. To temporally resolve the electron−hole separation process, we require a probe that is sensitive to the distance between the charges. The electric field created as the charges separate serves this purpose. Investigation of the dynamics of the EA signal has been already successfully employed to track the CT splitting kinetics.[21] In the present work, we addressed the CT splitting and subsequent charge transport by analyzing the EA signatures in conventional TA measurement together with the

investigation of the dynamics of the externally applied macroscopic electric field revealed by the optical electric field probing (OEFP) technique.[23]

Figure 7 shows the EA dynamics for PBDB-T:Y1 and PBDB-T:PCBM blends together with the GSB dynamics of donor molecules. The EA signal of PBDB-T:Y1 decays during several initial ps, when geminate recombination process is dominant. The decay of the EA signal is more pronounced. We attribute this difference to the above-discussed stabilization of the CT state slightly reducing the effective e−h separation distance and thus the electric field created by the CT state. The EA signal decay is less pronounced in PBDB-T:PCBM blend where geminate recombination is also less significant. It should be noted at this point that the observed EA dynamics is opposite than was observed in ref 21 for polymer:PCBM blend. However, there, the observed rise of the EA intensity was much faster, during tens of fs, and attributed to the electron delocalization within PCBM. Such delocalization was also confirmed theoretically.[27] The time resolution of our setup was insufficient to resolve this ED dynamics phase.

After the initial decay, the EA signal shows a weak but reproducible increase during tens of ps, in both (and also in all investigated) samples. The slow growth of the EA signal should be attributed to the electric field outspread with CT exciton splitting. Electric field energy increases during the separation of e−h pairs until the separation distance reaches the Langevin radius. Thus, the EA dynamics suggests that CT state separation takes place during ~30 ps in PBDB-T:Y1 blend and slightly longer in PBDB-T:PCBM blend. As Figure 7 shows, the bleaching of the donor absorption band continues to decrease slowly during this time. This is an additional confirmation of the made interpretation of the observed TA dynamics. We attributed this decrease to the geminate recombination. Although its rate, as was discussed, decreased during the CT state stabilization, recombination still continues with lower rates until the full separation of CT pairs.

Charge transport, obtained from OEFP data, which is described in detail below, gives additional information on the CT state splitting dynamics. Here, we just point that these investigations reveal the charge carrier drift dynamics along the applied external electric field. Figure 8a shows that the substantial drift distance of several nanometers appears on tens of ps time scale. Taking into account that both electrons and holes move to opposite directions, it converts to about 5−10 nm carrier separation along the electric field direction. Considering additional input of diffusion, which at short times might be even more substantial than that of the drift, these data are in agreement with the above-made conclusion that the Langevin carrier separation radius of about 15 nm is reached during tens of picoseconds.

The faster CT state separation rate in PBDB-T:Y1 blend than in the blend with PCBM suggests that the CT state binding energy in this NF blend is lower than in blend with fullerene. Quantum chemical calculations of the electronic states of the Y1 molecules show that the electron in the SUMO orbital (single occupied molecule orbital, which is occupied by electron transferred from the donor) is dominantly localized on two side groups separated by about 2 nm distance (see Supporting Information). Thus, electron delocalization over this large distance, apparently, significantly reduces the CT state binding energy.

2.5. Charge Transport. Now let us discuss carrier transport after the CT exciton splitting. To track the carrier
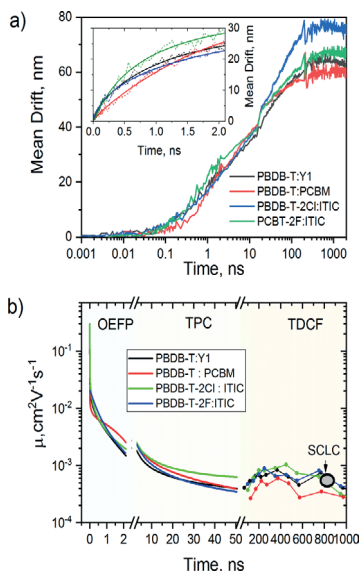

Figure 8. (a) Mean carrier drift distance kinetics in indicated systems under applied −2 V voltage. Inset shows initial kinetics (dotted lines) and fitted curves (solid lines). (b) Mobility kinetics in indicated systems obtained by OEFP, TPC, and TDCF measurement techniques. The black dot shows the mobility value obtained in PBDB-T:Y1 by the short-circuit limited current technique.

dynamics during initial 2 ns with ps time resolution, we used the time-resolved OEFP technique, when probing was performed by monitoring the EA signal.[23] The conventional transient photocurrent (TPC) technique with several ns time resolution was applied for tracking the carrier transport up to 1 μs. Briefly, the time-resolved OEFP technique is based on the optical probing of the electric field dynamics in an active layer of solar cells forming a plate capacitor, which is electrically charged by an applied external voltage prior optical excitation. Because drifting photogenerated carriers screen the electric field within the active layer, spectral EA signature, which is proportional to the square of electric field strength, allows probing the electric field strength dynamics within the sample. The electric field dynamics is directly related to the integrated TPC, which is a product of density and drift distance of charge carriers. OEFP allows achieving femtosecond time-resolution, characteristic for optical pump−probe techniques.

The TPC was also measured by the oscilloscope on much wider time-window, but with worse time-resolution than that of OEFP. The photocurrent was measured after sample excitation with a short laser pulse at specific effective voltage U_{eff} which is a sum of applied voltage U_{app} and built-in potential of a device ($U_{eff} = U_{app} + U_{built-in}$). Because carriers are generated within the entire active layer, the charge carriers (electron or hole) travel on average half the sample thickness until they are extracted from the sample. Based on such an assumption, the measured U_{eff} drop can be converted to mean carrier drift distance.

Figure 8a presents the mean carrier drift distance dynamics obtained by merging both time-resolved OEFP and TPC data

at U_{app} = −2 V applied voltage, which together with the built-in field creates ~2.3 × 10⁵ V/cm effective electric field. The obtained drift distance is averaged over all carriers; thus, electrons and holes are separated and still bound in CT states. The carrier drift distance in all investigated samples increases almost logarithmically; thus, the drift rate dramatically decreases with time. Similar strongly decreasing carrier drift rate, reflecting decreasing carrier mobility, has been observed in other polymer/fullerene blends.[28] The inset in Figure 8a shows the initial part of the drift dynamics on a linear time scale. The drift kinetics shows that the drift rate is surprisingly similar for all investigated NF blends; however, initially, it is slightly more rapid than in PCBM-based system. This is consistent with the above-stated slightly slower CT splitting in PCBM-based samples.

Following simple relation between mean carrier drift and their mobility

$$\mu = \frac{dx}{dt}\frac{1}{E_0}$$

where x means drift distance of the carrier and E_0 means electric field, we plot mobility kinetics during initial 50 ns (Figure 8b). For the mobility plot, we used fitted mean carrier drift distance curves presented in Figure S6. It is shown that the initial mobility value for the fullerene-based system is several times lower than in well-performing NF devices. Nevertheless, during initial ~100 ps, mobility drops drastically in all samples because of carrier relaxation within the density of states and becomes similar in all blends 500 ps after excitation. Because the majority of carriers are extracted within 50 ns, mobility evaluation using TPC measurements would give less accurate results at later times. Nevertheless, by performing time-delayed collection field (TDCF) measurements, which are described below, we were able to obtain mobility values at much longer times, up to 1 μs. It showed that mobility continues to decrease slowly for a few hundreds of ns, until it reaches quasi-equilibrium, which is about one-two orders of magnitude lower than its initial value. In the case of PBDB-T:Y1 sample, a very similar mobility value of ~5 × 10⁻⁴ cm²V⁻¹s⁻¹ was obtained by space charge-limited current measurements.[13] In general, we observed no substantial differences in carrier extraction dynamics between fullerene- and NF-based devices.

2.6. Non-geminate Recombination. Non-geminate recombination was investigated by the TDCF technique, which is often used for such purpose.[29,30] In TDCF measurements (Figure 9b), the sample is excited at specific pre-bias generation voltage (U_{eff}^{gen}), and then, after varying delay time, strong electric field (U_{eff}^{ext} = −1.8 V), so-called extraction field, is turned on to extract charge carriers remaining at this moment. The minus sign shows that carriers are collected in the reverse direction. If the pre-bias voltage is set to compensate for the internal electric field ($U_{app} = -U_{built-in}$, thus U_{eff}^{gen} = 0 V), then photocurrent is equal to zero and photogenerated carriers are not extracted before extraction field application. In such a case, carrier density during extraction delay time decreases only because of their recombination (red line in Figure 9b). It allows us to determine the carrier recombination rate, which, for all investigated samples, is presented in Figure 9c. These data were obtained at times much longer than the geminate recombination time; therefore, they correspond to the nongeminate recombination. They are similar as reported
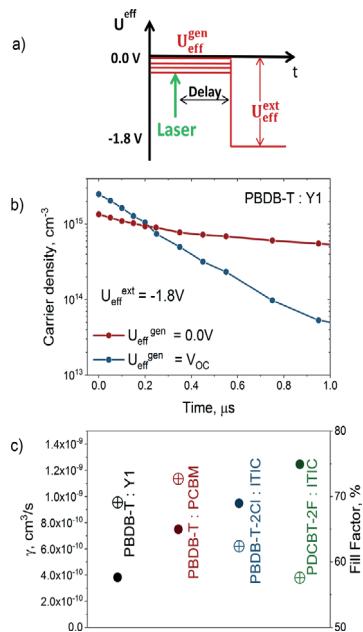

Figure 9. (a) Schematic representation of TDCF measurement; (b) extracted (with U_{eff}^{ext} = −1.8 V) charge carrier density decay kinetics after sample excitation at generation voltage U_{eff}^{gen} = 0.0 V and U_{eff}^{gen} = V_{OC} for PBDB-T:Y1 device; (c) bimolecular recombination rate and PCE values for the indicated device.

values in other organic solar cells;[31,32] however, they differ nearly three times for different samples. The slowest recombination rate was obtained for the best performing solar cell based on PBDB-T:Y1 blend; moreover, anti-correlation (Figure 9c) is established between the carrier recombination rate and device FF indicating that sufficiently strong internal field is required to rapidly extract charge carriers and compete with their recombination. However, it remains unclear how much the nongeminate recombination rate is determined by the electronic structure of materials and by their morphology.

In the case of non-zero effective pre-bias voltage during the time period between sample excitation and application of the collection field, the carrier number within the active layer decreases because of their recombination and additional extraction (blue curve, Figure 9b). Because the recombination rate was already obtained, we can evaluate how many carriers were extracted after the given delay time. The extracted carrier number is proportional to their mobility; thus, we obtain mobility values in longer timescale, which are presented in Figure 8b and were already discussed in the previous paragraph.

3. CONCLUSIONS

We have analyzed all significant processes, determining the operation of an organic solar cell, in devices with Y1, ITIC, and PCBM acceptor materials.

NF low band gap acceptors enable the collection of low-energy photons; however, conversion of absorbed photon energy to electrical current is more challenging than in the case of cells with a fullerene acceptor. It requires a subtle balance between long-wavelength absorption, open-circuit voltage, and HOMO level offset. Small offset does not guarantee efficient conversion of Frenkel excitons into interfacial CT states, particularly for photons absorbed by acceptor molecules. Efficient hole transfer from the excited acceptor to the donor takes place only from the nonrelaxed Frenkel exciton state, and its efficiency strongly depends on the HOMO level offset. In the case when the offset is close to zero, the CT state formation efficiency hardly exceeds 20–30%, while 100 meV offset in PBDB-T:Y1 device enabled to reach about 90% efficiency. Thus, depending on the structure of donor and acceptor molecules, offset of about 100 meV may be sufficient to ensure efficient carrier generation. Geminate CT state recombination mostly taking place during several initial ps creates additional loss channel. Small HOMO level offset allows hole transfer from the donor to the acceptor, consequently recreating rapidly relaxing donor excited states. The geminate recombination causes ~20% loss, in the case of about 100 meV HOMO level offset, and ~50% when the offset is close to zero. Therefore, we conclude that the HOMO level offset should be 100 meV or more. Otherwise, significant losses via inefficient CT state formation and hole transfer to the acceptor would outbalance minor gain in VOC.

Comparing other processes, we found that CT state separation into independent charge carriers was slightly faster in all investigated NF solar cells than in cells with fullerene acceptors, probably due to the electron delocalization within large acceptor molecules. Mobility and extraction dynamics of separated charge carriers were very similar for all investigated cells, including that with fullerene acceptors. Values of bimolecular recombination rates were determined for the investigated devices, and they anticorrelate with the cell FF, which indicates that the nongeminate recombination is also an important loss channel in real operation conditions..

■ ASSOCIATED CONTENT

ⓈⒾ Supporting Information

The Supporting Information is available free of charge at https://pubs.acs.org/doi/10.1021/acs.jpcc.0c05263.

Materials and devices, experimental section, and supporting characterization data (PDF)

■ AUTHOR INFORMATION

Corresponding Author

Vidmantas Gulbinas − *Center for Physical Sciences and Technology, Vilnius 10257, Lithuania; Institute of Chemical Physics, Faculty of Physics, Vilnius University, Vilnius 10222, Lithuania;* Email: vidmantas.gulbinas@ftmc.lt

Authors

Rokas Jasiūnas − *Center for Physical Sciences and Technology, Vilnius 10257, Lithuania;* ⓘ orcid.org/0000-0002-2259-408X

Huotian Zhang − *Department of Physics Chemistry and Biology (IFM), Linköping University, Linköping SE-58183, Sweden*

Jun Yuan − *Department of Physics Chemistry and Biology (IFM), Linköping University, Linköping SE-58183, Sweden;*

College of Chemistry and Chemical Engineering, Central South University, Changsha 410083, P.R. China

Xuehong Zhou − *Department of Physics Chemistry and Biology (IFM), Linköping University, Linköping SE-58183, Sweden*

Deping Qian − *Department of Physics Chemistry and Biology (IFM), Linköping University, Linköping SE-58183, Sweden*

Yingping Zou − *College of Chemistry and Chemical Engineering, Central South University, Changsha 410083, P.R. China;* ⓘ orcid.org/0000-0003-1901-7243

Andrius Devižis − *Center for Physical Sciences and Technology, Vilnius 10257, Lithuania*

Juozas Šulskus − *Institute of Chemical Physics, Faculty of Physics, Vilnius University, Vilnius 10222, Lithuania*

Feng Gao − *Department of Physics Chemistry and Biology (IFM), Linköping University, Linköping SE-58183, Sweden;* ⓘ orcid.org/0000-0002-2582-1740

Complete contact information is available at:
https://pubs.acs.org/10.1021/acs.jpcc.0c05263

Notes

The authors declare no competing financial interest.

■ REFERENCES

(1) Inganäs, O. Organic Photovoltaics over Three Decades. *Adv. Mater.* **2018**, *30*, 1800388.

(2) Li, G.; Zhu, R.; Yang, Y. Polymer Solar Cells. *Nat. Photonics* **2012**, *6*, 153–161.

(3) Heeger, A. J. 25th Anniversary Article: Bulk Heterojunction Solar Cells: Understanding the Mechanism of Operation. *Adv. Mater.* **2014**, *26*, 10–28.

(4) Graetzel, M.; Janssen, R. A. J.; Mitzi, D. B.; Sargent, E. H. Materials Interface Engineering for Solution-Processed Photovoltaics. *Nature* **2012**, *488*, 304–312.

(5) Fan, B.; Zhang, D.; Li, M.; Zhong, W.; Zeng, Z.; Ying, L.; Huang, F.; Cao, Y. Achieving over 16% Efficiency for Single-Junction Organic Solar Cells. *Sci. China: Chem.* **2019**, *62*, 746–752.

(6) Hou, J.; Inganäs, O.; Friend, R. H.; Gao, F. Organic Solar Cells Based on Non-Fullerene Acceptors. *Nat. Mater.* **2018**, *17*, 119–128.

(7) Deibel, C.; Mack, D.; Gorenflot, J.; Schöll, A; Krause, S.; Reinert, F.; Rauh, D.; Dyakonov, V. Energetics of Excited States in the Conjugated Polymer Poly(3-Hexylthiophene). *Phys. Rev. B: Condens. Matter Mater. Phys.* **2010**, *81*, 085202.

(8) Richter, T. V.; Braun, C. H.; Link, S.; Scheuble, M.; Crossland, E. J. W.; Stelzl, F.; Würfel, U.; Ludwigs, S. Regioregular Polythiophenes with Alkylthiophene Side Chains. *Macromolecules* **2012**, *45*, 5782–5788.

(9) Zhao, W.; Qian, D.; Zhang, S.; Li, S.; Inganäs, O.; Gao, F.; Hou, J. Fullerene-Free Polymer Solar Cells with over 11% Efficiency and Excellent Thermal Stability. *Adv. Mater.* **2016**, *28*, 4734–9.

(10) Liu, J.; Chen, S.; Qian, D.; Gautam, B.; Yang, G.; Zhao, J.; Bergqvist, J.; Zhang, F.; Ma, W.; Ade, H.; et al. Fast Charge Separation in a Non-Fullerene Organic Solar Cell with a Small Driving Force. *Nat. Energy* **2016**, *1* ( ). DOI: DOI: 10.1038/nenergy.2016.89.

(11) Cheng, P.; Zhang, M.; Lau, T.-K.; Wu, Y.; Jia, B.; Wang, J.; Yan, C.; Qin, M.; Lu, X.; Zhan, X. Realizing Small Energy Loss of 0.55 EV, High Open-Circuit Voltage >1 V and High Efficiency >10% in Fullerene-Free Polymer Solar Cells via Energy Driver. *Adv. Mater.* **2017**, *29*, 1605216.

(12) Baran, D.; Kirchartz, T.; Wheeler, S.; Dimitrov, S.; Abdelsamie, M.; Gorman, J.; Ashraf, R. S.; Holliday, S.; Wadsworth, A.; Gasparini, N.; et al. Reduced Voltage Losses Yield 10% Efficient Fullerene Free Organic Solar Cells with >1 V Open Circuit Voltages. *Energy Environ. Sci.* **2016**, *9*, 3783–3793.

(13) Yuan, J.; Huang, T.; Cheng, P.; Zou, Y.; Zhang, H.; Yang, J. L.; Chang, S.-Y.; Zhang, Z.; Huang, W.; et al. Enabling Low Voltage

Losses and High Photocurrent in Fullerene-Free Organic Photovoltaics. *Nat. Commun.* **2019**, *10*, 570.

(14) Kan, B.; Zhang, J.; Liu, F.; Wan, X.; Li, C.; Ke, X.; Wang, Y.; Feng, H.; Zhang, Y.; Long, G.; et al. Fine-Tuning the Energy Levels of a Nonfullerene Small-Molecule Acceptor to Achieve a High Short-Circuit Current and a Power Conversion Efficiency over 12% in Organic Solar Cells. *Adv. Mater.* **2018**, *30*, 1704904.

(15) Ma, X.; Mi, Y.; Zhang, F.; An, Q.; Zhang, M.; Hu, Z.; Liu, X.; Zhang, J.; Tang, W. Efficient Ternary Polymer Solar Cells with Two Well-Compatible Donors and One Ultranarrow Bandgap Nonfullerene Acceptor. *Adv. Energy Mater.* **2018**, *8*, 1702854.

(16) Younts, R.; Danilov, E.; Gundogdu, K.; Gautam, B. Charge Generation Dynamics in Polymer Nonfullerene Solar Cells with Low Energy Loss. *J. Photonics Energy* **2018**, *8*, 1.

(17) Li, X.; Liang, Z.; Wang, H.; Qiao, S.; Liu, Z.; Jiang, H.; Chen, W.; Yang, R. Fluorinated D1(0.5)−A−D2(0.5)−A Model Terpolymer: Ultrafast Charge Separation Kinetics and Electron Transfer at the Fluorinated D/A Interface for Power Conversion. *J. Mater. Chem. A* **2020**, *8*, 1360−1367.

(18) Bin, H.; Gao, L.; Zhang, ZG; Yang, Y.; Zhang, Y.; Zhang, C.; Chen, S.; Xue, L.; Yang, C.; Xiao, M.; et al. 11.4% Efficiency Non-Fullerene Polymer Solar Cells with Trialkylsilyl Substituted 2D-Conjugated Polymer as Donor. *Nat. Commun.* **2016**, *7*, 13651.

(19) Huang, B.; Chen, L.; Jin, X.; Chen, D.; An, Y.; Xie, Q.; Tan, Y.; Lei, H.; Chen, Y. Alkylsilyl Functionalized Copolymer Donor for Annealing-Free High Performance Solar Cells with over 11% Efficiency: Crystallinity Induced Small Driving Force. *Adv. Funct. Mater.* **2018**, *28*, 1800606.

(20) Qin, R.; Wang, D.; Zhou, G.; Yu, Z.-P.; Li, S.; Li, Y.; Liu, Z.-X.; Zhu, H.; Shi, M.; Lu, X.; et al. Tuning Terminal Aromatics of Electron Acceptors to Achieve High-Efficiency Organic Solar Cells. *J. Mater. Chem. A* **2019**, *7*, 27632−27639.

(21) Gélinas, S.; Rao, A.; Kumar, A.; Smith, S. L.; Chin, A. W.; Clark, J. Ultrafast Long-Range Charge Separation in Organic Semiconductor Photovoltaic Diodes. *Science* **2014**, *343*, 512.

(22) Devižis, A.; Jenatsch, S.; Diethelm, M.; Gulbinas, V.; Nüesch, F.; Hany, R. Dynamics of Charge Distribution in Sandwich-Type Light-Emitting Electrochemical Cells Probed by the Stark Effect. *ACS Photonics* **2018**, *5*, 3124−3131.

(23) Devižis, A.; De Jonghe-Risse, J.; Hany, R.; Nüesch, F.; Jenatsch, S.; Gulbinas, V.; Moser, J.-E. Dissociation of Charge Transfer States and Carrier Separation in Bilayer Organic Solar Cells: A Time-Resolved Electroabsorption Spectroscopy Study. *J. Am. Chem. Soc.* **2015**, *137*, 8192−8198.

(24) Müller, J. G.; Lupton, J. M.; Feldmann, J.; Lemmer, U.; Scharber, M. C.; Sariciftci, N. S.; Brabec, C. J.; Scherf, U. Ultrafast Dynamics of Charge Carrier Photogeneration and Geminate Recombination in Conjugated Polymer:Fullerene Solar Cells. *Phys. Rev. B: Condens. Matter Mater. Phys.* **2005**, *72*, 195208.

(25) Moore, J. R.; Albert-Seifried, S.; Rao, A.; Massip, S.; Watts, B.; Morgan, D. J.; Friend, R. H.; McNeill, C. R.; Sirringhaus, H. Polymer Blend Solar Cells Based on a High-Mobility Naphthalenediimide-Based Polymer Acceptor: Device Physics, Photophysics and Morphology. *Adv. Energy Mater.* **2011**, *1*, 230−240.

(26) Yuan, J.; Guo, W.; Xia, Y.; Ford, M. J.; Jin, F.; Liu, D.; Zhao, H.; Inganäs, O.; Bazan, G. C.; Ma, W. Comparing the Device Physics, Dynamics and Morphology of Polymer Solar Cells Employing Conventional PCBM and Non-Fullerene Polymer Acceptor N2200. *Nano Energy* **2017**, *35*, 251−262.

(27) Abramavicius, V.; Pranculis, V.; Melianas, A.; Inganäs, O.; Gulbinas, V.; Abramavicius, D. Role of Coherence and Delocalization in Photo-Induced Electron Transfer at Organic Interfaces. *Sci. Rep.* **2016**, *6*, 32914.

(28) Melianas, A.; Kemerink, M. Photogenerated Charge Transport in Organic Electronic Materials: Experiments Confirmed by Simulations. *Adv. Mater.* **2019**, *31*, 1806004.

(29) Kurpiers, J.; Neher, D. Dispersive Non-Geminate Recombination in an Amorphous Polymer:Fullerene Blend. *Sci. Rep.* **2016**, *6*, 26832.

(30) Kurpiers, J.; Ferron, T.; Roland, S.; Jakoby, M.; Thiede, T.; Jaiser, F.; Albrecht, S.; Janietz, S.; Collins, B. A.; Howard, I. A.; et al. Probing the Pathways of Free Charge Generation in Organic Bulk Heterojunction Solar Cells. *Nat. Commun.* **2018**, *9*, 2038.

(31) Hosseini, S. M.; Roland, S.; Kurpiers, J.; Chen, Z.; Zhang, K.; Huang, F.; Armin, A.; Neher, D.; Shoaee, S. Impact of Bimolecular Recombination on the Fill Factor of Fullerene and Nonfullerene-Based Solar Cells: A Comparative Study of Charge Generation and Extraction. *J. Phys. Chem. C* **2019**, *123*, 6823−6830.

(32) Zhang, X.; Zuo, X.; Xie, S.; Yuan, J.; Zhou, H.; Zhang, Y. Understanding Charge Transport and Recombination Losses in High Performance Polymer Solar Cells with Non-Fullerene Acceptors. *J. Mater. Chem. A* **2017**, *5*, 17230−17239.
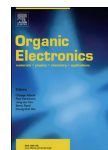
129

Interplay between charge separation and hole back transfer determines the efficiency of non-fullerene organic solar cells with low energy level offset

Rokas Jasiūnas [a,*], Huotian Zhang [b], Andrius Gelžinis [a,c], Jevgenij Chmeliov [a,c], Marius Franckevičius [a], Feng Gao [b], Vidmantas Gulbinas [a]

[a] *Department of Molecular Compound Physics, Center for Physical Sciences and Technology, Sauletekio av.3, Vilnius, 10257, Lithuania*
[b] *Department of Physics Chemistry and Biology (IFM), Linköping University, Linköping, SE-58183, Sweden*
[c] *Institute of Chemical Physics, Faculty of Physics, Vilnius University, Sauletekio av. 9, Vilnius, 10222, Lithuania*

ARTICLE INFO

ABSTRACT

Organic bulk heterojunction solar cells with electron acceptors based on small donor-acceptor type molecules show record efficiencies mainly due to their long wavelength absorption, which enables efficient harvesting of solar light and, thus, causes high current density. Meanwhile, relative positions of HOMO and LUMO levels of donor and acceptor materials determine the open circuit voltage. Here, we apply ultrafast transient absorption and transient luminescence techniques together with specially-designed modelling technique to address charge carrier generation and recombination dynamics in detail. We demonstrate the importance of careful adjustment of the HOMO and LUMO levels, as their positions determine formation and recombination rates of interfacial charge transfer (CT) states. An insufficient donor and acceptor LUMO level offset, lower than ~300 meV, leads to slow and inefficient CT state formation, while an offset of the HOMO level below ~100 meV leads to fast CT state recombination, which we attribute to the back transfer of a hole from the donor to the acceptor.

1. Introduction

Organic photovoltaic (OPV) technology has been steadily improving for several decades [1] to achieve remarkable power conversion efficiencies (PCE) of over 18% for single-junction devices [2–6]. However, for OPV commercialization, among other challenges, further improvement in PCE is required. One of the possible strategies for this is to minimize the voltage losses ΔV ($\Delta V = E_g/q$ - V_{oc}, where E_g is the optical bandgap, q is the elementary charge and V_{oc} is the open-circuit voltage), which are typically around 0.6 V or higher, while they are only ~0.3–0.4 V for GaAs and c-Si-based devices [7–9]. While there are examples of novel OPV devices with significantly reduced voltage losses [10–13], in general the voltage loss is higher than in inorganic semiconductors because the illumination of organic materials does not directly generate free charge carriers, but excitons, bound electron-hole pairs, which require excess energy to dissociate. In bulk hetero-junction devices, exciton dissociation into free charges is driven by the energy difference in ionization potential or electron affinity between donor and acceptor, or by the energy offset between the lowest unoccupied molecular orbitals (LUMO) and the highest occupied molecular orbitals

(HOMO) of the individual components between donor and acceptor materials [14–18].

It is generally accepted that an energy offset of at least 0.3 eV between the LUMO levels of the donor and acceptor is required for efficient charge separation, as demonstrated in fullerene derivative-based devices [19–21]. For decades, fullerene derivatives were considered a critical component of OPV, but the fullerene's poor absorption of a solar radiation limits the maximum PCE to less than 12% in such devices [22]. Recently, a new class of fused-ring non-fullerene acceptor (NFA) materials has emerged, which has been improving PCE in unprecedented rate. Typically, NFAs are narrow-bandgap molecules, which complement the absorption of the wide-bandgap donor in the near-infrared region of solar radiation and consequently enable short-current (Jsc) values as high as >25 mA/cm^2 [23–26]. Furthermore, such a combination of material ensures a high LUMO offset (~0.3eV) and also allows for HOMO energy offset adjustment to minimize voltage losses. Interestingly, it has been suggested that hole transfer from acceptor to donor, contrary to popular belief, can occur even at negligible HOMO offsets [13,27–32]. However, the apparent advantage of low voltage losses comes at a price, as a negligible energy offset sets no barrier for transfer

---

of holes back to an acceptor where they could recombine, increasing energy losses [33,34].

In this work, we have analyzed the effects of the LUMO and HOMO energy offsets on the charge generation efficiency in four different devices based on the same donor polymer and four conventional NFAs, which have similar chemical compositions but different energy level positions. We have investigated main optoelectronic processes using transient absorption (TA), transient photoluminescence (tPL) and originally developed multivariate curve analysis. We found out that LUMO offset of at least 300 meV is needed for efficient generation of interfacial charge transfer state (CT). Moreover, we show that HOMO offset lower than 100 meV, though beneficial for increasing Voc, leads to enhanced recombination due to hole back transfer between donor and acceptor HOMO levels.

This work is organized as follows: in the first section investigated materials and devices are introduced; in the second and third sections photophysics of the blends following excitation of donor polymer and of acceptor respectively is analyzed; in the fourth section peculiarities of PTO2:ITM sample are addressed; final remarks and conclusions are provided in fifth section.

2. Materials and devices

We investigated the benchmark non-fullerene acceptor 3,9-bis(2-methylene-(3-(1,1-dicyanomethylene)-indanone))-5,5,11,11-tetrakis(4-hexylphenyl)-dithieno[2,3-d:2′,3′-d`]-s-indaceno[1,2-b:5,6-b`]dithiophene, also known as ITIC, and three of its derivatives with different sidechains – ITM, ITCC and IT4F. The detailed chemical composition of each acceptor is depicted in Supplementary Information (S.I.) Fig. S1. As donor material, we chose the wide band-gap copolymer Poly[(2,6-(4,8-bis(5-(2-ethylhexyl)thiophen-2-yl)-benzo[1,2-b:4,5-b`]dithiophene))-alt-(2,2-ethyl-3(or4)-carboxylate-thiophene)] (PTO2) with electron-donating benzodithiophene and electron-withdrawing thiophene carboxylate ester as the main backbone, as it matches well with the energy levels of an acceptors, as shown in Fig. 1. Notably, commonly used methods for measuring HOMO and LUMO level of a material, such as cyclic voltammetry, suffer from poor reproducibility. For example, the value for HOMO level of ITIC span from 5.48 eV to 5.80 eV

depending on the research group [36–38]. Even in the same group, deviation up to 0.1 eV can be found [39,40]. Moreover, the concept of molecular orbitals is misleading in D/A blends, since the intermolecular interactions between the two components in blends alter the energy levels [41]. Therefore, the figures given here, taken from Ref. [35], indicate a gradual decrease in the energy from the PTO2:IT4F device to PTO2:ITCC, rather than exact quantitative values. The same tendency, IT4F > ITIC > ITM > ITCC for HOMO level distribution between the investigated acceptors, is also observed elsewhere [42–44].

The same table lists the photovoltaic properties of our devices. The best performing PTO2:IT4F sample had a PCE of 12.66%, along with high short-circuit current density of 20.95 mA/cm² , due to the good absorption of long wavelength photons by acceptor (Fig. 1b). These values are comparable to those obtained elsewhere [45]. The remaining samples had decent PCE values between 7 and 8%. These lower efficiencies compared to PTO2:IT4F are mainly due to 30–50% lower short-circuit currents. The poorer absorption of long-wavelength photons can lead to differences in short-circuit currents by about 10–15%, but the main difference is obviously due to the less efficient charge carrier generation.

3. Results

3.1. Excitation of a donor

We begin our analysis by addressing excited state dynamics of a polymer PTO2 in a neat film and in blends. PTO2 was used as an electron donor in all investigated blends. PTO2under excitation at 515 nm shows broad photoluminescence (PL) spectrum with the peak at about 627 nm, while the blends show spectra consisting of multiple bands attributable to both donor and acceptors (See S.I. Fig. S2a). Acceptors have weak absorbance at 515 nm excitation wavelength, therefore their PL may also originate from excitation energy transfer from excited donor [58]. However, PL dynamics of acceptors show no growth simultaneous with the donors PL decay, which suggests that this mechanism is not dominating. Fig. 2a shows PTO2 PL band dynamics both in neat film (brown curve) and in blends. Here the samples were excited with short (200 fs) 515 nm laser pulses and PL was recorded with a streak camera. For the

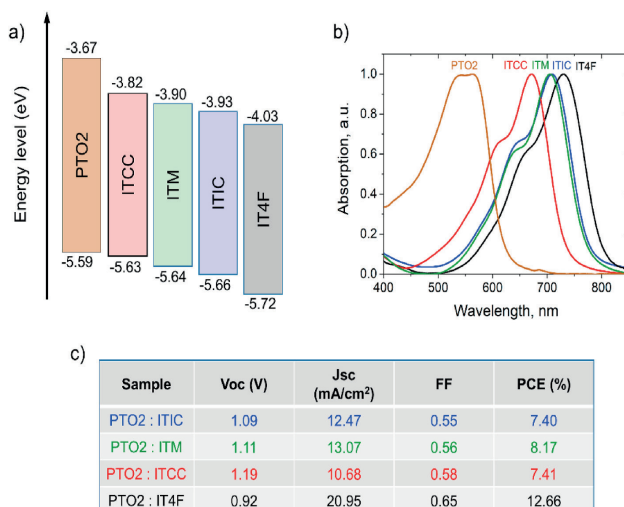| Sample	Voc (V)	Jsc (mA/cm²)	FF	PCE (%)
PTO2 : ITIC	1.09	12.47	0.55	7.40
PTO2 : ITM	1.11	13.07	0.56	8.17
PTO2 : ITCC	1.19	10.68	0.58	7.41
PTO2 : IT4F	0.92	20.95	0.65	12.66

Fig. 1. a) Energy levels of used materials, as measured in Ref. [35]. B) Normalized steady-state absorption spectra of indicated materials. c) Table of photovoltaic characteristics.
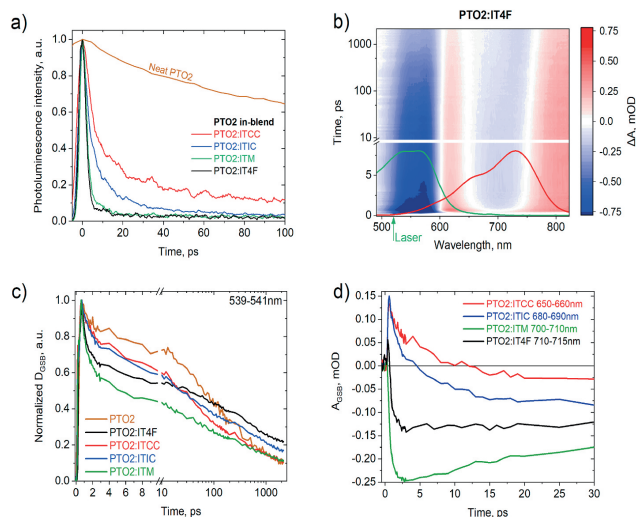
Fig. 2. Experimental data under excitation of donor. a) Transient photoluminescence of neat and in-blend PTO2; b) TA of PTO2:IT4F blend after 520 nm ($I_{exc} = 0.76$ μJ/cm^2) excitation. Solid lines indicate steady-state absorption spectra of PTO2 (green curve) and IT4Facceptor (red curve); Normalized D_{GSB} decay dynamics in neat PTO2 and blend films (c) and A_{GSB} dynamics of indicated blends (d) after 520 nm excitation.

analysis of the PTO2 PL dynamics in blends we used the short wavelength (595–615 nm) part of the PL band, as it less overlaps with the PL spectra of acceptors (see Fig. S2). Rapid PL quenching, which is clearly seen when the donor polymer is blended with any of acceptors, indicates the formation of a charge transfer (CT) exciton, i.e. a rapid electron transfer from the LUMO level of the donor to the LUMO of acceptor. Notably, the PL quenching rates correlate with the energy offsets between LUMO levels, except of ITM acceptor. In the PTO2:ITCC blend, which has the lowest LUMO offset (~150 meV), the PL of the excited donor reveals relatively slow decay and is still present even 100 ps after excitation. In PTO2:IT4F blend, where the LUMO offset is ~360 meV, PL decays faster than the time resolution of our measurement setup of about 4 ps. Interestingly, we also observe a similarly rapid PL decay in case of PTO2:ITM, although LUMO offset is not as high (~230 meV), but this blend exhibits even more peculiar properties, therefore, we will specifically address it in more detail later. The fast and almost complete PL quenching indicates that CT state formation is close to 100% in these blends. The clear correlation between the LUMO offsets and the PL quenching rates indicates that the small LUMO offset slows down the CT state formation. On the other hand, the fast CT state formation might not necessarily be essential for the CT state formation efficiency until it is much faster than the excited state relaxation of the donor. This may be the case for the PTO2:ITCC solar cell, which features only slightly lower I_{SC} than cells with ITM or ITIC acceptors despite of much slower CT state formation.

To gain further insight into the dynamics of electron transfer after donor excitation, we turn to transient absorption measurements (Fig. 2b–d). In Fig. 2b, transient absorption 3D plot is presented for the PTO2:IT4F blend (plots for other samples are provided in S.I., see Fig. S3). The solid curves represent normalized steady-state absorption spectra of a donor (green curve) and a corresponding acceptor (red curve). We have used 520 nm excitation here to minimize the excitation of the acceptors. Importantly, our experiments were performed within low excitation intensity ($I_{exc} \sim 0.76$ μJ/cm^2) range, when annihilation and higher order recombination could be ignored, as demonstrated in Fig. S7. In all blends, we observe ground state bleaching (GSB) of PTO2 in the range of 500–600 nm emerging immediately after excitation.

Fig. 2c and d shows the transient absorption kinetics in the donor (normalized for convenient comparison between blends) and acceptor absorption band bleaching peak regions. The excited donor (D*) may either relax to the ground state, restoring the original absorption spectrum, or may form the interfacial CT state by transferring electron to acceptors' domain, which also causes GSB of the acceptor (A_{GSB}). The A_{GSB} appears dominantly on a subpicosecond time scale in PTO2:IT4F and in PTO2:ITM blends in agreement with the PL data and similarly as observed in many other fullerene [46–49] and non-fullerene devices [50–53]. The electron transfer rate is even slightly faster in PTO2:ITM blend than in PTO2:IT4F where we initially observe a positive peak due to the induced absorption of D* state. In the case of PTO2:ITCC and PTO2:ITIC, it takes more than 30 ps for the A_{GSB} signal to peak, supporting the correlation between LUMO offset and electron transfer rate described above. Interestingly, bleaching of donor absorption slightly decreases during the CT state formation time as shown in Fig. 2c. CT formation can hardly cause parallel D* relaxation to the ground state, therefore, it shows that CT states cause weaker bleaching of a donor absorption than D* state. This explanation is supported by the observation that this fast relaxation is the most significant in PTO2:ITM and PTO2:IT4F blends characterized by the most efficient CT state generation.

To assess the actual dynamics of CT state formation more precisely, we performed a special global analysis of the transient absorption data, called multivariate curve resolution, which is described in detail in S.I. Briefly, the analysis assumed that the TA spectra consist of two independently evolving spectral components of D* and CT/CS states. Here we do not distinguish between charge transfer (CT) and separated charge (CS) states, since both states lead to similar transient absorption spectra. We also do not consider other possible processes, such as energy transfer from excited donor to acceptor [58], formation of triplet states [59], or reverse electron transfer discussed below. The two-state model, as discussed below, reproduces the experimental data well, indicating that D* and CT/CS states are dominating. We also demonstrate below that the transient absorption dynamics are very different under excitation of donor and acceptor, which should not be the case if excitation of a donor creates excited acceptor state by rapid energy transfer. Whereas

formation of the triplet state is expected to occur at longer times than our investigated time domain. Thus, although, we cannot completely rule out these processes, apparently, they do not play essential roles in the investigated blends at our experimental conditions. Unlike conventional global analysis, we did not use the assumption of exponential phenomenon dynamics here, but used fixed spectra and modelled their kinetics. The D* spectrum was obtained from the TA spectrum of the neat PTO2 film and was therefore identical for all investigated blends. For the CT/CS state spectral signature, we used the TA signal at times >1.5 ns after excitation, as it is very unlikely that the D* is still present at this time, as also shown by the tPL measurements. All spectral components used in modelling are provided in S.I. Model Description section. Despite some oversimplification, this model worked quite well, as fairly good fits were obtained for all investigated samples (see Model Results section in S.I.). The modeling gives time evolutions of D* and CT/ST states concentrations, however, in relative values. The evaluated CT/CS dynamics are presented in Fig. 3b. Even though the absolute values of the CT/CS state generation yield cannot be obtained, the model, nonetheless, enables comparison of CT/CS state yields and their kinetics between different blends. It gives the highest CT/CS formation efficiency in PTO2:ITM blend, while efficiencies are lower by 1.1, 1.7 and 2.6 times for blends with IT4F, ITIC and ITCC respectively. The highest CT/CS concentration for PTO2:IT4F and PTO2:ITM blends is obtained at about 3 ps, while in case of PTO2:ITIC and PTO2:ITCC, the maximal value is reached at about 40 ps and 100 ps, respectively. After reaching the maximum values, the densities of the CT/CS states start to decrease due to recombination, but the decrease rates are significantly different.

To characterize the CT/CS formation and decay rates we have fitted the modelled CT/CS kinetics by simple biexponential function:

$$y = \left[A_1 + (1 - A_1) \times \left(1 - exp\left(-t/\tau_{growth} \right) \right) \right]$$
$$\times \left[A_2 + (1 - A_2) \times exp\left(-t/\tau_{decay} \right) \right], \quad (1)$$

where τ_{growth} and τ_{decay} correspond to formation and decay times of CT/SC states, A_1 shows fraction of CT/CS states formed faster than our time resolution, and A_2 shows a fraction of CT/CS states, which do not experience recombination on a several ns time scale. As seen from Fig. 3b, the fitting is not ideal, since these processes are not expected to be exponential, yet it provides reasonable comparison between the blends. The fitting results are presented in Table 1. The CT/CS formation rates correlate with the LUMO level offset, again except for the PTO2: ITM blend. A_1 values are given only for the blends with the lowest LUMO offsets, because for other two blends, the formation rate was too fast to discriminate it form the apparatus function. While in case of PTO2:ITIC and PTO2:ITCC we clearly observe two formation phases. The ultrafast phase should be attributed to the CT/CS state formation from the non-stabilised D* state.

The fraction A_2 of slowly recombining CT/CS states should be

Table 1
Biexponential fitting parameters for CT/CS dynamics.

Blend	A_1	τ_{growth}, ps	A_2	τ_{decay}, ps
PTO2:ITM	0	0.31	0.35	84
PTO2:IT4F	0	0.26	0.66	253
PTO2:ITIC	0.26	2.09	0.50	819
PTO2:ITCC	0.36	3.47	0.18	2500

attributed to the CT states, which separate into CS states, thus form free charge carriers, and recombine much slower. This fraction increases with the HOMO offsets and together with the formation efficiency of CT/CS states determines charge carrier generation yield. Clear correlation of this fraction with the HOMO offset suggests that efficient dissociation of the CT states depends on the offset value. We have previously discussed that thermally activated reverse electron transfer from the acceptor to donor's HOMO level may take place in OPV devices with sufficiently low HOMO level offset [33,34]. We hypothesize that this process causes incomplete charge transfer from donor to acceptor, as explained in Fig. 4, making CT state dissociation into CS state more difficult. This process should also cause appearance of the excited acceptor state A* during the CT/CS state relaxation. Dynamics of both states is expected to be similar, therefore, we cannot explicitly distinguish the A* state, however, we cannot exclude that it contributes to the evaluated CT/CS state spectrum.

At this point, we emphasize the fact that our measurements were carried out at zero electric field. Under short-circuit conditions, when a strong electric field is present, both the relaxation and recombination dynamics would be different due to the prevailing charge carrier extraction and field-assisted CT state dissociation. In the case of a zero field, no charge carriers are extracted, so they are more prone to recombination.

3.2. Excitation of an acceptor

An analogous transient absorption analysis was performed with excitation pulses tuned to specifically excite acceptor molecules in bulk heterojunction films. Fig. 5 a,b show time evolution of the transient absorption spectra for PTO2:IT4F and PTO2:ITCC blends (3D plots for other blends are provided in S.I.). Same as in case of donor excitation, we observe donor and acceptor absorption bleaching bands, however, the acceptor band is much stronger. Fig. 5c and d shows the transient absorption kinetics measured close to the maxima of donor and acceptor bleaching bands. In this case, the D_{GSB} signal appears due to the hole transfer from excited acceptor's HOMO level to the HOMO level of the donor creating identical CT/CS state as in case of electron transfer form photoexcited donor. Bleaching of acceptor A_{GSB} appears both due to the A* and CT/CS states. We also observe decay of the A_{GSB} on an ultrafast time scale, which should be also attributed to the formation of the CT/CS states, since ionized acceptors A^- apparently cause weaker absorption
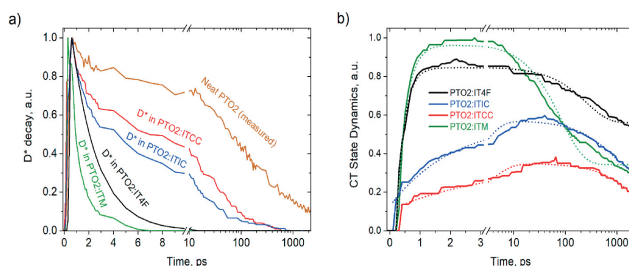

Fig. 3. Multivariate curve resolution modelling results under excitation of donor. Modelled D* (a) and CT/CS (b) state dynamics in indicated blends. Dashed curves in (b) show fitting of the kinetics by biexponential grow-decay function.
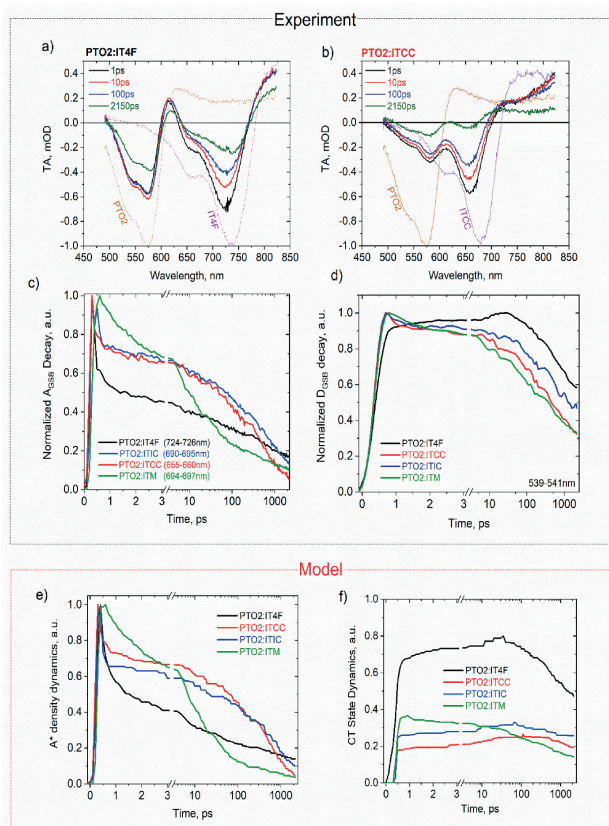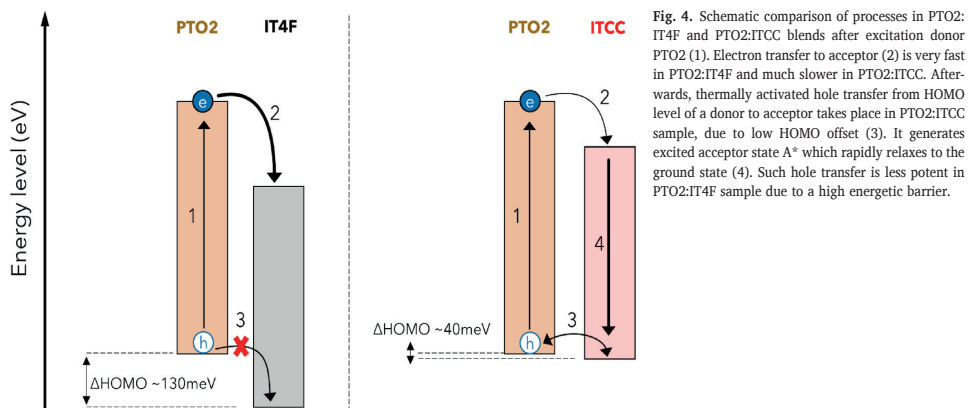
Fig. 4. Schematic comparison of processes in PTO2: IT4F and PTO2:ITCC blends after excitation donor PTO2 (1). Electron transfer to acceptor (2) is very fast in PTO2:IT4F and much slower in PTO2:ITCC. Afterwards, thermally activated hole transfer from HOMO level of a donor to acceptor takes place in PTO2:ITCC sample, due to low HOMO offset (3). It generates excited acceptor state A* which rapidly relaxes to the ground state (4). Such hole transfer is less potent in PTO2:IT4F sample due to a high energetic barrier.

Fig. 5. Excitation of an acceptor. a,b)TA of PTO2:IT4F and PTO2:ITCC blends after 670 nm or 730 nm excitation ($I_{exc} \sim 2\,\mu J/cm^2$). Solid lines indicate normalized steady-state absorption spectra of PTO2 (green curve) and respective acceptor (red curve); c) Normalized ground state bleaching dynamics of acceptor (c) and donor (d) in indicated blends; e,f) Modelled transient absorption measurement results of A* (e) and CT/CS (f) dynamics in indicated blends.

5

bleaching than A*, as was also demonstrated by quantum chemical calculations for acceptor Y1 [33].

The effective charge transfer is visible immediately after excitation in all investigated blends, as shown by the instantaneous appearance of the D_{GSB} signal. Notably, energy difference between the HOMO levels, i.e. the driving force for the charge transfer, is much smaller than the difference between the LUMO levels. For example, LUMO offset in the PTO2:ITCC sample is ~150 meV, while HOMO offset is ~40 meV. Therefore, this ultrafast CT/CS state formation is surprising. Nevertheless, this finding is in line with the reported high CT state formation efficiencies in blends with a very low or even near zero HOMO level offset [32,54–57]. This ultrafast phase takes place on a subpicosecond time scale independently of the HOMO level offset. These features suggest that the hole transfer takes place from the nonequilibrated excited state.

We have also used modeling to evaluate the A* and CT/CS state dynamics more accurately. In this case we fixed the CT/CS spectrum as obtained in the case of excitation of donor and used the A* spectra as obtained for the pure acceptor films, only shifted along the wavelength scale by the same values as obtained by comparing absorption bands positions in blends and pure films. Fig. 5e and f shows the evaluated A* and CT/CS state dynamics. Unfortunately, in this case evaluation of the absolute CT/CS state formation efficiencies is even more complicated because of different spectral properties of A* and CT/CS states of different acceptors. Therefore, Fig. 5f presents the evaluated CT/ST state dynamics in relative units. In contrast to the fast D* decay, A* states are present during the entire 2 ns measurement range confirming that only a fraction of the A* form CT/CS states on a subpicosecond time scale. Additional much slower CT/CS state formation phase is also observed in all blends except for PTO2:ITM, where additional formation may be eliminated by the fast CT/CS recombination. This slow formation phase has been also observed before for the PM6:IT4F blend and attributed to the migration of excitons created in bulk of acceptor domain at some distance form donor acceptor interface [57]. In our samples, this formation phase is the fastest, lasting for about 30 ps, in PTO2:IT4F blend and the slowest in PTO2:ITCC, lasting for several hundreds of ps. Thus, the rate of this phase correlates with the HOMO level offset, which suggests that the hole driving force plays an important role in such charge transfer exciton formation.

3.3. PTO2:ITM sample

The PTO2:ITM sample shows somewhat peculiar properties compared to other samples studied. In the case of donor excitation, the rapid quenching of the D* state by effective ultrafast CT/CS state formation, seen in both tPL and TA measurements, is followed by rapid CT/CS state relaxation. In the case of acceptor excitation, the fast formation of the CT/CS state is followed by rapid recombination. Considering that the measured HOMO/LUMO levels of ITM are intermediate between those of ITCC and ITIC acceptors, these phenomena seem to contradict the tendency observed for other acceptors. However, the HOMO/LUMO values measured on neat materials should only be applied to blends with great caution. As mentioned earlier, CV measurements are prone to large errors and, more importantly, HOMO/LUMO levels of acceptor shift when the molecules are incorporated into a heterojunction with the donor polymer and also undergo an excited state stabilization observed as a Stokes shift of the PL bands. All acceptors show a blue shift of the absorption band in the blend compared to pure films, but this shift is less significant for the ITM (see Fig. 6). Therefore, the absorption band of the ITM appears between absorption bands of ITIC and IT4F. Moreover, the ITM fluorescence shows significantly stronger Stokes shift, even more red-positioned than that of IT4F. Orange lines in Fig. 6 are guides-for-an-eye, connecting peak absorption values of neat and in-blend acceptors. It demonstrates that absorption shift is very similar for all acceptors, except for ITM, for which in-blend absorption is further away from the orange line compared to neat ITM. Moreover, same line connecting peak
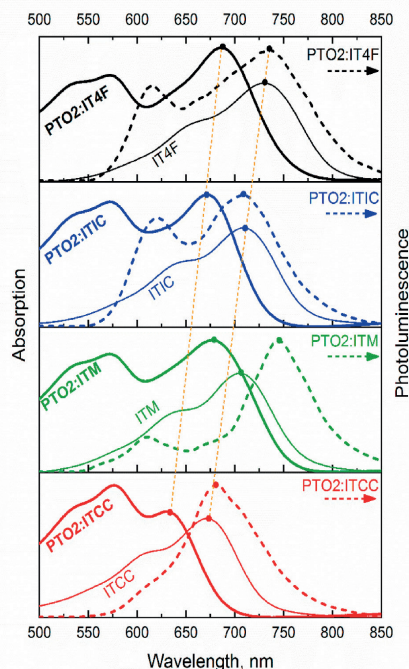

Fig. 6. Steady-state absorption of blends (thick solid curves) and neat acceptor materials (thin solid curves). Dashed curves show transient (0–120ps) photoluminescence spectra of the blends. Orange lines are guide-for-an-eye with explanations in the text.

absorption values of neat acceptors also connects red-shifted PL spectra peaks, however, it fails drastically to do so for PTO2:ITM sample, due to much stronger Stokes shift than in other samples. Taking this correction into account, the ITM performance, which is closer to the IT4F than to the other two acceptors, ranks properly in the sequence of all devices studied. In particular, CT state dynamics (see Fig. 3b) shows a rapid formation of the CT state, indicating that the LUMO level of ITM in-blend is indeed shifted downwards compared to ITIC and ITCC. The larger energy gaps of the acceptors in the blends also indicates that the LUMO energy offsets are somewhat smaller than the values determined from positions of the energy levels in pure materials, so that the offset values of about 300 meV estimated above might actually be lower.

The blue shift of the absorption bands of the acceptors when mixed with PTO2 donor molecules also suggests that these donor-acceptor molecules are well mixed with the less polar donor material. We suggest that the less significant shift of the absorption band and the strong PL Stokes shift of the ITM molecules is caused by poorer mixing due to the greater difference in polarity of the two components, i.e. the stronger polarity of ITM.

4. Conclusions

In conclusion, we have used transient absorption and transient photoluminescence techniques to investigate formation and recombination of charged states in blends of PTO2 donor and IT-class small molecule acceptors. Our results emphasize the need of careful

6

consideration of interplay between the long-wavelength absorption and the positions of the energetic levels to further improve solar cell efficiencies. We show that a fast and efficient interfacial charge transfer state formation requires an offset of about 300 meV between the LUMO levels of donor and acceptor, assuming correct reported energy level positions. On the other hand, even a small HOMO level offset is sufficient for the ultrafast hole transfer from photoexcited acceptor molecules, but efficiency of the CT state formation decreases at low HOMO offsets. Efficiency of the CT state dissociation into a pair of separated charge carriers also decreases at low HOMO offsets, which we attribute to the back hole transfer causing incomplete carrier separation in CT state.

Declaration of competing interest

The authors declare that they have no known competing financial interests or personal relationships that could have appeared to influence the work reported in this paper.

Data availability

Data will be made available on request.

Appendix A. Supplementary data

Supplementary data to this article can be found online at https://doi.org/10.1016/j.orgel.2022.106601.

References

[1] O. Inganäs, Organic photovoltaics over three decades, Adv. Mater. 30 (35) (2018), 1800388, https://doi.org/10.1002/adma.201800388.

[2] Q. Liu, Y. Jiang, K. Jin, J. Qin, J. Xu, W. Li, J. Xiong, J. Liu, Z. Xiao, K. Sun, S. Yang, X. Zhang, L. Ding, 18% efficiency organic solar cells, Sci. Bull. 65 (4) (2020) 272–275, https://doi.org/10.1016/j.scib.2020.01.001.

[3] Y. Qin, Y. Chang, X. Zhu, X. Gu, L. Guo, Y. Zhang, Q. Wang, J. Zhang, X. Zhang, X. Liu, K. Lu, E. Zhou, Z. Wei, X. Sun, 18.4% efficiency achieved by the cathode interface engineering in non-fullerene polymer solar cells, Nano Today 41 (2021), 101289, https://doi.org/10.1016/j.nantod.2021.101289.

[4] Y. Cui, Y. Xu, H. Yao, P. Bi, L. Hong, J. Zhang, Y. Zu, T. Zhang, J. Qin, J. Ren, Z. Chen, C. He, X. Hao, Z. Wei, J. Hou, Single-junction organic photovoltaic cell with 19% efficiency, Adv. Mater. 33 (41) (2021), 2102420, https://doi.org/10.1002/adma.202102420.

[5] M. Zhang, L. Zhu, G. Zhou, T. Hao, C. Qiu, Z. Zhao, Q. Hu, B.W. Larson, H. Zhu, Z. Ma, Z. Tang, W. Feng, Y. Zhang, T.P. Russell, F. Liu, Single-layered organic photovoltaics with double cascading charge transport pathways: 18% efficiencies, Nat. Commun. 12 (1) (2021) 309, https://doi.org/10.1038/s41467-020-20580-8.

[6] C. Li, J. Zhou, J. Song, J. Xu, H. Zhang, X. Zhang, J. Guo, L. Zhu, D. Wei, G. Han, J. Min, Y. Zhang, Z. Xie, Y. Yi, H. Yan, F. Gao, F. Liu, Y. Sun, Non-fullerene acceptors with branched side chains and improved molecular packing to exceed 18% efficiency in organic solar cells, Nat. Energy 6 (6) (2021) 605–613, https://doi.org/10.1038/s41560-021-00820-x.

[7] J. Yao, T. Kirchartz, M.S. Vezie, M.A. Faist, W. Gong, Z. He, H. Wu, J. Troughton, T. Watson, D. Bryant, J. Nelson, Quantifying losses in open-circuit voltage in solution-processable solar cells, Phys. Rev. Applied 4 (1) (2015), 014020, https://doi.org/10.1103/PhysRevApplied.4.014020.

[8] K. Vandewal, K. Tvingstedt, A. Gadisa, O. Inganäs, J.V. Manca, On the origin of the open-circuit voltage of polymer–fullerene solar cells, Nat. Mater. 8 (11) (2009) 904–909, https://doi.org/10.1038/nmat2548.

[9] Polman Albert, Mark Knight, C. Garnett Erik, Ehrler Bruno, C. Sinke Wim, Photovoltaic materials: present efficiencies and future challenges, Science 352 (6283) (2016) aad4424, https://doi.org/10.1126/science.aad4424.

[10] D. Baran, T. Kirchartz, S. Wheeler, S. Dimitrov, M. Abdelsamie, J. Gorman, R. S. Ashraf, S. Holliday, A. Wadsworth, N. Gasparini, P. Kaienburg, H. Yan, A. Amassian, C.J. Brabec, J.R. Durrant, I. McCulloch, Reduced voltage losses yield 10% efficient fullerene free organic solar cells with >1 V open circuit voltages, Energy Environ. Sci. 9 (12) (2016) 3783–3793, https://doi.org/10.1039/C6EE02598F.

[11] D. Yang, Y. Wang, T. Sano, F. Gao, H. Sasabe, J. Kido, A minimal non-fullerene acceptor for efficient non-fullerene all-small-molecule organic solar cells with a low energy loss of 0.54 eV and high open-circuit voltage of 1.15 V, J. Mater. Chem. 6 (28) (2018) 13918–13924, https://doi.org/10.1039/C8TA04665D.

[12] A. Mishra, M.L. Keshtov, A. Looser, R. Singhal, M. Stolte, F. Würthner, P. Bäuerle, G.D. Sharma, Unprecedented low energy losses in organic solar cells with high external quantum efficiencies by employing non-fullerene electron acceptors, J. Mater. Chem. 5 (28) (2017) 14887–14897, https://doi.org/10.1039/C7TA04703G.

[13] H. Zhang, S. Li, B. Xu, H. Yao, B. Yang, J. Hou, Fullerene-free polymer solar cell based on a polythiophene derivative with an unprecedented energy loss of less than 0.5 eV, J. Mater. Chem. 4 (46) (2016) 18043–18049, https://doi.org/10.1039/C6TA07672F.

[14] Y. Zhu, F. Zhao, W. Wang, Y. Li, S. Zhang, Y. Lin, Exciton binding energy of non-fullerene electron acceptors, Advanced Energy and Sustainability Research (2022), https://doi.org/10.1002/aesr.202100184 n/a (n/a), 2100184.

[15] R.S. Bhatta, M. Tsige, Chain length and torsional dependence of exciton binding energies in P3HT and PTB7 conjugated polymers: a first-principles study, Polymer 55 (11) (2014) 2667–2672, https://doi.org/10.1016/j.polymer.2014.04.022.

[16] A.W. Hains, Z. Liang, M.A. Woodhouse, B.A. Gregg, Molecular semiconductors in organic photovoltaic cells, Chem. Rev. 110 (11) (2010) 6689–6735, https://doi.org/10.1021/cr9002984.

[17] S.D. Dimitrov, J.R. Durrant, Materials design considerations for charge generation in organic solar cells, Chem. Mater. 26 (1) (2014) 616–630, https://doi.org/10.1021/cm402403z.

[18] T.M. Clarke, J.R. Durrant, Charge photogeneration in organic solar cells, Chem. Rev. 110 (11) (2010) 6736–6767, https://doi.org/10.1021/cr900271s.

[19] W. Li, K.H. Hendriks, A. Furlan, M.M. Wienk, R.A.J. Janssen, High quantum efficiencies in polymer solar cells at energy losses below 0.6 eV, J. Am. Chem. Soc. 137 (6) (2015) 2231–2234, https://doi.org/10.1021/ja5131897.

[20] K. Vandewal, Z. Ma, J. Bergqvist, Z. Tang, E. Wang, P. Henriksson, K. Tvingstedt, M.R. Andersson, F. Zhang, O. Inganäs, Quantification of quantum efficiency and energy losses in low bandgap polymer:fullerene solar cells with high open-circuit voltage, Adv. Funct. Mater. 22 (16) (2012) 3480–3490, https://doi.org/10.1002/adfm.201200608.

[21] M.C. Scharber, D. Mühlbacher, M. Koppe, P. Denk, C. Waldauf, A.J. Heeger, C. J. Brabec, Design rules for donors in bulk-heterojunction solar cells—towards 10 % energy-conversion efficiency, Adv. Mater. 18 (6) (2006) 789–794, https://doi.org/10.1002/adma.200501717.

[22] J. Zhao, Y. Li, G. Yang, K. Jiang, H. Lin, H. Ade, W. Ma, H. Yan, Efficient organic solar cells processed from hydrocarbon solvents, Nat. Energy 1 (2) (2016), 15027, https://doi.org/10.1038/nenergy.2015.27.

[23] B. Fan, D. Zhang, M. Li, W. Zhong, Z. Zeng, L. Ying, F. Huang, Y. Cao, Achieving over 16% efficiency for single-junction organic solar cells, Sci. China Chem. 62 (6) (2019) 746–752, https://doi.org/10.1007/s11426-019-9457-5.

[24] Q. He, M. Shahid, J. Wu, X. Jiao, F.D. Eisner, T. Hodsden, Z. Fei, T.D. Anthopoulos, C.R. McNeill, J.R. Durrant, M. Heeney, Fused cyclopentadithienothiophene acceptor enables ultrahigh short-circuit current and high efficiency >11% in as-cast organic solar cells, Adv. Funct. Mater. 29 (40) (2019), 1904956, https://doi.org/10.1002/adfm.201904956.

[25] Z. Zheng, R. Wang, H. Yao, S. Xie, Y. Zhang, J. Hou, H. Zhou, Z. Tang, Polyamino acid interlayer facilitates electron extraction in narrow band gap fullerene-free organic solar cells with an outstanding short-circuit current, Nano Energy 50 (2018) 169–175, https://doi.org/10.1016/j.nanoen.2018.05.034.

[26] F. Cai, H. Peng, H. Chen, J. Yuan, J. Hai, T.-K. Lau, J. Wang, Y. Hu, W. Liu, X. Lu, Y. Zou, An asymmetric small molecule acceptor for organic solar cells with a short circuit current density over 24 MA Cm $^{-2}$, J. Mater. Chem. 8 (31) (2020) 15984–15991, https://doi.org/10.1039/D0TA01636E.

[27] S. Chen, Y. Liu, L. Zhang, P.C.Y. Chow, Z. Wang, G. Zhang, W. Ma, H. Yan, A wide-bandgap donor polymer for highly efficient non-fullerene organic solar cells with a small voltage loss, J. Am. Chem. Soc. 139 (18) (2017) 6298–6301, https://doi.org/10.1021/jacs.7b01606.

[28] H. Bin, Y. Yang, Z. Peng, L. Ye, J. Yao, L. Zhong, C. Sun, L. Gao, H. Huang, X. Li, B. Qiu, L. Xue, Z.-G. Zhang, H. Ade, Y. Li, Effect of alkylsilyl side-chain structure on photovoltaic properties of conjugated polymer donors, Adv. Energy Mater. 8 (8) (2018), 1702324, https://doi.org/10.1002/aenm.201702324.

[29] C. Li, Q. Yue, H. Wu, B. Li, H. Fan, X. Zhu, Small bandgap non-fullerene acceptor enables efficient PTB7-Th solar cell with near 0 EV HOMO offset, J. Energy Chem. 52 (2021) 60–66, https://doi.org/10.1016/j.jechem.2020.03.058.

[30] S. Chen, H. Yao, Z. Li, O.M. Awartani, Y. Liu, Z. Wang, G. Yang, J. Zhang, H. Ade, H. Yan, Surprising effects upon inserting benzene units into a quaterthiophene-based D-A polymer–improving non-fullerene organic solar cells via donor polymer design, Adv. Energy Mater. 7 (12) (2017), 1602304, https://doi.org/10.1002/aenm.201602304.

[31] Y. Li, D. Qian, L. Zhong, J.-D. Lin, Z.-Q. Jiang, Z.-G. Zhang, Z. Zhang, Y. Li, L.-S. Liao, F. Zhang, A fused-ring based electron acceptor for efficient non-fullerene polymer solar cells with small HOMO offset, Nano Energy 27 (2016) 430–438, https://doi.org/10.1016/j.nanoen.2016.07.019.

[32] S. Li, L. Zhan, C. Sun, H. Zhu, G. Zhou, W. Yang, M. Shi, C.-Z. Li, J. Hou, Y. Li, H. Chen, Highly efficient fullerene-free organic solar cells operate at near zero highest occupied molecular orbital offsets, J. Am. Chem. Soc. 141 (7) (2019) 3073–3082, https://doi.org/10.1021/jacs.8b12126.

[33] R. Jasiunas, H. Zhang, J. Yuan, X. Zhou, D. Qian, Y. Zou, A. Devižis, J. Šulskus, F. Gao, V. Gulbinas, From generation to extraction: a time-resolved investigation of photophysical processes in non-fullerene organic solar cells, J. Phys. Chem. C 124 (39) (2020) 21283–21292, https://doi.org/10.1021/acs.jpcc.0c05263.

[34] R. Jasiūnas, H. Zhang, A. Devižis, M. Franckevičius, F. Gao, V. Gulbinas, Thermally activated reverse electron transfer limits carrier generation efficiency in PM6:Y6 non-fullerene organic solar cells, Solar RRL (2022), https://doi.org/10.1002/solr.202100963 n/a (n/a).

[35] C. Yang, J. Zhang, N. Liang, H. Yao, Z. Wei, C. He, X. Yuan, J. Hou, Effects of energy-level offset between a donor and acceptor on the photovoltaic performance of non-fullerene organic solar cells, J. Mater. Chem. 7 (32) (2019) 18889–18897, https://doi.org/10.1039/C9TA04789A.

[36] F. Lin, W. Huang, H. Sun, J. Xin, H. Zeng, T. Yang, M. Li, X. Zhang, W. Ma, Y. Liang, Thieno[3,4-c]Pyrrole-4,6(5H)-Dione polymers with optimized energy level alignments for fused-ring electron acceptor based polymer solar cells, Chem. Mater. 29 (13) (2017) 5636–5645, https://doi.org/10.1021/acs.chemmater.7b01335.

[37] W. Zhao, D. Qian, S. Zhang, S. Li, O. Inganäs, F. Gao, J. Hou, Fullerene-free polymer solar cells with over 11% efficiency and excellent thermal stability, Adv. Mater. 28 (23) (2016) 4734–4739, https://doi.org/10.1002/adma.201600281.

[38] Y. Lin, J. Wang, Z.-G. Zhang, H. Bai, Y. Li, D. Zhu, X. Zhan, An electron acceptor challenging fullerenes for efficient polymer solar cells, Adv. Mater. 27 (7) (2015) 1170–1174, https://doi.org/10.1002/adma.201404317.

[39] Y. Qin, M.A. Uddin, Y. Chen, B. Jang, K. Zhao, Z. Zheng, R. Yu, T.J. Shin, H.Y. Woo, J. Hou, Highly efficient fullerene-free polymer solar cells fabricated with polythiophene derivative, Adv. Mater. 28 (42) (2016) 9416–9422, https://doi.org/10.1002/adma.201601803.

[40] S. Li, L. Ye, W. Zhao, S. Zhang, S. Mukherjee, H. Ade, J. Hou, Energy-level modulation of small-molecule electron acceptors to achieve over 12% efficiency in polymer solar cells, Adv. Mater. 28 (42) (2016) 9423–9429, https://doi.org/10.1002/adma.201602776.

[41] J.-L. Brédas, J.E. Norton, J. Cornil, V. Coropceanu, Molecular understanding of organic solar cells: the challenges, Acc. Chem. Res. 42 (11) (2009) 1691–1699, https://doi.org/10.1021/ar900099h.

[42] B. Xue, G. Huang, B. Wang, H. Wang, X. Shi, B. Han, H. Zhang, Y. Zhang, H. Zhou, The role of ending groups in nonfullerene acceptors for interfacial modification in perovskite solar cells, Solar RRL 6 (1) (2022) 2100864, https://doi.org/10.1002/solr.202100864.

[43] X. Wan, C. Li, M. Zhang, Y. Chen, Acceptor–donor–acceptor type molecules for high performance organic photovoltaics – chemistry and mechanism, Chem. Soc. Rev. 49 (9) (2020) 2828–2842, https://doi.org/10.1039/D0CS00084A.

[44] J. Hou, O. Inganäs, R.H. Friend, F. Gao, Organic solar cells based on non-fullerene acceptors, Nat. Mater. 17 (2) (2018) 119–128, https://doi.org/10.1038/nmat5063.

[45] H. Yao, Y. Cui, D. Qian, C.S. Ponseca, A. Honarfar, Y. Xu, J. Xin, Z. Chen, L. Hong, B. Gao, R. Yu, Y. Zu, W. Ma, P. Chabera, T. Pullerits, A. Yartsev, F. Gao, J. Hou, 14.7% efficiency organic photovoltaic cells enabled by active materials with a large electrostatic potential difference, J. Am. Chem. Soc. 141 (19) (2019) 7743–7750, https://doi.org/10.1021/jacs.8b12937.

[46] A. Devižis, A. Serbenta, K. Meerholz, D. Hertel, V. Gulbinas, Ultrafast dynamics of carrier mobility in a conjugated polymer probed at molecular and microscopic length scales, Phys. Rev. Lett. 103 (2) (2009), 027404, https://doi.org/10.1103/PhysRevLett.103.027404.

[47] H. Tamura, I. Burghardt, Ultrafast charge separation in organic photovoltaics enhanced by charge delocalization and vibronically hot exciton dissociation, J. Am. Chem. Soc. 135 (44) (2013) 16364–16367, https://doi.org/10.1021/ja4093874.

[48] S. Gélinas, A. Rao, A. Kumar, S.L. Smith, A.W. Chin, J. Clark, Ultrafast Long-Range Charge Separation in Organic Semiconductor Photovoltaic Diodes, vol. 343, 2014, p. 6.

[49] V. Abramavicius, V. Pranculis, A. Melianas, O. Inganäs, V. Gulbinas, D. Abramavicius, Role of coherence and delocalization in photo-induced electron transfer at organic interfaces, Sci. Rep. 6 (1) (2016), 32914, https://doi.org/10.1038/srep32914.

[50] S. Chen, S. Myeon Lee, J. Xu, J. Lee, K. Cheol Lee, T. Hou, Y. Yang, M. Jeong, B. Lee, Y. Cho, S. Jung, J. Oh, Z.-G. Zhang, C. Zhang, M. Xiao, Y. Li, C. Yang, Ultrafast channel II process induced by a 3-D texture with enhanced acceptor order ranges for high-performance non-fullerene polymer solar cells, Energy Environ. Sci. 11 (9) (2018) 2569–2580, https://doi.org/10.1039/C8EE01546E.

[51] V.A.C. Franco, N. Gasparini, T. Nagahara, L. Lüer, G. Cerullo, C. Brabec, Instantaneous charge separation in non-fullerene acceptor bulk-heterojunction of highly efficient solar cells, EPJ Web Conf. 205 (2019), 05010, https://doi.org/10.1051/epjconf/201920505010.

[52] D.M. Stoltzfus, J.E. Donaghey, A. Armin, P.E. Shaw, P.L. Burn, P. Meredith, Charge generation pathways in organic solar cells: assessing the contribution from the electron acceptor, Chem. Rev. 116 (21) (2016) 12920–12955, https://doi.org/10.1021/acs.chemrev.6b00126.

[53] N. Gasparini, A. Wadsworth, M. Moser, D. Baran, I. McCulloch, C.J. Brabec, The physics of small molecule acceptors for efficient and stable bulk heterojunction solar cells, Adv. Energy Mater. 8 (12) (2018), 1703298, https://doi.org/10.1002/aenm.201703298.

[54] Z. Chen, X. Chen, Z. Jia, G. Zhou, J. Xu, Y. Wu, X. Xia, X. Li, X. Zhang, C. Deng, Y. Zhang, X. Lu, W. Liu, C. Zhang, Y. Yang, Michael), H. Zhu, Triplet exciton formation for non-radiative voltage loss in high-efficiency nonfullerene organic solar cells, Joule 5 (7) (2021) 1832–1844, https://doi.org/10.1016/j.joule.2021.04.002.

[55] Q.-Q. Zhang, Y. Li, D. Wang, Z. Chen, Y. Li, S. Li, H. Zhu, X. Lu, H. Chen, C.-Z. Li, Intrinsically chemo- and thermostable electron acceptors for efficient organic solar cells, BCSJ 94 (1) (2021) 183–190, https://doi.org/10.1246/bcsj.20200231.

[56] C. Sun, S. Qin, R. Wang, S. Chen, F. Pan, B. Qiu, Z. Shang, L. Meng, C. Zhang, M. Xiao, C. Yang, Y. Li, High efficiency polymer solar cells with efficient hole transfer at zero highest occupied molecular orbital offset between methylated polymer donor and brominated acceptor, J. Am. Chem. Soc. 142 (3) (2020) 1465–1474, https://doi.org/10.1021/jacs.9b09939.

[57] Z. Chen, H. Zhu, Photoinduced charge transfer and recombination dynamics in star nonfullerene organic solar cells, J. Phys. Chem. Lett. 13 (4) (2022) 1123–1130, https://doi.org/10.1021/acs.jpclett.1c04247.

[58] S. Karuthedath, J. Gorenflot, Y. Firdaus, N. Chaturvedi, C.S.P. De Castro, G. T. Harrison, J.I. Khan, A. Markina, A.H. Balawi, T.A.D. Peña, W. Liu, R.-Z. Liang, A. Sharma, S.H.K. Paleti, W. Zhang, Y. Lin, E. Alarousu, S. Lopatin, D.H. Anjum, P. M. Beaujuge, S. De Wolf, I. McCulloch, T.D. Anthopoulos, D. Baran, D. Andrienko, F. Laquai, Intrinsic efficiency limits in low-bandgap non-fullerene acceptor organic solar cells, Nat. Mater. 20 (3) (2021) 378–384, https://doi.org/10.1038/s41563-020-00835-x.

[59] A.J. Gillett, A. Privitera, R. Dilmurat, A. Karki, D. Qian, A. Pershin, G. Londi, W. K. Myers, J. Lee, J. Yuan, S.-J. Ko, M.K. Riede, F. Gao, G.C. Bazan, A. Rao, T.-Q. Nguyen, D. Beljonne, R.H. Friend, The role of charge recombination to triplet excitons in organic solar cells, Nature 597 (7878) (2021) 666–671, https://doi.org/10.1038/s41586-021-03840-5.

Check for updates

Thermally Activated Reverse Electron Transfer Limits Carrier Generation Efficiency in PM6:Y6 Non-Fullerene Organic Solar Cells

Rokas Jasiūnas,* Huotian Zhang, Andrius Devižis, Marius Franckevičius, Feng Gao, and Vidmantas Gulbinas

Transient absorption and time-resolved fluorescence measurements in a wide temperature range are used to investigate the mechanism of charge carrier generation in efficient organic solar cells based on a PM6:Y6 donor–acceptor blend. The generation mechanisms differ significantly under excitation of a donor or acceptor. The investigations reveal a temperature-dependent interplay between the formation of interfacial charge transfer (CT) states and intramoiety CT states of the acceptor, their separation into free charge carriers and carrier recombination. The efficient charge carrier generation is ensured by the carrier separation over a small energy barrier, which is easily surmountable at room temperature. However, the overall yield of charge carrier generation at room temperature is reduced by the recombination of charge carriers due to the thermally activated back transfer of electrons from the acceptor to the donor via the highest occupied molecular orbit (HOMO) levels, which is enabled by the small energy offset between HOMO levels of the donor and the acceptor.

1. Introduction

Organic photovoltaic (OPV) technology has been gradually developing for few decades[1] and has experienced unprecedented improvement in recent years. The replacement of previously used fullerene derivatives with novel organic molecules known as non-fullerene acceptors (NFAs) has led to state-of-the-art power conversion efficiencies (PCEs) of over 17% in binary bulk heterojunction organic solar cells.[2–4] NFA-based blends exhibit short-circuit currents (J_{sc}) of over 25 mA cm^{-2} at standard

1.5 AM illumination conditions due to strong acceptor absorption, which is complementary redshifted compared to a donor.[5–8] Moreover, high J_{sc} values have been demonstrated in NFA systems with remarkably low HOMO energy offsets at the donor–acceptor heterojunctions.[9] Such low carrier generation reaction energies provide low voltage losses, typically slightly above 0.5 V.[10–12] Moreover, nonradiative voltage losses are suppressed in NFA-based devices compared to fullerene-based devices, due to the hybridization of the interfacial charge transfer (CT) state with the first excited state, which increases the oscillator strength of the CT state via an intensity borrowing mechanism.[10] In other work, the enhanced radiative decay efficiency in the NFA devices with negligible energy offset has been attributed to stationary-state equilibrium between excitons and CT states,[13] suggesting the use of highly luminescent near-infrared emitters for high-efficiency OPV devices.

In 2019, Zou et al. reported a novel NFA 2,20-((2Z,20Z)-((12,13-bis(2-ethylhexyl)- 3,9-diundecyl-12,13-dihydro-[1,2,5]thiadiazolo [3,4-e]thieno [2,″30′ :4′,50]thieno [20,30:4,5]pyrrolo [3,2-g]thieno [20,30:4,5]thieno [3,2-b]indole-2,10-diyl) bis (methanylylidene)) bis(5,6-difluoro-3-oxo-2, 3-dihydro-1H-indene-2,1-diylidene)) dimalononitrile (**Y6**), by employing a ladder-type electron deficient-core-based central fused ring with a benzothiadiazole core.[14] Matched with polymer donor poly[(2,6-(4,8-bis(5-(2-9 ethylhexyl-3-fluoro) thiophen-2-yl)-benzo [1,2-b:4, 5-b0] dithiophene))-alt-(5,5-(10,10 30-di-2-thienyl-50,70-bis(2-ethylhexyl) benzo [10,20-c:40,50-c0]dithiophene-4,8-11 dione))] (PM6), it became one of the best performing material combinations in OPVs, not only in single junction, but also in ternary configuration[15,16] and even in upscaled modules.[17] In recent years, several review articles have been devoted solely to the progress of the PM6:Y6 system.[18–20] Although the technical aspects of optimizing PM6:Y6 devices have been extensively covered, there is a clear lack of a comprehensive understanding of the physical basis of charge generation in these materials, which is critical for further improving device performance and developing even better NFAs. For example, two major works,[21,22] which scrutinize the photo-physics behind the operation of these PM6:Y6

R. Jasiūnas, A. Devižis, M. Franckevičius, V. Gulbinas
Department of Molecular Compound Physics
Center for Physical Sciences and Technology
LT-10257 Vilnius, Lithuania
E-mail: rokas.jasiunas@ftmc.lt

H. Zhang, F. Gao
Department of Physics Chemistry and Biology (IFM)
Linköping University
Linköping SE-58183, Sweden

The ORCID identification number(s) for the author(s) of this article can be found under https://doi.org/10.1002/solr.202100963.

DOI: 10.1002/solr.202100963

solar cells, reach somewhat different conclusions regarding the role of temperature in electron-hole separation. Wang et al.[21] argue that temperature-assisted charge hopping is involved in charge generation, whereas Perdigón-Toro et al.[22] conclude that the activation energy for dissociation of the CT states is extraordinarily low, at about 6 meV, and therefore photocurrent is efficiently generated down to 100 K. Notably, the studies were limited to 200 and 75 K, lowest temperatures, respectively.

Here, we report a detailed investigation of the charge carrier generation mechanism in the PM6:Y6 blend combining transient absorption (TA) and transient photoluminescence (tPL) at various temperatures down to 15 K. The wide temperature range has helped us to uncover previously undiscovered aspects of charge generation in this state-of-the-art photovoltaic material. We show that three distinctly different charge generation pathways coexist: one under excitation of the donor and two under excitation of the acceptor. All of these pathways ensure efficient charge carrier generation at room temperature (RT). However, the final generation efficiency is reduced by the carrier recombination channel opened by the small offset between the HOMO levels of donor PM6 and acceptor Y6.

2. Results

Figure 1 presents the main spectroscopic and electronic properties of PM6 and Y6 materials and their solar cells. The absorption spectra of this donor–acceptor pair ensure efficient absorption of all visible and near IR light and result in a high short-circuit current of over 23 mA cm^{-2}. A small energy offset between the HOMO levels of the donor and acceptor causes high open-circuit voltage (V_{OC}). The charge carrier generation efficiencies upon light absorption by the donor and the acceptor are comparable, but, as we will show, the generation pathways are very different. We have investigated both pathways through TA studies of the blend films and the pure donor and acceptor films. The blend study was performed with two different excitation wavelengths to ensure a dominant excitation of the donor or the acceptor. Time-resolved photoluminescence spectroscopy was also used to reveal additional details of the charge carrier generation mechanism.

2.1. Transient Absorption: Excitation of the Donor

To investigate the generation of charge carriers in the PM6:Y6 blend upon excitation of a donor PM6, the donor was preferentially excited with 560 nm light, which is only weakly absorbed by the acceptor (see Figure 1). **Figure 2**a shows the time evolution of the TA spectrum at RT. The black and brown dashed lines also show the normalized TA spectra of the pure donor PM6 and pure acceptor Y6 films, which clearly show the ground state absorption bleaching (GSB) bands of the respective materials. TA spectrum of the blend shows the same bleaching bands at
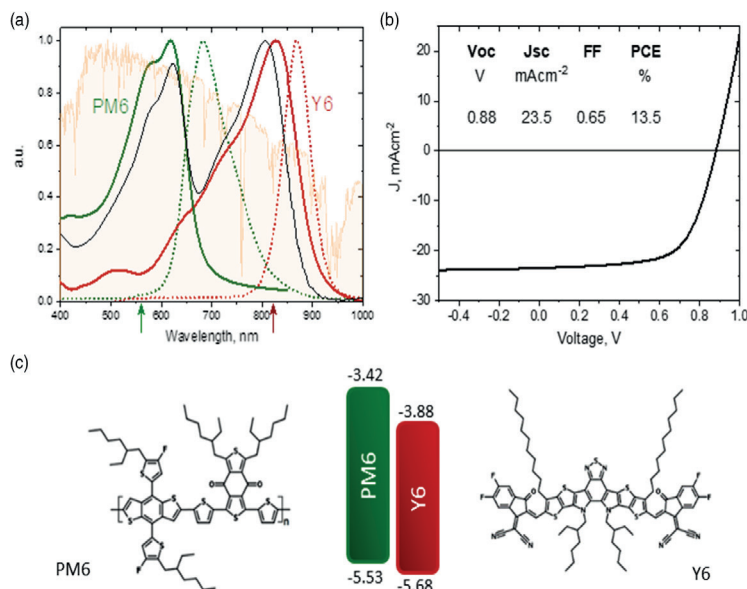

Figure 1. a) Steady-state absorption spectra of the PM6:Y6 blend (black curve) and the neat PM6 and Y6 films (green and red solid curves) and photoluminescence spectra of the neat films (dashed curves). The light orange curve represents 1.5 AM solar irradiation spectrum. The arrows indicate the wavelength used to excite the blend in the transient absorption (TA) measurements; b) *J–V* characteristics of the PM6:Y6 device. c) Chemical structure and energy levels of PM6 and Y6 materials as measured by cyclic voltammetry (CV) (see Supporting Information for details and Figure S1, Supporting Information, for CV curves).

625–650 nm and 820–860 nm corresponding to the GSB of donor PM6 (D_{GSB}) and acceptor Y6 (A_{GSB}). Figure 2b,c shows the kinetics of the GSB intensities of the two components at different temperatures. To avoid inaccuracies in the GSB signal dynamics caused by the GSB band shift, the kinetics shown were obtained by integrating the TA signal values in the 570–650 nm
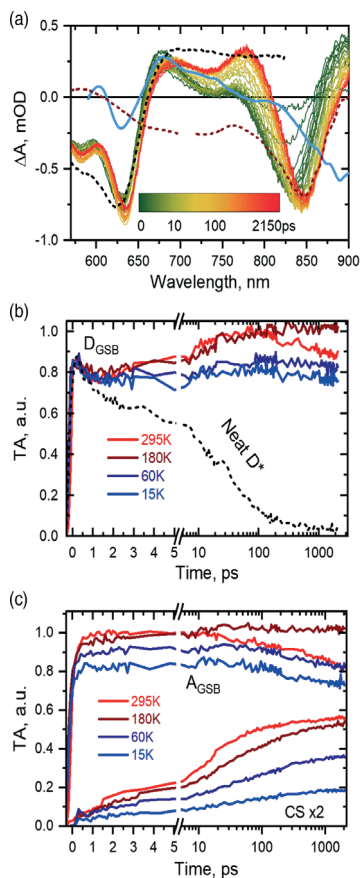

Figure 2. a) Evolution of the TA spectra of the blend at RT after excitation with 560 nm laser pulse. The black and brown dashed curves show the normalized TA spectra of donor and acceptor neat films 1 ps after excitation with a 560 or 820 nm laser pulse, respectively (see Figure S2, Supporting Information, for full spectral dynamics). The solid light blue curve indicates the electroabsorption spectrum of the blend; b) Kinetics of ground state bleaching of the donor obtained by integrating the TA spectrum in the donor absorption band region (570–650 nm); c) Kinetics of the ground state bleaching of the acceptor, obtained by integrating the TA spectrum in the acceptor absorption band region (770–890 nm), and kinetics of the induced absorption of charge-separated (CS) states, obtained by integrating the TA spectrum in the 750–775 nm region.

range for D_{GSB}, and in the 770–890 nm range for A_{GSB}. Next, to avoid possible slight variations in excitation intensity at different temperatures, the kinetics were corrected by normalizing the initial donor absorption bleaching intensity, based on the reasonable assumption that the number of donor molecules initially excited at a fixed excitation intensity is independent of temperature. Excitation of the donor leads to an immediate (within the response time of the device) increase in the D_{GSB} signal, while bleaching of the acceptor is slightly delayed (≈1 ps), which is consistent with the time required for complete electron transfer from the excited donor (D*) to the acceptor to form an interfacial CT state or a pair of free charge carriers (referred as CS [charge separated]) with holes and electrons located in the donor and acceptor domains, respectively. Thus, both CT and CS states correspond to the ionized donor D^+ and acceptor A^-. Notably, the strong instantaneous A_{GSB} signal component indicates that most electrons are transferred from the excited donor to the acceptor much faster than our time resolution of about 200 fs, which is also typical for fullerene[23–26] and other non-fullerene blends.[27–30] The A_{GSB} signal value is slightly lower at reduced temperatures (by ≈20% at 15 K [Figure 2c]), indicating that the efficiency of CT state formation decreases slightly at low temperatures. Such a slight decrease is expected because the diffusion lengths of the excitons are shorter at low temperatures and thus the excitons cannot reach the D–A interface.[31] Importantly, the weak temperature dependence shows that the electron transfer involved in the formation of the CT state is a barrierless process, in agreement with the large difference between the lowest unoccupied molecular orbit (LUMO) energies of the donor and acceptor (≈0.6 eV).

After the immediate appearance, the D_{GSB} decreases slightly during the first 1 ps, regardless of temperature. This decrease occurs simultaneously with the final development of A_{GSB} and, thus probably reflects the difference between TA caused by the D* and D^+ states. A stronger TA, caused by D*, is to be expected, as stimulated emission may contribute to TA in addition to D_{GSB}. Such a decrease may also be caused by the rapid relaxation of fraction of the D* states to the ground state (which is supported by the similar decay rate of a neat donor, dotted curve as shown in Figure 1b). Importantly, the discussed decay of the D_{GSB} signal was identical at the reduced excitation intensity (see Figure S3, Supporting Information), which ensures that our measurements were performed within the limit of low excitation intensity when the nonlinear intensity-dependent recombination processes can be neglected. After the slight decay, the D_{GSB} increases again on a time scale of tens of picoseconds, but this increase is less pronounced at low temperatures. A similar increase was previously reported by Wang et al.[21] and was vaguely attributed to an additional electro-absorption (EA) component that enhances the D_{GSB} signal. The EA signal is caused by alternated absorption of unexcited molecules in the presence of induced local electric fields generated by the CT and CS states. The electric field in the CT state is mainly confined between donor and acceptor molecules forming the CT state and therefore has only a weak effect on neighboring molecules. A larger distance between separated charge carriers in CS states leads to expansion of the electric field area. Neutral molecules appear in a strong electric field between and around the charges and enhance the EA spectral signature. Therefore,

the EA signal has been used as a probe to track the charge carrier separation dynamics.[25,32]

To verify the role of the EA in the formation of the TA spectra and their dynamics in the given blend, we measured the EA spectra induced by an external electric field (Figure S5, Supporting Information). The shape of the EA spectrum with a small kink at ≈600 nm, the main D_{GSB} band at ≈630 nm, and the induced absorption at 675 nm strongly resembles the measured TA spectra, however, is blueshifted by about 20 nm. To illustrate this similarity, the light blue curve in Figure 2a shows the spectrum of EA redshifted by 20 nm. Such a shift can be caused by different EA formation conditions under macroscopic and local electric fields. The local fields mainly affect molecules that are close to the donor–acceptor interfaces and may have slightly different spectral properties. The local fields may also be much stronger than the applied macroscopic field. Indeed, the measured EA spectrum tends to broaden and redshift with increasing electric field strength (as shown in Figure S3, Supporting Information), approaching the TA spectrum of the blend. Consequently, our results confirm the hypothesis about the effect of EA on the growth of the D_{GSB} signal and, more importantly, provide a tool to probe the dynamics of CT state dissociation to CS state. An alternative approach to probe the dynamics of the formation of CS in the PM6:Y6 blend was proposed by Wang et al.,[21] where the authors attributed the 750–790 nm induced absorption band to the absorption of CS states or, more specifically, to the holes in PM6. Though, our data suggest that an attribution to the absorption of holes is rather rash: there are several different constituents in the 750–790 nm range, originating from the **A***, **D***, EA, CT, and CS states; therefore, this band might be only phantomlike and originate from a changed equilibrium between these constituents during charge separation. Nevertheless, we agree with authors of ref.[21] that the intensity of this band is roughly proportional to the CS state concentration. The dynamics of CS state formation and its temperature dependence, which results from the dynamics of this band intensity, is shown in Figure 1c. On the time scale of 1–100 ps, it closely matches the increasing D_{GSB} signal at all temperatures, which is also due to the fact that the CS state formation increases the EA signal.

Although an accurate quantitative assessment of charge separation efficiency based on the spectral features described earlier is problematic, we can reasonably assume that the CS state formation rate is roughly proportional to the increase rate of these spectral features and therefore apply the Arrhenius formalism to estimate the barrier to the formation of the CS state. The procedure for evaluating CS state formation rate is illustrated in SI Figure S4, Supporting Information (SI), together with the Arrhenius plot obtained. Arrhenius plot deviates strongly from the linear dependence. At 300 and 180 K, we obtain an activation energy of ≈14 meV, while at lower temperatures activation energies are lower. Nevertheless, the deduced low activation energy is in reasonable agreement with the value of 6 meV reported by Perdigón-Toro et al.[22] Such low activation energy was explained by the electrostatic bias potential arising from the large quadrupolar moments of Y6 and the specific acceptor–donor–acceptor molecular architecture that compensates for the Coulomb bonding of the CT state. Our data show that the formation rate of CS states at low temperatures is much larger than predicted by Arrhenius dependence. The 15 K used in our work corresponds

to a kT of ≈1 meV, at which even a marginal barrier of a few meV for the dissociation of the CT state can hardly be overcome. It should be noted that, according to the CS kinetics presented in Figure 2c, most CS states are generated during a several picoseconds after excitation, especially at 15 K. It hints that CT state dissociation occurs at least in part from non-equilibrated (hot) CT state, similar to what is observed in some fullerene-based solar cells.[33–35] A higher degree of delocalization of the hot CT excitons compared to the relaxed ones increases the probability of charge dissociation.[36] Such hot-state dissociation together with a low activation energy explains the very weak temperature dependence of the CS state formation.

The TA dynamics during 0.1–2 ns deserves special attention. The simultaneous decay of donor and acceptor bleaching bands shows that the charge carrier recombination takes place in this time range. Recombination is the most pronounced at RT, but does not occur or is much weaker at 180 K and regains significance at very low temperatures. This process reduces the electron and hole densities by about 10% during 2 ns at RT. The enhanced recombination at very low temperatures can be explained by the fact that large fraction of CT states does not split into CS states. Therefore, CT states eventually recombine by the retransfer of electron from the LUMO of the acceptor to the HOMO of the donor. This process becomes less efficient at higher temperatures, when the CT states split into CS states more rapidly. However, this mechanism also predicts that carrier recombination at RT should be particularly weak when the CT states split very quickly. The rapid recombination at RT therefore suggests that there is an additional, thermally-activated recombination channel. Considering a small energy offset of ≈150 meV between the HOMO levels of donor and acceptor, there could be a thermally activated reverse electron transfer from HOMO of the acceptor to HOMO of the donor (it may also be considered as a reverse hole transfer), producing the A* state of the acceptor. This channel may also cause recombination of already generated charge carries if they geminately or non-geminately recreate CT states. Since the relaxation of the excited acceptor Y6 (as discussed later) is much faster than the direct recombination (relaxation) of the CT state, this reverse transfer process creates an additional recombination channel activated at RT.

2.2. Excitation of the Acceptor

Let us now examine the path of charge generation by excitation of acceptor Y6. **Figure 3**a shows the time evolution of the TA spectrum of the PM6:Y6 blend excited at 820 nm at RT. The instantaneous (within experimental resolution) A_{GSB} signal is followed by a two-phase D_{GSB} signal growth (Figure 3b,c). The fast phase, which is limited by our time resolution, accounts for about 40% of the total D_{GSB} signal at RT. We assign it to conventional direct hole transfer from the excited acceptor (**A***) to the donor, which forms identical interface CT states as in the case of excitation of a donor. The remaining ≈60% of the D_{GSB} evolves on a timescale of several hundreds of picoseconds. According to Wang et al.,[21] this slow hole transfer channel is mediated via peculiar intramoiety CT state (xCT) of an acceptor, which forms at RT during ≈0.2 ps and dissociates into free polarons within ≈15 ps. Our data are consistent with this interpretation. Accordingly, we
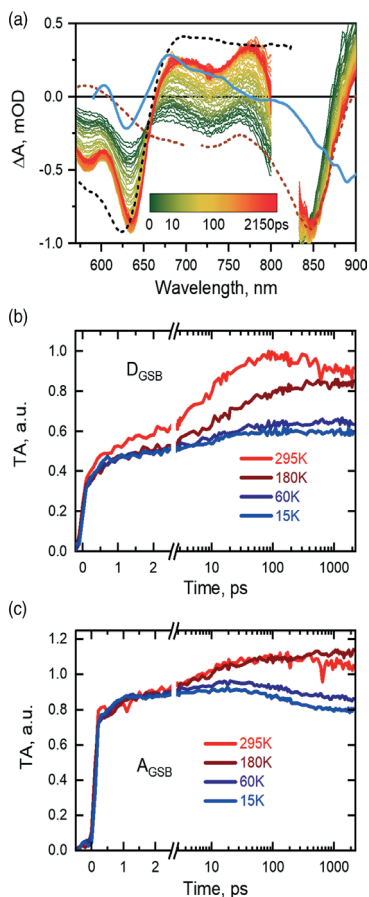
Figure 3. a) Evolution of the transient absorption spectra of the PM6:Y6 blend after 820 nm laser excitation. The black and brown dashed curves show the normalized TA spectra of donor and acceptor neat films 1 ns after 560 or 820 nm excitation, respectively. The light blue curve shows electroabsorption spectrum; b) Donor ground state bleaching kinetics obtained by integrating the TA spectrum in the donor absorption band region (570–650 nm). c) Acceptor ground state bleaching kinetics, obtained by integrating TA spectrum in the acceptor absorption band region (770–890 nm).

attribute the slow D_{GSB} growth phase to delayed hole transfer from the xCT state or from free electron-hole pairs formed in the acceptor. An additional contribution to the D_{GSB} growth may come from the formation of CS states. This process is supported by the delayed (≈ 10 ps) appearance of a kink at 570–625 nm (Figure 3a) in the TA signal, which is specifically characteristic of EA spectra and absent in the initial D_{GSB} signal. However, the contribution of EA can hardly be greater than in the case of donor excitation, resulting in a D_{GSB} growth by about

20% at RT. Therefore, most of the growth should still be attributed to delayed hole transfer mediated by xCT states. Importantly, D_{GSB} growth slows at low temperatures and is marginal at 15 K, indicating that hole transfer mediated by xCT states requires thermal assistance.

The evolution of TA on a timescale of hundreds of picoseconds and a few nanoseconds is very similar to that observed under excitation of the donor: we observe a decay of the entire TA spectrum at RT, which disappears at a temperature reduced to 240 K, but is observed again at even lower temperatures. Consequently, both donor and acceptor excitation lead to approximately the same system state during about 100 ps. This state is composed of the CT and CS states, with the ratio depending on the temperature. As with donor excitation, the observed TA decay at RT should be attributed to the reverse electron transfer to the donor.

2.3. Transient Photoluminescence

To confirm the earlier made conclusions and to further elucidate the mechanisms of charge carrier generation, we have performed tPL studies with a temporal resolution of less than 5 ps. We used an excitation wavelength of 515 nm, which predominantly excites the donor, although weak excitation of the acceptor is also present. It was shown in ref.[37] that the CT state manifold in the PM6:Y6 blend emits only very weakly and is even referred to as dark. Therefore, we can state that PL originates only from neutral-excited singlet states of donor and acceptor (D* and A*), so that the intensity of PL unambiguously represents the concentrations of D* and A*. **Figure 4**a shows the temporally (0–120 ps) integrated PL spectra of the blend at different temperatures. Despite the dominant excitation of the donor, the time-integrated PL of the donor is very weak and changes only slightly with temperature, which is in good agreement with the rapid and barrierless formation of interfacial CT states.

In contrast, the PL intensity of the acceptor is much stronger and decreases sharply with temperature. Zhu et al. have recently demonstrated that the photoluminescence intensity of pure Y6 film also decreases at lower temperatures.[38] This unconventional behavior was explained by the assumption that strong polarization effects reduce the energy of the charge-separated state (xCT) even below that of the lowest excited singlet state, resulting in effective charge separation within the Y6 material. The fluorescence of Y6 is attributed to thermal repopulation of the A* state—a kind of thermally activated luminescence (TAL) with an activation energy of ≈ 185 meV, which is easily overcome at RT, but strongly hinders exciton reforming and thus luminescence at lower temperatures. We observe a similar trend in blend, where PL intensity decreases about threefold when the temperature is reduced from RT to 60 K (see Figure 4a), and remains stable at lower temperatures. However, this decrease is much weaker than the ≈ 20-fold PL decrease in the pure Y6 film (Figure 4b).

The PL kinetics of Y6 in the neat film and in the PM6:Y6 blend presented in Figure 4c explain the mentioned difference in temperature dependence (Figure S6, Supporting Information, shows the decay kinetics at more temperature points). At very low temperatures, PL of the neat Y6 film and the PM6:Y6 blend decays identically, indicating that only intramolecular processes in Y6,
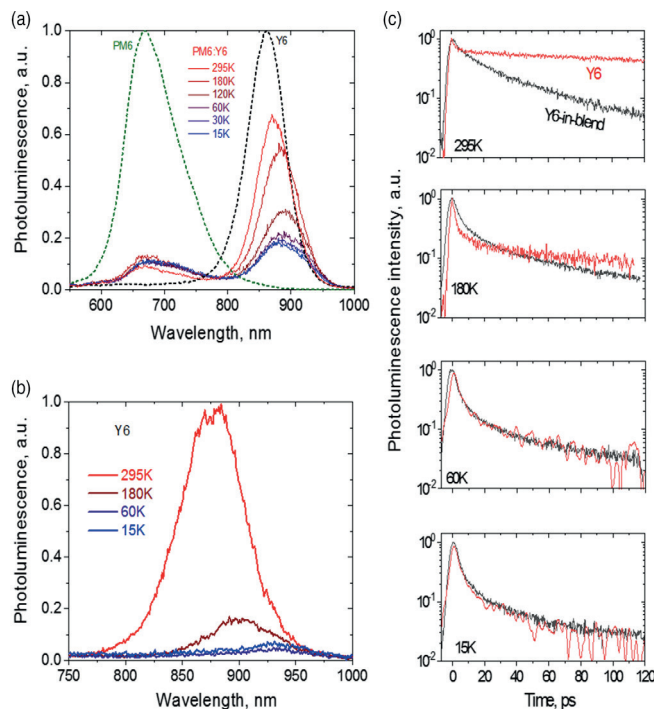
Figure 4. Temporally integrated (0–120 ps) photoluminescence spectra of a) PM6:Y6 blend and b) Y6 film at various temperatures after excitation with a 515 nm laser pulse. The green and black dashed curves in (a) indicate the photoluminescence spectra of the neat PM6 and Y6 films; c) Y6 and Y6-in-blend photoluminescence kinetics at various temperatures.

namely the barrierless formation of nonfluorescent xCT states determines the PL decay. At 180 K and higher temperatures, a slow PL component appears in the neat Y6 film due to thermal repopulation of the A* state and causes a dramatic increase in the steady-state PL as shown in Figure 4b. While at high temperatures, the PL decay of the blend becomes much faster than that of the neat Y6 because hole transfer from the xCT state to the donor rapidly decimates the xCT state population and prevents the repopulation of the A* state, thus mitigates the increase of the steady-state PL intensity with temperature making it less impressive than in the pure Y6 film. This agrees well with the TA kinetics of the blend under excitation of the acceptor, which shows that only the ultrafast PM6 bleaching component caused by hole transfer from the "hot" A* state takes place at very low temperatures, while at higher temperatures PM6 bleaching related to the hole transfer continues for hundreds of picoseconds.

3. Carrier Generation and Recombination Model

The schematics shown in **Figure 5** summarize the experimental data and show the main electronic processes that occur in the

solar cell during the first few nanoseconds under excitation of the donor and acceptor. Black arrows show processes that do not require thermal activation, while red arrows show thermally activated processes. As it is shown, the formation of the CT states does not require thermal assistance under either donor or acceptor excitation. Moreover, some of the **D*** (or **A***) states that are not yet in equilibrium form CS even without thermal assistance in a time scale of less than one picosecond (denoted as (a)). In contrast, the formation of the CS states from equilibrated CT states requires thermal assistance and stops almost completely at 60 K (b). Excitation of the acceptor also leads to additional, temperature-independent formation of the xCT state during a few picoseconds (c). However, the subsequent formation of CS states requires thermal assistance (d). Consequently, the generation of free charge carriers occurs by a temperature-independent process from non-equilibrated **D*** and **A*** states (a) and by thermally activated separation of CT (b) and xCT (d) states. The solid black arrows show the non-radiative recombination pathways (e). The partial recovery of the acceptor absorption on an nanoseconds time scale at temperatures below 180 K, when the reformation of **A*** and the formation of the CT state do not occur (see Figure 2 and 3), indicates the presence of a
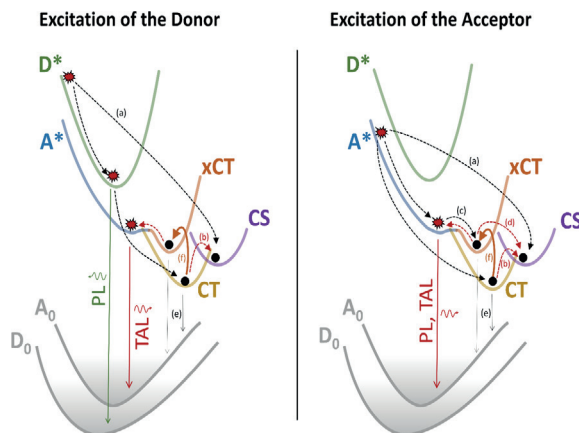
143

Figure 5. Schematic representation. Explanation in the text.

temperature-independent relaxation channel of the xCT state to the acceptor ground state. This is a loss channel but is less efficient at higher temperatures when the formation of the CT state and the reformation of the A* state are present. The xCT state is also subject to recombination through the reformation of the A* state. This pathway is represented by the TAL. However, the TAL signal decays much faster in the blend at RT than in the pure Y6 film, so this loss channel is obviously not significant.

The thick dark orange curves (f) show the reverse electron transfer to the donor (or hole transfer to the acceptor) opened by a small HOMO level offset that reopens the e–h recombination pathway in the acceptor and creates an additional channel for the solar cell efficiency loss.

4. Conclusions

In this work, we have investigated the mechanism of charge carrier generation in PM6:Y6 bulk heterojunctions using TA and tPL at temperatures ranging from 295 K down to 15 K. There are different pathways of charge carrier generation and recombination that depend on either excitation of the donor or acceptor. When the donor is photoexcited, the generation of interfacial CT excitons is almost temperature independent, while their separation into free charge carriers is highly suspended at low temperatures and dominated by ultrafast separation from nonequilibrated interfacial CT state. When an acceptor is excited, charge carrier generation occurs via two different pathways: the interfacial CT state and the intra-moiety xCT state, and both pathways contribute about equally at RT. The conventional pathway is almost temperature independent, whereas charge carrier generation via the xCT state requires thermal assistance. Charge carrier recombination also occurs via thermally independent recombination of interfacial CT and xCT states, and via thermally activated reverse electron transfer from the acceptor to the donor, which is related to the small HOMO level offset and restores the singlet exciton state of the acceptor. The latter channel is the

most significant at RT and causes a loss of charge carrier generation efficiency of more than 10%. Consequently, a small energy offset between the HOMO levels of donor and acceptor opens an additional loss channel. This relaxation pathway requires a subtle balance between minimizing the HOMO level offset, which increases *Voc* but causes current losses due to reverse electron transfer.

Supporting Information

Supporting Information is available from the Wiley Online Library or from the author.

Conflict of Interest

The authors declare no conflict of interest.

Data Availability Statement

Research data are not shared.

Keywords

[1] O. Inganäs, *Adv. Mater.* **2018**, *30*, 1800388.
[2] F. Qi, K. Jiang, F. Lin, Z. Wu, H. Zhang, W. Gao, Y. Li, Z. Cai, H. Y. Woo, Z. Zhu, A. K.-Y. Jen, *ACS Energy Lett.* **2021**, *6*, 9.

[3] L. Liu, Y. Kan, K. Gao, J. Wang, M. Zhao, H. Chen, C. Zhao, T. Jiu, A. Y. Jen, Y. Li, *Adv. Mater.* **2020**, *32*, 1907604.

[4] R. Ma, T. Liu, Z. Luo, Q. Guo, Y. Xiao, Y. Chen, X. Li, S. Luo, X. Lu, M. Zhang, Y. Li, H. Yan, *Sci. China Chem.* **2020**, *63*, 325.

[5] B. Fan, D. Zhang, M. Li, W. Zhong, Z. Zeng, L. Ying, F. Huang, Y. Cao, *Sci. China Chem.* **2019**, *62*, 746.

[6] Q. He, M. Shahid, J. Wu, X. Jiao, F. D. Eisner, T. Hodsden, Z. Fei, T. D. Anthopoulos, C. R. McNeill, J. R. Durrant, M. Heeney, *Adv. Funct. Mater.* **2019**, *29*, 1904956.

[7] Z. Zheng, R. Wang, H. Yao, S. Xie, Y. Zhang, J. Hou, H. Zhou, Z. Tang, *Nano Energy* **2018**, *50*, 169.

[8] F. Cai, H. Peng, H. Chen, J. Yuan, J. Hai, T.-K. Lau, J. Wang, Y. Hu, W. Liu, X. Lu, Y. Zou, *J. Mater. Chem. A* **2020**, *8*, 15984.

[9] B. Kan, J. Zhang, F. Liu, X. Wan, C. Li, X. Ke, Y. Wang, H. Feng, Y. Zhang, G. Long, R. H. Friend, A. A. Bakulin, Y. Chen, *Adv. Mater.* **2018**, *30*, 1704904.

[10] F. D. Eisner, M. Azzouzi, Z. Fei, X. Hou, T. D. Anthopoulos, T. J. S. Dennis, M. Heeney, J. Nelson, *J. Am. Chem. Soc.* **2019**, *141*, 6362.

[11] X. Liu, X. Du, J. Wang, C. Duan, X. Tang, T. Heumueller, G. Liu, Y. Li, Z. Wang, J. Wang, F. Liu, N. Li, C. J. Brabec, F. Huang, Y. Cao, *Adv. Energy Mater.* **2018**, *8*, 1801699.

[12] D. Yang, Y. Wang, T. Sano, F. Gao, H. Sasabe, J. Kido, *J. Mater. Chem. A* **2018**, *6*, 13918.

[13] A. Classen, C. L. Chochos, L. Lüer, V. G. Gregoriou, J. Wortmann, A. Osvet, K. Forberich, I. McCulloch, T. Heumüller, C. J. Brabec, *Nat. Energy* **2020**.

[14] J. Yuan, Y. Zhang, L. Zhou, G. Zhang, H.-L. Yip, T.-K. Lau, X. Lu, C. Zhu, H. Peng, P. A. Johnson, M. Leclerc, Y. Cao, J. Ulanski, Y. Li, Y. Zou, *Joule* **2019**, *3*, 1140.

[15] T. Yan, W. Song, J. Huang, R. Peng, L. Huang, Z. Ge, *Adv. Mater.* **2019**, *31*, 1902210.

[16] Q. Ma, Z. Jia, L. Meng, J. Zhang, H. Zhang, W. Huang, J. Yuan, F. Gao, Y. Wan, Z. Zhang, Y. Li, *Nano Energy* **2020**, *78*, 105272.

[17] A. Distler, C. J. Brabec, H. Egelhaaf, *Prog. Photovolt. Res. Appl.* **2021**, *29*, 24.

[18] Z.-C. Wen, H. Yin, X.-T. Hao, *Surf. Interfaces* **2021**, *23*, 100921.

[19] Q. Guo, Q. Guo, Y. Geng, A. Tang, M. Zhang, M. Du, X. Sun, E. Zhou, *Mater. Chem. Front.* **2021**, *5*, 3257.

[20] R. Yu, G. Wu, Z. Tan, *J. Energy Chem.* **2021**, *61*, 29.

[21] R. Wang, C. Zhang, Q. Li, Z. Zhang, X. Wang, M. Xiao, *J. Am. Chem. Soc.* **2020**, *142*, 12751.

[22] L. Perdigón-Toro, H. Zhang, A. Markina, J. Yuan, S. M. Hosseini, C. M. Wolff, G. Zuo, M. Stolterfoht, Y. Zou, F. Gao, D. Andrienko, S. Shoaee, D. Neher, *Adv. Mater.* **2020**, *32*, 1906763.

[23] A. Devižis, A. Serbenta, K. Meerholz, D. Hertel, V. Gulbinas, *Phys. Rev. Lett.* **2009**, *103*, 027404.

[24] H. Tamura, I. Burghardt, *J. Am. Chem. Soc.* **2013**, *135*, 16364.

[25] S. Gélinas, A. Rao, A. Kumar, S. L. Smith, A. W. Chin, J. Clark, *Science* **2014**, *343*, 6.

[26] V. Abramavicius, V. Pranculis, A. Melianas, O. Inganäs, V. Gulbinas, D. Abramavicius, *Sci. Rep.* **2016**, *6*, 32914.

[27] S. Chen, S. Myeon Lee, J. Xu, J. Lee, K. Cheol Lee, T. Hou, Y. Yang, M. Jeong, B. Lee, Y. Cho, S. Jung, J. Oh, Z.-G. Zhang, C. Zhang, M. Xiao, Y. Li, C. Yang, *Energy Environ. Sci.* **2018**, *11*, 2569.

[28] V. A. C. Franco, N. Gasparini, T. Nagahara, L. Lüer, G. Cerullo, C. Brabec, *EPJ Web Conf.* **2019**, *205*, 05010.

[29] D. M. Stoltzfus, J. E. Donaghey, A. Armin, P. E. Shaw, P. L. Burn, P. Meredith, *Chem. Rev.* **2016**, *116*, 12920.

[30] N. Gasparini, A. Wadsworth, M. Moser, D. Baran, I. McCulloch, C. J. Brabec, *Adv. Mater. (Weinheim, Ger.)* **2018**, *8*, 1703298.

[31] O. V. Mikhnenko, F. Cordella, A. B. Sieval, J. C. Hummelen, P. W. M. Blom, M. A. Loi, *J. Phys. Chem. B* **2008**, *112*, 11601.

[32] Y. Tamai, Y. Fan, V. O. Kim, K. Ziabrev, A. Rao, S. Barlow, S. R. Marder, R. H. Friend, S. M. Menke, *ACS Nano* **2017**, *11*, 12473.

[33] K. Chen, A. J. Barker, M. E. Reish, K. C. Gordon, J. M. Hodgkiss, *J. Am. Chem. Soc.* **2013**, *135*, 18502.

[34] S. D. Dimitrov, A. A. Bakulin, C. B. Nielsen, B. C. Schroeder, J. Du, H. Bronstein, I. McCulloch, R. H. Friend, J. R. Durrant, *J. Am. Chem. Soc.* **2012**, *134*, 18189.

[35] A. Devizis, K. Meerholz, D. Hertel, V. Gulbinas, *Phys. Rev. B* **2010**, *82*, 155204.

[36] G. Grancini, M. Maiuri, D. Fazzi, A. Petrozza, H.-J. Egelhaaf, D. Brida, G. Cerullo, G. Lanzani, *Nat. Mater.* **2013**, *12*, 29.

[37] L. Perdigón-Toro, L. Q. Phuong, S. Zeiske, K. Vandewal, A. Armin, S. Shoaee, D. Neher, *ACS Energy Lett.* **2021**, *6*, 557.

[38] L. Zhu, J. Zhang, Y. Guo, C. Yang, Y. Yi, Z. Wei, *Angew. Chem., Int. Ed.* **2021**, *60*, 15348.

NOTES

NOTES